Synthèse de matériaux nitrures fonctionnels à base de bore ou d'aluminium pour des applications en énergie (production et stockage de l'hydrogène)

Chrystelle Salameh

Collège Doctoral du Languedoc-Roussillon

THÈSE

Pour obtenir le grade de

Docteur

Délivré par **l'Université Montpellier 2**

Préparée au sein de **l'école doctorale de chimie**
Et de l'unité de recherche **UMR5635**

Spécialité : **Chimie et physico-chimie des matériaux**

Présentée par **Chrystelle Mounir SALAMEH**

Synthèse de matériaux nitrures fonctionnels à base de bore ou d'aluminium pour des applications en énergie (production et stockage de l'hydrogène)

Soutenue le 04/12/14 devant le jury composé de

Prof. Gian Domenico SORARU, Professeur - Université de Trento, Italie	Rapporteur
Prof. Petra E. DE JONGH, Professeur - Université d'Utrecht, Pays-bas	Rapporteur
Prof. Christel LABERTY, Professeur - Université Paris 6	Examinatrice
Prof. Etienne DUGUET, Professeur - Université de Bordeaux	Président
Prof. Philippe MIELE, Professeur - ENSCM	Directeur de thèse
Dr. Samuel BERNARD, Chargé de Recherche - CNRS	Co-encadrant
Dr. Umit B. DEMIRCI, Maître de Conférences - Université Montpellier 2	Co-encadrant

UNIVERSITÉ MONTPELLIER 2
SCIENCES ET TECHNIQUES

DEFINITION

AlN: Aluminum nitride

AC: Activated Carbon

AB: Ammoniaborane

BN: Boron nitride

CVD: Chemical Vapor Deposition

DOE: Department of energy

DVB: Divinyl benzene

H_2: Molecular hydrogen

H: Atomic hydrogen

HHV: Higher Heating Value

LHV: Lower Heating Value

PEMFC: Proton Exchange Membrane Fuel Cell

PDCs: Polymer-Derived Ceramics

PMMA: Polymethylmethacrylate

SiAlCN: Aluminum-modified Silicon CarboNitride

SiBCN: Boron-modified Silicon CarboNitride

SiC: Silicon Carbide

Si_3N_4: Silicon Nitride

SPS: Spark Plasma Sintering

WP: Warm Pressing

TABLE OF CONTENTS

General introduction....2
I- Literature survey....10
1. Introduction....14
2. Hydrogen production and storage....15
2.1. Hydrogen production....15
2.1.1 Off-board hydrogen production....15
2.1.2 On-board hydrogen production....16
2.2. Hydrogen storage....18
2.2.1 Liquid hydrogen....18
2.2.2 High pressure gas....18
2.2.3 Solid-state hydrogen storage....19
3. (Carbo)Nitride ceramics and derivatives....30
3.1. Definition/Applications of (Carbo)Nitride Ceramics....30
3.2. Synthesis of (Carbo)Nitride ceramics....31
3.2.1 Chemical Vapor Deposition....31
3.2.2 Sol-Gel....31
3.2.3 Polymer-Derived Ceramics....32
4. Polymer-Derived (Carbo)Nitrides....36
4.1. Alumium Nitride....36
4.1.1 Structure and properties....36
4.1.2 Fabrication routes of Aluminum Nitride....38
4.1.3 Polymer-Derived Aluminum Nitride....39
4.2. Boron Nitride....41
4.2.1 Structure and properties....41
4.2.2 Hexagonal Boron Nitride....42
4.2.3 Polymer-Derived Boron Nitride....43
4.3. Aluminum- and Boron-containing SilicoCarboNitrides....48
4.3.1 Aluminum-modified SilicoCarboNitride....49
4.3.2 Boron-modified SilicoCarboNitride....50
5. Polymer-Derived Porous (Carbo)Nitrides....55
5.1. Definition of the porosity....55
5.2. Process methods of porous ceramics....56
5.2.1 Porous BN....59
5.2.2 Porous SiBCN....60
6. Conclusion....61

II- Porous AlN as host material for the nanoconfinement of $NaAlH_4$ 64
1. Introduction 68
2. PEIA-derived AlN 68
2.1. Introduction 68
2.2. Experimental part 69
2.2.1 Materials 69
2.2.2 Preparation of PEIA-derived AlN 69
2.2.3 Experiments 71
2.3. Results and discussions 71
2.3.1 PEIA synthesis and characterization 71
2.3.2 PEIA-to-AlN conversion 74
3. Porous AlN from CMK-3 81
3.1. Experimental part 81
3.1.1 Materials 81
3.1.2 Elaboration of meso-/macroporous AlN 82
3.1.3 Experiments 83
3.2. Results and discussion 84
4. AlN AEROGELS 89
4.1. Experimental part 89
4.1.1 Materials 89
4.1.2 Elaboration of PEIA-derived AlN aerogels 89
4.1.3 Experiments 91
4.2. Results and discussion 92
5. Nanoconfinement of $NaAlH_4$ 96
5.1. Introduction 96
5.2. Experimental part 98
5.2.1 Materials 98
5.2.2 Nanoconfinement protocol 99
5.2.3 Experiments 99
5.3. Results and discussion 99
5.3.1 Preparation of $NaAlH_4$@host material 99
5.3.2 Characterization of $NaAlH_4$@porous AlN 100
6. Conclusion 102
III- Porous BN as host material for the nanoconfinement of ab 104
1. Introduction 108
2. PB-derived BN 109
2.1. Experimental part 109

2.1.1 Materials 109
2.1.2 Preparation of PB-derived BN 109
2.1.3 Experiments 112
2.2. Results and discussion 113
3. Mesoporous BN from Activated Carbon 116
3.1. Experimental part 116
3.1.1 Materials 116
3.1.2 Elaboration of mesoporous BN monoliths 117
3.1.3 Experiments 118
3.2. Results and discussion 119
4. BN aerogels 123
4.1. Experimental part 123
4.1.1 Materials 123
4.1.2 Preparation of PB-derived BN aerogels 124
4.1.3 Experiments 125
4.2. Results and discussion 126
5. Nanoconfinement of ammoniaborane 132
5.1. Introduction 132
5.2. Experimental part 133
5.2.1 Materials 133
5.2.2 Nanoconfinement protocol 133
5.2.3 Experiments 134
5.3. Results and discussion 134
6. Conclusion 139
IV- Ordered Mesoporous SiAlCN AND Si_3N_4 ceramics for hydrogen generation 140
1. Introduction 144
2. Preparation of Pt supported ordered mesoporous SiAlCN ceramics 149
2.1. Experimental part 149
2.1.1 Materials 149
2.1.2 Preparation and characterization of polyaluminosilazanes 150
2.1.3 Nanocasting and ceramic transformation 151
2.1.4 Preparation of of nanocatalysts 151
2.1.5 Experiments 152
2.2. Results and discussion 152
2.2.1 Synthesis and characterization of polyaluminosilazanes 152
2.2.2 PASZ-to-SiAlCN conversion 154
2.2.3 Characterization of ordered mesoporous SiAlCN 159

2.2.4 Monodispersed Pt nanoparticles supported on ompSiAlCNxy supports 169
2.2.5 H_2 evolution from $NaBH_4$ over Pt/ompSiAlCNxy nanocatalysts 172
3. Preparation of Pt supported ordered mesoporous Si_3N_4 173
3.1. Experimental part 175
3.1.1 Materials 175
3.1.2 Preparation of ordered mesoporous Si_3N_4 175
3.1.3 Preparation of nanocatalysts 176
3.1.4 Experiments 176
3.2. Results and discussion 177
3.2.1 Preparation and characterization of ordered mesoporous Si_3N_4 177
3.2.2 Characterization of Pt/omp-Si_3N_4 nanocatalysts 183
3.2.3 H_2 evolution from $NaBH_4$ over Pt/ompSi_3N_4 nanocatalysts 186
4. Conclusion 188
V- SiAlCN and SiBCN:from elaboration to application.....190
1. Introduction.....194
2. Synthesis and characterization of "home-made" Al-modified polycarbosilazanes.....195
2.1. Experimental part 195
2.1.1 Materials 195
2.1.2 Synthesis of polyaluminosilazanes-derived SiAlCN ceramics 195
2.1.3 Experiments.....197
2.2. Results and discussions 197
2.2.1 Synthesis and characterization of polyaluminosilazanes 197
2.2.2 Polyaluminosilazanes-to-SiAlCN conversion.....207
2.2.3 PMVAZ structure evolution: RT→ 1000°C 211
2.2.4 Characterization of SiAlCN: 1000→ 1800°C.....214
3. Microcellular foams elaboration.....223
3.1. Introduction 223
3.2. Experimental part 223
3.2.1 Materials.....223
3.2.2 Preparation of foams 223
3.2.3 Experiments.....224
3.3. Results and discussion.....225
3.3.1 Preparation of SiAlCN microcellular foams 225
3.3.2 Characterization of SiAlCN microcellular foams 227
4. Synthesis and characterization of Al- and B-modified commercial polysilazanes.....235
4.1. Experimental part 235
4.1.1 Materials.....235

4.1.2 Synthesis of Al- and B-modified polycarbosilazanes 235
4.1.3 Polymer-to-ceramic conversion 236
4.2. Results and discussion 237
4.2.1 Preparation and characterization of Al- and B-modified polycarbosilazanes 237
4.2.2 PAZ/PBZ-to-SiAlCN/SiBCN conversion 240
5. Conclusion 250
General conclusion and Outlook 252
References 262

GENERAL INTRODUCTION

Throughout history, the use of **energy** has been central to the development of human society. Moreover, during the 19th and 20th centuries, humanity learned how to harness the highly-concentrated forms of energy contained within fossil fuels. These provided the power that drove the industrial revolution. They increased unparalleled affluence regarding industrialization and productivity. The world's current energy systems have been built around the many advantages of fossil fuels, and we now depend overwhelmingly upon them [1].

Why does energy cause a worldwide problem?

We use more than we make!!

If today man relies on the well-controlled **energy carriers** like the previously mentioned, inevitable tightening of constraints will impose an evolution of the nature of these vectors. Their **limitations** appear indeed clearly. **Fossil fuels** are handicapped by **two constraints** that are gravely affecting the world economy in this 21th century:

- A **depletion of the fossil fuels** which will be problematic in the near-future;
- The **emission of greenhouse gases** like carbon dioxide (CO_2), which is associated to the use of such energy carriers and is the main responsible for the global warming.

One of the biggest challenges facing humanity during the 21st century must surely be that of giving everyone on the planet access to **safe, clean and sustainable energy supplies**.

What can be the solution?

For allowing a smooth transition from fossil fuels to **future sustainable energy**, an energy carrier that would have the virtues of electricity and fuels without their disadvantages is required. Only **hydrogen** has the potential to play a vital role in these scenarios [2]. Nevertheless, the development of a **hydrogen economy** is hampered by three main issues that can be problematic: i) **production**, ii) **storage** and iii) **purification**. The present thesis is focused on the two first issues.

Hydrogen has the **highest gravimetric energy density** and can be produced from a variety of feedstocks including fossil resources as well as renewable resources [3]. It is mainly produced from natural gas (95%), which means a severe evolution of CO_2. Moreover, **liquid-phase carriers** can be used in combination with fuel cells to produce electrical energy (for automobiles, stationary applications such as power generators and portable electronics) with zero emissions excepted water [4]. Based on the important opportunities offered by this new-born technology, we have been interested in the **hydrogen generation** from such processes.

Of the issues of the **hydrogen economy**, the **storage** one is considered to be a major drawback in the widespread use of **hydrogen**. Several investigations are being highlighted and besides the conventional technologies like high pressure and cryogenic liquid, alternative novel solutions involving glass microspheres, ionic liquids, ice hydrates, chemical hydrides, even if they are still at laboratory level and not yet technologically developed, have been proposed [5]. In particular we were motivated by the **chemical hydrogen storage** through the **nanoconfinement** of **Aluminum-based** and **Boron-based hydrides** into **materials with intrinsic porosity**.

Trying to refine solutions for the **hydrogen generation** and **storage**, the motivation of the research in our group, among other disciplines, was to **design, study** and **apply** new inorganic materials and in particular **functional (carbo)nitrides** for **energy applications.** This PhD thesis is part of the **FUNEA project** "Functional Nitrides for Energy Applications" within the **Marie Curie ITN 7th Framework Program** in which the European Institute of Membranes (IEM) is involved. The objective of this project is to ensure the principal needs of the 21st century by focusing on the **energetic applications of nitride-based materials**. To reach this goal, **eight European academic** research groups with complementary expertise in the synthesis, processing and characterization of materials, and **five industrial partners**, have proposed a collaboration for conducting research and training eleven Early Stage Researchers ESRs and Experienced Researchers ERs, as well as emerging a **new area of materials with advanced functionalities and exceptional levels of performance** (Figure 1).

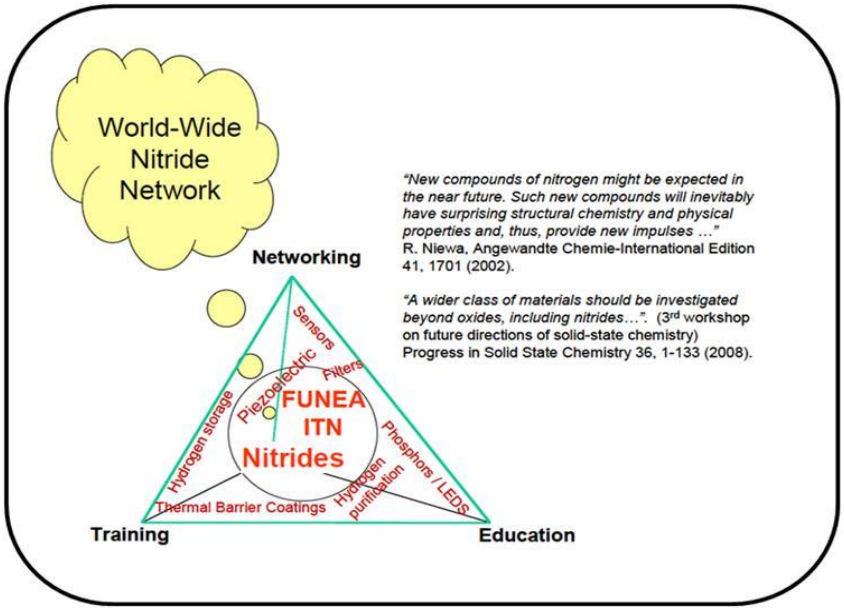

Figure 1 : Schematic view of the interdisciplinary and intersectoral environment of the FUNEA project.

The research presented in this thesis is focused on the **synthesis and characterization** of different types of **(carbo)nitride materials with tailored porosity** derived from preceramic polymers, involving binary (aluminum nitride **AlN,** boron nitride **BN)** and quaternary (aluminum and boron modified-silicocarbonitride, respectively, **SiAlCN** and **SiBCN**) systems. These compositions have been prepared in form of **porous materials** allowing a great interest as:

- **Catalytic support for hydrogen generation** from catalytic hydrolysis of sodium borohydride;
- **Host material for solid state hydrogen storage** by nanoconfinement of alanes and boranes.

Chapter I will start with the two main points we mentioned previously: i) **production,** and ii) **storage of hydrogen**. We will describe for each point, the materials we have considered in the present thesis. Then we will give an overview not only on the **(carbo)nitride ceramics**, but also on the **porous** ones especially those derived from **preceramic polymers**. The focus of this part will concern the interest of the **Polymer-Derived Ceramics (PDCs)** route to prepare **porous ceramics** and in particular **(carbo)nitrides**.

It was possible to classify the chapters either by **type of materials** or by **type of application** (hydrogen generation/storage). Finally we decided to classify the following chapters by type of material going from binary systems which are conventional materials (**AlN** and **BN**) to quaternary systems (**SiAlCN** and **SiBCN**) which are more sophisticated materials.

Chapters II, III and IV are related to material processing and science whereas the last chapter (Chapter V) is more focused on material chemistry. All these chapters apply the PDCs strategy to prepare the involved materials. In detail:

Chapter II describes the synthesis and characterization of **meso-/macroporous aluminum nitride** as well as **aluminum nitride aerogels** for assessing the **dehydrogenation of sodium alanate** that combines a relatively high gravimetric hydrogen content with reasonable desorption/absorption characteristics and **reversibility** in view of practical applications.

Chapter III is devoted to the synthesis and characterization of **mesoporous boron nitride monoliths** as well as **boron nitride aerogels**, that will serve as host materials to confine **ammoniaborane**, a chemical hydrogen storage complex that was considered by the Department of Energy (DOE) as an applicant for polymer electrolyte membrane fuel cell [6].

Chapter IV reports the preparation of ordered mesoporous Si- and/or Al- based (carbo)nitrides as catalytic supports for **hydrogen production** from **sodium borohydride.** In

particular, we focus on the preparation of **SilicoAluminoCarboNitride (SiAlCN)** and **Silicon Nitride (Si_3N_4)** as support for growing **Platinum (Pt) nanoparticles**.

The addition of **AlN** (Chapter II) as well as **BN** (Chapter III) to **Si-based ceramics** is known to optimize some of the properties of the resulting materials. Within this context, **Chapter V** is dedicated to the synthesis of polycarbosilazanes modified by aluminum and boron through a **single source precursor approach**. A detailed investigation of the polymer synthesis and the polymer-to-ceramic conversion is provided. As a proof of concept of the interest of this approach, microcellular **foams** have been prepared.

The manuscript ends with a **conclusion** that summarizes the results and discussions proposed in each chapter, and underlines its prospective future by evaluating some **perspectives**.

A productive collaboration with different laboratories, which led to the present work, must be highlighted:

- The **LCPM-Paris** for the solid state **NMR investigations** on the preceramic polymers and the derived ceramics (Prof. Christel GERVAIS).
- The **Crismat-Caen** for the **TEM study** of some of the final materials to valorize the textural properties of the boron- and aluminum- based nitrides (Prof. Sylvie MALO and Dr. Alina BRUMA).
- The "**Institut des Sciences chimiques de Rennes**- équipe verre et ceramiques" for the oxygen and nitrogen elemental analysis as well as the surface modification of Si-based foams by tantalum nitride (Dr. Franck TESSIER).
- The **INSA-Lyon** for the **mechanical properties** of the materials (Prof. Gilbert FANTOZZI).
- The **LMI-Lyon** for the **gas analysis** regarding the AB decomposition (Dr. Rodica CHIRIAC).
- The **LMI-Lyon** for the **tomography measurement** on SiAlCN ceramic foams (Dr. Jérôme ADRIEN).
- The **LCTS** (Prof. Gérard L. VIGNOLES) **+ CRPP-Bordeaux** (Prof. Renal BACKOV) for the **thermal conductivity** of the materials.
- The "**Dipartimento di Ingegneria Industriale, Università di Trento"-Italy,** during an exchange program in the frame of the FUNEA project where all the boron- and aluminum- based aerogels were prepared (Prof. Gian Domenico SORARU).

- The **"Dipartimento di Ingegneria Industriale, Università Degli Studi di Padova"-Italy** for the elaboration of microcellular foams with the poly(methylmethacrylate) sacrificial microbeads (Prof. Paolo COLOMBO).

I-

LITERATURE SURVEY

I- Literature survey 10
1. Introduction 14
2. Hydrogen production and storage 15
2.1. Hydrogen production 15
2.1.1 Off-board hydrogen production 15
2.1.2 On-board hydrogen production 16
2.2. Hydrogen storage 18
2.2.1 Liquid hydrogen 18
2.2.2 High pressure gas 18
2.2.3 Solid-state hydrogen storage 19
3. (Carbo)Nitride ceramics and derivatives 30
3.1. Definition/Applications of (Carbo)Nitride Ceramics 30
3.2. Synthesis of (Carbo)Nitride ceramics 31
3.2.1 Chemical Vapor Deposition 31
3.2.2 Sol-Gel 31
3.2.3 Polymer-Derived Ceramics 32
4. Polymer-Derived (Carbo)Nitrides 36
4.1. Alumium Nitride 36
4.1.1 Structure and properties 36
4.1.2 Fabrication routes of Aluminum Nitride 38
4.1.3 Polymer-Derived Aluminum Nitride 39
4.2. Boron Nitride 41
4.2.1 Structure and properties 41
4.2.2 Hexagonal Boron Nitride 42
4.2.3 Polymer-Derived Boron Nitride 43
4.3. Aluminum- and Boron-containing SilicoCarboNitrides 48
4.3.1 Aluminum-modified SilicoCarboNitride 49
4.3.2 Boron-modified SilicoCarboNitride 50
5. Polymer-Derived Porous (Carbo)Nitrides 55
5.1. Definition of the porosity 55
5.2. Process methods of porous ceramics 56
5.2.1 Porous BN 59
5.2.2 Porous SiBCN 60
6. Conclusion 61

1. INTRODUCTION

Hydrogen is the simplest and most abundant element on earth. Molecular **hydrogen** is an **energy carrier** rather than an energy source. It has the **highest energy content** per unit of weight of any known fuel (120 $MJ.kg^{-1}$ (LHV) and 142 $MJ.kg^{-1}$ (HHV) [7]). Hydrogen is **chemically active** and is found **chemically bonded** in water, hydrocarbons/carbohydrates, biomass etc. The concept of using hydrogen as fuel has been advocated by environmentalists, researchers, industrials and others for at least three decades. The attraction is that hydrogen is both inexhaustible and clean (its combustion produces only water). The biggest impediments in hydrogen fuel, once **produced**, are **storage** and **purification**, which makes this technology not yet, advanced enough for hydrogen to be commercial. Notwithstanding the need for significant development prior to commercialization, long-term scenarios based on hydrogen must be developed to supply energy needs in power generation and in transport. Accordingly, the **hydrogen economy** would emerge and replace the old hydrocarbon economy.

What are the barriers to a hydrogen economy?

There are many barriers to implementing a hydrogen economy. The biggest overarching problem consists in the need for a paradigm shift from an energy system that has been in place for more than one hundred years to a hydrogen economy.

A typical **hydrogen cycle** shown in Figure I-1 consists of the major steps which are **hydrogen production**, **transportation/storage** and **final use**. Each of these steps is associated with several **technical challenges** that must be resolved prior to using hydrogen as an energy carrier.

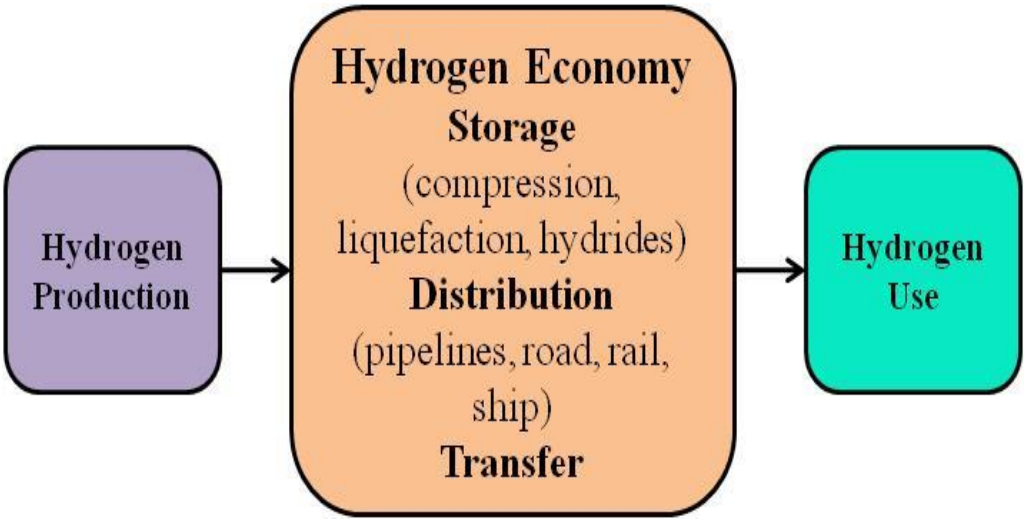

Figure I-1: The hydrogen issue.

The aim of the present chapter is to report an overview; firstly on the **hydrogen issue** (production and storage), that is systematically associated with a **material issue.** Secondly, we will focus on **(carbo)nitrides** and in particular on their preparation through the **Polymer-Derived Ceramics** route. Among these polymer-derived (carbo)nitrides, Boron Nitride **(BN)** and Aluminum Nitride **(AlN)** as well as their quaternary derivatives SilicoAluminum CarboNitride **(SiAlCN)** and SilicoBoron CarboNitride **(SiBCN)** are described. Since **porous materials** have been considered for the hydrogen issue, the third part of this chapter will focus on the development of the **porosity** in the **polymer-derived (carbo)nitrides**.

2. HYDROGEN PRODUCTION AND STORAGE

2.1. Hydrogen production

Hydrogen can be produced from multiple feedstocks that can include fossil resources as well as renewable resources, such as biomass and water with input from renewable energy sources (e.g. wind, wave, sunlight or hydro-power). This is what we call **off-board** hydrogen production. A variety of chemical, biological, electrolytic, photolytic and thermo-chemical process technologies are being used for the **on-board** hydrogen production. Each technology is at a different stage of development, and presents many advantages but also many challenges to face.

2.1.1 Off-board hydrogen production

For hydrogen to be used as a fuel, it must be first separated from other elements through different processes such as **electrolysis**, **gasification** (high temperature heating in the absence of oxygen), or **reforming** (high temperature heating through a catalyst).

From all the **hydrogen sources**, Figure I-2 illustrates the **fossil resources** (natural gas and coal) and the **renewable ones** (biomass and water with input from renewable energy sources).

The marketplace witnessed several technologies when it comes to the **off-board production of hydrogen.** Starting with the **electrolysis of water** in the 1960s [8], the industrial production of hydrogen shifted slowly towards a **fossil-based feedstock**, which is the main source for **hydrogen production** today (96% of world hydrogen production [9, 10]). In the **short and medium term**, the production options for hydrogen are focused on distributed **hydrogen production** from the **electrolysis of water** and on the **reforming of natural gas and coal**. **Larger centralized hydrogen production** plants, based on **fossil fuels with CO_2 capture**, are more likely to be introduced at a later stage. Other methods of generating hydrogen are being investigated, but none of them is likely

to be available on a production scale, namely: the ammonia dissociation where the ammonia is dissociated into its simpler components hydrogen and nitrogen; the partial oxidation where hydrocarbons are reacted with oxygen to produce hydrogen and carbon monoxide; and the photocatalytic water splitting where photocatalysts, under solar light, are used to split water into hydrogen and oxygen.

The other ways of producing hydrogen from biomass, for example, anaerobic digestion, photo-fermentation, microbial electrolysis etc. remain far from commercialization and need to be implemented in order to become economically sustainable at a large scale [8].

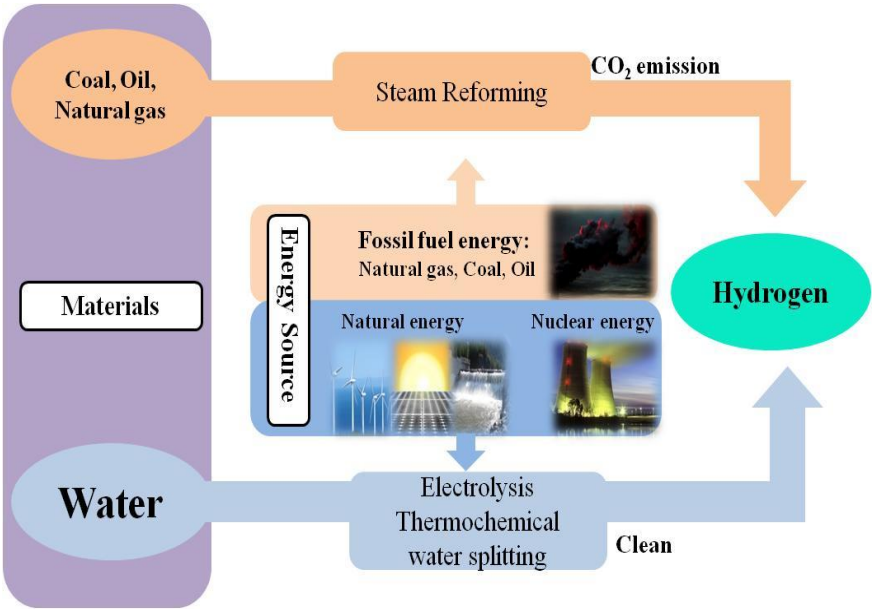

Figure I-2: Hydrogen sources and off-board production processes.

When it comes to this work, an investigation on the feasibility of an **on-board hydrogen production** is carried out.

2.1.2 On-board hydrogen production

A number of **hydrogen storage materials** are being developed in order to generate hydrogen whether by thermal decomposition or by catalytic release and that is what we call **on-board** hydrogen production.

Among the various possibilities for the on-board hydrogen production is the **formic acid** (HCOOH) because it offers high energy density, is non-toxic and can be safely handled in aqueous solutions. Ever since Laurenczy and Fukuzumi [11, 12] demonstrated independently that formic acid can be used as an efficient material for **hydrogen generation**, the work has accelerated towards finding catalytic ways to produce hydrogen at ambient conditions suitable for practical applications.

Catalytic decomposition of formic acid yields H_2 and CO_2, the latter can be hydrogenated back to formic acid to complete the hydrogen storage/delivery cycle.

Another potential **hydrogen carrier** is **hydrazine borane** N_2H_4-BH_3 containing 15.4 wt% of H ($4H^{\delta+}$, $3H^{\delta-}$) whose dehydrogenation can be approached either by hydrolysis [13], methanolysis [14] or thermolysis [15].

Our group was interested in a particular metal borohydride that is **sodium borohydride ($NaBH_4$)** due to its **high gravimetric and volumetric capacities** and reported the challenges facing, on one hand the **hydrolysis** phenomenon and on the other hand the **catalysis** (nature of catalysts, conditions, etc.) [16]. **Sodium borohydride** carries **10.8 wt% of hydridic hydrogen ($H^{\delta-}$)** which can be spontaneously recovered by reaction with a **protic hydrogen ($H^{\delta+}$)** from **water** according to the following reaction (Equation I-1):

$$NaBH_4 + 4H_2O \rightarrow NaB(OH)_4 + 4H_2 \quad \text{(I-1)}$$

To avoid the **exothermic self-hydrolysis** that can be, if not controlled, undesirable for practical applications, an **alkaline medium** is necessary to stabilize the aqueous solution of $NaBH_4$. In such conditions an efficient catalyst is then needed to decrease the energy activation and to accelerate the hydrogen generation rate. **Metal-based catalysts** have been widely investigated. Moreover **supporting the metal catalysts on a porous template**, thus avoiding any risk of agglomeration of the catalytic particles, was found to be well controlled and efficient when it comes to the **hydrolysis** reaction of **$NaBH_4$**. **Catalysts** like Ru supported on anion-exchange resin [17], fluorinated Mg-based alloy [18], Pt supported on carbon [19], Pt/Ru supported on metal oxide [20], Pd supported on carbon [21], are generally used to accelerate the hydrolysis reaction of the $NaBH_4$ if we are not considering the famous **cobalt-based salts** that, even though have revealed their effectiveness in accelerating the dehydrogenation as well as their cost-efficiency, they tend to suffer from a **severe instability** over successive **hydrolysis** cycles because of the nature of the interface between the cobalt and the borates [22].

In the present thesis, we investigate the **catalytic hydrolysis** of **$NaBH_4$ for H_2 production** using **platinum-supported (carbo)nitride nanocatalysts.** Indeed, the issue that can no longer be evaded is the fact that the previous mentioned supports cannot resist to harsh environments implicating very high rates of **hydrogen generation** on the active sites, alkaline solutions and presence of an excess of water. This is a motivation for us to investigate strong **catalytic supports** reliable to face such extreme conditions, in order to assess our objective of a clean, efficient on-board **hydrogen production.**

Currently our group is also involved in the application of **ammoniaborane NH_3BH_3** as a source of H_2. It is found to be another promising chemical boron-based hydride. With 19.6 wt% of H, it is in particular investigated for the **hydrogen storage.** The latter is a crucial challenge facing the **application of hydrogen**, especially for vehicles; it must be safe, compact, light and reasonably economic. The hydrogen storage will be overviewed in the next section of this chapter.

2.2. Hydrogen storage

A hydrogen fuel cell vehicle, to be competitive with the gasoline or diesel one, should be able to drive 500 km or more before refueling, which corresponds roughly to 5 kg of hydrogen. A lot of research has been developed in the past decade in order to investigate a **viable storage material** capable of reaching high targets, ultimately a **gravimetric** and **volumetric** capacities respectively equal to **7.5 wt% H_2** and **70 g (H_2)/L** [23].

At present, hydrogen can be stored *via* two physical approaches [2]: **cryogenic storage** and **high pressure storage**.

2.2.1 Liquid hydrogen

Liquefaction of hydrogen occurs at -252.9°C (20 K) which consumes more than 30% of the energy content of the hydrogen. There is also a continual loss of energy due to thermal conduction through the insulated walls, whether the liquid is stored in a service station or a vehicle, therefore this storage method, hampered by continuous loss, is not considered viable for application in cars at a large scale. Even so, there may be applications for liquid hydrogen in heavy vehicles and long-range aircraft, where the weight is critical.

2.2.2 High pressure gas

Hydrogen can be stored at high pressure in gas cylinders that can hold up to 200 bars H_2 and have a gravimetric density of approximately 1wt%. Higher hydrogen densities, capable of reaching 10 wt%, are achieved using light carbon fiber composite cylinders which are capable of storing hydrogen at pressures between 700–1000 bars. High pressure cylinders are currently expensive and even at these high pressures, the volumetric density is less than that of gasoline tanks. Another limitation is the safety issue. Despite these drawbacks, it is currently the most mature technology for automotive applications [24].

Another promising alternative, taken into serious consideration, to provide greater security and better gravimetric and volumetric capacities, when compared to liquid and gaseous hydrogen, is the **solid-state hydrogen storage.**

2.2.3 Solid-state hydrogen storage

Solid-state materials have the ability to reversibly release and take-up hydrogen. There are **two processes** in which hydrogen can bind onto materials:

Physisorption: In this first physical mechanism, **molecular hydrogen (H_2)** is adsorbed onto the surface of a material by the weak interactions of Van Der Waals. Since the amount of H_2 adsorbed is proportional to the surface area of the material, porous materials with high surface areas have been investigated and envisaged as potential hydrogen storage materials [25, 26] such as zeolites, carbon based materials: carbon nanotubes, fibers, fullerenes, activated carbon, metal organic frameworks (MOFs) [27, 28] as well as covalent organic frameworks (COFs) [29] and polymers with intrinsic porosity (PIP, PIM) [30]…

Chimisorption: In this second class of solid-state hydrogen storage, the **atomic hydrogen (H)** is absorbed by metal or metal alloys to form a metal hydride [31]. Metal hydrides can be divided into ionic hydrides (such as LiH, MgH_2…) or metallic (interstitial) hydrides (such as $LaNi_5H_6$, TiH_2…), depending on the nature of the bonding between hydrogen and the metal. Each of these hydrides presents some advantages and drawbacks. For instance, the ionic hydrides feature high gravimetric hydrogen densities but due to their stability, coming from the fact that a strong ionic bond is linking the hydrogen to the metal, the release of the hydrogen will not occur at low temperatures, which is not suitable for fuel cell applications. Whereas in the case of metallic hydrides, some compounds can release and reabsorb hydrogen continuously at ambient temperature and pressure but, because of the heavy transition metals present in their structure, they are limited by the low gravimetric hydrogen contents (3 wt% H_2).

Another class is the so-called "**complex metal hydrides**" This type of hydrides includes compounds formed by a stable ionic bond between hydrogen and some light elements of the periodic table (for example **boron** leading to **borohydrides**, **aluminum** leading to **alanates**). They raised an intense interest with respect to their potential capacities. For example this fact has spread mainly after the discovery of Bogdanovic *et al.* [32] regarding the **reversible hydrogen storage in sodium alanate doped with titanium**. Before this, the applicability of alanates was far from reality in the on-board hydrogen storage. Also Züttel *et al.* have shown that the decomposition of $LiBH_4$ could be successfully catalyzed by the addition of SiO_2 starting 200°C [33].

Apart from the above mentioned hydrides, other hydrides such as **ammoniaborane (NH_3BH_3)** [34] and metal-amidoboranes [35], referred to as **chemical hydrides**, are also being intensively investigated.

Extensive efforts are underway to design and synthesize materials for efficient chemical hydrogen storage, which remains one of the most critical issues to be addressed for hydrogen.

Although many complex hydrides have been investigated as attractive materials for the chemical hydrogen storage, the high hydrogen capacities needed for transportation applications exclude most compounds. Hereafter, we will focus on two examples of **complex hydrides** that were found to be noticeable.

2.2.3.1 Ammoniaborane

Foremost among complex hydrides are boron-based compounds, especially amine boranes that seem to be very important for the hydrogen economy concept in order to reach the 2015 target of 9 wt% set by the US Department of Energy (DOE) [2]. Amine boranes' high hydrogen densities, for example 24.5 wt% for ammonium borohydride NH_4BH_4, 19.6 wt% for ammoniaborane NH_3BH_3, and 17.8 wt% for ammonia triborane $NH_3B_3H_7$, were the primary attribute that made these materials attractive. The other interesting property of amine boranes comes from the different electronegativities of B(2.04) and N(3.04) that result in **protonic hydrogen ($H^{\delta+}$)** in the N-H bond or NH_3 groups and **hydridic hydrogen ($H^{\delta-}$)** in the B-H bond or BH_3 moieties. Thus, the elimination of H_2 is favorable owing to the ability of $H^{\delta+}$ and $H^{\delta-}$ to interact.

Ammoniaborane is currently being considered as the best hydrogen storage source since it has potential to meet the stringent targets needed for transportation sector [36] due to a low molecular weight (30.7 $g.mol^{-1}$), remarkably high H_2 densities (**gravimetric** and **volumetric hydrogen capacities** are respectively **19.6 wt% and 140 $g.L^{-1}$**), and an off-board high regeneration yield reported by Sutton *et al.* in 2011 [37].

2.2.3.1.a. Description

Ammoniaborane (Figure I-3) (denoted **AB**), or borazane, (**NH_3BH_3**) was discovered in the 1950s. It is a white crystalline material, stable at room temperature with a body-centered tetragonal *I4mm* phase [38]. The AB molecule is **highly polar**. The dipolar moment is 4.88 D [39], 5.02 D in dioxane solution [40], and 5.22 D in the gas phase measurements by microwave spectroscopy [41]. This polarity is oriented along the c axis of the tetragonal structure of the B-N dative bond.

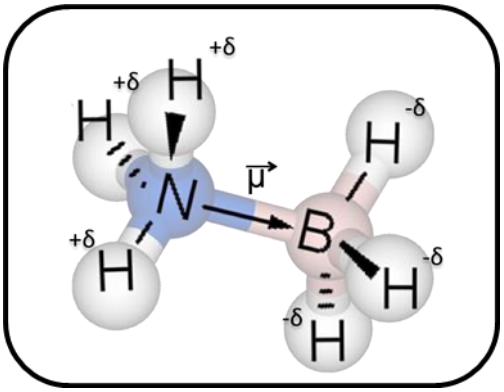

Figure I-3: Molecular structure of AB.

AB is soluble in water and in many organic solvents. It possesses **high solubility**, that is, >5 wt%, in H_2O, EtOH, THF, diglyme, triglyme; around 0.5–1 wt%, in Et_2O, and dioxane; and a lower solubility, that is <0.1 wt%, in toluene. Although AB possesses 19.6 wt% H_2 and releases about 6.5 wt% of the hydrogen at temperatures around 100°C, the hydrogen release is concurrently associated with ammonia, borazine and diborane [36]. More importantly, the dehydrogenation is exothermic and hence non reversible under realistic conditions which prevents the use of the pristine AB as H_2 energy carrier in on-board fuel-cell applications.

2.2.3.1.b. Synthesis

Since AB is a simple donor-acceptor complex, it was expected that it could be directly synthesized from diborane and NH_3 more or less easily. However, some studies carried out at low temperatures (78°C) did not produce AB but instead they produced the ionic isomer diammoniate of diborane (DADB) [42]. The structure of this compound was the object of debate for a long time and was subject to intensive investigations. Shore *et al*. [43] showed, as well as subsequent work by other authors using ^{11}B-NMR and Raman studies [44, 45], its ionic nature and clarified its structure.

Currently, AB is produced by two main processes. The first method, the most suitable for laboratory scale production with respect to safety and simplicity in handling, is the **salt-metathesis** based on borohydrides and ammonium salts dissolved in organic solvents [46, 47] as shown by the following reaction (Equation I-2):

$$2NaBH_4 + (NH_4)_2SO_4 \rightarrow 2NH_3BH_3 + Na_2SO_4 + 2H_2 \quad \text{(I-2)}$$

The second consists in a **direct reaction of ammonia with diborane** [48], $BH_3.O(CH_3)_2$ [49] or $BH_3.S(CH_3)_2$ [50].

Of all available studies on the standard laboratory synthesis based on ammonium salts, Ramachandran *et al.* [47] have conducted the most extensive survey, screening 33 reactant variations at different temperatures (the study included two hydrides, seven salts, and eight solvents). A selection of all available results, are presented in Table I-1.

Table I-1: Synthesis of AB [47].

Ammonium salt	Borohydride	Solvent	Yield
NH_4Cl	$LiBH_4$	Et_2O	33%
$(NH_4)_2SO_4$	$LiBH_4$	Et_2O	47%
NH_4HCOO	$NaBH_4$	THF	95%
$(NH_4)_2SO_4$	$NaBH_4$	THF	95%
NH_4CH_3COO	$NaBH_4$	THF	81%
$(NH_4)_2CO_3$	$NaBH_4$	THF	80%
NH_4Cl	$NaBH_4$	THF	45%

AB stored under vacuum at room temperature showed no significant hydrogen loss for a period of two months and its solubility in organic solvents remained unchanged [48]. In contrast, reports of its storage in air indicated a slow hydrogen loss, presumably induced by humidity [49, 51]. Thus, it does not come as a surprise to distinguish different decomposition processes of AB.

2.2.3.1.c. AB dehydrogenation

One of the main challenges is to release efficiently the maximum of the stored hydrogen in AB. To succeed in that, several routes have been considered so far: i) hydrolysis [52], ii) methanolysis [47], iii) thermolysis [53], iv) hydrothermolysis [54]. With respect to the solvolysis reactions, the theoretical hydrogen densities are of 9.0% for the **hydrolysis with water** and 3.8% for the **methanolysis with methanol.** However these theoretical values are difficultly achieved because of some problems that might occur while performing the solvolysis, namely formation of thermodynamically stable borates, excess of solvent for hydrolyzing them, volume expansion, and liberation of ammonia that is unlikely to decompose into N_2 and H_2 in the hydrolysis conditions [55]. Nevertheless, the H_2 release is not an issue anymore as very reactive catalysts could be able to convert the totality of AB with variable hydrogen generation rates. The issue with the catalytic materials is rather the **durability** [56].

When it comes to the hydrolysis of AB, the first published studies date back to the middle of the 2000s. Our group brought out in 2010 the highest capacity ever reported, regarding AB hydrolysis, at least at laboratory scale, which is equal to 7.8 wt% [57]:

$$NH_3BH_3 + 4H_2O \rightarrow NH_4B(OH)_4 + 3H_2 \quad (I\text{-}3)$$

Regarding the methanolysis of AB, several metallic catalysts were studied in order to accelerate the reaction such as $RuCl_3$, $RhCl_3$, $CoCl_2$, $PdCl_2$, $NiCl_2$ or bi-metallic nanoparticles CoPd [58]. The most important study could be associated to the work of Ramachandran *et al.* in 2007 [47] where they reported not only the metal-catalyzed methanolysis of AB generating 3 equivalent of hydrogen, but also the regeneration of AB after isolating the intermediate ammonium tetramethoxyborate. Therefore, with respect to the **AB dehydrogenation**, we are more interested in the **thermolysis**, unlike the case of **$NaBH_4$** where the **hydrolysis** seems more benefic for a higher hydrogen release.

One of the purposes of the research in this dissertation, highlighted in Chapter III, is much involved in the **thermolysis of AB.** The thermolysis of **AB** is exemplified in Figure I-4.

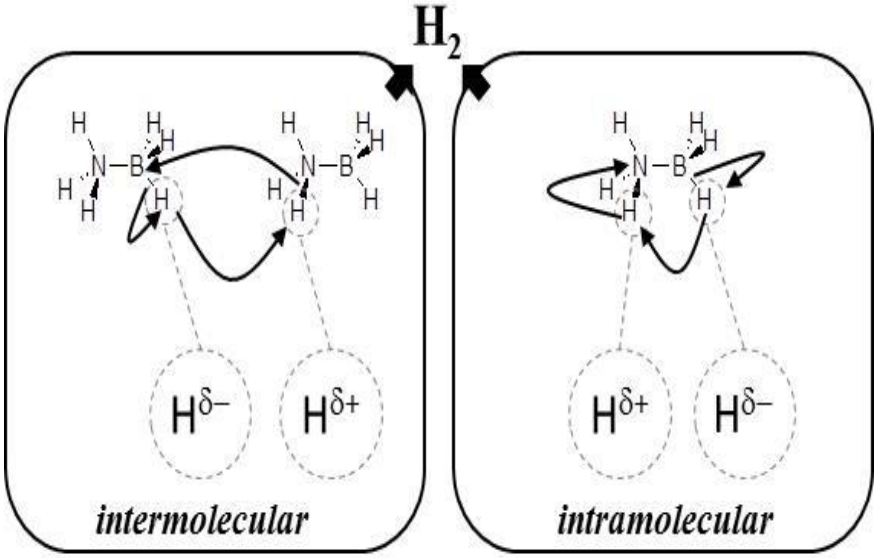

Figure I-4: Thermolysis of AB (adapted from [55]).

The **thermolysis** of **AB** is a simple reaction to implement for releasing stored hydrogen but in the meantime it is the most difficult to chemically achieve. **AB decomposition** can be attained through an **exothermic three-step reaction.** The first equivalent of H_2 is generated at temperatures up to 120°C. It can also be released at 85°C after a long induction period. The second equivalent H_2 is released at temperatures slightly below 200°C and the third one at temperatures up to 500°C. Such

releasing rate is unacceptable for applications. In the following, the three dehydrogenation steps preceded by an induction period are examined.

- **Induction period:** A detailed insight by solid-state NMR and XRD clarified that structural modification occurs during this induction period where no hydrogen is released [59].
- **First reaction step:** The first stage of AB decomposition starts with a nucleation phase, the formation of $H_2B(NH_3)_2^+BH_4^-$ was identified, together with linear and cyclic dimmers. The release of molecular hydrogen was proven to be easier by the presence of $H_2B(NH_3)_2^+BH_4^-$ as the N-H and B-H bonds present in this compound are believed to be more reactive than the ones in AB [60]. 7.6 wt% of hydrogen are released during this decomposition stage, which is in good agreement with the formation of $(BH_2NH_2)_n$. Figure I-5 shows the successive steps of the first decomposition of AB.

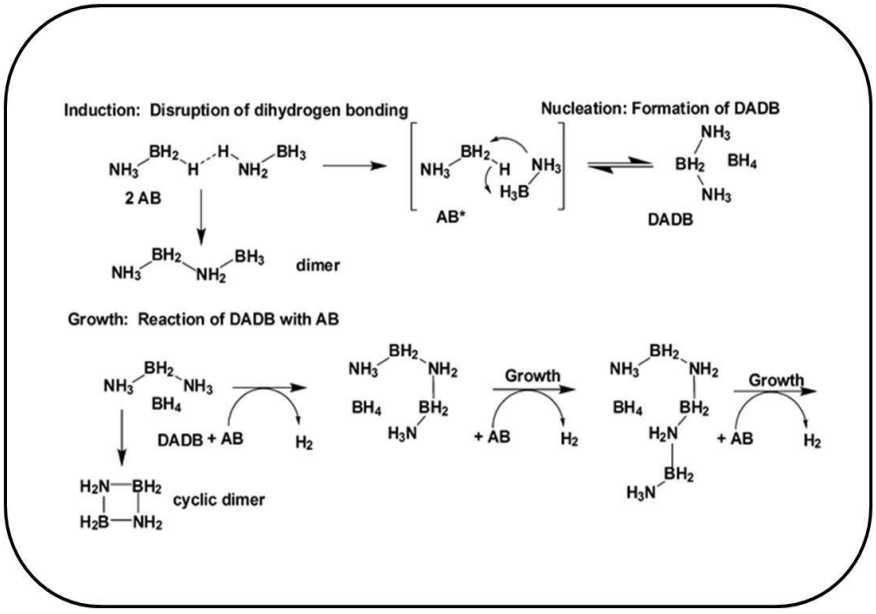

Figure I-5: Thermal dehydrogenation mechanism of AB [60].

- **Second reaction step:** The second dehydrogenation phase corresponds to the decomposition of $(BH_2NH_2)_n$ into the polyiminoborane $(BNH_y)_x$ with $1.2<y<2.4$ [61] which composition depends strongly on the decomposition conditions.
- **Third reaction step:** A complete dissociation of AB into boron nitride happens above 500°C. The high stability of boron nitride and the very high dissociation temperature inhibit the consideration of this last step for practical use.

2.2.3.2 Sodium alanate

2.2.3.2.a. Description

Complex aluminum hydrides of alkali and alkaline earth metals have been intensively studied for solid-state hydrogen storage [62, 63]. Sodium alanate ($NaAlH_4$) is one of the most investigated compounds among complex hydrides because of the reversibility of the (de)hydrogenation process when combined with catalysts under moderate conditions. All other known complex aluminum hydride systems are non-reversible or have a limited storage capacity.

$NaAlH_4$ offers good prospects due to the **high purity** of its released hydrogen, its **high reversible hydrogen storage capacity** and its **optimal thermodynamic stability** for reversible hydrogen storage at moderate temperatures. Since Bogdanovic demonstrated that the kinetic barriers of both hydrogenation and **dehydrogenation of $NaAlH_4$ can be lowered by doping with transition metals** [32], it became an important candidate in view of practical applications. $NaAlH_4$ has a theoretical hydrogen storage capacity of 7.4 wt% for a complete decomposition to metallic Al and Na.

$NaAlH_4$ decomposes to release hydrogen according to the subsequent three steps reaction reported below [64]:

$$\mathbf{3NaAlH_4 = Na_3AlH_6 + 2Al + H_2} \qquad \mathbf{3.7\ wt\%H_2\ (210\text{-}230°C)} \quad \mathbf{(1)}$$

$$\mathbf{Na_3AlH_6 = 3NaH + Al + 3/2H_2} \qquad \mathbf{1.9\ wt\%H_2\ (250\text{-}300°C)} \quad \mathbf{(2)}$$

$$\mathbf{NaH = Na + 1/2H_2} \qquad \mathbf{1.9\ wt\%H_2\ (425°C)} \quad \mathbf{(3)}$$

First, $NalAlH_4$ decomposes into sodium hexahydride (Na_3AlH_6) and metallic aluminum accompanied with the release of H_2. Na_3AlH_6 reacts further into sodium hydride (NaH) with the simultaneous formation of metallic aluminum and release of H_2. NaH finally splits into metallic sodium and H_2.

The structures of $NaAlH_4$, Na_3AlH_6 and NaH are presented in Figure I-6 where the white spheres correspond to hydrogen and the yellow ones to sodium, as for the aluminum element it is represented by the red pyramids [5]. $NaAlH_4$ has a body-centered tetragonal unit cell with the space group *I41/a*. It consists of $[AlH_4]^{-1}$ tetrahedra surrounded by Na^+ atoms. Na_3AlH_6 has space group $P2_1/n$ and consists of $[AlH_6]^{-3}$ octahedra surrounded by Na^+ atoms too. Although the exact mechanistic pathway of $NaAlH_4$ is not fully understood, the mobility of the Al and Na species was identified as the key for absorption/desorption mechanisms. As for the reaction kinetics, it is limited by the segregation of solid phases formed causing the slow mass transport.

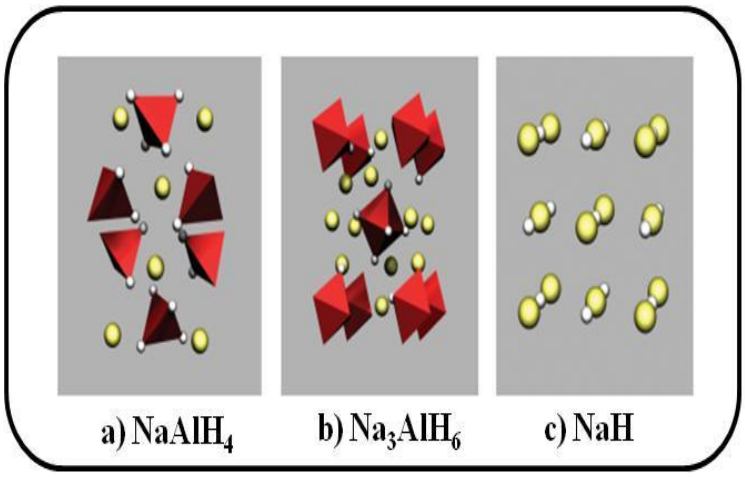

Figure I-6: Crystalline structures of the decomposition intermediates of $NaAlH_4$ [5].

The correlation between the temperature and the pressure is determined by the thermodynamic properties. These properties define the stability of $NaAlH_4$, Na_3AlH_6, NaH and Al under specific conditions. In Figure I-7, the pressure-temperature relations for $NaAlH_4$ are shown. For the first and second desorption step, the equilibrium temperatures at 1 bar H_2 are ~30°C (37 $kJ.mol^{-1}$) and ~100°C (47 $kJ.mol^{-1}$), respectively. In detail the first step of decomposition takes place at 210-230°C with a release of 3.7 wt% of H_2 and the second step of decomposition occurs around 250°C with a release of 1.9 wt% of H_2 to give a total release of 5.6 wt% of H_2 (70 $g_{H_2}.L^{-1}$). The third reaction step from NaH to metallic Na has an equilibrium temperature of 425°C (56 kJ/mol) at 1 bar H_2. No doubt that this third step was excluded because the temperature is too high to be used in most practical applications [65].

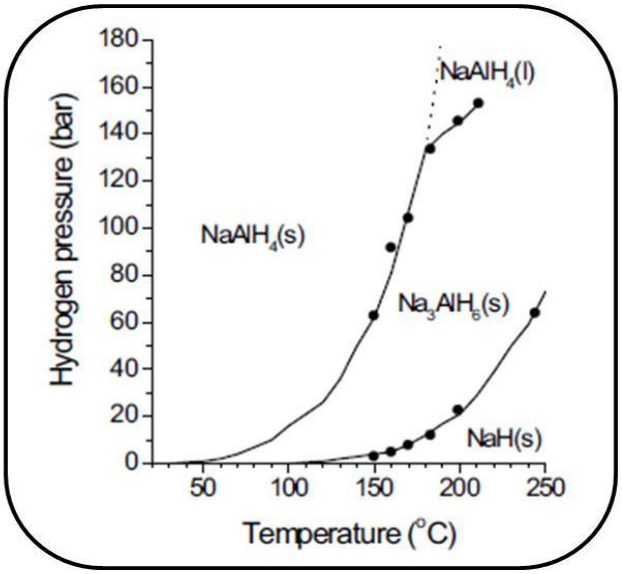

Figure I-7: Pressure-temperature relations for $NaAlH_4$ [65].

The actual desorption and absorption rates of hydrogen are determined by kinetic properties. In spite of the favorable thermodynamic properties of $NaAlH_4$, its decomposition temperatures are high because of kinetic limitations. No hydrogen is released from pure $NaAlH_4$ at 30-100°C under 1 bar H_2, although Na_3AlH_6/Al is the most stable phase at these conditions. Temperatures above the melting temperature of $NaAlH_4$ of 181°C are needed to release hydrogen. In fact the decomposition of Na_3AlH_6 starts typically around 250°C. Additionally, the decomposition reactions are practically irreversible.

Based on the literature review on complex hydrides, we can observe that the main issue of the compounds is **the high temperature of dehydrogenation of the first H_2 equivalent. Two solutions** are considered:

1) **The use of metal-based catalysts**
2) **The nanoconfinement**

2.2.3.3 Stategies to optimize H_2 storage for complex hydrides

2.2.3.3.a. Metal-based catalysts

The hydrogen desorption and absorption kinetics of complex hydrides can be dramatically improved by the addition of various **catalysts.** This has been particularly studied for **$NaAlH_4$** but also some examples regarding **NH_3BH_3** will be highlighted.

In 1997, Bogdanovic *et al.* reported strongly improved kinetics of the hydrogen desorption reactions in $NaAlH_4$. This improvement was achieved by the addition of a few mol% of a Ti-based catalyst. The result is a decrease of the onset temperature for hydrogen desorption to 33°C [32]. The effect of the catalyst depends not only on the nature of the catalyst and the preparation method but also on the concentration of the catalyst [66]. Different types of materials and methods were investigated, some of them are cited here: the **wet impregnation** process involving titanium compounds chloride, titanium n-butoxide ($Ti(OBu^n)_4$) and titanium chloride ($TiCl_3$) [32], the **mechanical mixing** of the Ti precursors with the alanate [67], the **ball milling** of TiN nanopowders with the alanate [68], the **"urea glass" route** involving TiN catalyst [69], the ball milling of NaH, Al and Ti powders [70]… Doping with both Ti and Zr also lowered the decomposition temperature to 100°C [71]. Other metal-based precursors were also used, for example cerium and scandium, and showed outstanding kinetic properties on the decomposition reactions [72]. Direct synthesis of lanthanum and samarium doped $NaAlH_4$ was also reported [73]. However among the multiple transition metal catalysts, TiO_2 nanoparticles were the best catalysts for both **desorption** and **reversibility** [74].

Significant achievements resulted in transition-metal-catalyzed reactions that activated the **dehydrocoupling of amine-boranes compounds** [75]. Since AB is an ethane analogue, the use of transition-metal catalysis was a logical path to explore to activate AB for H_2 release. Research has focused on both heterogeneous catalysis, mainly nanomaterials, and homogenous catalysts. These catalysts were used for both thermolysis and hydrolysis/methanolysis reactions. Moreover, it was reported for the AB, a hydrogen generation catalyzed by nickel and platinum based hollow spheres with a quick hydrogen release in case of AB hydrolysis and a dehydrogenation at low temperatures for the thermolysis [76]. The application of transition metal catalysis was studied by Jaska *et al.* for a dehydrogenation of aminoboranes under mild conditions and using rhodium was found to be very interesting for this sake [77].

2.2.3.3.b. Nanoconfinement

It has become clear that nanoconfinement is a strong tool to change physico-chemical properties of hydrogen carrier materials [78], which might not only be of relevance for hydrogen storage but also for other applications. Hereafter we will consider **combining nanoconfinement and solid-state hydrogen storage materials such as $NaAlH_4$ and AB**, as a destabilizing way to improve the kinetics of dehydrogenation of these materials.

Nanoconfinement was imagined based on the fact that materials at nanoscale exhibit particular physical and chemical properties not found in other types of materials. For complex hydrides, it has been shown that nanoconfinement is a promising technique to improve the properties of nanomaterials such as the kinetics and thermodynamics for hydrogen release and uptake and the stability during cycling [34].

Small particles are intrinsically unstable and prone to grow into larger crystallites. In suspensions, they can be stabilized by ligands, but in the solid phase, stabilization is typically achieved by placing the material inside a porous host (support, scaffold or matrix). In the case of hydride storage systems, the host should comply with several requirements including low weight, low cost, high porosity and sufficient chemical inertness to limit possible reaction with the hydrides.

By this bottom-up approach, nanoparticles are created which limits the particle size of the hydride to the pore size of the scaffold and therefore hinders the agglomeration and particles growth, keeping them in close contact.

i) Nanoconfinement of AB

Nanostructured materials have been demonstrated to efficiently act in changing the thermodynamics of different hydrides, making the hydrogen release much easier.

Using a 1:1 mixture of AB and mesoporous silica SBA-15 scaffold, enabled the release of 1 equivalent of hydrogen at temperatures as low as 50°C in 85 min [34]. If using SBA-15 as host for confining AB has a remarkable advantage on the dehydrogenation temperature, more recent studies showed that supporting palladium nanoparticles into the channels of SBA-15 held a high performance in the dehydrogenation kinetics of AB by releasing 2 equivalent of hydrogen in 1 h even at a low catalyst concentration of 10 wt% Pd NPs. [79].

MOFs are very important host materials because of their unique interior active metal-centers for AB binding and well defined and ordered pores, and thus they merit further exploration. The flexibility in tuning pore shape and size coupled with the choice of metal center are the key parameters to explore for nanoconfinement of AB in MOFs. Li and co-workers were the first to show successful AB nanoconfinement in Y-based MOF with fast hydrogen release kinetics at reduced temperatures and highly suppressed byproduct release [80]. Various types of MOFs have been successfully explored to confine AB, the rigid frameworks [80, 81] and the flexible ones [82] (by flexibility the authors mean the ability of the pores to open and contract upon the molecule absorption and desorption). However, their use was excluded in this work, since they do not show any ability in **recycling the AB after dehydrogenation** because of their instability regarding high temperature and reductive medium. We, therefore, headed towards **nitride porous hosts** to investigate the recyclability of our composites.

ii) Nanoconfinement of $NaAlH_4$

Porous carbon materials have been largely investigated and played the role as host to confine $NaAlH_4$. The advantages of combining carbon supports with $NaAlH_4$ were reported, among them, a series of nanoporous carbon aerogels with different pore sizes [83], a CO_2 activated aerogel that once functionalized with Ti combined the high storage capacity with fast hydrogen release kinetics from $NaAlH_4$ which fully decomposes into $NaAlH_6$ at T≤ 100°C, nanoporous carbons [84, 85] *via* melt-infiltration that allows high loadings of $NaAlH_4$. Other materials were also tested such as ordered mesoporous silica [86], Ti-functionalized MOF [87].

Baldé *et al.* have prepared, using a wet chemical synthesis, carbon-nanofibers supported $NaAlH_4$ and showed the correlation between the size of the particles and the performance of the dehydrogenation [88].

To converge to a practical solution regarding the problematic of hydrogen, there are still several issues. One of the most key challenges concerns the “materials” which are used in combination with hydrides to produce and store hydrogen. They are expected to fill a lot of

requirements in terms of properties to optimize the production and storage of hydrogen from hydrides. Chemistry may be the way to achieve this goal. Indeed, with chemists, ceramists and engineers and the spark of the idea of hydrogen clean generation and storage, the current decade is witnessing intensive activity in the area of functional nitrides for energy applications. There is much scope to investigate different (carbo)nitride promoters, which not only possess important properties, but may also be able to alter the dehydrogenation of the complex hydrides.

3. (CARBO)NITRIDE CERAMICS AND DERIVATIVES

3.1. Definition/Applications of (Carbo)Nitride Ceramics

Until recently, each time the word **"ceramics"** was used, the visions were directly conducted towards white wares, and clay products. It is not deniable that common oxides like silica and alumina have largely dominated the ceramic field, and the understanding of their chemistry, processing and properties is highly developed. However, a growing interest in **non-oxide** ceramics, particularly **nitrides** and **carbonitrides,** we define as the **(carbo)nitride family** (Figure I-8), are promising candidates for **technological applications**. They have seen the light, because many of them exhibit fascinating properties such as hardness, chemical inertness, thermal conductivity, high temperature stability, etc. Due to these unique features, they are interesting for a great variety of applications, mechanical as well as electronic.

Without listing in an exhaustive way, the major versatile nitrides, denoted as advanced or **functional ceramics**, ranking high on the list of important inorganic materials are boron nitride **BN**, and aluminum nitride **AlN**. In the category of carbonitrides (those combining carbide, nitride and free carbon), silicon carbonitrides are the most investigated. Here we studied silicon carbonitrides modified by aluminum and boron, respectively **SiAlCN** and **SiBCN**.

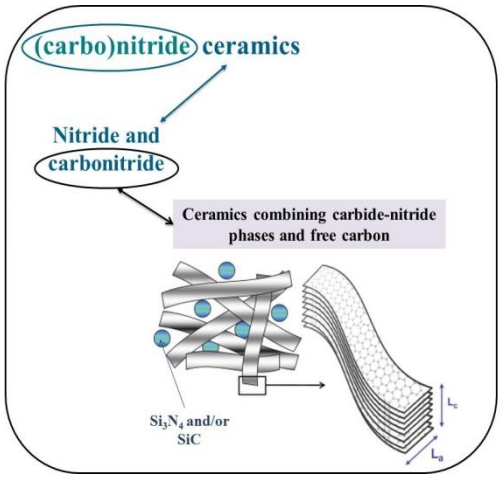

Figure I-8: Polymer-Derived (Carbo)Nitrides [89].

The aim of this work concerns the elaboration (starting with the synthesis and ending with the application) of different types and shapes of (carbo)nitrides using the **Polymer-Derived Ceramics (PDCs) route**.

3.2. Synthesis of (Carbo)Nitride ceramics

The main family of ceramics having a great extent of physical and chemical properties, which are extensively used today, is oxide. Therefore, the majority of studies in materials chemistry and physics are focused on such materials which are nowadays the best characterized group of inorganic compounds. However, they do not always cover the current technological needs, especially as porous candidates according to their limited thermostructural and thermochemical stabilities. Accordingly, there are growing efforts to find new oxygen-free compounds satisfying these technological requirements for porous materials. The most promising candidates for that are carbides, nitrides and carbonitrides.

The objective of **fabricating functional (carbo)nitrides** (that include nitrides and carbonitrides) is the production, from suitable starting materials, of a solid product with the **desired shape** such as **films**, **fibers**, or **monoliths** and with the **desired nano-/microstructure** and **texture**. The main fabrication methods can be classified, in a spontaneous attempt, into **three categories of process** in gas, liquid and solid synthesis such as **Chemical Vapor Deposition** [90], **Sol-Gel** [91] **and Polymer-Derived Ceramics** [92]. These three methods will be described in the following sections.

3.2.1 Chemical Vapor Deposition

The Chemical Vapor Deposition or **CVD** is by far the most important **gas-phase reaction** where reactive species are decomposed in the gas phase and transported to a surface where they can chemically react and form a solid film. It is a well-established technique that can be used to deposit all classes of materials, including metals, ceramics, and semiconductors, for variety of applications [93]. There are many excellent reports on CVD and their related applications [90]. Among other materials, many nitrides such as BN, AlN [94, 95], carbides [96], and carbonitrides [97, 98] have been reported using this method. However, the low space-time yield limits this technique to the layers of completed parts and is thus not considered here.

3.2.2 Sol-Gel

Sol-gel route to ceramics has been widely used for the synthesis of tailored oxide ceramics [99, 100].

In the sol–gel process, a solution of metal compounds or a **suspension** of very fine particles in a liquid (referred to as a **sol**) is converted into a highly **viscous mass** (the **gel**). It is best applied to the formation of films and fibers and, with careful drying, to a few monolithic ceramics. In 1997, Riedel and co-workers developed for the first time a **non-aqueous sol-gel process** which allowed the synthesis of **carbides** and **nitrides** [101]. A reaction between the methyltrichlorosilane CH_3SiCl_3 and bis(trimethylsilyl)carbodiimide, can lead to a non-oxide poly(methylsilylcarbodiimide) gel that can be transformed to ceramic by a thermal treatment (1000-1300°C). Jansen and co-workers took advantage of the sol-gel chemistry for the **synthesis of nitride ceramics** by adapting it to non-oxidic systems through co-ammonolysis of elemental alkylamides into silicon-based nitrides [102]. These methods are considered as **non-oxidic sol-gel** processes which in fact are related to the **polymer-derived ceramics route.**

3.2.3 Polymer-Derived Ceramics

The Polymer-Derived Ceramics **(PDCs)** route represents a **bottom-up approach** based on the use of single-source molecular precursors combining the elements of the desired ceramics at atomic scale. This route has become a rich and rapidly developing field of modern materials research. The apparent fascinatingly simple concept of preparing ceramics by the pyrolysis of polymeric precursors was first suggested by Chantrell and Popper about 50 years ago [103]. Ten years later, a manufacture of small-diameter Si_3N_4/SiC ceramic fibers [104] from polyorganosilicon compounds was developed in Germany for high temperature applications. Then, a significant breakthrough was made in Japan in the development of organopolysilanes and carbosilanes suitable for conversion to a SiC-based fiber [103]. This process, originally derived from the method described by Yajima, involves the melt- or dry-spinning of organosilicon polymers followed by a curing step and a subsequent pyrolysis of the polymer fiber providing the ceramic fiber [104]. The intermediate curing step results in an increased cross-linking of the polymer and hence in the formation of an infusible polymer fiber necessary for the shape retention during the thermal conversion into the ceramic material. Besides the commercial fabrication of ceramic fibers, the organoelement polymers are presently under research and development for a large variety of compositions and shapes and therefore applications. Thus, highly pure synthetic precursors in which uniform chemical composition is established at molecular scale are making an increasingly important contribution to the research development and manufacture of ceramic materials. This concept has two major advantages compared to conventional ceramic powders processing using solid-state reactions between powder reactants. The first advantage is to generate materials with enhanced physical and chemical properties and possibly new properties. The second advantage is to develop ceramic

objects, for example coatings, monoliths, fibers, with tailored textural and structural properties. Figure I-9 summarizes the different possibilities or strategies to prepare PDCs.

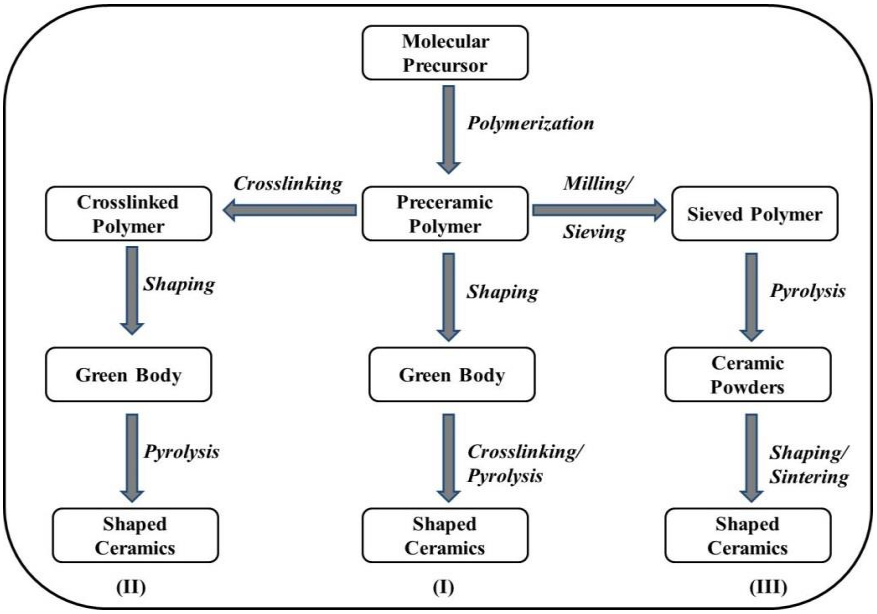

Figure I-9: Schematic representation of the PDCs method to prepare shaped ceramics.

Figure I-10 develops the different steps that are involved during the transformation of molecular precursors (=monomers) into PDCs (=crystalline ceramics). The preparation of silicon carbide SiC is taken as an example [105].

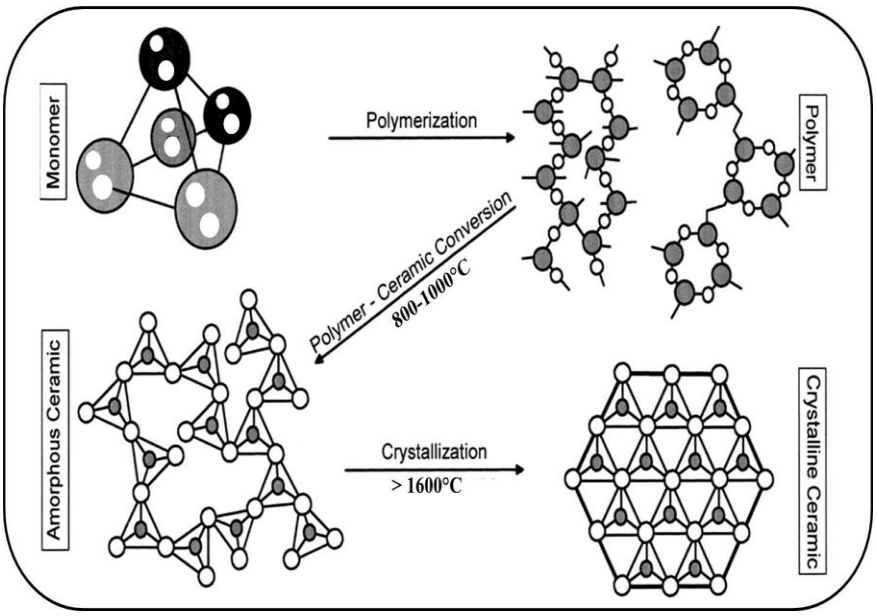

Figure I-10: From the monomer to the crystalline ceramic (adapted from [105]).

Polymerization is the first step. In general it involves either a thermal polymerization (thermolysis of the monomer through condensation reactions) or a chemical polymerization (reaction of the monomer with a linking reagent for example ammonia, methylamine…) This means that we have lattitude to synthesize polymers in a large variety of composition and structure. The as-obtained polymers may be subsequently modified with other molecular precursors. Polymerization can be more complex. It can involve different precursors that can be mixed homogeneousely as neat liquids or in solution. They can react during mixing to form a polymer or during the subsequent pyrolysis.

The transition for the polymer to ceramic proceeds continuously. It includes **cross-linking**, **mineralization** and **ceramization** steps. During the polymer-to-ceramic conversion, different reactions occur. For example, rearrangement and radical reactions result in the cleavage of chemical bonding and the release of organic functional groups (CH_4, C_6H_6, CH_3NH_2, etc.) which induce a **weight loss**. Associated with the density change from the polymer to the ceramic, **volume shrinkage** occurs. After the polymer-to-ceramic conversion, the material consists in an **amorphous network** containinig the consituents homogeneously dispersed on the atomic level. The use of the amorphous network is expected to be beneficial for the high temperature creep behavior of these materials. Admittendly, amorphous materials are not in the global thermodynamic equilibrium state which might be a disadvantage with respect to the desired thermal and/or chemical durability. Moreover, by a proper choice of the element combination at an atomic level for which the binding energies are derived from strong local covalent bonds, amorphous materials of high kinetic stability and thus durability are available. For example, the incorporation of ionic species (**Al**, **B**) to **silicon carbonitrides** allows to control the density (microporosity) of the amorphous network [106], and to improve its stability [107, 108]. A **crystallization** of the amorphous state leads to the preparation of i) monophasic crystalline ceramics (binary systems) such as **boron nitride** or **aluminum nitride** which are only stable as polycristalline materials, ii) homogeneous mixtures or solid-state solutions of pseudo binary combinations of ceramic parts (=composite or nanocomposite materials) and iii) new multinary crystalline phases. All four classes (amorphous, monophasic, multiphasic, nanocomposites) are equally attractive for basic research (chemical and structural systematics) and application technology. Depending on the polymer composition, precipitation of excessive carbon and/or nucleation and growth of crystalline phases such as SiC, Si_3N_4, SiO_2, B_4C, BN, etc. occur at different temperatures ranging from 800 to 1800°C.

The major advantages of this concept are evident; it enables an easy control of the composition at atomic level as well as an elemental homogeneity. In principle, the polymer can be easily shaped since the vast variety of materials developed for processing organic polymers can be

applied. As an illustration, the PDCs route offers an easy way to synthesize ceramic fibers [109], thin layers [110, 111] or composite materials [112] which in principle cannot be produced using powder technology. Furthermore, the relatively low temperatures (1000-1300°C) to produce ceramics, especially the Si-based ones, is of economical interest.

PDCs retain a memory of the polymer chemistry and structure from which they evolve, which is why the starting precursors must, themselves, be carefully chosen. A compromise of properties that an ideal preceramic polymer should possess has been set forth since the work of Wynne and Rice in 1984 [113]:

- Molecular weight sufficiently high to prevent any volatilization of oligomers;
- Cages/rings-containing structure to decrease the volatile fragments resulting from backbone cleavage;
- Desired viscoelastic properties (fusibility, malleability, or solubility) to apply the polymer in the desired shape before the pyrolysis;
- Presence of latent reactivity (functional substituent) to obtain thermosetting or curing properties;
- Low organic group content to increase ceramic yield and avoid the production of undesired free carbon excess.

It is evident that a same polymer cannot display all these properties which are sometimes incompatible and it is clear that varying the microstructure of the preceramic precursor as well as the nature of the functional substituents, will affect, upon judicious crosslinking and shaping, the properties of the ceramic. Thus, the choice of the adequate polymer has to be done in function of the desired shape and the previewed applications.

The most famous classes of PDCs are in the binary systems **Si_3N_4**, SiC, **AlN** and **BN**, the ternary systems SiCO, BCN, and SiCN as well as in the quaternary systems SiCNO, SiBCO, **SiBCN, SiAlCN** and SiAlON. Since the degree of maturity reached by the PDCs materials is rather developed, pentanary systems have also been reported.

The following sections will concern the systems that pioneered the work of this PhD: starting with binary systems **AlN** and **BN** and finishing by quaternary systems **Si(E)CN** where **E=Al and B**, and the challenging task of introducing **porosity** inside these materials.

4. POLYMER-DERIVED (CARBO)NITRIDES

4.1. Alumium Nitride

4.1.1 Structure and properties

Aluminum nitride **(**AlN**)** is a III-V compound. It represents a semi-conductor with a high band gap (6.2 eV). It is an attractive nitride due to its important properties including chemical and high-temperature stability, high thermal conductivity, low electrical conductivity and low thermal expansion coefficient, which make it an important substrate material for electronic devices [114]. It also has excellent molten metal corrosion resistance and stability at high temperatures. Extensive high-temperature creep and compressive strength measurements have been carried out on **AlN** [115]. Table I-2 summarizes some representative properties for AlN [116].

Table I-2: AlN properties [116].

Property	**AlN**
Density (g/cm^3)	3.26
Hardness (GPa)	12
Young's modulus (GPa)	308
Flexure strength (MPa)	400
Compressive strength (GPa)	1.5-4.0
Fracture toughness (MPa m$^{1/2}$)	3.0-4.0
Bulk modulus (GPa)	200
Shear modulus (GPa)	127-130
Poisson's ratio	0.23-0.24
Thermal conductivity (W/m/°C)	180-220
Coefficient of expansion (/°C)	5.6
Melting temperature (°C)	Sublimes
Electrical band gap (eV)	6
Dielectric constant (1MHz)	8.9
Dielectric constant (7GHz)	8.2
Dielectric loss (1MHz)	0.001
Dielectric loss (7GHz)	0.002
Longitudinal sound velocity (Km/s)	7.0-9.4

The most thermodynamically stable structure of AlN is the wurtzite with *P63mc* as space group. The lattice parameters are equal to a=b= 0.3111 nm and c= 0.4980 nm. However, under high temperature and pressure, AlN can be obtained in its cubic form.

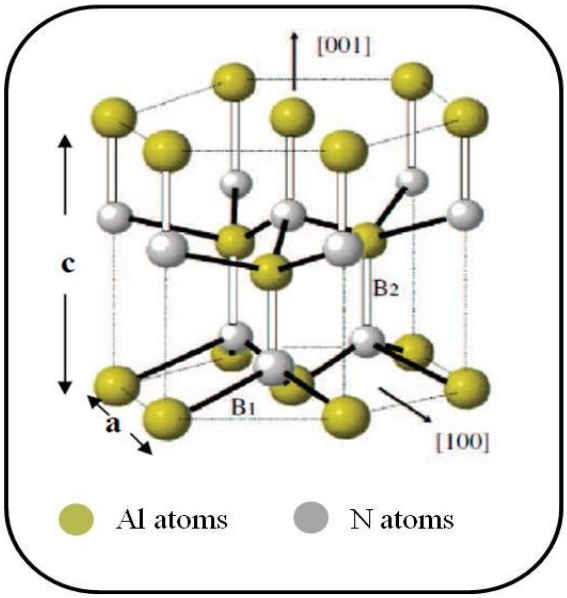

Figure I-11: 3-D view of the Wurtzite AlN [117].

According to Figure I-11 the Al-N bonds do not have the same length or the same energy. Each Al atom is surrounded by four N atoms, with three strong bonds of type B_1 and one of type B_2 parallel to the c axis.

AlN has its first industrial success to its high thermal conductivity (six times that of alumina and comparable to that of copper), and to its non-toxic character (compared to BeO). In its massive form, it was used mainly in industrial devices to dissipate heat losses. Due to its additional properties of low thermal expansion and high resistance to thermal shocks, AlN was developed as thin films for microelectronics applications for instance, the microelectromechanical systems or MEMS. Moreover, the fact that the coefficient of expansion of AlN is close to that of silicon, facilitates its integration into multilayers [117].

Wurtzite AlN, also known for its piezoelectric aspect, has a high speed acoustic propagation, which makes it quite interesting for the fabrication of acoustic devices. It is normally used for SAW (Surface Acoustic Wave) and BAW (Bulk Acoustic Wave) devices [118, 119], and is currently integrated in mobile devices.

If the thermal conductivity of pure AlN single crystals is high (285 $W.m^{-1}.K^{-1}$), it is strongly reduced though in polycrystalline materials (80-200 $W.m^{-1}.K^{-1}$) owing to the presence of oxygen, impurities and grain boundaries [114].

4.1.2 Fabrication routes of Aluminum Nitride

Using AlN in various application fields (electronics, engineering, metallurgy…) is intimately related to the final object properties, which depend themselves on the starting AlN properties.

Commercial AlN powders can be produced by direct nitridation of metallic aluminum at temperatures above 1600°C or by carbonitridation of alumina starting from 1400°C [120, 121]. However by these means of fabrication, a high amount of impurities is present due to the contamination of the starting materials and the contamination by the mechanical milling of the reaction elements. The chemical vapor deposition has also been developed for AlN film preparation [122].

The purity, particle size, particle-size distribution and specific surface area of the powders affect their sinterability and the density and properties of the AlN ceramics obtained. The thermal conductivity, in particular, depends critically on the chemical purity and density, for example, samples containing 3-4 wt% of oxygen and having a density of 3.1 $g.cm^{-3}$ have a thermal conductivity at 300 K of 0.4 $W.cm^{-1}.K^{-1}$, typical of a non-thermal conductor and only one-eighth of the value of 3.2 $W.cm^{-1}.K^{-1}$ found for pure single-crystal A1N (density 3.25 $g.cm^{-3}$).

Recent interest has centered on synthetic routes involving organometallic or polymeric precursors in order to obtain AlN of high purity and different morphologies at low temperatures. Organoaluminum and organonitrogen-based polymers and copolymers as precursors have been reported during the last period [123-127]. The most important route starting from organoaluminum compounds consists in the reaction of alkylaluminum compounds with ammonia under an inert atmosphere at room temperature followed by a thermal treatment under nitrogen or ammonia at 1000°C [128, 129]. Schleich patented in 1988 the reaction between aluminum chloride ($AlCl_3$) and hexamethyldisilazane $HN(SiMe_3)_2$ in order to synthesize pure AlN at temperatures ranging from 200 to 700°C [130]. One year later, Riedel and Petzow proceeded to the characterization of the highly pure residue of the same reaction by different analytical methods [114]. The pyrolysis technique based on preceramic polymers as precursors offers alternative routes for the preparation of non-oxide ceramics with desirable shapes, such as coating and if a precursor is soluble or fusible. Polymer-Derived AlN are the topic of the next section.

4.1.3 Polymer-Derived Aluminum Nitride

As mentioned before, the development of a number of applications requires high purity AlN processable into different morphologies; the often used inorganic synthetic routes to AlN are unable to fulfill these requirements. Therefore pyrolytic conversion of preceramic precursors (organoaluminum compounds, aluminum containing inorganic compounds) has been intensively investigated in the past few decades. Among polymeric precursors containing Al-N bonds [126, 131-152], **poly[N-(alkylimino)alanes] of the type $[HAlNR]_n$** (with R= H, Et, ^{i}Pr) prepared from lithium aluminum hydride and various alkylammonium chloride, represent a well-known cage-type compound firstly proposed by Ruff and Hawthorne [127]. Depending on the nature of the carbon-based pendant groups, the polymers display various physical states going from viscous liquid to soluble solid. Such properties offer interesting possibilities in the preparation of complex-shaped ceramics including thin coatings and 1D nanostructures [134]. Sugahara *et al.* [153] published a review dedicated to these polymers. Depending on the alkyl group linked to the nitrogen element in these polymers, they showed that the aggregation degree (Table I-3) as well as their structure (Figure I-12) differed.

Table I-3: Aggregation degree of poly(alkyliminoalane) $(HAlNR)_n$ [154].

R	Aggregation degree	Structure
Me	-	Highly cross-linked
Et	8	Cage-type
^{n}Pr	6,7,8	Cage-type
^{i}Pr	4,6	Cage-type
^{n}Bu	6,7,8	Cage-type
^{i}Bu	6	Cage-type
^{s}Bu	6	Cage-type
^{t}Bu	4	Cage-type
C_6H_{11}	4,6	Cage-type

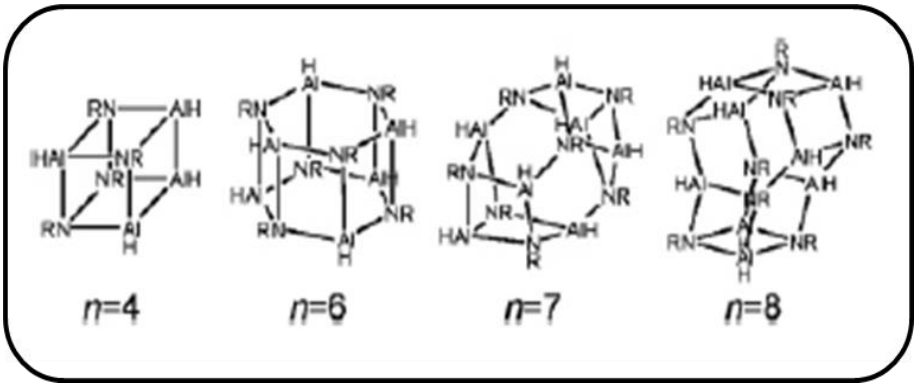

Figure I-12: Structure of poly(alkyliminoalane) $[HAlNR]_n$ with n = 4, 6, 7, 8 [154].

To a much lesser degree, the potentiality for shaping such polymers was studied. Our group tested a series of poly[N-(alkylimino)alanes] suitable as precursors for thin coatings and nanostructures in the liquid state by changing the nature of the alkyl groups [134]. Table I-4 lists some of the properties of these polymeric precursors.

Table I-4: Properties of AlN preceramic polymers [134].

R	Physical state	Chemical formula
1: CH_3	Solid	$[Al_{1.0}N_{1.5}C_{1.8}H_{7.2}Li_{1.2}Cl_{0.8}]_n$
2: CH_2CH_3	Solid	$[Al_{1.0}N_{0.9}C_{2.1}H_{6.8}]_n$
3: $CH(CH_3)_2$	Solid	$[Al_{1.0}N_{0.9}C_{2.8}H_{8.1}]_n$
4: $CH_2CH(CH_3)_2$	Solid	$[Al_{1.0}N_{1.0}C_{4.3}H_{10.8}]_n$
5: $(CH_2)_4CH_3$	Liquid	$[Al_{1.0}N_{0.9}C_{5.7}H_{14.1}]_n$
6: $(CH_2)_7CH_3$	Liquid	$[Al_{1.0}N_{0.8}C_{7.7}H_{20.1}]_n$

In this PhD work, our choice focused on the **poly(ethyliminoalane)**. Its structure is proposed in Figure I-13 [125].

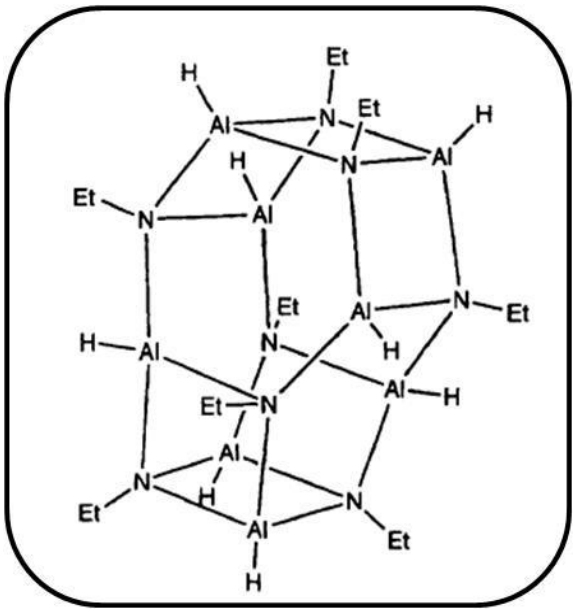

Figure I-13: Structure of poly(ethyliminoalane) [125].

One of the main advantages of this route is the low cost and easy (quantitative) synthesis of the polymer. Furthermore, the poly(ethyliminoalane) is soluble in THF or ether and displays a suitable ceramic yield (57% under NH_3-N_2). We used this precursor to elaborate **porous AlN**. It should be mentioned that porous AlN has not yet been the focus of publications; so we felt it was desirable and challenging to report on the elaboration of porous AlN for energy applications.

4.2. Boron Nitride

4.2.1 Structure and properties

Boron nitride (BN) is a material whose properties make it of large interest, not only scientifically but also technologically. It also represents a synthetic III-V binary compound. However, in terms of polymorphism and mechanical characteristics, its properties are closer to the carbon rather than those of other III-V compounds. These similarities can be explained by the isoelectronic structure of BN and carbon.

Four polymorphic forms can be found: two dense sp^3 hybridization (cubic BN (c-BN) and wurtzite BN (w-BN)) and two graphite-like sp^2 hybridization (rhombohedral BN (r-BN) and hexagonal BN (h-BN)). Figure I-14 shows the different crystalline forms of BN. Each polymorph exhibits special properties which render them potential candidates for different applications.

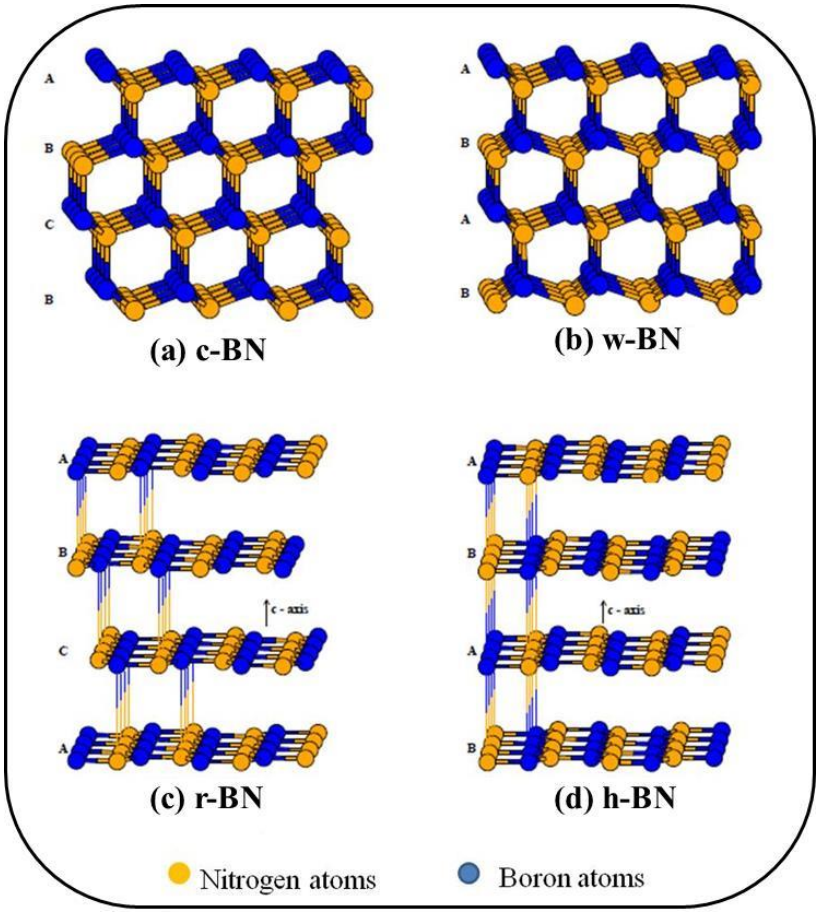

Figure I-14: Crystalline structure of BN [155].

Wentorf reported the preparation of c-BN by high temperature and pressure in 1957 similar to the diamond elaboration [156]. The c-BN exhibits many attractive properties similar to those of diamond. However, c-BN displays a greater resistance against oxidation.

The wurtzitic boron nitride, originally prepared by Bundy and Wentorf [157] is a super hard form of BN with properties closely resembling those of c-BN. With its polycrystalline structure, w-BN provides superior cutting properties, high shock resistance, stress induced shear transformation responsible for toughening [158].

In contrast to the rhombohedral form of BN which is the less studied, the h-BN is probably the most studied phase. It is therefore described in details in the following section.

4.2.2 Hexagonal Boron Nitride

The h-BN lattice consists of a layer sequence of ABAB where boron and nitrogen atoms alternate along the c axis (Figure I-14-d). Two types of B-N bonds can be found: the strong intralayer covalent bonds (*sp2* hybridization) in the direction of hexagons and the weak interlayer Van Der

Waals bonds between the hexagons. In 1952, Pease firstly described the structure of h-BN [159]. He reported lattice parameters of 2.504 Å (for a) and 6.661 Å (for c). The h-BN displays a large band gap (~5.5 eV). It offers the lowest density (d= 2.27 $g.cm^{-3}$) among the non-oxide ceramics, a relatively good thermal stability in particular in air and vacuum, as well as specific properties such as high thermal conductivity, a good thermal shock resistance, a high electrical resistance, a low dielectric constant and loss tangent, a microwave transparency, a non-toxicity and an easy machinability. Furthermore, it is non-abrasive, lubricious and non-reactive towards molten metals. However, such properties are strongly affected by its crystallinity and crystalline quality.

Like a large number of ceramics, h-BN can be prepared through different methods including, powder metallurgy technologies where BN is generally obtained by reaction of boric oxide with ammonia (T >900°C), or with organic nitrogen compounds such as melamine/urea (T >1000°C), or by nitridation of calcium hexaboride in the presence of boric oxide (T >1500°C) [160]. Chemical Vapor Deposition method by combining boron and nitrogen containing precursors such as B_2H_6/NH_3, $B_2H_6/NH_3/H_2$, BF_3/NH_3, BCl_3/NH_3, $BC1_3/NH_3/H_2$, $H_3B_3N_3H_3$, $C1_3B_3N_3H_3$, and $B_{10}H_{14}/NH_3$ [94] and the PDCs route are alternative preparative methods to prepare h-BN. In our study, the PDCs route has been investigated to prepare h-BN (expressed BN in the following sections of the document).

4.2.3 Polymer-Derived Boron Nitride

BN can be prepared from different classes of molecular precursors such as B-(trichloro)borazine $Cl_3B_3N_3H_3$, ammonia borane NH_3BH_3, tris(alkylamino)borane $B(NHR)_3$ and borazine $H_3B_3N_3H_3$. The selection of the BN precursor is important and precursors with the good B:N ratio while hydrogen (H) is the only element added to B and N, are preferentially used. The main advantage of such molecular and polymeric precursors is the possibility to produce BN at relatively low temperatures (1000- 1450°C) without the necessity to use specific treatments such as ammonia (used with oxygen and/or carbon-containing precursors) and chemical etching (when alkali metal-based precursors are used). Furthermore, the control of the stoichiometry of BN at atomic scale is easier with such precursors because the B:N ratio is already fixed and only light gases are evolved such as H_2 and ammonia during the precursor-to-ceramic transformation. **Borazine** and the derived **polyborazylene** fit with this category of precursors. They are, therefore, described in details in the next sections.

4.2.3.1 Borazine

Borazine (Figure I-15) is an inorganic compound isoelectronic with benzene that exhibits some aromatic character. It was first described in 1926 by Alfred Stock and Erich Pohland [161]. However, the preparation at laboratory scale was not possible before the work of Wideman and Sneddon in 1995 [162]. Among the starting compounds that lead to borazine, the reaction between sodium borohydride ($NaBH_4$) and ammonia sulfate ($(NH_4)_2SO_4$) in tetraglyme is a convenient and economical reaction.

$$3(NH_4)_2SO_4 + 6\ NaBH_4 \rightarrow 2\ H_3B_3N_3H_3 + 3Na_2SO_4 + 18H_2 \quad \text{(I-4)}$$

This particular reaction was applied during the PhD work.

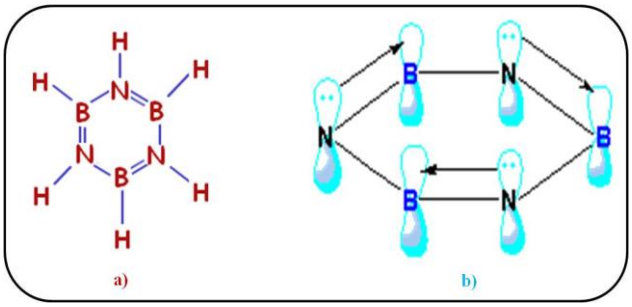

Figure I-15: a) Structure of borazine b) Electron delocalisation.

Borazine exhibits a high reactivity according to the presence of N-H and B-H units. Furthermore, it exhibits a high volatility at room temperature (the melting point of borazine is -58°C and the boiling point 53°C [163]); therefore it can be used in different processes involving gas phase-based processes such as CVD [164] or spray-pyrolysis [165]. However, to extend the shaping potentialities of borazine, it can be firstly converted into a preceramic polymer called polyborazylene by a thermolysis at low temperatures in an autoclave before shaping and pyrolysis to obtain BN.

4.2.3.2 Polyborazylene

A large number of studies have been focused on the self-condensation of borazine and the identification of polymerization mechanisms [111, 166-175]. In the fifties and sixties, several authors studied the self-condensation of borazine. It generates biphenylic and naphtalenic-type structures (Figure I-16 a-b) through condensation reactions of BH and NH units as well as probable ring-opening mechanisms in the **polyborazylene** (Figure I-16-c).

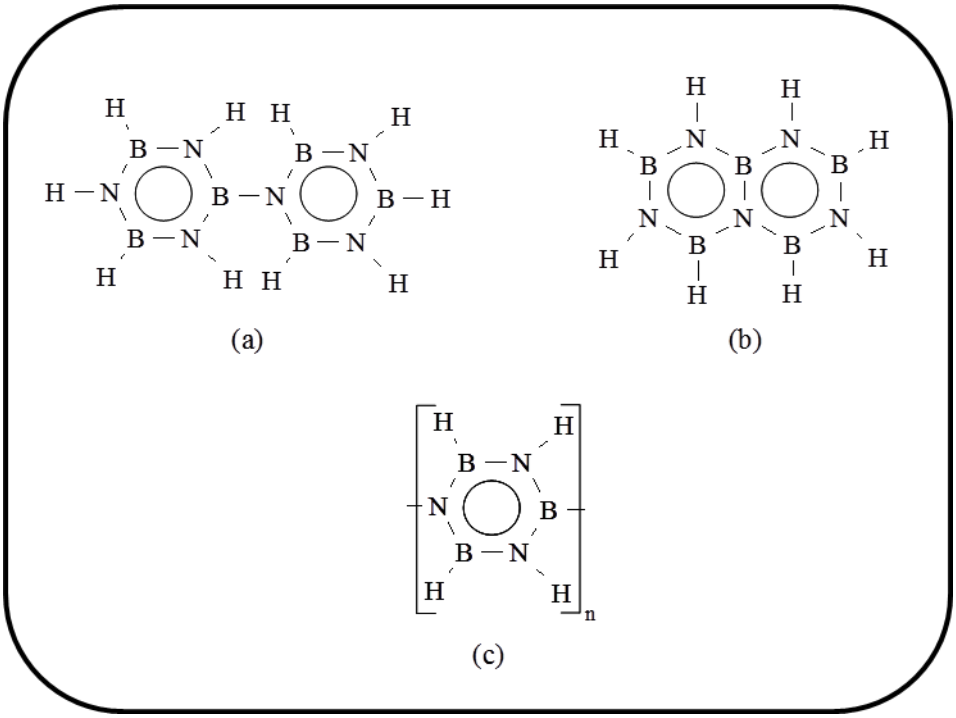

Figure I-16: Biphenyl (a) and naphtalenic (b) –type units generated during the self-condensation of borazine leading to polyborazylene structure (c).

Sneddon *et al.* have been the first authors to isolate a solid polyborazylene through the self-condensation of borazine under vacuum at 70°C for approximately 48 h [170]. This polyborazylene displayed a ceramic yield of 87-93% after pyrolysis up to 1200°C under argon (theoretical ceramic yield being of 95%). Later, Sneddon and co-workers [174] demonstrated that polyborazylene can be considered as an ideal BN precursor due to its high yield synthesis, good solubility in polar solvents (tetrahydrofuran, glyme etc) and high ceramic yield. Elemental analyses of the compound suggested the formation of a branched-chain or partially cross-linked structure. Despite this crosslinked structure, this polyborazylene was soluble and appeared an excellent precursor to prepare fiber coatings. Polyborazylene delivered BN by pyrolysis under argon or ammonia in the temperature range 900-1450 °C in excellent chemical (89-99%) and ceramic yield (84-93%). The increase of the temperature increased the density of BN as well as the crystallinity of samples based on X-ray diffraction investigations. However, the structure of BN remained turbostratic. This did not affect the stability in air of polyborazylene-derived BN. In air, polyborazylene-derived BN is stable up to 900°C (no weight changes were observed by TGA in air). Above 900°C, weight gain occurred to form boron oxide. The excellent stability in air of polyborazylene-derived BN was confirmed by Economy *et al.* [173]. Authors reported in 1993 the preparation of C/BN composites from a viscous polyborazylene which was obtained by self-condensation of borazine in an autoclave in a nitrogen

atmosphere at 70°C for 40 h. The as-obtained viscous polymer displayed a chemical formula of $B_{3.0}N_{3.6}H_{3.7}$. In another paper [172], authors prepared the first inorganic mesophase by low-temperature thermolysis of the borazine. Indeed, based on the synthesis procedure reported by Sneddon *et al.* as well as on the prediction made on the formation of biphenyl and naphtalenic-type units and requirements for the formation of pitch mesophases, authors modified the thermolysis rate to maintain certain mobility in as-formed molecules, and therefore obtain optically anisotropic phases during thermolysis of borazine. The formation of a liquid-crystalline phase during thermolysis provided an efficient way to produce a final BN material with a high degree of crystalline order on heating to 1800°C. In particular, TEM of BN revealed the presence of a polycrystalline microstructure with a long-range preferred orientation.^{15}N and ^{11}B solid-state NMR [171], performed to characterize the structure of polyborazylene, suggested the presence of tricoordinated boron and nitrogen atoms, present in two types of boron sites (BHN_2, BN_3) and two types of nitrogen sites (NHB_2, NB_3) if only the first neighboring atoms are considered. No tetracoordinated atoms could be detected, which means that the majority of the B and N atoms are included in ring structures. Some ring-opening reactions can occur, followed by reformation of cyclic structures. This reaction leads to eight membered-ring structure shown in Figure I-17.

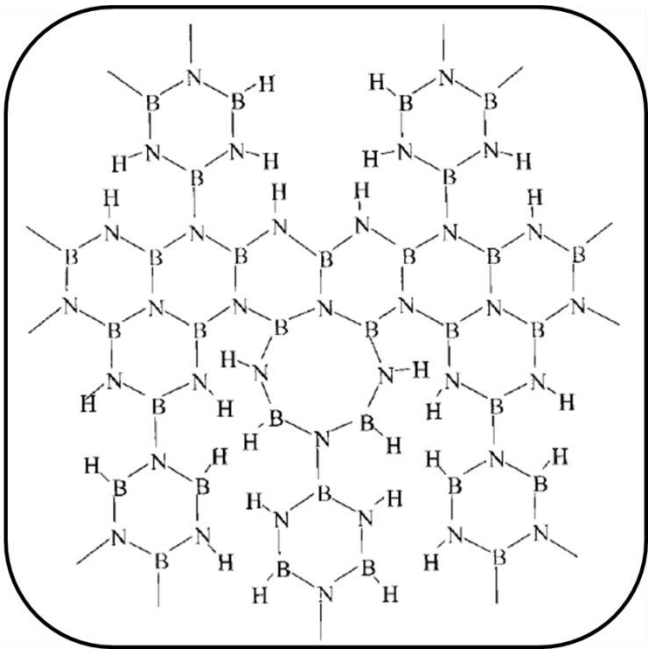

Figure I-17: Structure of polyborazylene [171].

Through the study of the self-condensation of borazine at low temperature (45-60°C) under argon in an autoclave, our group demonstrated the possibility to control the physical state of

polyborazylene from liquid (45-55°C) state (with viscosity increasing with the increase of the synthesis temperature) to solid state (⩾ 60°C) by adjusting the temperature of thermolysis. Since polyborazylenes varied in their physical state from liquids to solids, they appeared suitable for various processing and shaping techniques. This is illustrated in Figure I-18.

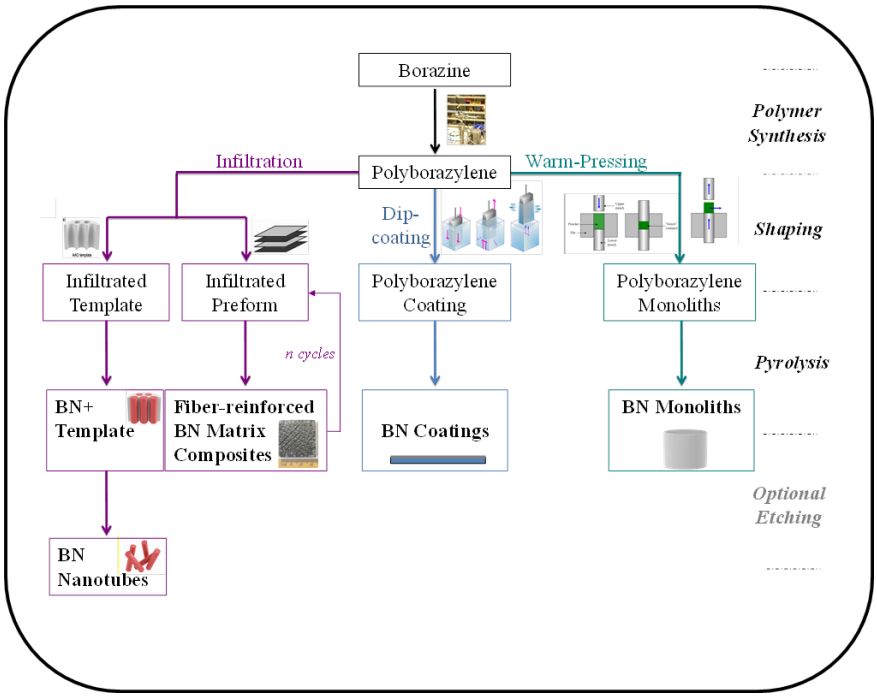

Figure I-18: Examples of shaped BN derived from polyborazylenes.

Table I-5 exhibits the properties of the as-obtained polyborazylenes. **PB45** and **PB50** are liquid polyborazylenes obtained by thermolysis of borazine at 45 and 50°C. They represent candidates to prepare BN coatings [166], BN foams [176] and BN nanotubes [177]. **PB60** is obtained by thermolysis of borazine at 60°C. It is the ideal precursor for shaped BN. It can be used to prepare BN monoliths [167], and according to its good solubility, it can be used to prepare BN composites [178] and coatings. In the present study, it was prepared to elaborate **porous BN in various shapes**.

Table I-5: Properties of different polyborazylenes.

PB	$M_{borazine(g)}$	$T_{synthesis}$ (°C)	Pressure (bar)	Timing (hours)	Physical state	Chemical formula	Weight loss (%)
PB45	14.6	45	5.6	120	Liquid	$[B_{3.0}N_{3.0}H_{4.8}]_n$	70
PB50	16.2	50	30.1	192	Liquid	$[B_{3.0}N_{3.8}H_{4.0}]_n$	53.2
PB60	17.8	60	121.1	240	Solid	$[B_{3.0}N_{3.5}H_{4.5}]_n$	8.8

We have seen that AlN and BN are very interesting compounds based on their properties. These materials do not only display notable benefits as monolithic ceramic, but they can be added to other structural ceramics such as silicon carbide and silicon nitride to generate homogeneous mixtures of pseudo-binary combinations of ceramics. The potential interest in such materials stems in part from observations of improved mechanical properties (such as toughness), thermal shock resistance and microstructural stability in certain cases and improved machinability as well as the appearance of new functions [179-183]. For example, the addition of aluminum nitride (AlN) to BN [184], BN to Si_3N_4 [179] and titanium nitride (TiN) to BN [185] have been found to improve the toughness, the sinterability and other specific properties. Excellent crystallization compatibility was also found between SiC and AlN and a complete solid solution can be formed under certain conditions. The sintering activity, microstructure, mechanical properties, functional properties and oxidation resistance of materials were largely improved with the formation of solid solutions [186].

Functions of these composite materials can be controlled by adjusting the configuration and arrangement of the dispersed phases. However, in order to achieve the desired performance properties, these phases need to be homogeneously dispersed. Fabrication of multiphase materials of covalent ceramics is problematic using conventional powders and processing techniques because:

i) The grain sizes and grain size distribution typically obtained by most powder productions methods are too large;
ii) The ability to control the purity and crystalline form of the product is limited;
iii) Mixing two or more ceramic powders to form a composite which is homogeneous at the nanoscale is often difficult, if not impossible and this inherently involves compositional and structural inhomogeneities.

Sol-gel processing of mixed metal alkoxides has provided an effective alternative to prepare homogeneous multiphase oxide ceramics. Following the same way, we investigated the pyrolysis of appropriately designed polymeric precursors providing general routes to AlN- and BN-based multiphase ceramic materials including silicoaluminum carbonitride (SiAlCN) and silicoboron carbonitride (SiBCN) materials.

4.3. Aluminum- and Boron-containing SilicoCarboNitrides

The pyrolysis of appropriately designed molecular and/or polymeric precursors provided a general route to multiphase ceramic materials. This approach uses either single-source precursors that contain the elements of the final ceramic composites chemically bound together in the requisite

proportions , *i.e.*, either one cationic component or two or more electropositive elements in a specific arrangement [102] or reactions of preformed polymers with molecular species or polymeric precursors of a second ceramic phase that result in the formation of new polymeric species [187, 188] or mixture of two or more polymers in a common solvent, each one being a precursor of a phase of the desired materials. In that case, the polymers react during the subsequent pyrolysis [189, 190]. The phase distribution and crystallite size can be controlled in the final material by a proper choice of the pyrolysis atmosphere, the heating rate and the annealing temperature of the starting precursors. In addition to provide a homogeneous distribution of the component elements, this approach offers the possibility of obtaining a processable polymer.

4.3.1 Aluminum-modified SilicoCarboNitride

The addition of aluminum to silicon-based ceramics contributes to the improvement of the hydrothermal stability of the derived materials. As an illustration, the addition of Al to silicon oxynitrides forming SiAlON [191] results in an improved thermal and chemical stability in oxidizing atmosphere. Similarly, the addition of aluminum to silicon carbonitride results into a non-parabolic oxidation curve (at $T \geq 1000°C$) which decreases more rapidly with time, down to a negligible level. This has been well-demonstrated by An *et al.* [192]. The authors suggested that the remarkably low oxidation rates of these materials were attributed to the lower permeability of the formed oxide layer to molecular oxygen, which resulted from the incorporation of aluminum in the silica network. The passivating layer is shown to hinder diffusion-controlled oxidation in the bulk. As a consequence, Polymer-Derived SilicoAluminum CarboNitride (**SiAlCN**) are considered promising candidates for high-temperature and harsh environment applications.

Two general techniques have been investigated for the synthesis of **SiAlCN** precursors:

i) **"Building block" approach** or **co-pyrolysis** of homogeneous mixtures of precursors of the stable phases which compose the composite (organosilicon and organoaluminum precursors);

ii) **"Single source precursor" approach** in which Al and Si are precombined in a common structure. Several SiAlCN polymeric precursors were reported such as $[(Me_3Si)_2AlNH_2]_2$ [193], $(Et_2AlNH_2)_3$ [194], $(CH_3)_2AlNH_2$ that led to the highest SiAlCN yield [195] and $(Al(OCH(CH_3)_2)_3$ [196].

It has been reported the synthesis of SiAlCN from commercial polysilazane namely polyureamethylvinylsilazane (Ceraset) that reacted with an aluminum isopropoxide [196]. The

formation of polyaluminosilazane resulted from a dehydrocoupling reaction between the N-H units in Ceraset and Al-O units in the aluminum isopropoxide. The authors provided a detailed characterization of the polymer-to-ceramic transformation by means of FTIR and NMR spectroscopies and they revealed the effect of Al content on the structural behavior of the material. Three stages were observed when it comes to the polymer-to-ceramic conversion: i) cross-linking reaction forming SiC_3N units, ii) thermal decomposition forming $SiCN_3$ units and iii) structural rearrangement resulting in the formation of AlN_5/AlN_6.

Müller and co-workers [197] prepared polyaluminosilazanes from polysilazanes and polysilylcarbodiimides by means of hydroalumination of vinyl substituents at Si and subsequent dehydrocoupling of N-H reactive sites. Based on the multinuclear solid-state NMR (^{1}H, ^{13}C, ^{27}Al, and ^{29}Si), EPR and FTIR techniques they investigated the structural evolution of the preceramic polymer. The latter transforms into an amorphous preceramic network around 500°C where AlN domains as well as SiCN clusters are formed. Above this temperature a complete transformation into the ceramic takes place and the amorphous state remains up to 1400°C.

We investigated the "**building block" approach** as well as the "**single-source precursor" route** to prepare SiAlCN as ordered mesoporous materials and foams. Results will be presented in Chapter IV and V.

4.3.2 Boron-modified SilicoCarboNitride

SiliconCarboNitride (SiCN) ceramics are prepared from polycarbosilazanes or polycarbodiimides. The polysilazane-derived ceramics contain mixed bonds where silicon is bonded to both nitrogen and carbon at the same time, as shown in Figure I-19, whereas the SiCN ceramics obtained by thermolysis of polysilylcarbodiimides at approximately 1100°C is consisting of three types of nanodomains (1–3 nm in size) of amorphous silicon nitride, amorphous silicon carbide and amorphous carbon up to 1450°C, as revealed by SAXS and MAS NMR. No mixed bonds were found in this structure. They exhibit excellent oxidation and creep resistance at annealing temperatures as high as 1480°C. One single phase amorphous SiCN ceramic can be obtained by thermal decomposition of polysilazanes at 1100°C [198].

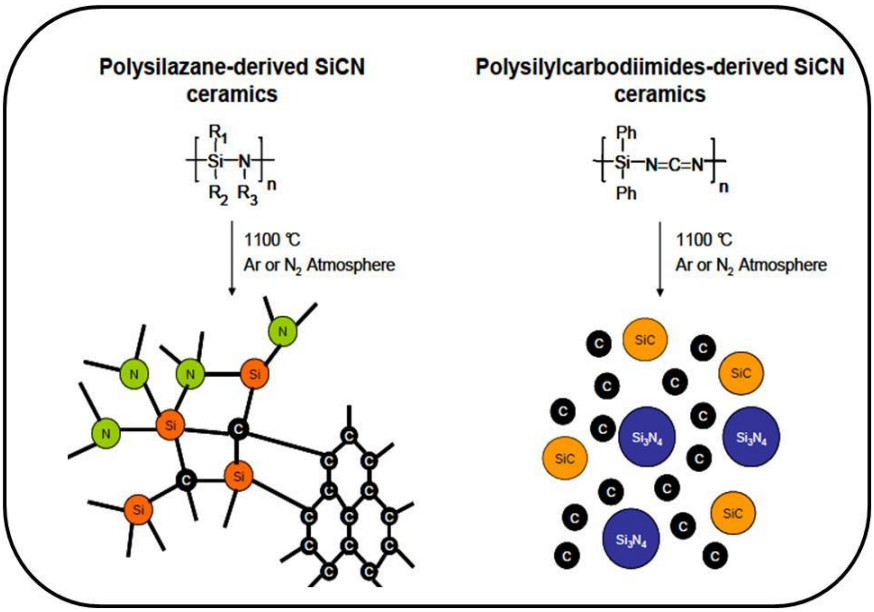

Figure I-19: Microstructure of SiCN ceramics derived from polysilazanes and polysilylcarbodiimides [198].

However, in the presence of excess carbon in the SiCN system, the solid-state reaction of Si_3N_4 with carbon generates SiC and nitrogen at 1480°C and the material crystallizes according to the following reaction [199]:

$$Si_3N_4 + 3C \rightarrow 3SiC + 2N_2 \quad \text{(I-5)}$$

It was demonstrated that incorporating boron (B) in the Si-C-N ceramics at atomic scale shifts the decomposition of **SiBCN** ceramics toward higher temperatures. This exceptional thermal stability of **SiBCN** ceramics is believed to be due to the fact that a turbostratic B-C-N phase is formed that retards Si_3N_4 decomposition reactions by a kinetic stabilization mechanism [200].

The two approaches described to prepare **SiAlCN** materials may be applied to prepare **SiBCN** materials. Sneddon and co-workers investigated the preparation of a borazine-substituted polysilazane by the reaction of hydridopolysilazane (HPZ) with borazine at moderate temperatures ranging from 60 to 90°C [201] as described below (Figure I-20).

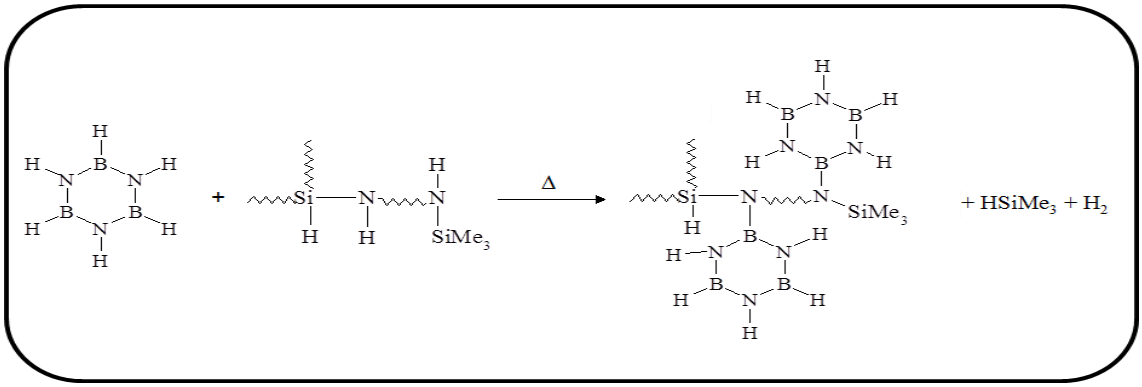

Figure I-20: Synthesis of borazine-substituted polysilazane [201].

A HPZ backbone substituted with pendant borazine rings through formation of B-N bonds by dehydrocoupling between N-H and Si-H bonds was generated. Depending on the synthesis conditions, these modified HPZs could be meltable and soluble in organic solvents. Hybrid polymers produced amorphous low-boron-content Si-B-C-N ceramics at 1400°C in an argon atmosphere in a 64% ceramic yield. Partial crystallization into several phases, *i.e.*, β-SiC, α-Si_3N_4 and β-Si_3N_4, was observed upon annealing to 1700°C. Extending this work, Sneddon *et al.* prepared co-polymers by the reaction of borazine with two types of silazanes, namely tris(trimethylsilylamino)silane (TTS) and hexamethylcyclotrisilazane (HCT) [202]. Co-polymers contained borazine-boron to silazane-nitrogen linkages. The pyrolysis of these hybrid polyborazinylsilazanes in an argon atmosphere at 1400°C delivered Si-B-C-N ceramic matrix materials (borazine-HCT) and BN coatings (borazine-TTS). Based on the same approach, Kim *et al*. reported the reaction between borazine and organosilazanes containing vinyl groups in THF solvent to produce soluble polymeric gels by hydroboration. Spin-coating followed by pyrolysis at 1400°C generated amorphous Si-B-C-N films which crystallized upon annealing at 1800°C into a crystalline composite made of SiC, Si_3N_4 and BN phases [203]. Paine and co-workers investigated the salt-elimination reactions involving B-trichloroborazine with $LiSi(SiMe_3)_3$ in a 1:1 ratio to form a borazine monomer $H_3N_3B_3(Cl)_2Si(SiMe_3)_3$. After filtration as-obtained compounds reacted with hexamethyldisilazane $(Me_3Si)_2NH$ to generate a glassy, colourless solid (Figure I-21) [204]. The pyrolysis of as-obtained oligomers in a nitrogen atmosphere provided ceramic products containing BN and a $Si_xN_yC_z$ phase which suppresses the crystallization of BN, and therefore improved the thermal stability of the material at high temperature.

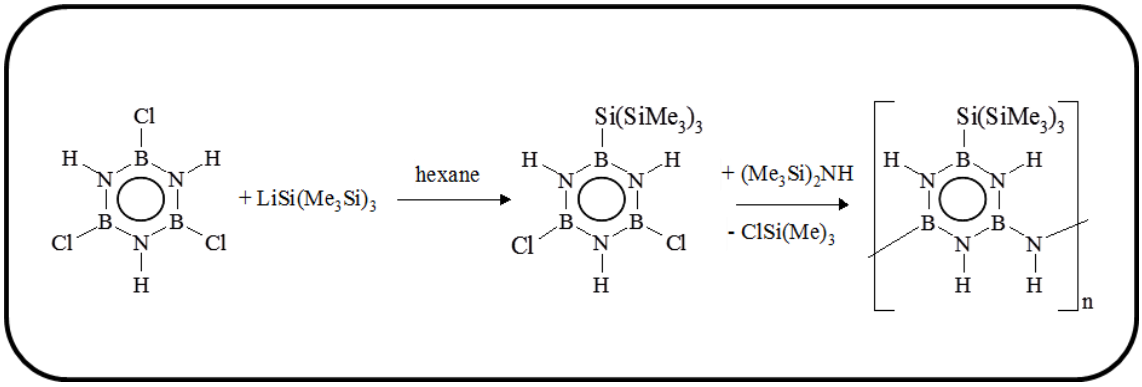

Figure I-21: $(Me_3Si)_3Si$-derivatized polyborazinylamine oligomer by Paine and co-workers [204].

Nesper and co-workers studied the synthesis of single-source molecular precursors based on the borazine ring *via* catalyzed hydrosilylation of *B*-triethynylborazine leading to *B*-tris(trichlorosilylvinyl)borazine and *B*-tris(dichloroalkylsilylvinyl)borazine [205, 206]. The latter reacted with methylamine CH_3NH_2 or lithium aluminum hydride $LiAlH_4$ (Figure I-22) to form preceramic polymers which offer an interesting way of controlling the chemical composition of the final SiBCN ceramics, thereby their thermal stability.

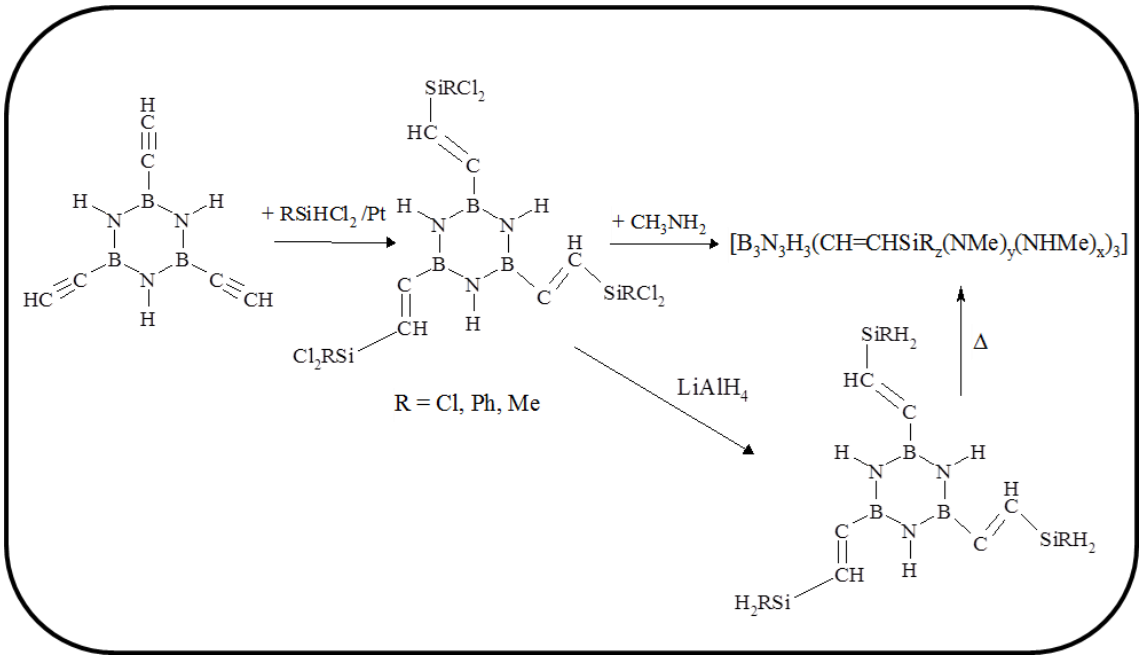

Figure I-22: Starting single-source borazine-based precursors used by Nesper and co-workers [205, 206].

There are mainly two polymer systems that lead to SiBCN ceramics through the "single-source precursor" approach. The first approach proposed by Jansen *et al.* makes use of the synthesis of polyborosilazanes, *i.e.*, polysilazanes cross-linked *via* -B-N-B- bridges [207]. The second synthetic pathway pioneered by Riedel *et al.* focuses on the synthesis of boron-modified polysilazanes (BmPSs) of the type $[B(C_2H_4SiCH_3NH)_3]_n$ [208]. They represent polysilazane rings which are cross-linked *via* -C-B-C- bridges (Figure I-23-a).

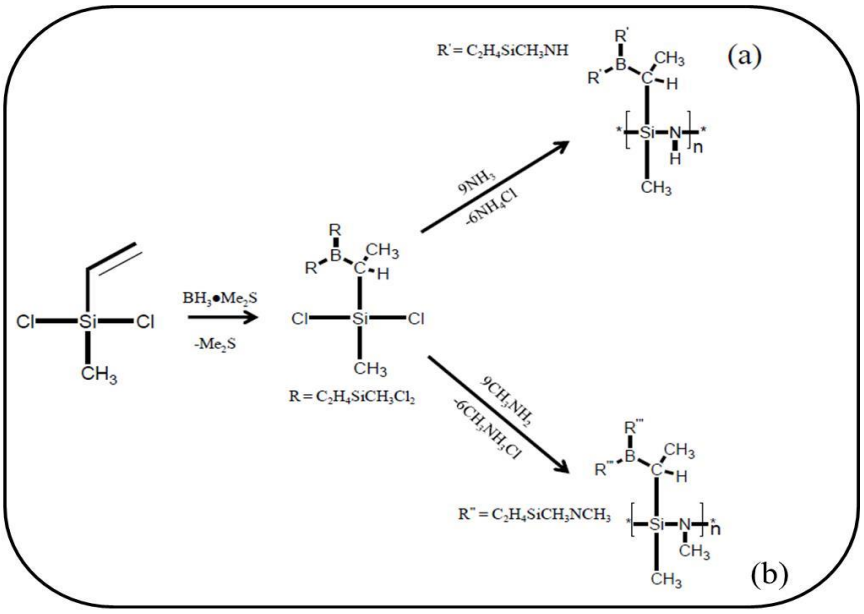

Figure I-23: Synthesis of polyborosilazane: monomer route.

There is a relatively large possibility to change the proportion of each element in the polymer, to modify the composition, and therefore the properties of the final ceramic. We can also change the nature of the linking reagent during polymerization. As an illustration, our group synthesized preceramic polymers by the reaction of tris(dichloromethylsilylethyl)borane with methylamine (Figure I-23-b). This polyborosilazane yielded a tractable polymer which was successfully processed into polymer green fibers by melt-spinning [209, 210]. More recently we reported in details the molecular chemistry and the polymer structure of a series of boron modified polysilazanes [109], as well as the study of the intermediate pyrolysis steps [211].

Alternatively, we can prepare in a first step the polymer by ammonolysis of a dichloromethylvinylsilane followed by the hydroboration of the latter in a second step. Figure I-24 reports this alternative route [212]. This strategy was already reported by Seyferth and co-workers in 1990 [213]. They prepared poly(borosilazanes) by the reaction of borane $BH_3.Me_2S$ with cyclic oligomers, such as $(CH_3SiHNH)_n$ obtained by the ammonolysis of dichloromethylsilane (CH_3SiHCl_2), which resulted in H_2 evolution and formation of a crosslinked product containing

boron atoms related to three nitrogen atoms. This product, when pyrolyzed under argon, resulted in a ceramic yield as high as 90%. Since then substantial progress have been made with the synthesis of the various poly(borosilazane) precursors including the choice of the starting Si-based material, synthesis route and also the Si:B ratio [212].

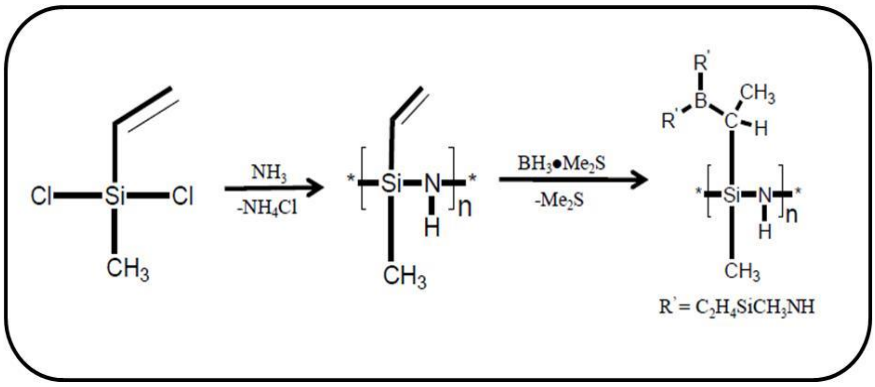

Figure I-24: Synthesis of polyborosilazane: polymer route.

We applied this strategy to prepare a novel generation of SiBCN precursors. This will be developed in Chapter V.

5. POLYMER-DERIVED POROUS (CARBO)NITRIDES

5.1. Definition of the porosity

Based on the pore diameter (IUPAC classification), porous materials are classified into **microporous** (< 2nm), **mesoporous** (2-50 nm) and **macroporous** (> 50 nm) [214] (Figure I-25).

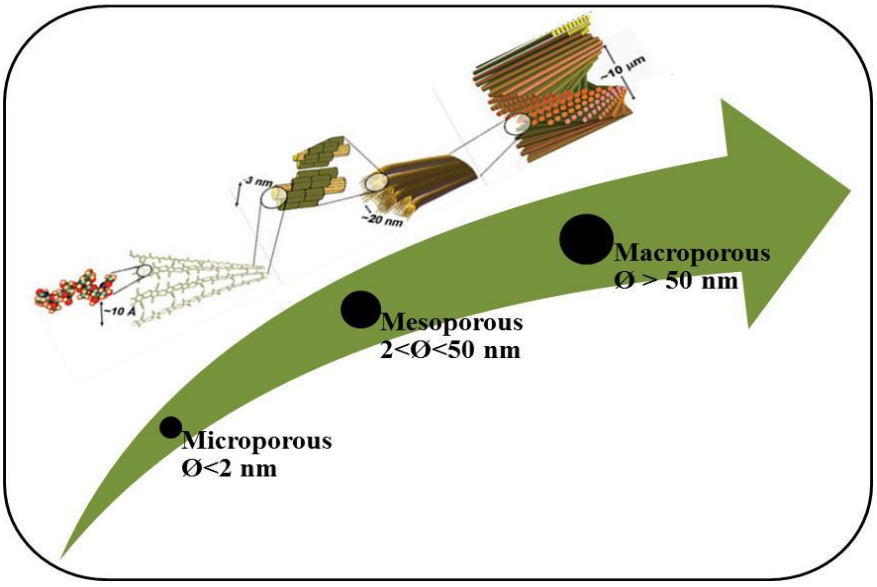

Figure I-25: Porous materials classification on the basis of pore diameter.

The **porous materials** offer many additional features to non-porous materials such as **high surface area** and **high adsorption capacity**. The industrial applications have witnessed a growing demand of **porous ceramics**. These porous materials can be synthesized by various template and non-template assisted techniques, with an attempt to control the pore characteristics. There has been a need for a thorough understanding of pore-related properties and thus of optimizing the processing parameters.

5.2. Process methods of porous ceramics

The structure and properties of porous ceramics are mainly controlled by their processing. Several processing routes for porous ceramics have been developed for specific applications as well as their associated requirements of porosity, pore size and degree of interconnectivity. Traditionally, porous ceramics have been produced by mixing ceramic powders with an organic material or calcium carbonate then formed into an appropriate shape. During the firing, the organic materials burn away or the carbonate calcines giving off carbon monoxide gas leaving pores in the ceramic body. This processing method is commonly used to form high temperature ceramics with coarse pore size of 20-50 μm and has been used in the refractory industry for many years [215]. The other traditional method that has been studied since the 1960s uses the acid leaching of silica based systems to produce pores [216]. With the extension of applications of porous ceramics, more and more techniques for processing the porous ceramics have been developed. Based on different pore structures, the main methods are summarized as following: direct foaming of ceramic slurries of sol–gel solution [217], direct blowing agents such as polyurethane (PU) [218], azodicarbonic acid diamide (ADA) [219], use of sacrificial fillers like polymethylmetacrylate (PMMA) [219, 220], chemical vapor deposition of various refractory materials on foamed carbon skeletons [221], sintering of hollow spheres [222], replicating a polymer foam/sponge and mixing an organic or polymer powders/fibers with ceramic precursor [222]. The recent development of porous non-oxide ceramics demonstrated that controlled high surface area and uniformly distributed porous structure could be developed using the **PDCs** route.

The fabrication of **porous (carbo)nitrides** *via* the PDCs route is a recent technique. Compared with the conventional processes, porous ceramics can be prepared from a chemically stable precursor. In the meantime, the pore characteristics of the achieved porous ceramic can be easily tailored using different types, sizes, amounts of porous materials (for reminder: porous templates, sacrificial spheres etc.). Furthermore, by this pathway the porous materials can be obtained at temperatures as low as 1000°C free of any additives and cost-efficient manners which is not known by any other technique. Even though several technologies of elaborating porous materials

have emerged (hard and soft templating methods [223], emulsions [224], foams [218], cellular materials [225]…) tailoring and controlling of the pores is still a major challenge in materials chemistry. During this PhD work, from the various methods used to produce porous PDCs, three ways of elaborating **porous (carbo)nitrides** were used:

- **The hard-templating method:** this method is also named **nanocasting** or **exo-templating approach.** It consists in three steps: i) infiltration into the pores of the template with the desired precursors, ii) pyrolysis of the infiltrated template to achieve the polymer-to-ceramic conversion and iii) removal of the template (Figure I-26) [226]. The hard templates are numerous, they include ordered mesoporous silica: cubic MCM-48 [227], cubic SBA-1 [228], hexagonal SBA-15 [229], cubic KIT-6 [230], hard macrocellular silica Si(HIPE) [231], aluminosilica zeolithes [232], as well as ordered mesoporous carbon (CMK-1, CMK-2, CMK-3 etc.). Such a route usually leads to the preparation of highly ordered mesoporous materials. Furthermore, multiple shapes, topologies and morphologies can be obtained.

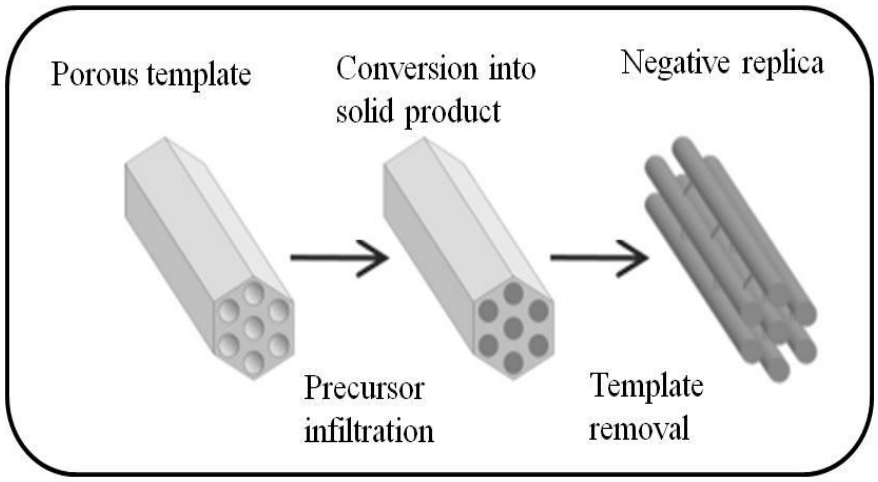

Figure I-26: Scheme of the hard-templating method.

- **Addition of sacrificial templates**: this approach relies on incorporating sacrificial templates such as poly(methylmethacrylate) (PMMA), polystyrene, wax etc. in solid polymer which are subsequently removed during pyrolysis to leave voids or pores in the final ceramic [233] (Figure I-27). This route leads to the preparation of cellular foams. The properties of such materials are affected by their relative density (amount of porosity), morphological characteristics (cell size and shape), distribution of the pores (pore interconnectivity and cell wall/strut porosity), and finally the material type. Due to their specific characteristics, as thermal stability, low thermal conductivity, low density,

resistance to thermal cycling, thermal shock resistance, low gas adsorption and absorption, these foams can find their use in different engineering applications ranging from metallurgy (removal of impurities from liquid metals) or high-temperature processing (thermal insulation) to the automotive (control of gas and diesel emissions), petrochemical (catalyst support), combustion technology [234].

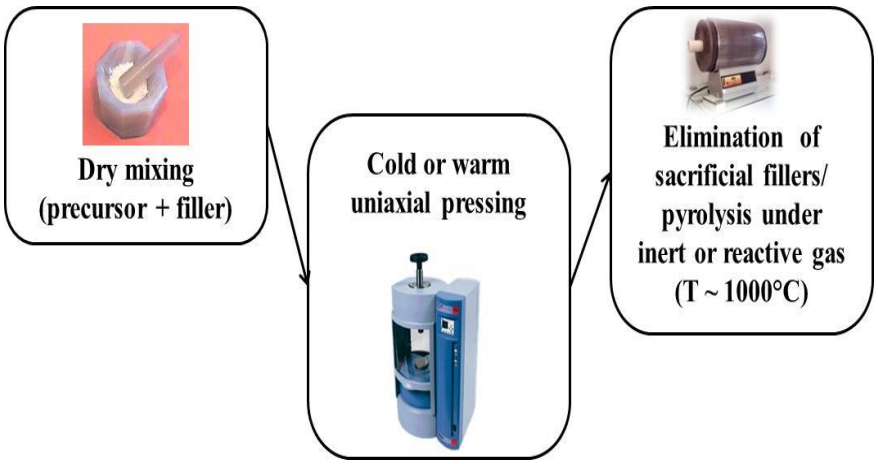

Figure I-27: Procedure for fabricating microcellular foams.

- **Aerogels preparation**: Aerogels are unique among solid materials. They have extremely low densities (up to 95% of their volume is air), large open pores, and a high inner surface area. This results in interesting physical properties, for example extremely low thermal conductivity and low sound velocity combined with high optical transparency. The initially formed gels have a sponge-like solid network filled with liquid. Special drying must be applied to exchange the pore liquid with air while maintaining the solid network (Figure I-28). Supercritical drying is most common, unlike the xerogels that derive also from sol-gels but are left to dry naturally. The structure of the gel network, and thus the physical properties of aerogels, decisively depends on the choice of the precursors and the chemical reaction parameters for preparing the gels. Therefore, the later material properties are predetermined at the beginning of the preparation process [235]. The preparation of inorganic aerogels from polymeric precursors is not as simple as oxide aerogels from the sol-gel approach, yet it was reported recently for the synthesis of polysiloxane and polycarbosilane aerogels *via* hydrosilylation of preceramic polymers [236].

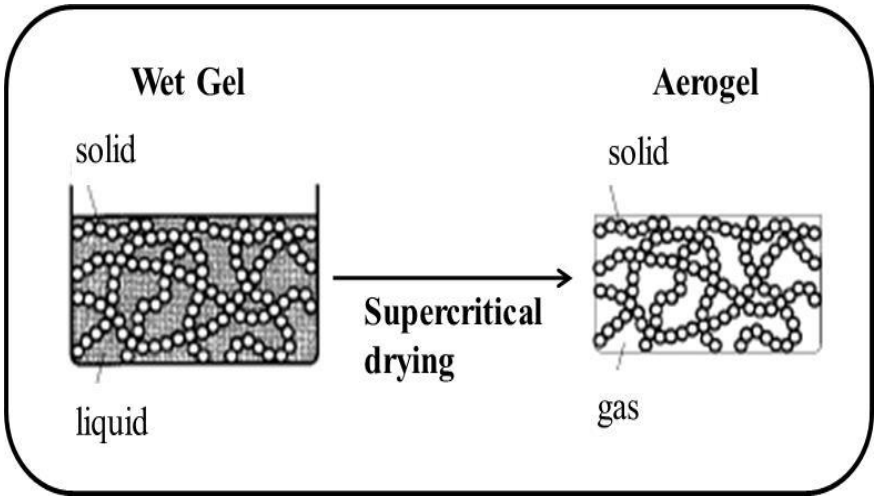

Figure I-28: Illustration of an aerogel formation.

In this section, we have introduced the different strategies we used to prepare **porous PDCs**. In the following sections, we will report a state of the art of porous (carbo)nitrides. To our knowledge there are no papers focused on Polymer-Derived porous AlN and SiAlCN. The main reports concern the BN and SiBCN materials. They mainly concern our group.

5.2.1 Porous BN

Boron nitride has been widely reported as porous material using the PDCs route. Highly **microporous BN** was firstly suggested in 1991, by vaccum pyrolysis of poly(4,6-borazinylamine), for gas adsorption [237]. In 1997, hydrazine borane was found to be able to decompose into porous boron nitride with high porosity (up to 99%) [238]. Our group was the first to report the preparation of **ordered mesoporous BN powde**rs in 2005 through the hard template process [239]. It was followed by numerous reports on **micro/mesoporous** [240, 241], **hierarchically porous foams** [176] using the hard template process. However, all these reports were concerned by the elaboration of the material and not the applications. Indeed, BN as porous material has attracted increasing interest due to plenty of its unique properties such as large specific surface area, tunable pore size, high thermal stability and chemical inertness which are useful in several fields, mainly in gas separation, catalysis and hydrogen storage. As an illustration, the development of the porosity in BN allowed to use it as a support to deposit platinum [242, 243], palladium [244], vanadium and molybdenum [245] etc. However, as far as it concerns this research work, the interest is more into **porous BN** for **hydrogen uptake**. Some perspectives for the (de-)hydriding properties of **porous BN** were investigated, and it was demonstrated that multiwall BN nanotubes can uptake up to 2.6 wt% of hydrogen under 10 MPa at room temperature [246]. Also nanoscale h-BN prepared by ball milling was tested for H_2 release from ammoniaborane and many beneficial effect of the combination

AB:nano-h-BN with regards to the dehydrogenation temperature, the exothermicity of hydrogen release [247]. Recently, a novel porous BN material in form of microbelts was reported to exhibit high and reversible H_2 uptake from 1.6 to 2.3 wt% at 77 K and a relatively low pressure of 1 MPa [248]. An extremely highly porous BN whiskers were prepared and were found to be useful not only in hydrogen storage but also in wastewater treatment applications [249]. In our group, we used another strategy; we focused on the nanoconfinement of ammoniaborane in the porosity of BN materials. Our first report concerned the **nanoconfinement of ammoniaborane in mesoporous/macroporous BN nanoparticles**, the nanocomposites liberated pure H_2 at 40°C [250]. This is the study we employed in this work through the development of new porous BN as host materials.

5.2.2 Porous SiBCN

Porous SiBCN was mainly reported by our group based on the expertise we gained on **porous BN** from **preceramic polymers**. As an illustration, **ordered mesoporous SiBCN** were prepared by **impregnation of CMK-3** with boron-modified polysilazanes of the type ($B[C_2H_5SiCH_3NCH_3]_3$). After pyrolysis under nitrogen at 1000°C and the template removal under ammonia, the material displayed high specific surface area (600 $m^2.g^{-1}$) and showed a good thermal stability in air [251]. More recently we reported the effect of the nature of the polymer on the properties of the **ordered mesoporous SiBCN** materials [252]. Furthermore, by applying Spark Plasma Sintering (SPS) on these ordered mesoporous SiBCN powders, we generated **hierarchically porous SiBCN** (Figure I-29) [252].

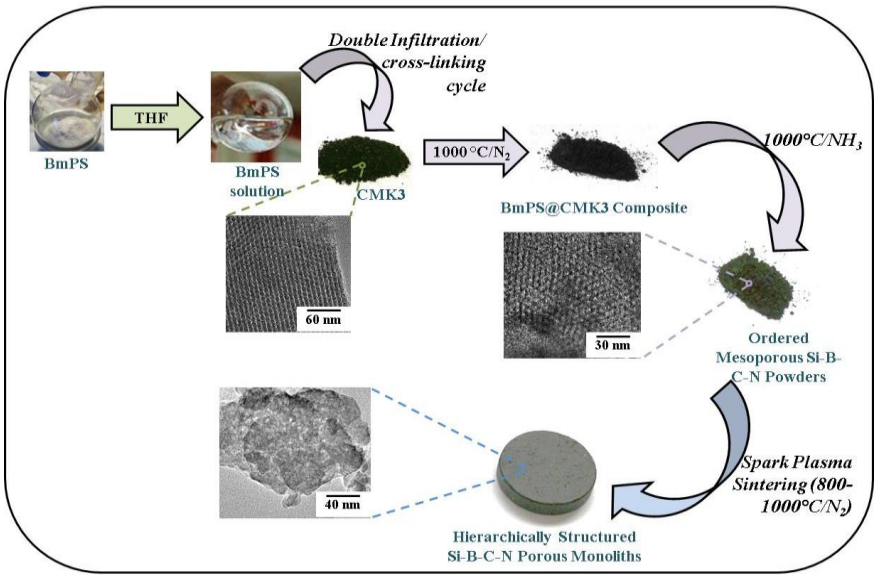

Figure I-29: Elaboration process of hierarchically structured SiBCN monoliths [252].

The main disadvantage of the investigated polymers is their volume shrinkage which occurs during pyrolysis. Within this context, we propose a study in the chapter V focused on the synthesis of a new generation of SiBCN precursors with the objective to elaborate cellular foams.

6. CONCLUSION

Because **hydrogen** is rapidly becoming one of the leading candidates to replace the fossil fuels energy, extensive efforts are underway to design, compute and synthesize materials for efficient generation, storage and purification. Previous works on **hydrogen generation/storage**, even if they dealt with the hydrogen sources considered here, namely **$NaBH_4$**, **$NaAlH_4$** and **NH_3BH_3,** have not been focused on the recycling and re-hydrogenation of the hydrogen sources when supported or confined, therefore the goal of the present work is to investigate the suitability of **porous polymer-derived (carbo)nitrides** for their application as **host** and **catalytic support** for the **hydrogen storage/generation.** In fact, due their physical, chemical and functional properties as well as their ability of being shaped using a wide variety of processing methods, **PDCs** have found application in several key fields: energy, technology, environment etc.

In the present chapter we have described all the materials that will be concerned by the PhD thesis, going from **hydrides** to generate hydrogen to the **polymer-derived (carbo)nitrides** which are used as host materials or supports. The aim of the study was to investigate different compositions of polymer-derived (carbo)nitrides, to process these materials while tailoring their porosity, and to explore their unusual properties in the hydrogen generation/storage ability.

As sketched in Figure I-30, the scope of the work will consist in delivering polymer-derived (carbo)nitrides with tailored porosity:

i) **Porous AlN** as host for the nanoconfinement of **$NaAlH_4$**.
ii) **Porous BN** as host for the nanoconfinement effect by thermolysis of **NH_3BH_3**.
iii) **Ordered-mesoporous Si_3N_4** and **SiAlCN** as catalyst support for the hydrogen generation from **$NaBH_4$**.

A last part will be focused on the synthesis of Si(Al/B)CN precursors which display appropriate properties to generate microcellular foams. Applications will be discussed as a main target for a close future.

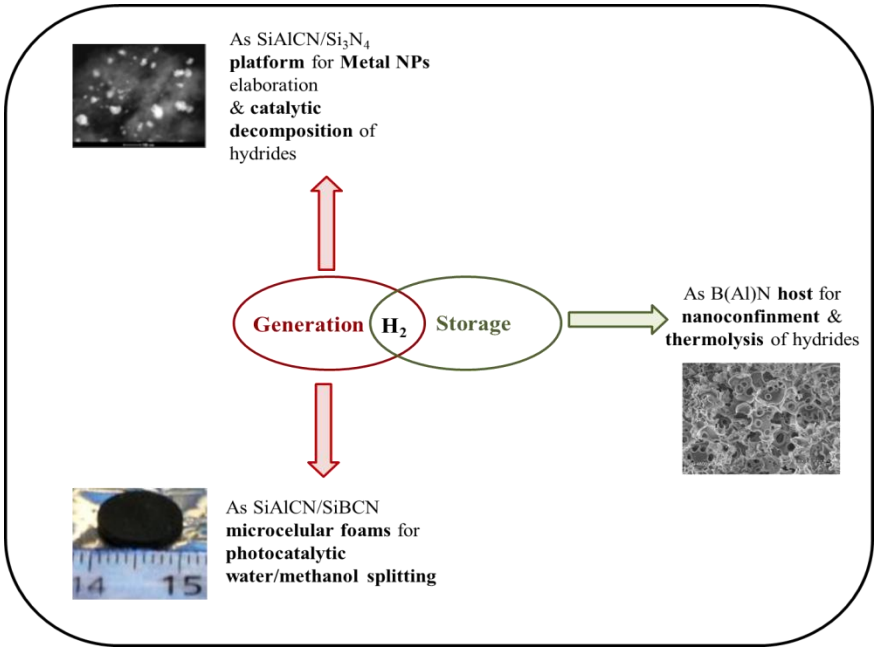

Figure I-30: Applications of different porous nitrides.

II-

POROUS AlN AS HOST MATERIAL FOR THE NANOCONFINEMENT OF $NaAlH_4$

II- Porous AlN as host material for the nanoconfinement of $NaAlH_4$ 64
1. Introduction 68
2. PEIA-derived AlN 68
2.1. Introduction 68
2.2. Experimental part 69
2.2.1 Materials 69
2.2.2 Preparation of PEIA-derived AlN 69
2.2.3 Experiments 71
2.3. Results and discussions 71
2.3.1 PEIA synthesis and characterization 71
2.3.2 PEIA-to-AlN conversion 74
3. Porous AlN from CMK-3 81
3.1. Experimental part 81
3.1.1 Materials 81
3.1.2 Elaboration of meso-/macroporous AlN 82
3.1.3 Experiments 83
3.2. Results and discussion 84
4. AlN AEROGELS 89
4.1. Experimental part 89
4.1.1 Materials 89
4.1.2 Elaboration of PEIA-derived AlN aerogels 89
4.1.3 Experiments 91
4.2. Results and discussion 92
5. Nanoconfinement of $NaAlH_4$ 96
5.1. Introduction 96
5.2. Experimental part 98
5.2.1 Materials 98
5.2.2 Nanoconfinement protocol 99
5.2.3 Experiments 99
5.3. Results and discussion 99
5.3.1 Preparation of $NaAlH_4$@host material 99
5.3.2 Characterization of $NaAlH_4$@porous AlN 100
6. Conclusion 102

1. INTRODUCTION

Nitride ceramics are of widespread technological importance in many application fields as we already mentioned in the literature review. Generally their performance addresses corrosion resistance, high temperature stability, oxidation resistance, surface hardening and optical modifications. Their use for **energy applications** (hydrogen production and storage) is poorly developed. Among nitrides, aluminum nitride (AlN) is a very interesting compound as discussed in the Chapter I of the present thesis. As a porous material, AlN is only reported in a patent [253] to be used for the separator component in a secondary battery. However, it is produced by powder technology which does not allow tailoring the porosity. This chapter deals with the **preparation, characterization and energy application of porous aluminium nitride (AlN).**

In detail, our objective is to investigate the preparation of **porous AlN** by combining the **PDCs** routes with two processes: i) the **nanocasting** approach and ii) the **aerogel** technology. Then, characterization of the polymer, bulk as well as the porous ceramic has been done.

In Chapter I, we demonstrated that **nanoconfinement** is an effective mean to alter the physico-chemical properties of potential hydrides. This has been reported by Gutowska *et al* on the nanoconfinement of AB in mesoporous silica [34]. Here, we used the **porous AlN** as host materials for confining **sodium alanate $NaAlH_4$**. The choice of AlN is justified by the fact that it should be free of OH groups on its surface which are known to interact with the hydride leading to the instability of the composite as we have demonstrated using activated carbon [55].

The present chapter is divided into four scientific parts. The **first part** is focused on the **synthesis** and **characterization** of the **AlN precursors**, *i.e.,* **PolyEthylIminoAlane (PEIA)**, the **PEIA-to-AlN conversion** and the **characterization of AlN.** The **second part** is devoted to the **preparation of meso-/macroporous AlN** using CMK-3 as template (**nanocasting**). Characterization is detailed. The **third part** is dedicated to the **preparation of AlN aerogels** through the **CO_2 supercritical drying** from PEIA. The fourth part reports the investigation of **nanoconfinement of $NaAlH_4$** and the assessment of the potential for **chemical hydrogen storage**.

2. PEIA-DERIVED AlN

2.1. Introduction

Poly(N-alkylimino)alanes are AlN precursors if pyrolyzed at high temperatures (T ≥1000°C) under ammonia and nitrogen atmospheres [134]. Precursors should be fusible at relatively low

temperatures or soluble in common organic solvents to prepare porous AlN by the nanocasting process we introduced in Chapter I. Moreover, the preparation of precursors with high ceramic yields is another prerequisite to keep the maximum of matter in the template and avoid the structure collapsing after the template removal step. As already mentioned, it is challenging to synthesize a polymer which displays a relatively high ceramic yield and in the same time solubility (or fusibility) for nanocasting, especially in the AlN system. Therefore, a compromise had to be done. Within this context, our objective was to synthesize a **Poly(N-EthylImino)Alane** labelled as **PEIA** [134] **as AlN precursor,** which structure was illustrated in Chapter I (see Figure I-13).

2.2. Experimental part

2.2.1 Materials

The molecular and polymeric precursors are unstable in air. Therefore, all manipulations were carried out under inert conditions. All ceramic products were handled in an argon-filled glove box (MBraun M200B where the O_2 and H_2O concentrations were kept <0.1 ppm) due to their high relative surface area and affinity to moisture. Argon (>99.995%) was purified by passing through successive columns of phosphorus pentoxide, siccapent^{TM}, and BTS catalysts. Schlenks were dried at 120°C overnight before pumping under vacuum and filling them with argon for synthesis. Manipulation of the chemical products was made inside the glove box. Ethylamine hydrochloride (98%) and lithium aluminum hydride (powder reagent grade 95%) were purchased from Sigma-Aldrich. Diethylether (99.5%) extra-dry over molecular sieves and stabilized AcroSeal® was purchased from Acros Organics.

2.2.2 Preparation of PEIA-derived AlN

PEIA is obtained by reaction between ethylamine hydrochloride ($CH_3CH_2NH_3Cl$) and lithium aluminum hydride ($LiAlH_4$) at low temperature (0°C) according to equation II-1:

$$n\text{LiAlH}_4 + n\text{EtNH}_2\text{.HCl} \rightarrow (\text{HAlNEt})_n + n\text{LiCl} + 3n\text{H}_2 \qquad \text{(II-1)}$$

Typically, 6.80 g (177.2 mmol) of $LiAlH_4$ were dispersed in 100 ml of diethylether, and then added dropwise to a solution of 14.45 g (177.2 mmol) of $EtNH_2$.HCl in 200 mL of Et_2O at 0°C under vigorous stirring. Lithium chloride precipitated immediately and hydrogen was evacuated. After the complete addition of ethylammonium chloride, the mixture was maintained under stirring for 30 minutes at 0°C, and then, allowed to warm up to room temperature (RT) overnight until the gas evolution ceased. After filtration to remove LiCl, the solvent was extracted in a high vacuum

($RT/10^{-2}$ mbar) to leave a white solid. Figure II-1 illustrates the experimental protocol adopted for the synthesis of PEIA.

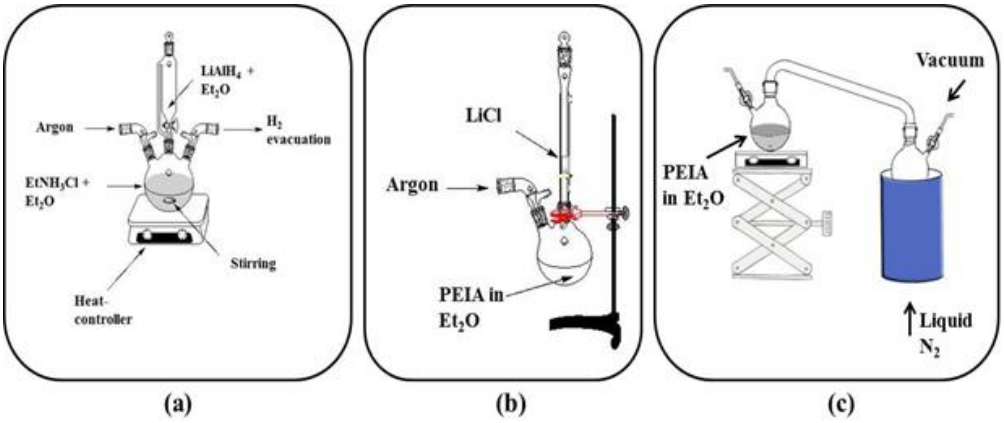

Figure II-1: Experimental protocol for the PEIA synthesis: (a) chemical reaction, (b) filtration, and (c) vacuum drying.

The PEIA polymer was characterized at room temperature by means of FTIR spectroscopy (Nicolet Magna-IR 550 Fourier transform-spectrophotometer 5Nicolet Instrument Co. USA): $\nu_{(N-H)}$=3450 cm^{-1} (m), $\nu_{(C-H)}$=2954 cm^{-1}(s), 2898 cm^{-1}(s), 2803 cm^{-1}(m), $\nu_{(Al-H)}$= 1850 cm^{-1}(m), $\delta_{sym(CH_3)}$=1378 cm^{-1}(w), $\delta_{asym(CH_2)}$=1460 cm^{-1}(w), $\delta_{asym(CH_3)}$=1463 cm^{-1}(w), $\nu_{(C-N)}$=1095 cm^{-1}(w), $\nu_{(Al-N)}$= 694 cm^{-1}(m). ^{1}H and ^{13}C liquid-state NMR spectroscopy (Bruker AM 300) were also performed operating at 300 MHz and 62.5 MHz, respectively: ^{1}H (500 MHz, C_6D_6): δ=1.1-1.6 ppm (C**H**$_3$), δ=3.1-3.6 ppm (C**H**$_2$), δ=4.6 ppm (Al-**H**); ^{13}C (75 MHz, C_6D_6): δ=19.7–21.5 ppm (**C**H_3), δ=41.3–42.4 ppm (**C**H_2); ^{27}Al (130.20 MHz, C_6D_6): δ=136 ppm (H**Al**N_3). An empirical formula of $[Al_{1.0}N_{0.9}C_{2.1}H_{6.8}]_n$ was found by the Chemical analyses made at the "Service Central de Microanalyse du CNRS, Lyon, France".

PEIA, placed in an alumina crucible, was transferred into a silica tube inserted in a horizontal furnace (Nabertherm type RS 80/500/11, Germany) which was connected to the glove-box to prevent oxygen contamination of the sample. The tube was pumped under vacuum and refilled with ammonia. After that, the samples were subjected to a cycle of ramping of 5°C.min^{-1} to 1000°C, dwelling therefore 2 h, and then cooling down to RT at 5°C.min^{-1}. A constant flow (120 mL.min^{-1}) of ammonia was passed through the tube during pyrolysis. The ammonia-treated samples were then introduced in a graphitic furnace (Gero Model HTK8) in graphite crucibles. The furnace was subsequently pumped and refilled with nitrogen to undergo a heating program through a cycle of ramping of 5°C.min^{-1} to 1200, 1400, 1600 and 1800°C, dwelling there for 2 h, and then cooling down to RT at 10°C.min^{-1}. A constant flow (200 mL.min^{-1}) of nitrogen was passed through the furnace.

2.2.3 Experiments

^{27}Al, ^{15}N and ^{13}C solid-state NMR spectroscopy was investigated at the "Laboratoire de Chimie de la Matière Condensée de Paris, Collège de France". ^{27}Al MAS and ^{13}C CP MAS NMR spectra were recorded at 11.7 T on a Bruker Avance500 wide-bore spectrometer operating at 130.3 and 125.7 MHz respectively, using a Bruker 4 mm probe and a spinning frequency of the rotor of 14 kHz. For the PEIA RT sample, an additional spectrum was recorded at 16.3 T on a Bruker Avance700 standard-bore spectrometer operating at 182.4 MHz, using a Bruker 3.2 mm probe and a spinning frequency of the rotor of 22 kHz. ^{15}N CP MAS spectra were recorded at 7 T using a Bruker 7 mm probe and a spinning frequency of the rotor of 5 kHz.

FTIR spectroscopy was performed on a Nicolet Magna-IR 550 (Fourier transform-spectrophotometer 5Nicolet Instrument Co. USA) using KBr pellets (2 wt% of polymer mixed with KBr powder followed by a compaction into a dense pellet). Preparation of samples for analyses has been done in a glove box filled with argon. This spectrophotometer is coupled with the ATTenuated Total Reflectance (ATR) accessory.

Thermogravimetric analyses (TGA) of the polymer-to-ceramic conversion were recorded on a Setaram system (model TGA 92 16.1892). The experiments were performed using silica crucibles (sample weight ~40 mg) at atmospheric pressure in ammonia or nitrogen atmosphere from RT to 1000°C, with a heating rate of $5°C.min^{-1}$. The samples are always purged with a vacuum cycle, then the chamber is filled with the suitable gas (ammonia or nitrogen) and the measurements start.

X-ray diffraction (Philips PW 3040/60 X'pert PRO X-ray diffraction system operating at 30 mA and 40 kV from 10 to 90° with a step size of 0.0167, using a Kα1 of copper as source) and Raman spectroscopy (Renishaw model RM 1000 Raman microscope operating at λ~ 514.5 nm) were performed on the AlN powders in order to study their microstructure evolution upon thermal treatment between 1000 and 1800°C.

2.3. Results and discussions

2.3.1 PEIA synthesis and characterization

PEIA is obtained as a white powder with a relatively high synthesis yield. It is soluble in common solvent. As mentioned in the introduction, it is expected to be represented by a cage-type structure (Figure I-13) [125]. PEIA is soluble in C_6D_6 but both ^{1}H and ^{13}C liquid-state NMR spectra are very complex and display broad signals as shown in Figure II-2.

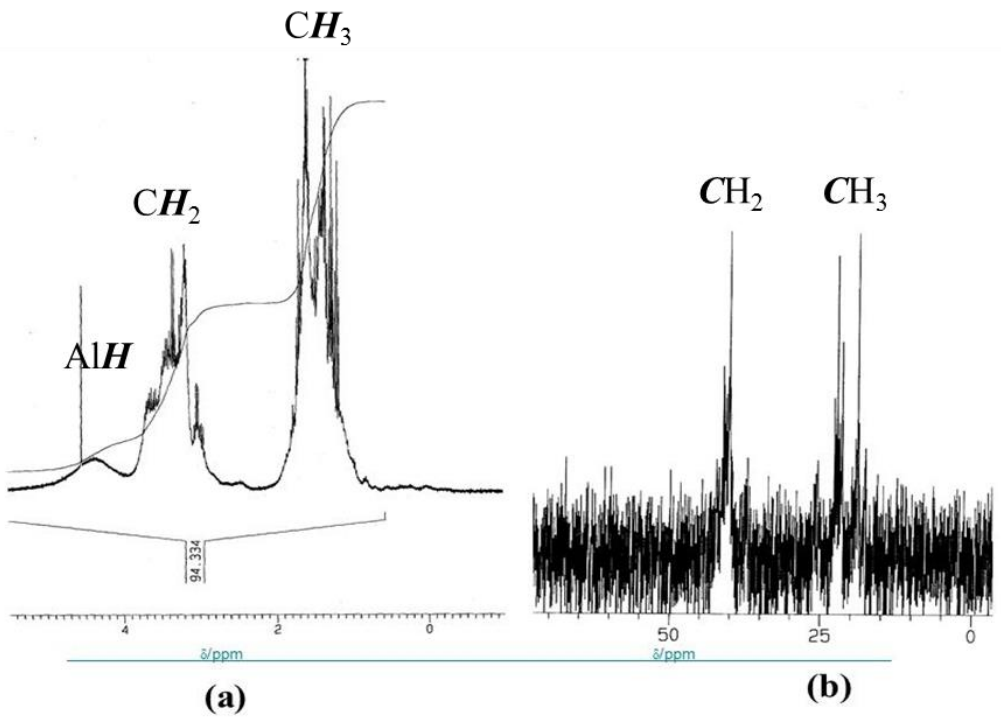

Figure II-2: Liquid-state NMR spectra of **PEIA** (a) ^{1}H and (b) ^{13}C.

In the ^{1}H spectrum (Figure II-2-a), PEIA shows a broad signal at 1.6 ppm most probably due to C***H₃*** groups. Signal at 3.5 ppm is attributed to C***H₂*** groups, whereas the signal at 4.3 ppm can be assigned to Al***H*** groups. The presence of some of these groups is confirmed by ^{13}C NMR (Figure II-2-b). The spectrum shows a broad signal around 24.6 ppm that is attributed to ***C***H_3 groups, whereas the signal at 41.2 ppm is assigned to ***C***H_2 groups in the CH_3CH_2N unit. Because of the poor resolution of the ^{13}C NMR spectrum of the diluted PEIA solution, we investigated ^{13}C solid-state NMR. The corresponding spectrum is shown in Figure II-3. We confirmed the resonances of the ethyl group at ~21 ppm (CH_3***C***H_2-N) and 45 ppm (CH_3***C***H_2-N). However, the ^{13}C spectrum suggests the presence of two CH_3 sites.

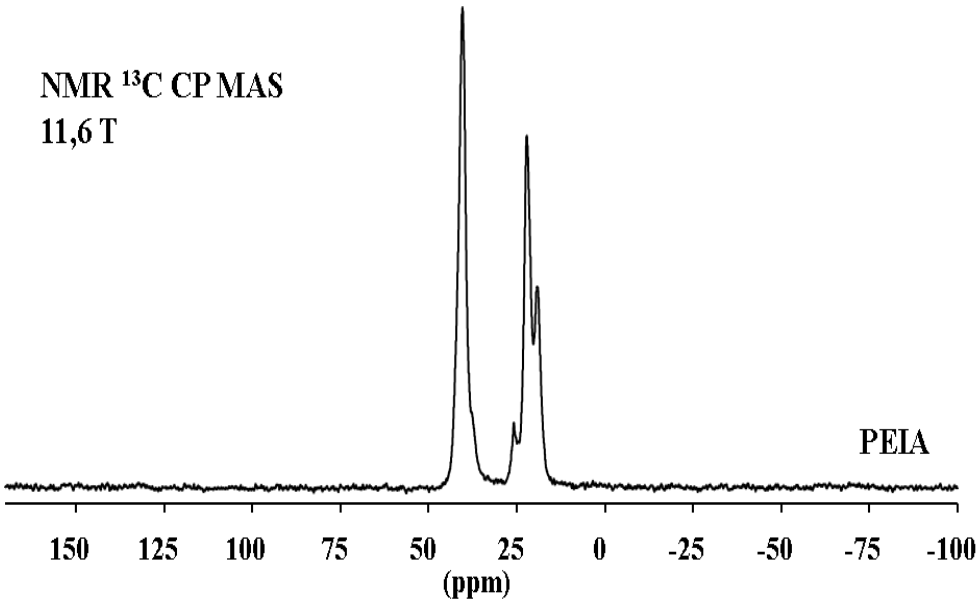

Figure II-3: ^{13}C CP MAS NMR spectrum of **PEIA.**

In addition to the NMR investigations, some absorption bands in the FTIR spectrum are useful indications for determining the structure of studied PEIA. The IR spectrum of PEIA (Figure II-4), shows the characteristic stretching and deformation bands of all expected motifs.

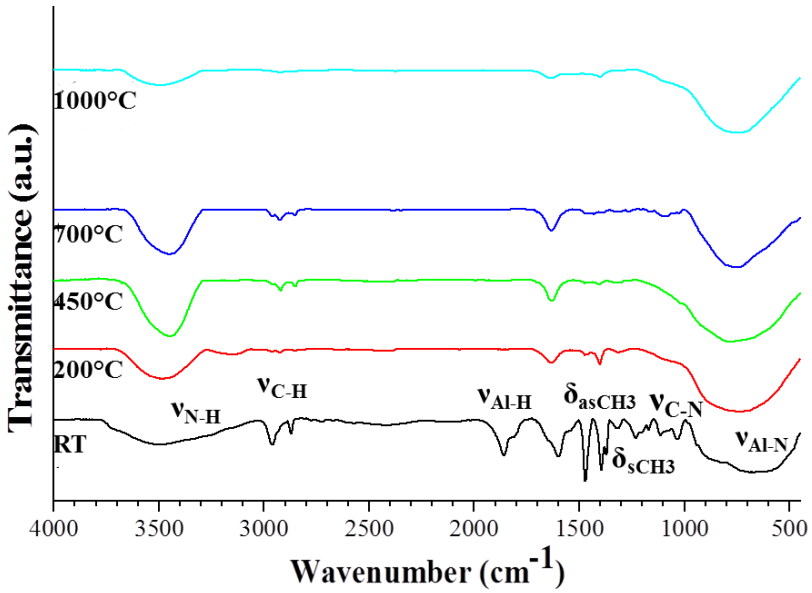

Figure II-4: FTIR spectra of **PEIA** at RT and of the **NH_3-treated intermediates** at 200, 450, 700 and 1000°C.

The broad signal at 3450 cm^{-1} shows the presence of NH units as ending groups. Strong and very broad adsorption C-H bands are also observed in the 2803-2954 cm^{-1} range. The Al-H

stretching band is observed at 1860-1820 cm^{-1}. The series of bands in the wavenumber range 1378-1463 cm^{-1} is assigned to the deformation of CH_3 groups. The band attributed to CH_2 groups in the NCH_2CH_3 units is present in the wavenumber range 1470-1450 cm^{-1}. Vibrations of C-N bonds are located at 1095 cm^{-1}. The vibration band corresponding to Al-N appears at 694 cm^{-1}. The assigned major observations in the infrared spectrum are compiled in the experimental section of this part.

According to elemental analyses, PEIA has the following empirical formula $Al_{1.0}N_{0.9}C_{2.1}H_{6.8}$ per monomer unit (oxygen values were found to be below 2 wt% and were therefore omitted). The elemental analysis data of PEIA definitively prove that the synthesis of the precursor occurs in the expected pathway since they reasonably agree with the theoretical values. Based on the structure illustrated in Figure I-13, the empirical formula was calculated to be $Al_{1.0}N_{1.0}C_{2.0}H_{6.0}$. In particular the Al:N ratio of 1:0.9 is obtained in PEIA (as expected it is close to 1). Moreover, the nitrogen, carbon and hydrogen experimental values are very close to the calculated ones.

Based on NMR, FTIR, elemental analyses and former studies, we have a relatively good representation of the structural arrangement of PEIA. However, solid-state NMR is more useful in the identification of the local environment around carbon, aluminum and nitrogen in the polymer and also in the determination of the changes in the local environment during the polymer-to-ceramic conversion. As a consequence, we investigated the structure of PEIA by solid-state NMR. This study was also performed on the derived pyrolysis intermediates obtained during pyrolysis under ammonia in the temperature range 200-1000°C. Solid-state NMR is presented in the following section. It has been coupled with TGA and FTIR measurements in this temperature range. Further annealing under nitrogen was performed in the temperature range 1000-1800°C, XRD and Raman spectroscopy was investigated.

2.3.2 PEIA-to-AlN conversion

In this part, we have distinguished two temperature ranges: **RT → 1000°C** and **1000 → 1800°C**. The purpose of this section is to investigate the first temperature region of the polymer-to-ceramic conversion (up to 1000°C under ammonia) by TGA, solid-state NMR and FTIR in order to identify the related structural changes which occur during pyrolysis. Then, we investigated the second temperature region (1000-1800°C under nitrogen) of the polymer-to-ceramic conversion by XRD and Raman spectroscopy to follow the evolution of the structure of AlN.

- *Temperature range: RT → 1000°C*

We used ammonia atmosphere in this temperature range to remove all of the carbon groups in PEIA and generate carbon-free AlN at the end of the pyrolysis process. The carbon removal takes place according to the equation II-2 [254]:

$$3C + 4NH_3 \rightarrow 3CH_4 + 2N_2 \qquad \text{(II-2)}$$

A single-step weight loss of 42.5% was recorded during heat-treatment of PEIA up to 1000°C under ammonia with a heating rate of 5°C.min^{-1}. A white residue was obtained (Figure II-5-a). It should be mentioned that a weight loss of 27.5% was measured during the heat-treatment of PEIA under nitrogen. The TGA residue was black (Figure II-5-b). This confirmed the interest of using ammonia to remove the carbon leading to a higher weight loss; thus a lower ceramic yield was obtained when compared with a nitrogen atmosphere.

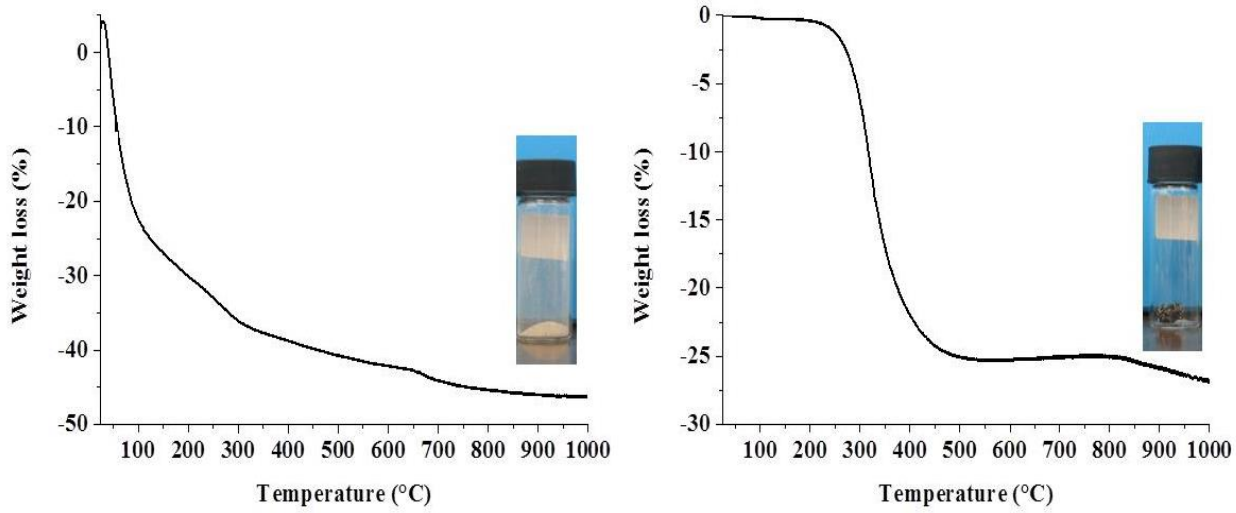

(a) (b)

Figure II-5: TGA curves of PEIA up to 1000°C with a heating rate of 5°C.min^{-1} (a) under NH_3 and (b) under N_2, with the corresponding TGA residues photos.

The infrared spectroscopy has enabled us to observe the evolution of the bonds present in the PEIA at various temperatures of the pyrolysis under ammonia. The FTIR spectrum of the polymer was discussed previously. The spectra of the pyrolysis intermediates isolated during the heat treatment under ammonia from RT up to 1000°C are shown in Figure II-4.

In comparison to the spectrum of PEIA, the spectrum of the sample isolated at 200°C is significantly changed. In particular, the intensity of the band around 3400 cm^{-1} has increased, whereas the bands characteristic of the vibrations of the C-H bonds and to the carbon moieties (1378,

1463 cm^{-1}) have decreased. This is clearly attributed to the presence of NH_2 groups [254]. In addition, the reaction with ammonia involves a sharp decrease of the band attributed to Al-H units (1850 cm^{-1}). The decrease in intensity of these bands is attributed to two reactions. Disappearance of carbon-based groups is clearly attributed to **transamination reactions** (**amine exchange reactions**) according to the schematized equation in Figure II-6.

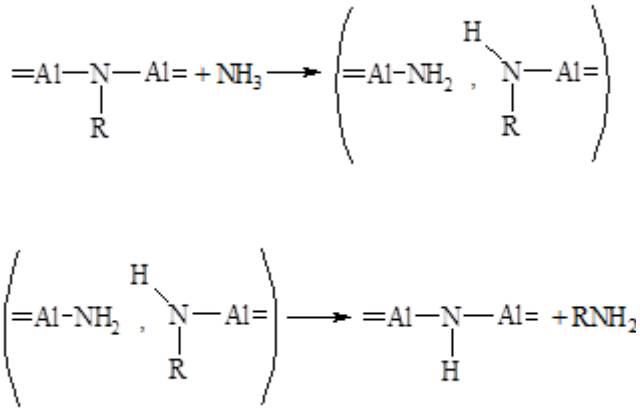

Figure II-6: Ammonolysis reactional mechanism.

The decrease of the bands characteristic of the C-H bonds is therefore attributed to the elimination of ethylamine. It is thus established that incorporation of ammonia into the polymer occurs below 200°C whereby reactive Al-NH_2 moieties form, instead of Al-NCH_2CH_3; the Al-NH_2 moieties then condense to form N-H units while leading to ethylamine. The appearance of a signal at 1680 cm^{-1} attributed to the deformation of NH_2 groups is consistent with the presence of NH_x (x=1, 2) groups. New bands around 1000-1100 cm^{-1} are also due to NH units [254].

The second reaction involves the **ammonolysis** of Al-H bands according to equation (II-3):

$$Al\text{-}H + NH_3 \rightarrow Al\text{-}NH_2 + H_2 \qquad (II\text{-}3)$$

Dehydrocoupling between Al-H and N-H bonds to form Al-N units liberating a molecule of H_2 may be also suggested.

The spectrum of the product isolated at 450°C is similar to the one at 200°C. This highly reflects the TGA data: the weight loss is significant at 200°C which means that reactions with ammonia have been already achieved at this temperature. The weight loss rate is decreased above 200°C which indicates that reactions occur more slowly. Above 450°C, the spectra tend progressively towards the spectrum of AlN with a band at 694 cm^{-1} corresponding to vibrational modes of Al-N bonds. The bands of the CH, CN and NH bonds decrease in intensity probably due to the release of amines. After pyrolysis to 1000°C, we can distinguish the poor intense bands

characteristic of N-H and C-H bonds which means that residual carbon and hydrogen are still present in the sample pyrolyzed at 1000°C which is majoritarly AlN.

We have investigated ^{15}N and ^{27}Al NMR of PEIA and ammonia-treated samples at different temperatures, in order to have complementary information on structural rearrangements that occur during the curing and pyrolysis.

In Figure II-7, we report the ^{27}Al MAS NMR spectra of PEIA and derived samples treated between 200 and 1000°C under ammonia.

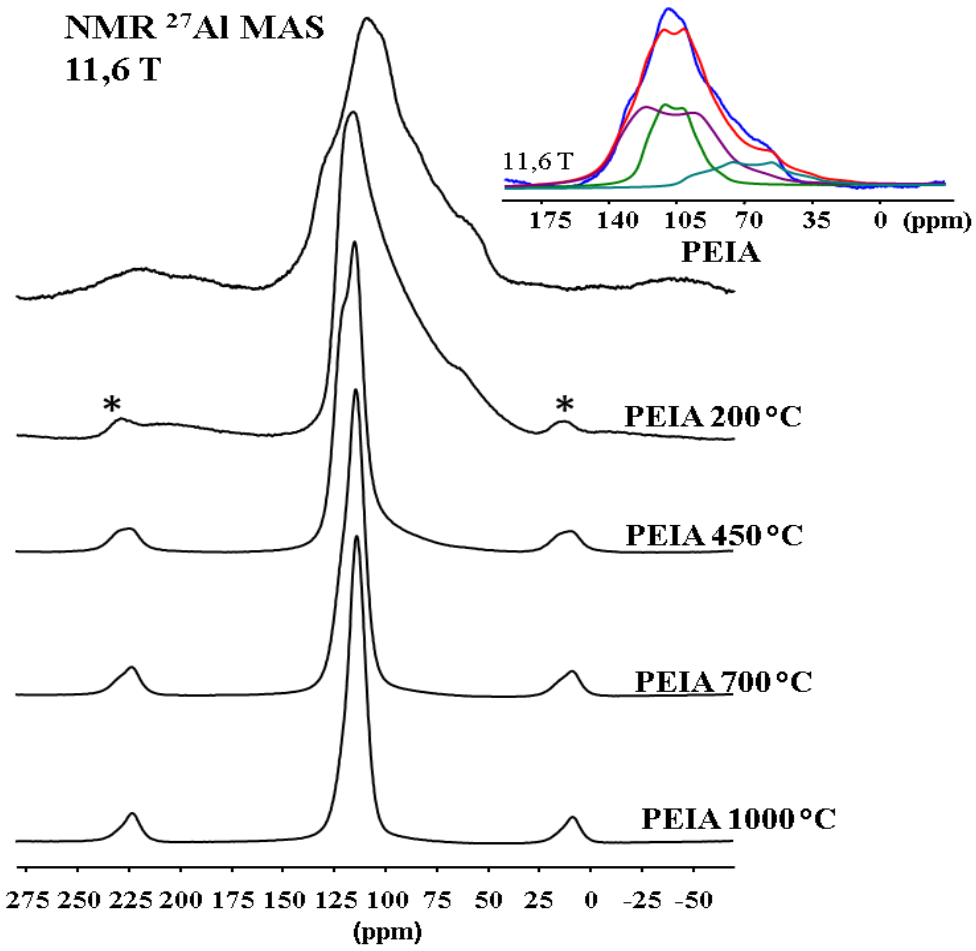

Figure II-7: ^{27}Al MAS NMR spectra of **PEIA** and **NH_3-treated intermediates**. Spinning side bands are marked with asterisks [125].

^{27}Al NMR spectrum of PEIA shows a complex signal at 110 ppm that was tentatively simulated with three coordinated Al-based sites based on the comparison of the data recorded at two magnetic fields (11.6 and 16.3 T). A first large signal is observed at 135 ppm (C_Q ~11 MHz), consistent with the presence of tetra-coordinated $HAlN_3$ [124, 125, 154]. Another signal centered

around 110 ppm is consistent with an environment which contains mainly tetra-coordinated Al-based units such as AlN_4 [255].

Heat-treatment to 200°C results in the sharpening of the major signal which slightly shifts to higher resonances. It is center at 115 ppm. This indicates that AlN_4 units are in a major proportion. The broad shoulders present around 135 ppm disappears confirming that Al-H bonds react with ammonia. After heat-treatment to 450°C, the major signal becomes sharper due to the disappearance of the signal around 70 ppm. The samples isolated at 700 and 1000°C show sharp signals at 112 ppm, which highly reflects the formation of AlN_4 environments as observed in AlN [256].

We completed the ^{27}Al NMR experiments with ^{15}N MAS NMR (Figure II-8).

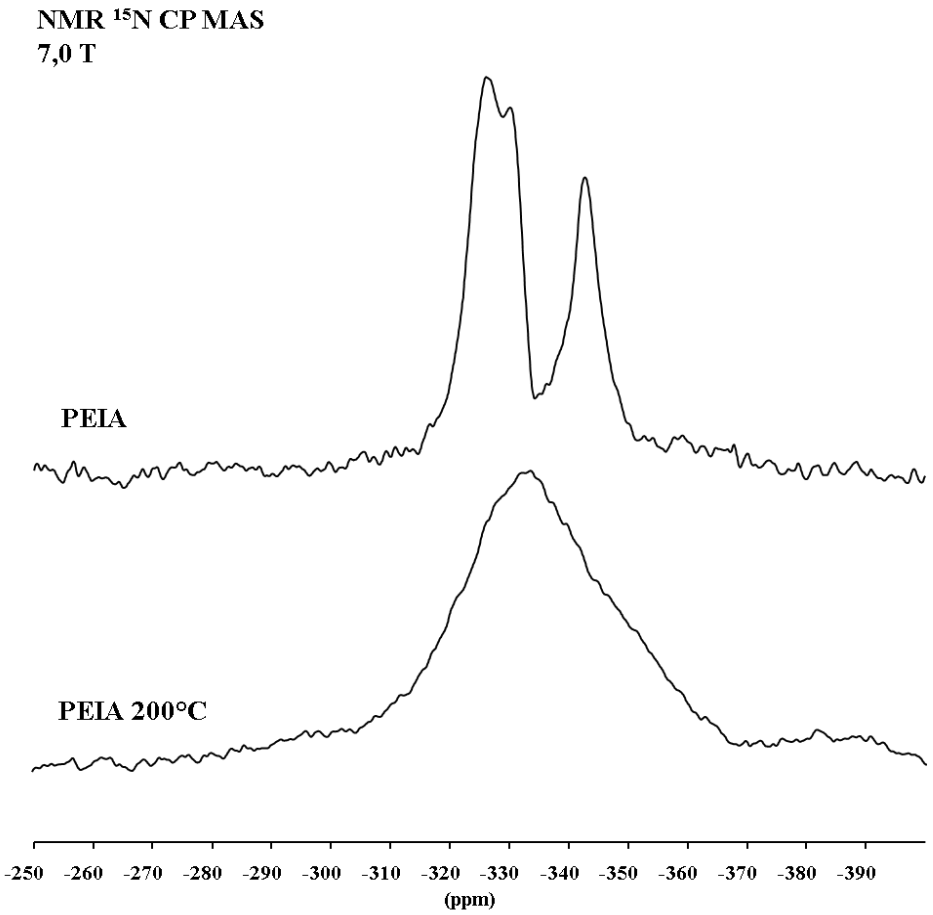

Figure II-8: ^{15}N CP MAS spectra of **PEIA** at RT and at **NH_3-treated intermediate** at 200°C.

According to the fact that the main changes occur below 200°C, we report the two characteristic ^{15}N MAS spectra of the PEIA and the sample heat-treated at 200°C. Cross Polarization CP techniques were used to obtain a reasonable signal to noise ratio. We can notice that the signals are concentrated in the region between -310 and -360 ppm. Two of them are observed around -330 and the third one at -345 ppm. They can be respectively assigned to peripheral $Al_2NCH_2CH_3$,

$Al_3NCH_2CH_3$ groups and $AlN(H)CH_2CH_3$. The latter (end-of-chain groups) clearly react with ammonia during the heat-treatment to 200°C since the corresponding signals decreased in intensity. This confirmed FTIR observations. As a consequence, the broad signal shifted to -335 ppm corresponds most probably to $NHAl_3$ and NAl_4 units [256].

Based on the TGA, FTIR spectroscopy and solid-state NMR analysis performed on PEIA and ammonia-treated samples between 200 and 1000°C, we were able to obtain information on the reaction mechanisms as well as structural changes which take place during of the polymer synthesis and the first temperature regime of the PEIA-to-AlN conversion. The occurrence of these reactions allows consolidating the AlN network. After the heat-treatment to 1000°C under ammonia, the structure of PDCs is in general amorphous. In fact, the first temperature regime is mainly associated with chemistry changes. The second temperature regime from 1000 to 1800°C occurs under nitrogen. It is associated with structural changes and ceramic crystallization. Therefore, we investigated XRD and Raman spectroscopy.

- *Temperature range: 1000 $\rightarrow$ 1800°C*

We followed the strategy we employed previously. We have isolated samples treated under nitrogen at different temperatures (1200, 1400, 1600 and 1800°C).

The X-ray diffraction patterns of the samples isolated at different temperatures from 1000 to 1800°C under nitrogen are reported in Figure II-9.

The XRD pattern of the sample obtained at 1000°C is consistent with that one corresponding to the 2H-wurtzite type AlN (according to the JCPDS file: N° 25-1133). Above a temperature of 1000°C, the diffraction patterns clearly show the improvement of the crystallinity of the material through the sharpening and increased intensity of the diffraction peaks corresponding to AlN.

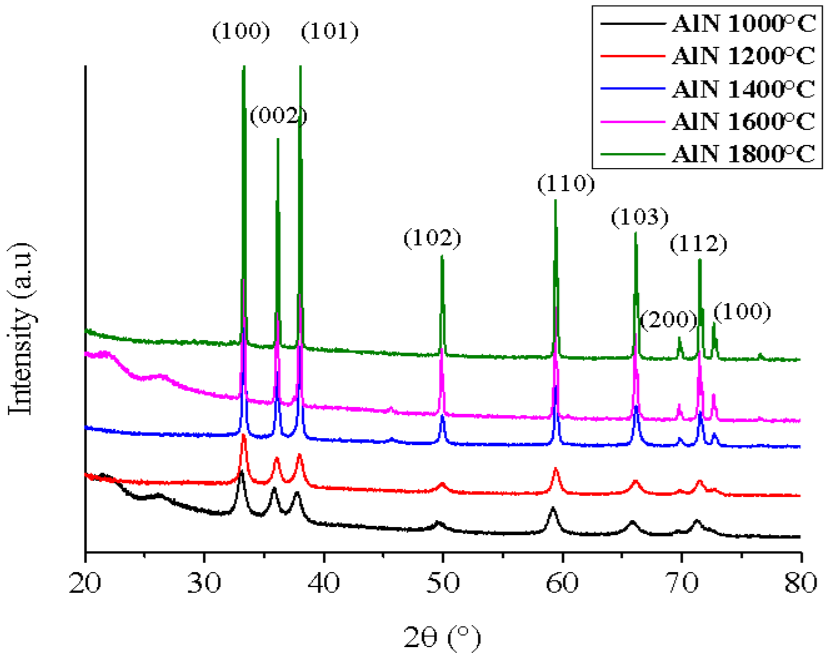

Figure II-9: XRD patterns of **PEIA-1000** between 1000 and 1800°C under N_2.

The samples were also analyzed with Raman spectroscopy, which is one of the most sensitive methods for the characterization of the crystalline phases as well as the presence of free carbon. The spectra are presented in Figure II-10. First of all, the Raman spectra of the samples do not exhibit the bands at 1337 and 1595 cm^{-1} consisting with the presence of amorphous carbon [257, 258]. This indicated the efficiency of the ammonia treatment and confirmed the occurrence of reactions involving elimination of carbon-based groups from the PEIA. The Raman spectrum of the sample heat-treated at 1000°C exhibits only one peak corresponding to the presence of the E_2 (high) phonon modes at 657 cm^{-1} characteristic of AlN. After heat-treatment to 1400°C, new small peaks appear around 611, 670 and 900 cm^{-1}; they are attributed respectively to A_1 (TO), E_1 (TO) and A_1 (LO) vibration modes of AlN [259]. The low E_2 mode in the range of 228-252 cm^{-1} is also identified in the sample treated at 1400°C. It disappears after heat-treatment to 1600 and 1800°C while other peaks remain.

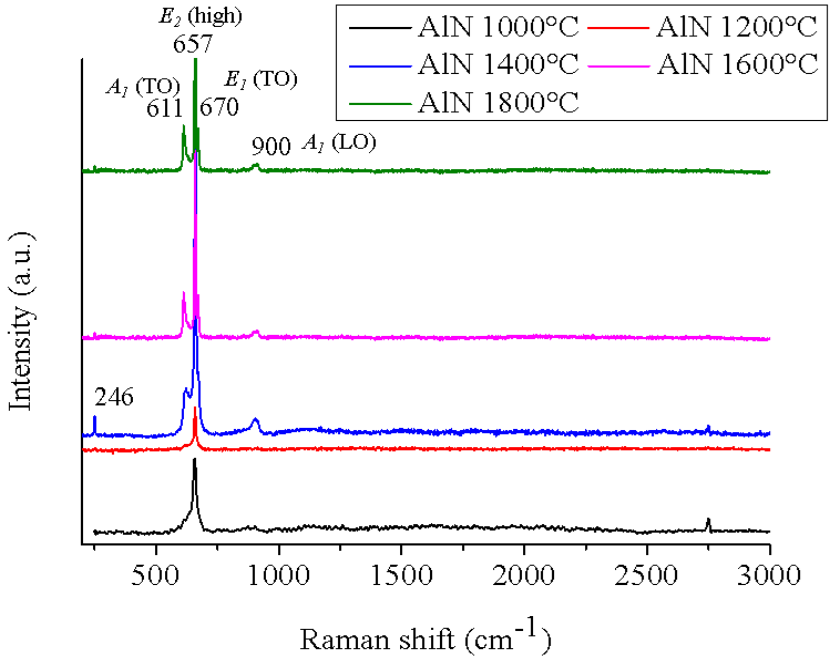

Figure II-10: Raman spectra of **PEIA-1000** between 1000 and 1800°C under N_2.

The objective of the first part of the chapter II was to discuss on the synthesis of PEIA and its pyrolysis behavior when heat-treated under ammonia (**RT → 1000°C**) and nitrogen (**1000 → 1800°C**) atmospheres. It was the purpose of this study to investigate the individual chemical processing steps, and then identify the related architectural and structural changes which occur during the PEIA-to-AlN conversion. The identification of the relevant chemical reactions was made based on the chemistry of PEIA using a combination of thermo-analytical experiments, solid-state NMR and FTIR spectroscopies. X-ray diffraction and Raman spectroscopy allowed us to gain information on the structural evolution of the AlN phase at high temperature. The second part of the present chapter is focused on the use of PEIA to replicate the ordered mesoporosity of CMK-3 after pyrolysis.

3. POROUS AlN FROM CMK-3

3.1. Experimental part

3.1.1 Materials

The PEIA has been described in the previous section; its manipulation was carried out under inert conditions since it is unstable in air. The ordered mesoporous carbon used as template to infiltrate with PEIA is a commercial CMK-3 which was purchased from ACS Materials®. The textural parameters of CMK-3 are reported in Table II-1.

Table II-1: Textural properties of CMK-3.

Type	Specific Surface Area ($m^2.g^{-1}$)	Pore Diameter (nm)	Total Pore Volume ($cm^3.g^{-1}$)	Micropore Volume ($cm^3.g^{-1}$)	Size (µm)
BET1000	**983**	**5.57**	**1.35**	**0.01**	**0.5-5**

CMK-3 was degassed overnight at 150°C under dynamic vacuum prior to infiltration. The solvent used for dissolving PEIA before impregnating the CMK-3 is toluene (99.85%, extra-dry over molecular sieve, AcroSeal®) obtained from Acros Organics. Argon (>99.995%) was purified by passing through successive columns of phosphorus pentoxide, siccapent, and BTS catalysts. Schlenk glassware was dried at 120°C overnight before pumping under vacuum and filling them with argon for synthesis. Manipulation of the chemical products was made inside an argon-filled glove box (MBraun MB200B) where the O_2 and H_2O concentrations were kept <0.1ppm.

3.1.2 Elaboration of meso-/macroporous AlN

All ceramic products were handled in the glove box, because of their high surface area and affinity for moisture adsorption before characterization.

Nanocasting of PEIA was carried out through an impregnation process in a Schlenk-type flask. 0.28 g of the PEIA were dissolved in 3 mL of toluene and then added to 0.2 g of the CMK-3 template previously dehydrated at 150°C overnight at reduced pressure. The mixture was then stirred at room temperature for 48 h under static vacuum. After absorption of the polymer into the pores of the template, a filtration step was performed to selectively remove the PEIA molecules deposited outside while the capillary forces kept the PEIA molecules effectively inside the pores and then the solvent was slowly evaporated at low pressure at 30°C to generate a black powder labeled **PEIA@CMK-3**.

The composite **PEIA@CMK-3** was introduced into a glove box under nitrogen, put in an alumina crucible, and then transferred into a silica tube inserted in a horizontal tube furnace (Gero Model type F-A 150-500/13) and connected to the glove box. The tube was pumped under a vacuum for 2 h and refilled with nitrogen (99.995%). The sample was subjected to a cycle of ramping of $1°C.min^{-1}$ to 1000°C dwelling there for 2 h, and then cooling to RT at $2°C.min^{-1}$. A constant flow (120 $mL.min^{-1}$) of nitrogen was passed through the tube. After this polymer-to-ceramic conversion process, the composite underwent a final thermal treatment in an ammonia flow (120 $mL.min^{-1}$) from RT to 1000°C and kept at this temperature for 5 h to remove the carbon CMK-3 template and

generate the AlN mesoporous material. A supplementary treatment under N_2 at 1400°C for 2 h, with a heating rate of 5°C.min^{-1} was done in a graphitic furnace (Gero Model HTK8) to further stabilize and crystallize the AlN mesoporous ceramic. A constant flow (200 mL.min^{-1}) of nitrogen was passed through the furnace. Another alternative of pyrolyzing consists in directly removing the template while ceramization. The textural properties of AlN elaborated by these two pyrolysis alternatives will be shown below. The sample prepared by **one-step direct pyrolysis under ammonia** is labeled **AlN 1000-1**, and the one obtained from **two-step pyrolysis** (treatment under N_2 followed by a curing under NH_3) is called **AlN 1000-2**. The temperature that follows the label of the sample corresponds to the final temperature at which we recovered the AlN.

3.1.3 Experiments

The porous AlN materials were characterized by different analyses techniques in order to study their textural parameters, and their eventual evolution with temperature:

BET: N_2 adsorption-desorption isotherms were carried on a Model Sorptomatic 1900 analyser (Fisons). Before adsorption measurements, all samples were outgassed for 4 h at 150°C in the degas port of the adsorption analyzer. The Brunauer.Emmett.Teller (BET) method was used to calculate the specific surface area. The pore-size distribution was derived from the adsorption branches of the isotherms using the Barrett.Joyner.Halenda (BJH) method. The total pore volume (Vp) was estimated from the amount of N_2 adsorbed at a relative pressure of $P/P_0 = 0.99$.

Scanning electron microscopy: SEM pictures were taken with a Hitachi S800 microscope coupled with EDX microanalysis system with IDFix and MaxViwe softwares from SamX. Maximum resolution of 2 nm at 30 kV for a working distance of 5 mm, range of acceleration tension between 1 to 30 kV, sample deplacement from 0 to 25 mm in X and Y axes, from 5 to 30 mm in Z axes. Tilt angle from -5° to +45°, complete rotation of 360°. Samples were mounted on copper tape and sputtered with (10 Å of a Pd/Au mixture) to prevent charging during the observation.

Transmission Electron microscopy: TEM was carried using a Tecnai G² 30 UT operating at 300 kV acceleration voltages with a 0.17 nm point resolution. The images were recorded from a 3-mm diameter specimen mounted on a double tilt holder in a conventional compu-stage that enables a tilting range of ±20-29° (Laboratoire CRISMAT: UMR 6508 mixte CNRS-ENSICAEN).

X-ray diffraction: SA-XRD patterns were recorded using a Philipps PW 3040/60 X'Pert PRO X-ray diffraction system operating at 30 mA and 40 kV, and between 0.7° and 5.0° with a step size of 0.0167.

3.2. Results and discussion

The preparation of porous PDCs by polymer nanocasting mainly requires two conditions: the polymer must display an excellent solubility while having a sufficient ceramic yield to avoid the presence of uncontrollable porosity. PEIA is soluble in toluene (25g/100mL). Nanocasting has therefore been performed in toluene. The first part of the present chapter showed that PEIA exhibited a ceramic yield of 67% under ammonia. Accordingly, it displays the required characteristics to generate porous AlN by nanocasting. Here, nanocasting provides access to pores in AlN by: i) replicating the nanostructure of CMK-3 through the impregnation of the pore template with PEIA solution, ii) the subsequent filtration step that consists in selectively removing the PEIA molecules deposited outside, while the capillary forces kept PEIA molecules effectively inside the pores, iii) the post-treatment of the infiltrated template at low pressure in order to slowly remove the solvent and iv) the heat-treatments to convert PEIA into AlN and remove CMK-3. In our study, we have applied two types of heat-treatment:

1) Heat-treatment under NH_3 at 1000°C (5 h) to convert PEIA into AlN while CMK-3 is removed leading to sample **AlN 1000-1**;
2) A first heat-treatment under N_2 at 1000°C (2 h) to convert PEIA into Al(C)N followed by a second heat-treatment under NH_3 (5 h) to remove free carbon in Al(C)N as well as CMK-3 leading to the sample **AlN 1000-2.**

The second procedure is usually applied to prepare **ordered mesoporous PDCs** [252] because we considered that a direct treatment under ammonia might disturb the structural integrity of the product. Using these two procedures, the sample appears white and exhibits a porous morphology as illustrated on the SEM image of the sample **AlN 1000-1** (Figure II-11).

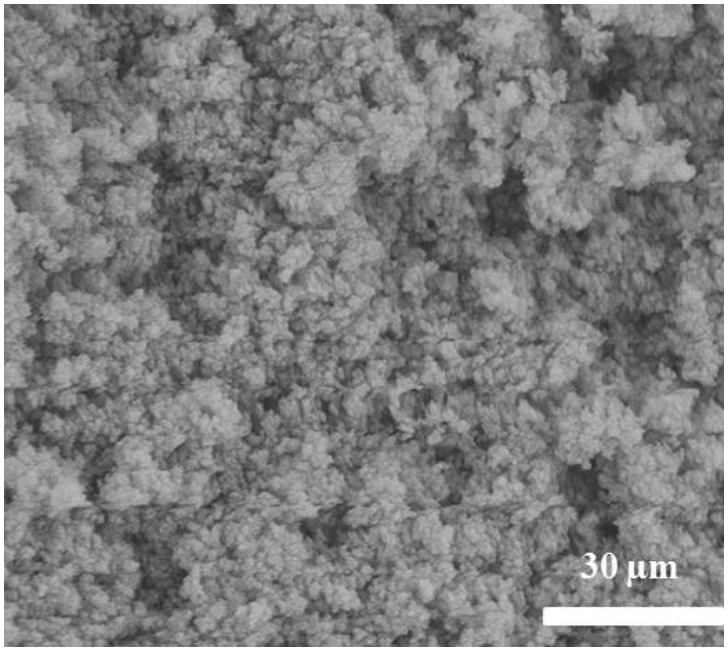

Figure II-11: SEM image of **AlN 1000-1**.

The analysis of the N_2 adsorption desorption isotherms of **AlN 1000-1** and **AlN 1000-2** at 1000°C (Figure II-12) allows estimating the porous network of the samples and deciding which strategy could be applied to prepare **porous AlN** by **PEIA nanocasting**. On the basis of the isotherms of samples, **AlN 1000-1** and **AlN-1000-2** display similar profiles with type II/IV compounds suggesting macroporous and mesoporous features with one hysteresis loop in the relative pressure range from 0.65 to 1.0. The type of the adsorption hystereses is relatively complex and tends to be characteristic of disordered channels. It represents a H1 hysteresis type. Specific BET surfaces of 217 and 222 $m^2.g^{-1}$ are measured for **AlN 1000-1** and **AlN 1000-2**, respectively. Pore volumes of 0.71 $cm^3.g^{-1}$ and 0.72 $cm^3.g^{-1}$ are calculated for **AlN 1000-1** and **AlN 1000-2**, respectively. As a consequence, we can consider that AlN samples are mesoporous with interconnected pores with a certain portion of macropores that most probably result from an agglomeration of mesopores. This is confirmed by the pore size distribution (inset in Figure II-12). We can distinguish two populations of pores: mesopores around 10 nm and macropores around 60 nm. According to the fact that the BET data are very close between the samples **AlN 1000-1** and **AlN 1000-2**, we have selected hereafter the sample elaborated directly under ammonia treatment (**AlN 1000-1**).

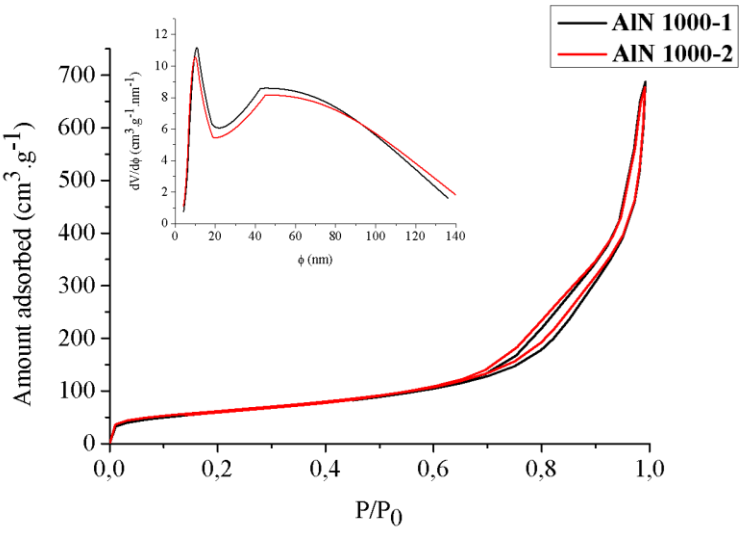

Figure II-12: N_2 adsorption-desorption isotherms recorded at 77K of **AlN 1000-1** and **AlN 1000-2** at 1000°C. Pore size distribution as inset.

We have observed by X-ray diffraction in the first part of the present chapter that the increase of the temperature of elaboration of **PEIA-derived-AlN** involves an increase of the degree of crystallization of the AlN phase. Let us discuss on the evolution of the BET data with the temperature of elaboration of AlN. It is reported that crystallization has a tendency to decrease the textural properties of porous materials [107]. The BET SSA significantly decreased from 217 to 50 $m^2.g^{-1}$ while the pore volume decreased from 0.72 to 0.42 $cm^3.g^{-1}$ through heat-treatment of the sample **AlN 1000-1** at 1400°C under nitrogen leading to the sample **AlN 1400-1**. The isotherm of **AlN 1400-1** is of type II (Figure II-13).

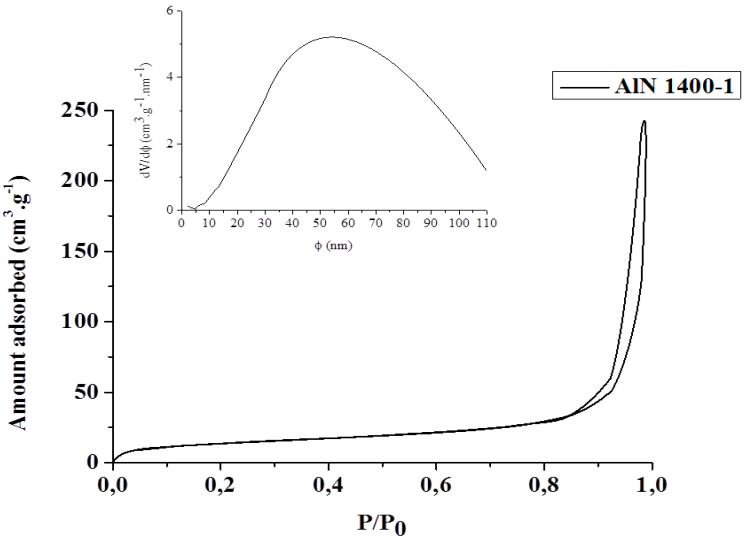

Figure II-13: N_2 adsorption-desorption isotherms recorded at 77K of **AlN 1400-1**. Pore size distribution as inset.

The decrease of the BET surface is due to the disappearance of the mesopores as shown with the pore size distribution calculated from the desorption branch by means of the Barett-Joyner-Halenda method (as inset). A BJH adsorption average pore diameter of 56.2 nm is calculated. As a consequence, it seems difficult to tailor the mesoporosity of AlN derived from PEIA by the temperature of elaboration. Having in mind that the weight loss of PEIA (~33%) might alter the porosity, we attempted to perform i) a double nanocasting-NH_3 pyrolysis cycle, ii) a double nanocasting- NH_3 crosslinking at 200°C-NH_3 pyrolysis cycle. Both attempts led to absolutely no change in the textural parameters. Several factors condition whether a particular combination of product and template can be successfully nanocasted [260]. Based on former studies published by our group [239, 252], preceramic polymers with ceramic yields higher than 50% could be used to infiltrate CMK-3 and generate ordered mesoporous PDCs. For a solution to spontaneously infiltrate a nanoporous template such as CMK-3, a positive capillary pressure must exist; this implies that the contact angle of the precursor with the pore walls must be less than 90° [261]. Thus, the surface chemistry of the template is a critical consideration in nanocasting. Here, CMK-3 possibly resists to the infiltration by the substantially incompatible solution of PEIA. This is confirmed in Chapter 4 with SiAlCN ceramics.

According to the relatively good textural properties of **AlN 1000-1**, we analyzed the latter by SA-XRD and HRTEM.

The SA-XRD pattern of **AlN 1000-1** (Figure II-14) exhibits a diffraction peak at 2θ = 1.39°. This peak is assigned to the (100) reflection of the 2D hexagonal lattice (space group *P6mm*) with a lattice parameter a_{100} = 7.24 nm. The corresponding cell parameter of **AlN 1000-1** is smaller than that of CMK-3 due to framework shrinkage that occurred during the pyrolysis of PEIA. Other peaks characteristic of the hexagonal structure and observed in CMK-3 do not appear because of a significant loss of the order in the **AlN 1000-1** due to the impregnation-heat treatment cycle as we discussed earlier.

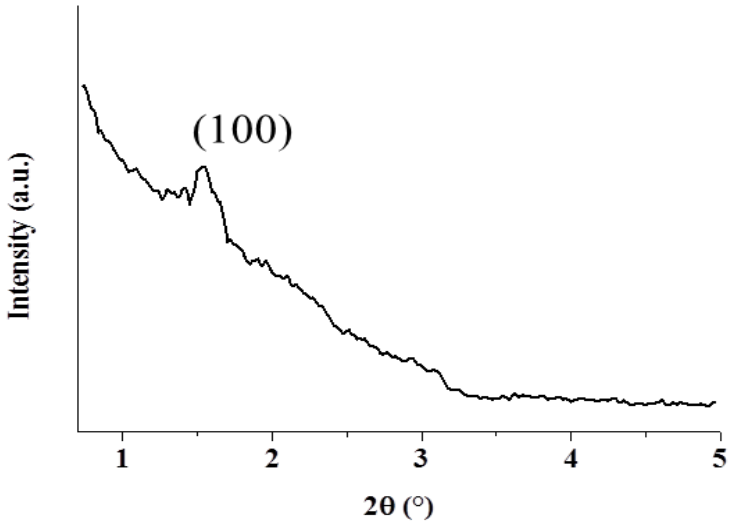

Figure II-14: SA-XRD pattern of **AlN 1000-1**.

The structural regularity of the porous AlN material was investigated by HRTEM. Figure II-15 shows the TEM images of the sample **AlN 1000-1**.

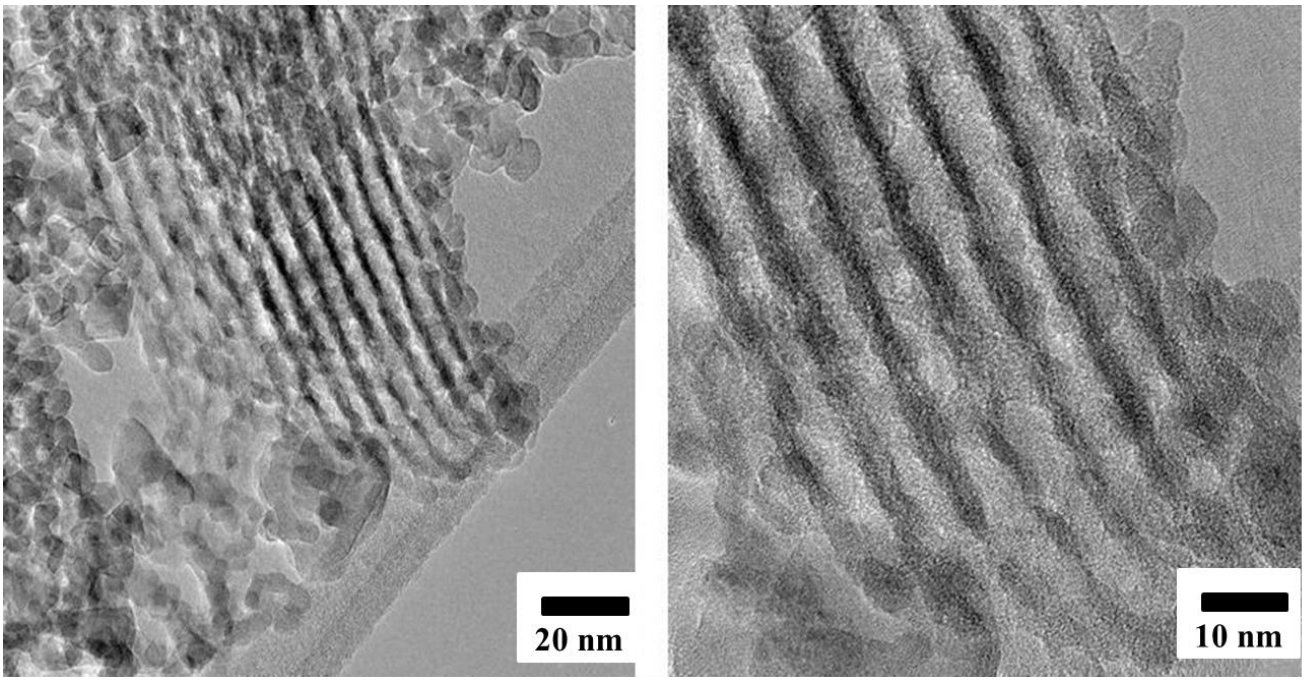

Figure II-15: TEM images of **AlN 1000-1**.

When viewed down the [100] direction of the sample, the HRTEM image shows one-dimensional channels that represent hexagonally ordered pores arranged in a linear array. The distance between the centers of the adjacent channels is not regular and ranges from 5 to 10 nm. However, we can observe irregular and disordered mesoporosity as well as some agglomeration spots which break the perfect order of the negative replication of CMK-3. As a consequence, it can

be concluded that the morphology of the original carbon template is in part retained in the final AlN product.

The preparation of ordered mesoporous AlN appears to be relatively complex as shown through our study. Based on the morphology, structure and texture of the material, we were able to produce **meso/macroporous AlN** powders displaying a BET SSA and a porous volume of 217 $m^2.g^{-1}$ and 0.71 $cm^3.g^{-1}$, respectively by the nanocasting of PEIA from CMK-3. Ordered mesoporosity was locally identified by HRTEM. The difficulties to maintain a general ordered porosity in these materials after replication of the structure of CMK-3 stimulated new approaches to develop the porosity in AlN. Within this context, we focused on the design of AlN aerogels that could be applied, like the meso-/macroporous AlN powders, for hydrogen storage applications without the disadvantages of the template processes

4. AlN AEROGELS

4.1. Experimental part

4.1.1 Materials

PEIA has been described in the first part of the present chapter. The cross-linking agent used is the divinylbenzene (DVB) and was purchased from Alfa Aesar (Alfa Aesar, Ward Hill, MA, USA) (technical grade 80%). The solvent was toluene (99.85%, extra dry over molecular sieve, AcroSeal®) obtained from Acros Organics. The presence of the catalyst is important to stimulate the reaction, therefore we used the platinum(0)-1,3-divinyl-1,1,3,3-tetramethyldisiloxane complex called Karsted Catalyst obtained from Sigma-Aldrich with 2% of Pt in xylene.

4.1.2 Elaboration of PEIA-derived AlN aerogels

In a typical reaction, PEIA was reacted with DVB in a toluene medium. The reaction is conducted in highly diluted solution conditions (total volume of the solution was varied between 70 vol% and 90 vol%) in the presence of the Pt catalyst. The reaction mixture was stirred for 1 to 2 minutes and then it was transferred into a pressure reactor (Digestion Vessel, mod. 4749, Parr, IL, USA) (Figure II-16) to heat it in the oven at the wanted temperature.

Figure II-16: Pressure reactor for the gel preparation.

The samples are labeled as follows: first we indicate the vol% of toluene, second the temperature and third the time. For example, the sample **1** as **70-25-20** refers to the material obtained from PEIA cured with DVD using **70** vol% of toluene at **25**°C during **20** h.

Table II-2 summarizes the experimental parameters varied during the preparation of the wet gels before their conversion into AlN.

Table II-2: Experimental parameters for the preparation of wet gels before AlN transformation.

	Sample*	Vol. (%)	PEIA (g)	DVB (g)	[Pt] Mol.L^{-1}	T (°C)	Time (h)	Observation
1	70-25-20	70	0.3	0.27	10^{-4}	25	20	**No gel**
2	70-70-20	70	0.3	0.27	10^{-4}	70	20	**Gel (low amount)**
3	90-70-20	90	0.3	0.27	10^{-4}	70	20	**No gel**
4	90-100-20	90	0.5	0.23	10^{-4}	100	20	**No gel**
5	90-100-20	90	0.3	0.27	10^{-4}	100	20	**No gel**
6	90-100-72	90	0.3	0.27	10^{-4}	100	72	**No gel**
7	90-150-20	90	0.3	0.27	10^{-4}	150	20	**Gel**
8	90-150-72	90	0.3	0.27	10^{-4}	150	72	**Gel**

*The samples are labelled as follows: dilution vol%-temperature-aging time.

The resulting wet gels were then supercritically dried with liquid CO_2 using an in-house made equipment (Figure II-17) (Prof. Soraru's group, University of Trento) with two glass windows, for visual monitoring of the entire process.

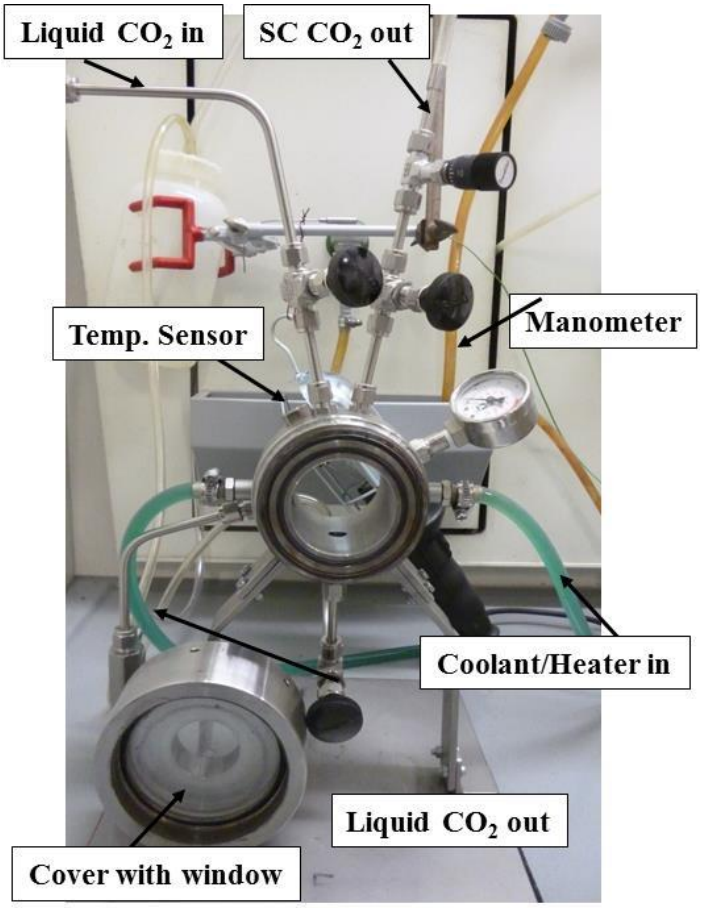

Figure II-17: CO_2 Supercritical drying device.

Before the supercritical drying, the samples have been exchanged with liquid CO_2 twice a day for at least 5 days. The supercritical conditions were obtained by increasing the temperature from room temperature up to 55°C and the pressure up to 100–110 bars. Finally the drying was performed at 55°C by decreasing the pressure down to 1bar over a period of 4–5 h.

The dried gels were then pyrolyzed in a Nabertherm type RS 80/500/11, Germany furnace connected to the glove box in a two-step process: i) under nitrogen for 2 h at 1000°C and ii) under ammonia for 5 h at 1000°C for the carbon removal. We selected a sample pyrolyzed at 1000°C to be heat-treated in a graphitic furnace (Gero Model HTK8). The furnace was pumped and refilled with N_2 to undergo a heating program through a cycle of ramping of 5°C.min^{-1} to 1400 dwelling there for 2 h, and then cooling down to RT at 10°C.min^{-1}. A constant flow (200 mL.min^{-1}) of nitrogen was passed through the furnace.

4.1.3 Experiments

BET (Model Sorptomatic 1900 analyser (Fisons)) and SEM (Hitachi S800 microscope) were investigated to study the porosity of the AlN aerogels.

4.2. Results and discussion

AlN aerogels are obtained by reaction of PEIA with a C=C-containing cross-linker (Divinylbenzene, DVB). The idea is to stimulate a reaction between the C=C bonds present in the DVB with the Al-H units present in **PEIA** by hydroalumination in the presence of the catalyst according to the following reaction (Equation II-4):

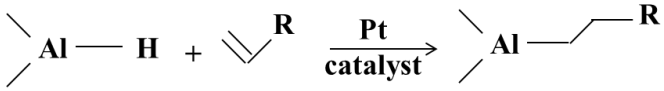

(II-4)

It should be mentioned that aluminum can be added at the α- (Equation II.4) and/or β-position of the vinyl group of DVB.

Based on Table II-2, we can observe that gelation of the solution mixture PEIA/DVB/Pt takes place at 150°C after aging of 20 h or more (samples 7 and 8). Therefore, we can suggest that the essential parameter of the gelation is the temperature applied to the vessel containing the reactive mixture. Monolithic wet gel samples are obtained as shown in Figure II-18. Then, the wet gels are supercritically dried with liquid CO_2 followed by a heat-treatment through two steps: i) the first step consists in pyrolyzing the sample under nitrogen at 1000°C for 2 h, and ii) the second step to remove the carbon issued from DVB by a treatment under ammonia at 1000°C for 5 h. We have applied this two-step pyrolysis program due to technological reasons: wet aerogels are relatively sensitive to air and moisture; therefore they underwent a first heat-treatment in nitrogen at 1000°C leading to relatively stable materials. The latter were transferred to our institute to undergo heat-treatment in ammonia to remove carbon residue from DVB.

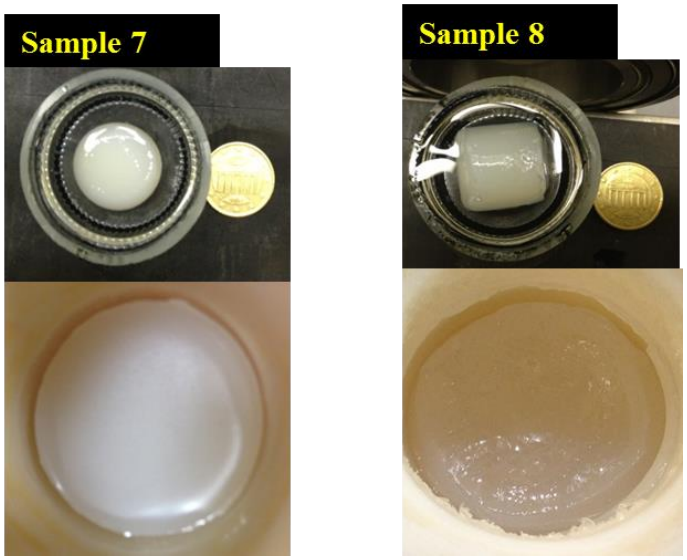

Figure II-18: Images of the wet gels **7** and 8.

After heat-treatments, ceramic samples are labelled **AlN_Aero-7** and **AlN_Aero-8**.

Both samples were firstly analyzed by BET. The adsorption–desorption isotherms are provided in Figure II-19. Based on the IUPAC classification [262], the isotherms of both samples appear also complex and tend to be characteristic of a type IV (characteristic of mesoporous materials). Above a relative pressure (P/P_0) of 0.6 **(AlN_Aero-7)** and 0.8 **(AlN_Aero-8),** the distinct hysteresis loops observed between the adsorption and desorption curves confirm the presence of mesopores. The hysteresis loop shapes correspond to the type H1 (adsorbents with a narrow pore size distribution) typically attributed to cylindrical pores.

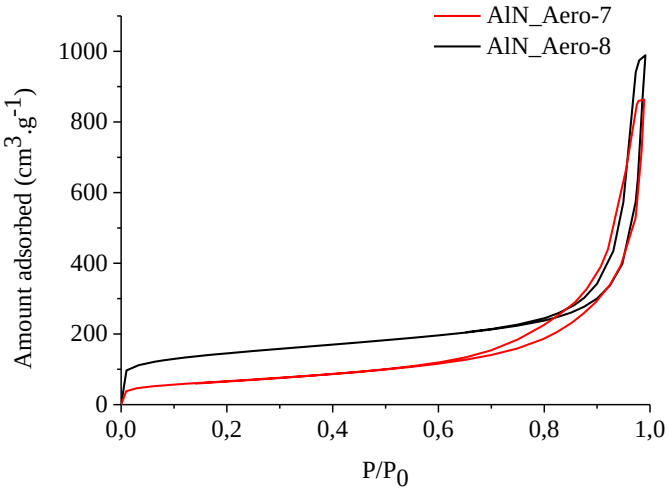

Figure II-19: N_2 adsorption-desorption isotherms recorded at 77 K of **AlN_Aero-7**and **AlN_Aero-8**.

The deduced values of the BET SSA and the porous volume are 511 $m^2.g^{-1}$ and 0.88 $cm^3.g^{-1}$ for **AlN_Aero-8**, respectively *versus* 239 $m^2.g^{-1}$ and 0.81 $cm^3.g^{-1}$ for **AlN_Aero-7**. The BJH derived pore size distribution plots give an average pore size of 20 nm for **AlN_Aero-8** *versus* 23 nm for **AlN_Aero-7**. This proves that, besides the temperature, it is important also to consider the aging time in order to fabricate highly mesoporous AlN aerogels as illustrated through the sample **AlN_Aero-8**. Another parameter that affects the development of the porosity is the temperature of elaboration of AlN aerogels.

Similarly to the study we achieved with meso/macroporous AlN by replication of CMK-3, we investigated the effect of the temperature of elaboration of AlN; therefore, the effect of the degree of crystallization of the AlN phase on the BET data. For this study we have selected the sample **AlN_Aero-8** owing to its higher BET data.

We performed an annealing of **AlN_Aero-8** at 1400°C under N_2 and we investigated the porosity of **AlN_Aero-8_1400** in the micropore and mesopore ranges by N_2 physisorption measurements at 77 K (Figure II-20). On the basis of the isotherm profile, the sample **AlN_Aero-8_1400** displays a type IV isotherm. There are no ambiguities on the hysteresis loop: it is of H2 type indicating that the sample is formed of a pore network of different sizes and shapes, most probably caused by the temperature increase from 1000 to 1400°C. BET SSA value decreased but remained at a suitable level: from 511 to 183 $m^2.g^{-1}$ whereas the pore volume decreased from 0.88 to 0.56 $cm^3.g^{-1}$. This definitely corroborates the fact that the textural properties are affected by the temperature of elaboration of AlN and thus the crystallization of the AlN phase.

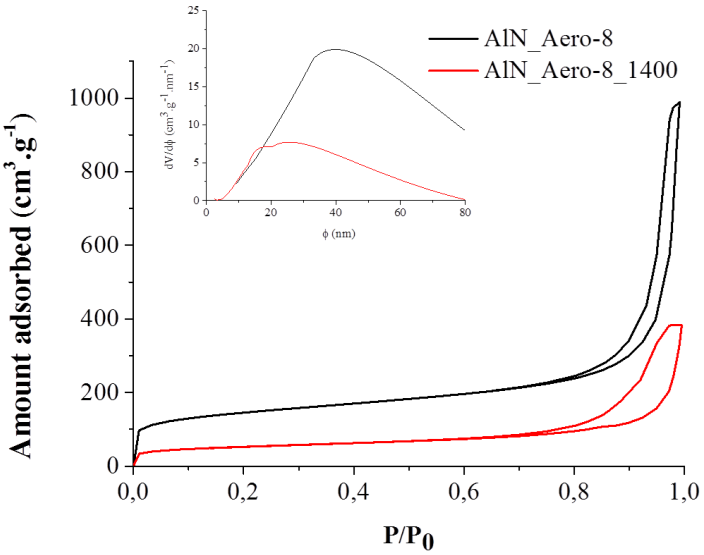

Figure II-20: N_2 adsorption-desorption isotherms recorded at 77 K of **AlN_Aero-8** and **AlN_Aero-8_1400**. Pore size distribution as inset.

Representative micrographs of the samples **AlN_Aero-8 and AlN_Aero-8_1400** are shown in Figure II-21.

The SEM observations confirm the porous character of the sample **AlN_Aero-8**. In this sample, we can notice a relatively uniform distribution of the pores that disappear in the sample **AlN_Aero-8_1400** confirming the BET analyses.

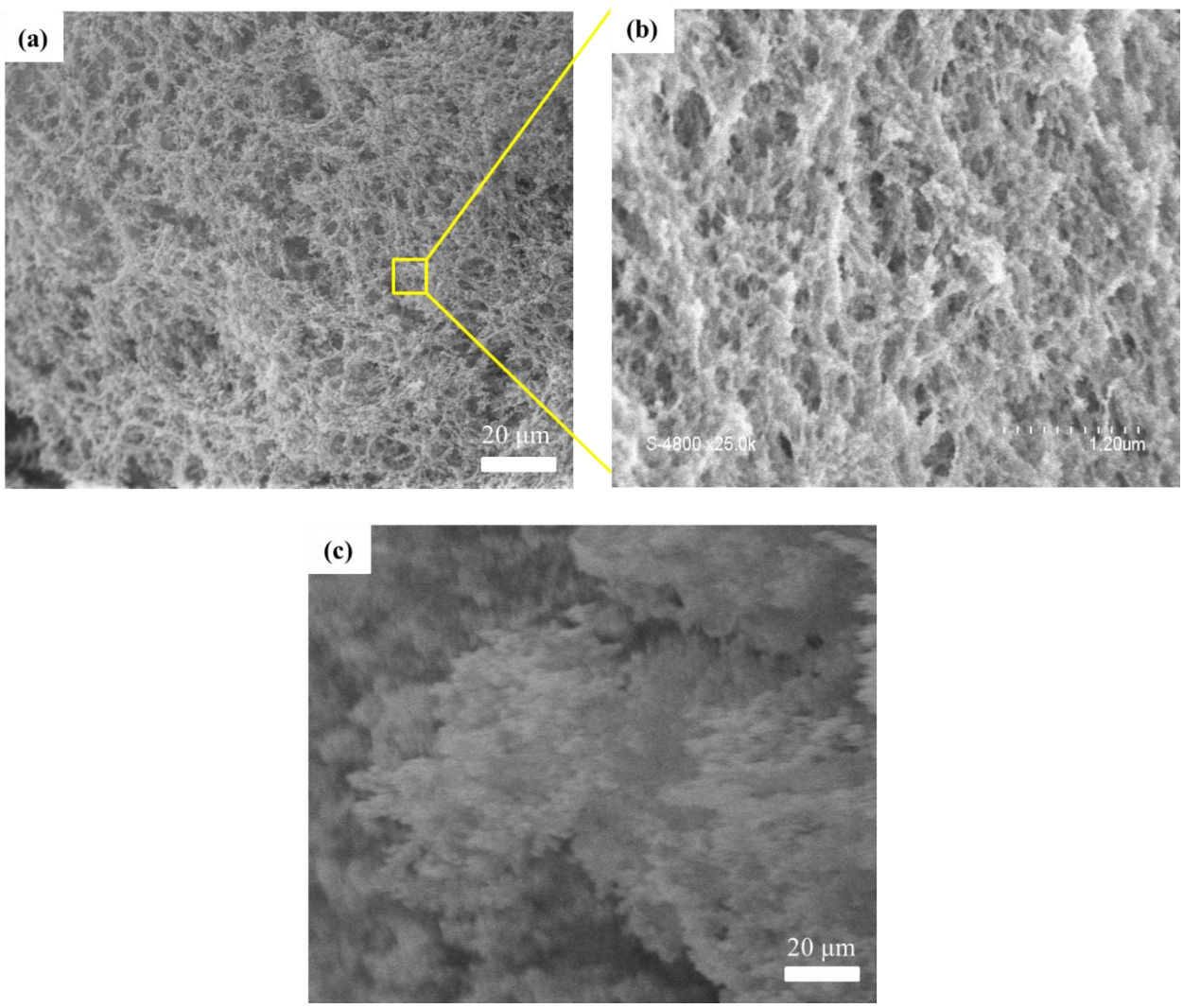

Figure II-21: SEM images of (a-b) **AlN_Aero-8** and (c) **AlN_Aero-8_1400**.

Our study tends to prove that the preparation of crystalline binary nitrides such as III-V compounds (AlN, BN…) with a tailored porosity from preceramic polymers is relatively complex according to the fact that they have to be prepared in their crystalline state to display their intrinsic properties (Young's modulus, thermal conductivity…). A compromise needs to be found between porosity and crystallization. In most of the cases, the crystallization degree of porous III-V compounds is poor. This will be confirmed with BN in Chapter III.

Based on the previously investigated experimental tools, it appears that three key parameters ensure the formation of AlN aerogels with high BET SSAs. The aerogel microstructural features firstly depend on the temperature and the aging time of the gel: the more the gel is left aging inside the vessel at 150°C, the more the porous structure is uniformly recovered after supercritical drying and subsequent pyrolysis. In addition and as expected, they depend on the temperature of annealing. A relatively low degree of crystallization is required to obtain high BET SSA values.

Porous AlN, including meso/macroporous compounds and aerogels, are potential candidates as templates to be filled with a variety of different materials, depending on the aim of investigations or applications. In the following section, we investigated the potential of meso-/macroporous AlN and AlN aerogels to confine hydrogen carrier like $NaAlH_4$ and realize its destabilization while improving its dehydrogenation kinetics.

5. NANOCONFINEMENT OF $NaAlH_4$

5.1. Introduction

Record crude oil prices combined with public interest in energy security have resulted in increased attention to a potential transportation economy based on hydrogen fuel. It has a number of advantages over other chemical energy carriers as we have seen in Chapter I. One of the greatest challenges is the discovery and development of materials and compounds capable of storing enough hydrogen on-board to enable a 300-mile range without adding significant weight or volume to today's conventional automobile. A minimum of five kilograms of hydrogen would be needed to be stored on-board to drive even the most fuel-efficient vehicle three hundred miles. At standard temperature and pressure (STP), five kilograms of hydrogen requires a volume of nearly 54 m^3. Unfortunately, even highly compressed hydrogen gas is unlikely to be of sufficient volumetric density (40 $g.L^{-1}$ at 700 bar) to enable a fuel system to meet the 300-mile target. Liquefied hydrogen at 70 $g.L^{-1}$ also falls short of reasonable volumetric system targets when cooling systems required keeping hydrogen liquefied (b.p. –253°C) are added to the storage system.

The U.S. Department of Energy's 2010 and 2015 technical targets for on-board vehicular hydrogen storage are a useful benchmark for comparing different storage methods [263]. Several of the current DOE technical targets are listed in Table II-3. Operational characteristics such as the temperature, the min/max delivery pressure, the re-filling time, the cycle life, and the fuel purity are also crucial to the performance of the storage system.

Table II-3: Current DOE revised technical targets for on-board hydrogen storage systems for light-duty vehicles [263].

Storage Parameter	Units	2010	2015	Ultimate
System gravimetric capacity[a]	$kg(H_2)/kg(System)$[b]	0.045	0.055	0.075
	kWh/kg	(1.5)	(1.8)	(2.5)
System volumetric capacity	kg/m^3	28	40	70
	kWh/m^3	(900)	(1300)	(2300)
Min/max delivery temperature	K	233/358	233/358	233/358
Cycle life	Cycles	1000	1500	1500
Min delivery pressure	atm	4FC/35ICE[c]	3FC/35ICE	3FC/35ICE
Max delivery pressure	atm	100	100	100
System fill time	kg/min	1.2	1.5	2.0
Fuel purity	Percent H_2		99.99 (dry basis)	

[a] The listed gravimetric and volumetric capacities are *system* targets that include the mass and volume of the system itself, including the tank, material, valves, regulators and other parts. Material capacities may need to be up to twice as large as system capacities.
[b] The standard practice here is to define the gravimetric (volumetric) density relative to the maximum final mass (volume) of the combined hydrogen-host system.
[c] FC=fuel cell, ICE=internal combustion engine

Hydrogen storage is a materials science challenge because, for all six storage methods currently being investigated, materials with either a strong interaction with hydrogen or without any reaction are needed. Besides conventional storage methods, i.e. high pressure gas cylinders and liquid hydrogen, chemical hydrogen storage materials that use light elements to chemically bind hydrogen are explored. In these chemical hydrogen storage materials, hydrogen is 'discharged' by a chemical reaction and the hydrogen is 'recharged' by a chemical processing pathway. This makes them unique compared to metal hydride materials or carbon sorbent materials where the hydrogen release and uptake is controlled by temperature and pressure.

Recently, there is a strong focus on the modification of the thermodynamic and kinetic properties and on the improvement of the cyclic properties of chemical hydrogen storage materials. A modification or an optimization of the hydrogen storage capacities and/or even reversible properties is considered necessary to reach the targets fixed by the DOE [264].

Nanoconfinement is one of the approaches which have been proposed to address the modification of kinetics, thermodynamics and reversibility in hydrogen carriers like $LiBH_4$ [265], NH_3BH_3 and $NaAlH_4$ [83]. Confinement involves size and interface effects to alter both kinetics and thermodynamics. However, this is mainly observed at the lower nanoscale [266]. Nanoconfinement consists in preparing a material, typically a hydride in the field targeted herein, in nanodispersed form through its infiltration in a nanoporous scaffold. This leads to nanoconfined systems. A major reason of the improved hydrogen storage performances is that the surface energy of nanoconfined

particles may be different due to their contact with the surrounding scaffold. This part addresses the nanoconfinement effects on sodium alanate while using AlN as porous host.

Sodium alanate ($NaAlH_4$) is one of the most investigated hydrogen carriers among complex hydrides mainly because of its reasonable hydrogen content and reversibility (even if achieved with severe conditions: 10% at 170°C with 150 bar H_2 pressure). However, reaction kinetics is hindered because of the slow mass transport of segregated solid phases especially upon re-hydrogenation. As we have shown in the literature review, $NaAlH_4$ decomposes in three subsequent reactions:

$$\mathbf{3NaAlH_4 = Na_3AlH_6 + 2Al + 3H_2} \quad \mathbf{(3.7\ wt\%\ H)} \quad \mathbf{(1)}$$

$$\mathbf{Na_3AlH_6 = 3NaH + Al + 3/2H_2} \quad \mathbf{(1.8\ wt\%\ H)} \quad \mathbf{(2)}$$

$$\mathbf{NaH = Na + \tfrac{1}{2}H_2} \quad \mathbf{(1.8\ wt\%\ H)} \quad \mathbf{(3)}$$

$NaAlH_4$, though it has an equilibrium pressure of 1 bar H_2 at 30°C, only starts to release hydrogen when the temperature reaches its melting point at 183°C. The release of hydrogen occurs together with the formation of Na_3AlH_6 and Al (reaction 1). At temperatures above 300°C, the respective Na_3AlH_6 decomposes releasing hydrogen and forming NaH and Al (reaction 2). These two reactions give a theoretical reversible storage capacity of 5.6 wt%. The desorption of hydrogen in the third step (reaction 3), is usually not considered important for hydrogen storage purposes because it occurs at too high temperatures for practical applications. As shown in a number of examples, the addition of halides, nitrides, hydrides of Ti and a few of other elements can be very effective, especially in the case of $NaAlH_4$ [66]. Here, our approach to address the sluggish kinetics issue and to improve reversibility is to decrease the particles size while confining the hydride into the pores of a host material.

We investigated, as a preliminary study, the impact of nanoconfinement of the porous AlN. However, there is usually a lack of direct comparison on the hydrogen storage performance among the host materials studied so far. As a consequence, we have also tested the nanoconfinement of $NaAlH_4$ in CMK-3 to understand, extrapolate and highlight the performance of porous AlN as host materials for the nanoconfinement of $NaAlH_4$.

5.2. Experimental part

5.2.1 Materials

$NaAlH_4$ was purchased from Aldrich (technical grade 90%). The ordered mesoporous carbon CMK-3 was purchased from ACS Material. The CMK-3 has a surface area of 1000 $m^2.g^{-1}$ and a pore volume of 1.35 $cm^3.g^{-1}$. The pore size distribution provides a narrow maximum around 5.5 nm. All

sample preparations and handlings were performed in the MBraun argon-filled glove box with H_2O and O_2 levels below 0.1 ppm. We used CMK-3 as well as samples **AlN 1000-1** and **AlN_Aero-8**as host materials. Before manipulation, all of the porous hosts were dried at 150°C under dynamic vacuum overnight. This pre-treatment was applied in order to remove traces of water adsorbed on the surface of the porous material.

5.2.2 Nanoconfinement protocol

We fixed a weight ratio $NaAlH_4$: host material = 1. Hence, 200 mg of $NaAlH_4$ dissolved in toluene were added under static vacuum to 200 mg of porous support by the means of a syringe. The solution of $NaAlH_4$ quickly fills the pores of the host material, this being evidenced by effervescence. The tube is then placed in an ultrasonic bath at 0° C for 15 min. This step optimizes the impregnation of the $NaAlH_4$ solution inside the porosity. The impregnated material is then left under static vacuum for 48 h at 0°C. Then, the sample is vacuum-dried to remove the solvent and rapidly washed with toluene to dissolve the residual $NaAlH_4$ left outside of the monolith. Finally, the sample at 0°C was dried for 48 h under dynamic vacuum to remove any solvent traces. The sample obtained was stored in a sealed vial under an inert atmosphere in the freezer at 0°C. The composites will be named **$NaAlH_4$@Host material** with the host material being CMK-3, **AlN 1000-1** and **AlN_Aero-8.**

5.2.3 Experiments

The loading of $NaAlH_4$ into the different porous materials was followed by FTIR (Nicolet Magna-IR 550 Fourier transform-spectrophotometer 5Nicolet Instrument Co. USA) and X-ray diffraction (Philips PW 3040/60 X'pert PRO X-ray diffraction system operating at 30 mA and 40 kV from 10 to 90° with a step size of 0.0167, using a Kα1 of copper as source). The desorption properties (considering only the two first reactions) of $NaAlH_4$ confined in the porous materials, were investigated by TGA analysis. TGA measurements were performed on a TGA Q 500 (TA instruments). A nitrogen flux of 50 $mL.min^{-1}$ was fixed with a heating rate of 5°$C.min^{-1}$ up to 200°C.

5.3. Results and discussion

5.3.1 Preparation of $NaAlH_4$@host material

To the best of our knowledge, AlN has never been considered as nanoscaffold of $NaAlH_4$. A major reason for this may be that the synthesis of nitrides is quite challenging because they usually require reaction conditions that exclude water and oxygen. Moreover, a major interest is the low density of nitrides, which maintain the gravimetric hydrogen content of the nanocomposite material. $NaAlH_4$ has been reported to infiltrate in its molten state a mesoporous carbon aerogel scaffold using

an elevated hydrogen pressure to minimize decomposition reactions at high temperature (162°C) [267, 268]. However, the melt-infiltration process is often ineffective and only half of the hydride is nanoconfined while the rest decomposes to Al and presumably NaH [267]. Here, we decided to perform infiltration of porous AlN and CMK-3 by using a solution through the dissolution of $NaAlH_4$ in THF (16g/100mL) (a ratio of 1 was fixed between the hydride and the template). After absorption of $NaAlH_4$, and the washing and drying, the as-obtained samples, labeled **$NaAlH_4$@AlN 1000-1**, **$NaAlH_4$@AlN_Aero-8** and **$NaAlH_4$@CMK-3**, were stored at 0°C.

5.3.2 Characterization of $NaAlH_4$@porous AlN

The FTIR spectra of $NaAlH_4$ and derived composites are presented in Figure II-22.

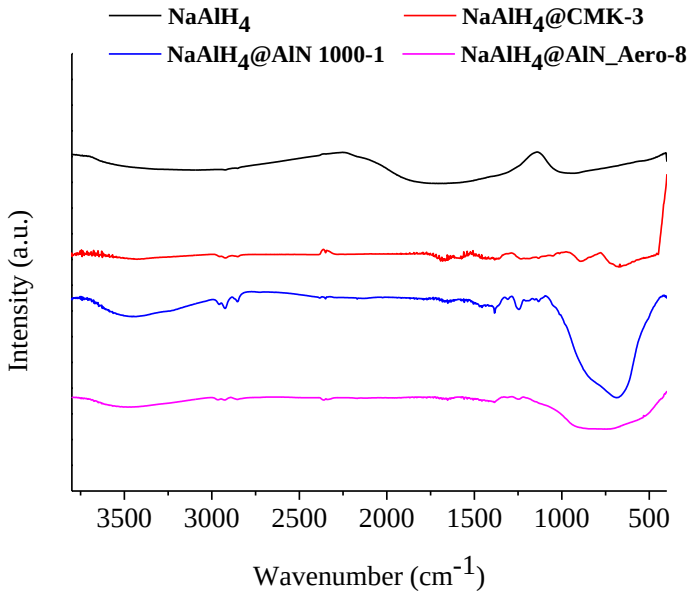

Figure II-22: FTIR spectra of neat **$NaAlH_4$**, **$NaAlH_4$@CMK-3, $NaAlH_4$@AlN 1000-1** and **$NaAlH_4$@AlN_Aero-8.**

The FTIR spectrum of $NaAlH_4$ displays the presence of two bands appearing at 1700 cm^{-1} and 876 cm^{-1}, which are attributed to the ν_3 $[AlH_4]^-$ stretching and ν_4 $[AlH_4]^-$ bending modes, respectively. For the AlN-based composites, we notice the absence of bands that are attributed to $NaAlH_4$. This proves that there are no molecules of $NaAlH_4$ on the outer surface of our host materials. This indicated that the nanoconfinement of $NaAlH_4$ is effective. Further, this shows that our procedure (infiltration, washing and drying) is suitable to the nanoconfinement.

The XRD patterns of $NaAlH_4$ and the three composites in Figure II-23 show the reflections of $NaAlH_4$. There are no apparent XRD peaks when analyzing the AlN-based composites which

indicate the success of the infiltration. However, it seems that the CMK-3 based composite displays some $NaAlH_4$ crystals on its surface due to the appearance of poorly intense $NaAlH_4$ XRD peaks.

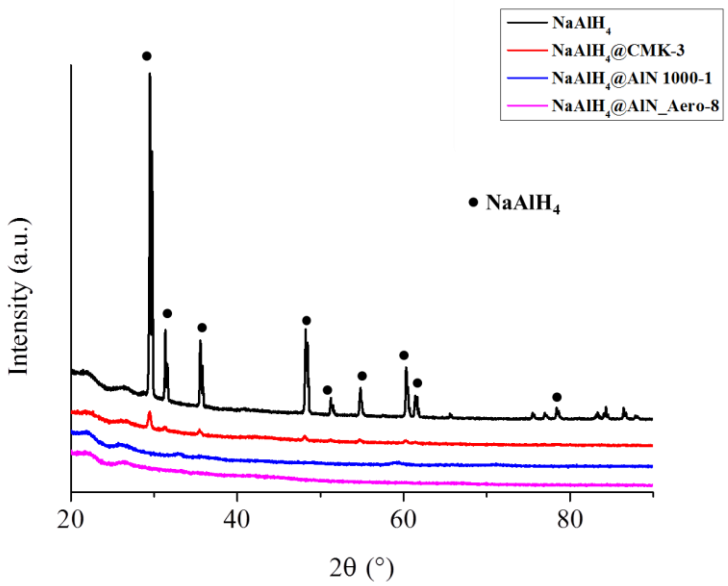

Figure II-23: XRD patterns of neat **$NaAlH_4$, $NaAlH_4$@CMK-3, $NaAlH_4$@Al 1000-1** and **$NaAlH_4$@AlN_Aero-8.**

Thermogravimetric experiment is an appropriate tool to measure the weight loss of $NaAlH_4$ and derived composites *versus* the temperature. It should be mentioned that the weight loss is exclusively attributed to H_2 since no other by-products are evolved in the temperature range considered here (RT → 200°C) under N_2 from $NaAlH_4$ [267].

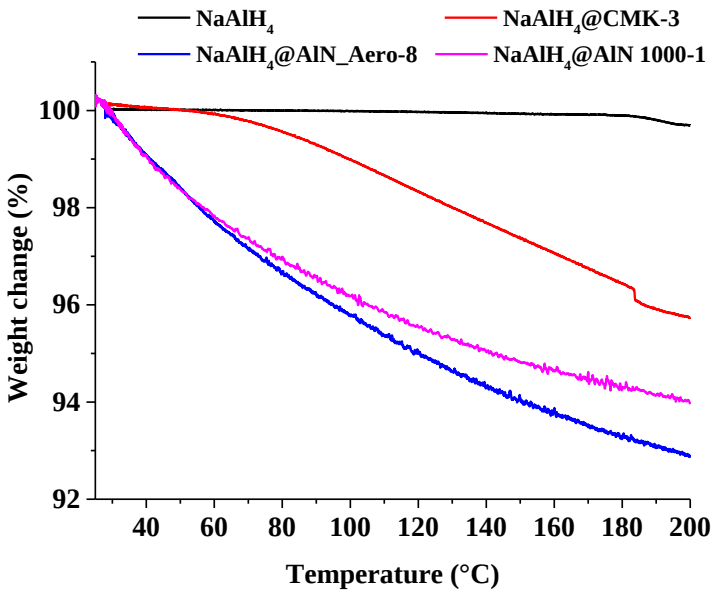

Figure II-24: TGA curves of neat **$NaAlH_4$, $NaAlH_4$@CMK-3, $NaAlH_4$@AlN 1000-1** and **$NaAlH_4$@AlN_Aero-8.**

Based on the TGA curves (Figure II-24), we can clearly observe that the neat $NaAlH_4$ remains stable up to 183°C, temperature at which it starts to melt while releasing hydrogen. In contrast, the decomposition occurs when $NaAlH_4$ is confined in the porous materials including CMK-3, meso/macroporous AlN (**AlN 1000-1**) and AlN aerogels (**AlN_Aero-8**). The **$NaAlH_4$@CMK-3** is stable up to 50°C, temperature at which weight loss occurs. The phenomenon identified at 183°C means that the $NaAlH_4$ is present at the surface of the CMK-3 highlighting XRD observations. A total weight loss of 3.8% has been recorded. It was reported by melt-infiltration of $NaAlH_4$ into CMK-3 a total mass loss of 3 wt% at 200°C [64]. Destabilization of $NaAlH_4$ is more pronounced in porous AlN. It occurs immediately at RT and no effect of the porosity of the host materials is identified up to 60°C (**AlN 1000-1** and **AlN_Aero-8** seem to have the same effect). Above 60°C, we can observe the effect of the textural properties of the scaffolds on the weight loss of the **$NaAlH_4$@AlN 1000-1** and **$NaAlH_4$@ AlN_Aero-8** composites. A maximum weight loss of 7 wt% at 200°C was measured for the composite **$NaAlH_4$@ AlN_Aero-8**. This is attributed to its high BET SSA (511 $m^2.g^{-1}$) and pore volume (0.88 $cm^3.g^{-1}$) compared to meso/macroporous AlN (**AlN 1000-1**) with a BET SSA of 217 $m^2.g^{-1}$ and a pore volume of 0.71 $cm^3.g^{-1}$. This weight loss (7 wt%) is higher than expected at this temperature. However, keeping in mind that CMK-3 has OH groups on its surface and displays the highest BET values (SSA of 1000 $m^2.g^{-1}$ and volume of pores 1.35 $cm^3.g^{-1}$) we suggested that the textural properties are not the only benefit effect to store hydrogen *via* complex hydrides. The chemical nature of the scaffold probably plays a key role. For example, it has been reported that hydrogen storage capacities are improved when $NaAlH_4$ is doped with Ti and nitrides such as TiN [32, 65]. This clearly indicated that nitrides exhibit high potential to store hydrogen from $NaAlH_4$. We should also keep in mind that AlN produced at 1000°C may display NH units at its surface even this has been not identified by solid-state NMR and FTIR. Such groups are known to react with hydrides *via* dehydrocoupling releasing hydrogen. However, there is a lack of evidence and discussion in the literature to support our suggestion. Further work is under investigation to confirm our discussion.

6. CONCLUSION

The nanocasting process of a mesoporous carbon template (CMK-3) and the aerogel technology were successfully applied to prepare **meso/macroporous AlN** materials. The primary objective of this chapter was to prepare and characterize AlN obtained from the PDCs route. Therefore, we investigated (i) the synthesis and characterization of a AlN precursor called Poly(EthylIminoAlane) (PEIA) (ii) the PEIA-to-AlN conversion, (iii) the characterization of the final materials with a particular attention on the effect of the temperature of elaboration on the structural

evolution of AlN from PEIA. Then, we focused on the preparation of two types of porous AlN: the first type was obtained by template synthesis based on CMK-3 through PEIA nanocasting followed by a single step pyrolysis under ammonia at 1000°C. A meso-/macroporous material with a BET SSA of 217 $m^2.g^{-1}$ and a pore volume of 0.71 $cm^3.g^{-1}$ was generated. In this study, it seems that the surface chemistry of the template is a critical consideration in the PEIA nanocasting. Here, CMK-3 possibly resists to the infiltration by the substantially incompatible solution of PEIA. The second type of porous AlN was obtained by CO_2 supercritical drying followed by a two-step pyrolysis process under nitrogen then ammonia up to 1000°C. AlN aerogels in form of monoliths were obtained with BET SSA as high as 511 $cm^3.g^{-1}$ and a pore volume of 0.88 $m^2.g^{-1}$). This has never been reported and therefore opens the way to the development of AlN as catalytic support (because of its high thermal conductivity), as piezoelectric materials to be used for microscale sensors and actuators, despite the fact that they can pose material compatibility challenges. In the present thesis, we investigated the use of porous AlN for hydrogen storage.

On the basis of the above results, it appeared that the dehydrogenation of $NaAlH_4$ is enhanced by nanoconfinement into porous nanoscaffolds and in particular in the AlN aerogels. First results show that the decomposition of the hydride starts at low temperature with a total weight loss of almost 7% at 200°C. The actual reason for this marked difference in hydrogen storage capacities, especially in comparison to CMK-3, is not yet unequivocally known but we have proposed a generalized discussion in the present chapter.

III-

POROUS BN AS HOST MATERIAL FOR THE NANOCONFINEMENT OF AB

III- Porous BN as host material for the nanoconfinement of ab 104
1. Introduction 108
2. PB-derived BN 109
2.1. Experimental part 109
2.1.1 Materials 109
2.1.2 Preparation of PB-derived BN 109
2.1.3 Experiments 112
2.2. Results and discussion 113
3. Mesoporous BN from Activated Carbon 116
3.1. Experimental part 116
3.1.1 Materials 116
3.1.2 Elaboration of mesoporous BN monoliths 117
3.1.3 Experiments 118
3.2. Results and discussion 119
4. BN aerogels 123
4.1. Experimental part 123
4.1.1 Materials 123
4.1.2 Preparation of PB-derived BN aerogels 124
4.1.3 Experiments 125
4.2. Results and discussion 126
5. Nanoconfinement of ammoniaborane 132
5.1. Introduction 132
5.2. Experimental part 133
5.2.1 Materials 133
5.2.2 Nanoconfinement protocol 133
5.2.3 Experiments 134
5.3. Results and discussion 134
6. Conclusion 139

1. INTRODUCTION

Our group has recognized expertise in the synthesis of **BN**, in particular as **porous materials**. We were the first to publish on the preparation of **ordered mesoporous BN** from trimethylaminoborazine [239]. However, the choice of the BN precursor is important. BN precursors with the good B:N ratio, the hexagonal symmetry and with only light elements in addition to B and N are preferred. Within this context, **borazine** and the polymeric derivative, *i.e.*, polyborazylene, are the most appropriate candidates to produce BN. Since 2007, we focused on the preparation of BN from borazine [165] and polyborazylenes [167, 176, 269]. In particular we demonstrated the possibility to prepare BN foams [178] as well as micro/mesoporous BN from polyborazylene [269]. The latter is obtained by thermolysis of borazine. Depending on the temperature of thermolysis, different polymers, in terms of degree of physical state, crosslinking and molecular weight can be obtained. In the present thesis, we synthesized PolyBorazylene by thermolysis of borazine at 60°C in an autoclave. It is labeled **PB**.

We showed in Chapter II that AlN, with their high surface areas can be considered as host materials to improve the hydrogen storage of complex hydrides, *i.e.*, destabilizing the hydride network and therefore decreasing its dehydrogenation temperature while increasing the hydrogen release. We think that BN has also potential to be used as host material for hydrides which display the potential to meet DOE's goals for onboard storage. After confinement into scaffolds, the idea behind this concept is that the BN materials serve as a container for ammoniaborane (AB), and hence not only promote the synthesis of the nanostructured AB, but also physically prevent agglomeration and phase segregation during the H_2 absorption and desorption cycles by thermolysis of the composite. Because BN is composed of light elements, it is very interesting to be used as scaffold like carbon. However, it displays different surface properties that can alter the hydrogen storage capacities of AB. We recently reported for the first time the nanoconfinement of AB in the porosity of mesoporous shell/macroporous core BN nanoparticles [270]. AB was able to liberate hydrogen at temperatures as low as 40°C with traces of NH_3 above 80°C. Here, we have concentrated our effort on the preparation of a **new generation of BN with tailored porosity**. In the first part, we describe the **synthesis** as well as the **characterization** of **mesoporous BN monoliths** obtained by replication of activated carbon monoliths. In the second part, we applied the method described in Chapter II to prepare aerogels. **BN aerogels** are reported. The third part deals with **the impregnation of AB** in the porous BN.

2. PB-DERIVED BN

2.1. Experimental part

2.1.1 Materials

The molecular and polymeric precursors are unstable in air. Therefore, all manipulations were carried out under inert conditions. All ceramic products were handled in an argon-filled glove box (MBraun MB200B) where the O_2 and H_2O concentrations were kept <0.1ppm, because of their high surface area and affinity for moisture before characterization. Argon (>99.995%) was purified by passing through successive columns of phosphorus pentoxide, siccapent, and BTS catalysts. Schlenk glassware was dried at 120°C overnight before pumping under vacuum and filling them with argon for synthesis. Manipulation of the chemical products was made inside the glove box

The reagents we used during the synthesis of borazine are sodium borohydride $NaBH_4$ (Acros, 99% purity), ammonium sulphate $(NH_4)_2SO_4$ (Sigma Aldrich, purity ≥99%) and tetraethylene glycol dimethyl ether as solvent noted tetraglyme (Sigma Aldrich, 99% purity).

2.1.2 Preparation of PB-derived BN

Borazine, molecular BN precursor, was prepared according to the experimental protocol reported by Widemann and Sneddon in 1995 [162]. Despite the relative complexity of this protocol, it remains very attractive due to the inexpensive starting materials and the relatively high yield of borazine obtained.

41 g of $NaBH_4$ were mixed with 186 g of $(NH_4)_2SO_4$ in 500 mL of tetraglyme according to the Equation III-1.

$$\mathbf{6NaBH_{4(s)} + 3(NH_4)_2SO_{4(s)} \rightarrow 2B_3N_3H_{6(g)} + 18H_{2(g)} + 3Na_2SO_{4(s)}} \qquad \text{(III-1)}$$

It should be mentioned that $(NH_4)_2SO_4$ was dried in an oven at 120°C for three days and then put under vacuum during cooling for 1 h.

Figure III-1 displays the typical experimental procedure for the synthesis of borazine.

Figure III-1: Experimental procedure for borazine synthesis.

The reaction system contains a three-neck round-bottomed flask, which was equipped with a water reflux condenser and a magnetic stirrer. The exit of the reflux condenser was connected to a standard vacuum line equipped with three liquid-nitrogen traps. At room temperature, 41 g of $NaBH_4$ and 186 g of $(NH_4)_2SO_4$ were dissolved in 500 mL of tetraglyme under argon atmosphere (350 mL of tetraglyme were added to $(NH_4)_2SO_4$ and 150 mL added once $NaBH_4$ was put in the reaction medium) . A BH_4^-/NH_4^+ mole ratio of 0.385 was fixed. With vigorous stirring, the reaction mixture was carefully heated under dynamic vacuum from room temperature up to 120°C; a holding time of 3 h was maintained at this temperature. The borazine was continuously collected in the cold traps, the trapped borazine was further purified by the vacuum fractionation through a series of three traps, the liquid retained in the last trap was finally transferred towards a new Schlenk, to recover colorless liquid borazine that was stored at -18°C to avoid the progressive evaporation of borazine at room temperature because of its high vapor pressure at this temperature. Borazine featured the following data: FTIR (CsI windows/cm^{-1}): $\nu_{(N-H)}$ = 3475 cm^{-1}, $\nu_{(B-H)}$ = 2525 cm^{-1}, $\nu_{(B-N)}$ = 1464 cm^{-1}, $\delta_{(B-N)}$ = 916 cm^{-1}, and $\delta_{(B-H)}$ = 718 cm^{-1}. ^1H NMR (300 MHz/$CDCl_3$, 7.22 ppm): δ = 5.06, 4.57, 4.11, 3.65 (3.30 - 5.35 ppm, quadruplet, 3H, B-H), δ = 5.68, 5.46, 5.24 (5.35 - 6.05 ppm, triplet, 3H, N-H).

It should be mentioned that elemental analysis could not be performed due to the volatility of borazine as well as its extreme sensitivity to air and moisture.

Polyborazylene (PB), polymeric BN precursor, was prepared by polymerization of the borazine. 17.8 g of borazine were introduced in a 75 mL autoclave with controlled temperature and

pressure features (Parr N 4836 Model) (Figure III-2) at 0°C in an argon-filled glove-box using Teflon-lining to easily remove the polymer from the autoclave.

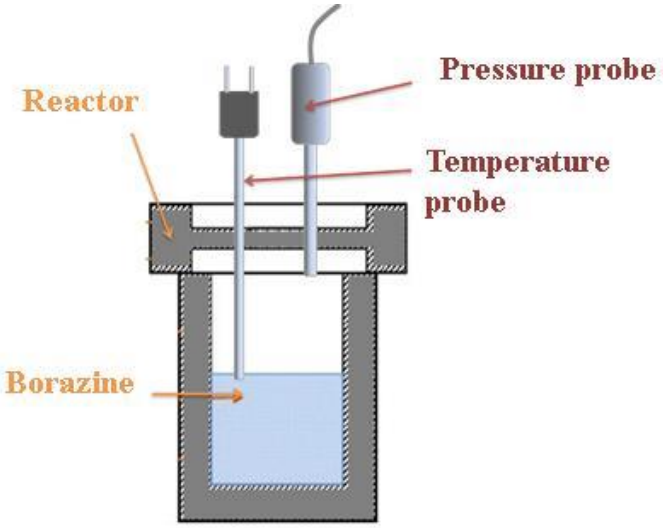

Figure III-2: Layout of the autoclave for polyborazylene synthesis.

We gradually heated the borazine up to 60°C (5°C.min^{-1}), and then kept it at this temperature until stabilization of the internal pressure. The process created a final internal pressure of 121.1 bars after a dwelling time of ~240 h. The increase of the internal pressure is mainly due to the H_2 generation caused by the condensation of borazine molecules, for example reaction between N-H and B-H units and cycles deformation. After cooling down to room temperature and removing H_2 under argon atmosphere, the autoclave was then introduced inside an argon-filled glove-box to recover ~15.2 g of white powder. Polyborazylene featured the following data:

Elemental analysis (wt %): B, 37.46; N, 56.47; H, 5.26; O, 0.81 $[B_{3.0}N_{3.5}H_{4.5}O_{0.04}]_n$. FTIR (KBr/cm^{-1}): $\nu_{(N-H)}$ = 3445 cm^{-1}; $\nu_{(B-H)}$ = 2509 cm^{-1}; $\nu_{(B-N)}$ = 1435 cm^{-1}; $\delta_{(B-N-B)}$ = 890 cm^{-1}; $\delta_{(B-H)}$ = 690 cm^{-1}. ^{11}B MAS NMR (128.28 MHz/ppm): δ = 31 ppm (BN_2H), 27 ppm (BN_3).

PB, placed in a BN crucible, was transferred into a silica tube inserted in a horizontal furnace (Nabertherm type RS 80/500/11, Germany) which was connected to the glove box to prevent oxygen contamination of the sample. The tube was pumped under vacuum and refilled with nitrogen. After that, the sample was subjected to a cycle of ramping of 5°C.min^{-1} to 300, 800 and 1000°C, dwelling there fore 2 h, and then cooling down to RT at 5°C.min^{-1}. A constant flow (120 mL.min^{-1}) of nitrogen was passed through the tube during pyrolysis. The nitrogen-treated sample was then introduced in a graphitic furnace (Gero Model HTK8) in graphite crucibles. The furnace was subsequently pumped and refilled with nitrogen to undergo a heating program through a cycle of

ramping of 5°C.min^{-1} to 1450, 1600 and 1800°C dwelling there for 2 h, and then cooling down to RT at 10°C.min^{-1}. A constant flow (200 mL.min^{-1}) of nitrogen was passed through the furnace.

2.1.3 Experiments

Fourier transform infrared (FT-IR) spectroscopy:

Fourier transform infrared (FT-IR) data was obtained from a Nicolet Magna-IR 550 Fourier transform-spectrophotometer (Nicolet Instrument Co. USA). The FT-IR spectra of **PB** were recorded by mixing 2 wt % polyborazylene with KBr powders followed by its compaction into a pellet in an argon-filled glovebox.

Elemental analysis:

Elemantal analysis of polyborazylene was made in the Service Central de Microanalyses de Vernaison (Vernaison, France) for boron, carbon, and hydrogen and in "équipe de verre et céramique" (Rennes, France) for nitrogen and oxygen elements.

NMR:

^{11}B MAS NMR spectras of **PB** and derived BN powders isolated at 300, 800, and 1000^{o}C were recorded at 9.4 T on a Bruker Avance 400 wide-bore spectrometer operating at 128.28 MHz, using a Bruker 4 mm probe and a spinning frequency of the rotor of 12.5 kHz.

Spectra were acquired using a spin-echo θ-τ-2 θ pulse sequence with $\theta = 90^{o}$ to overcome problems of probe signal. The delay (80 μs) was synchronized with the spinning frequency and recycle delay of 1s was used. Chemical shifts were referenced to $BF_3(OEt)_2$ ($\delta = 0$ ppm).

TGA:

Thermogravimetric analysis (TGA) of the polymer-to-ceramic conversion of PB was recorded on a Setaram TGA 92 16.18. Experiments were performed in a nitrogen atmosphere at 5^{o}C.min^{-1} from RT to 1000^{o}C by using silica crucibles (sample weight of ~80 mg) at ambient atmospheric pressure.

XRD:

BN powders derived from PB were characterized using a Philipps PW 3040/60 X'Pert PRO X-ray diffraction system with XRD sample holders (PVC) for data collection. Cu Kα ($\lambda = 1.54$ Å) radiation with a Ni filter was used with a working voltage and current of 40 kV and 30 mA, respectively. Scans were continuous from 20 to 90^{o} (2θ) with a time per step of 0.85 s in increments

of 0.017° (2θ). Peak positions were characterized by comparison with JCPDS files of the standard material (JCPDS card No 34-0421).

2.2. Results and discussion

The pyrolysis under N_2 up to 1450°C has been monitored by TGA under nitrogen (Figure III-3). PB delivered BN by pyrolysis under nitrogen in excellent ceramic yield (95%). Indeed, it can be clearly seen that the thermal decomposition of PB leads to an extremely low four-step weight loss (5%) with a majority of the loss which occurs below 1000°C. In details, PB undergoes a first weight loss (~0.8%) from 100 to 350°C. A second more important weight loss is identified in the temperature range 350-800°C (2.2%). Above 800°C, the weight loss continuously progresses up to 1000°C. At this temperature a weight loss of 4.5% is recorded. The polymer-to-ceramic conversion is not fully achieved at 1000°C; this is illustrated on the TGA curve through a fourth weight loss of 0.5%. This indicated that the PB-derived material produced at 1000°C contains residual hydrogen; higher temperature (1450°C) is needed to remove the residual hydrogen. At 1450°C, a stoichiometric BN is obtained (45 wt% of boron and 55 wt% of nitrogen found by EDX analysis on the TGA residue).

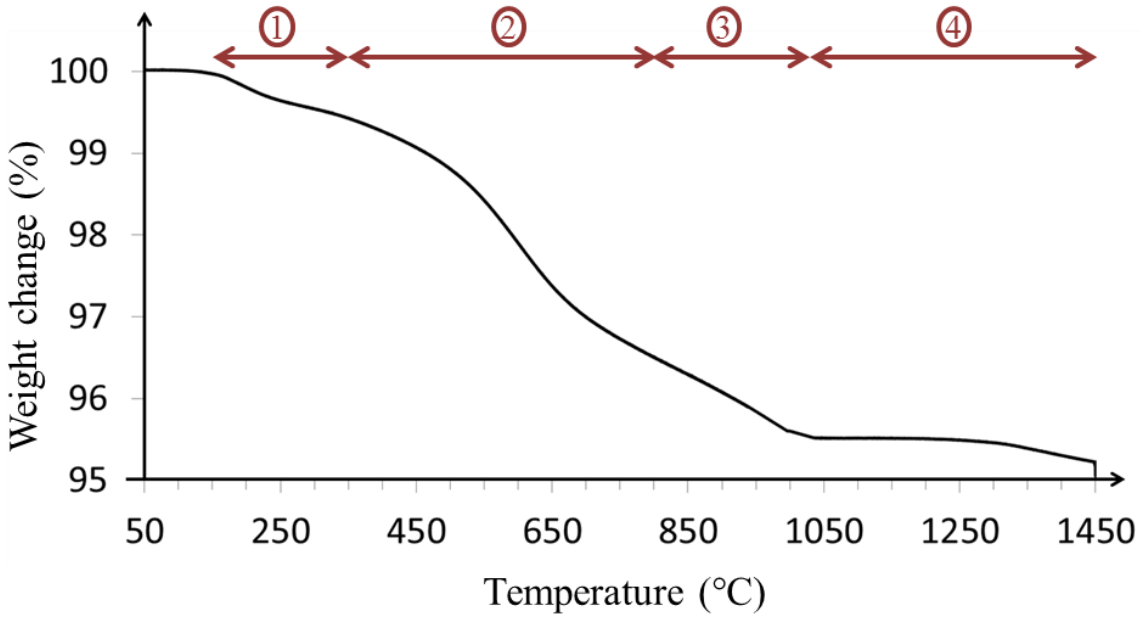

Figure III-3: TGA curve of the 4-step decomposition of **PB** up to 1450°C in N_2 atmosphere (dwelling time: 5°C.min^{-1}).

We studied the structure evolution of PB in the process of polymer-to-ceramic conversion by ^{11}B solid-state NMR. Figure III-4 presents the experimental and simulated ^{11}B MAS NMR spectra of PB and the PB heat-treated at 300, 800 and 1450°C.

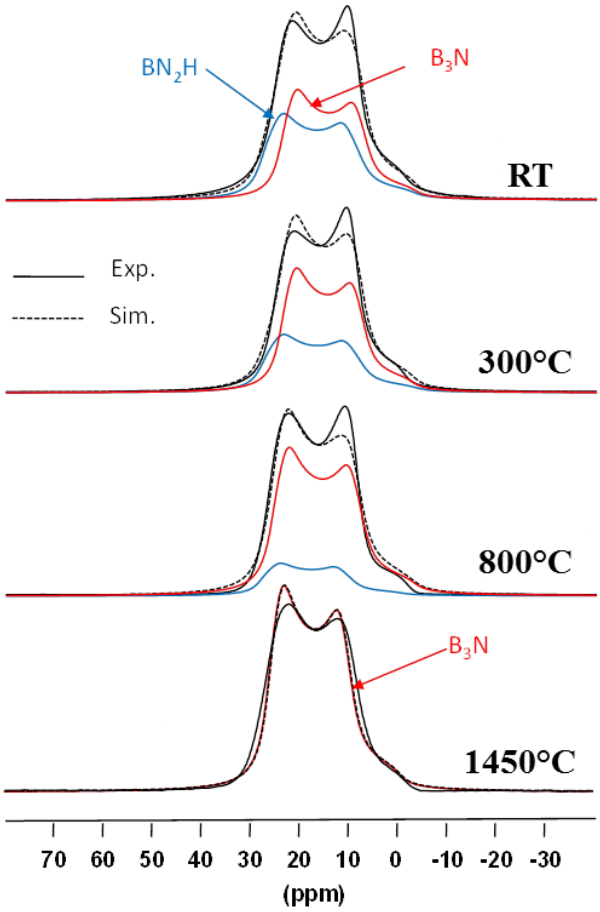

Figure III-4: Solid-state ^{11}B MAS NMR experimental and simulated spectra of **PB** and **N_2-treated intermediates** at 300, 800 and 1450°C.

Through the spectra it is obvious that the polymer-to-conversion of PB occurs with retention of the basic structure of the polymer with the existence of BN_3 and BHN_2 units. With increase of the temperature, the polymer shows an increase of the relative amount of BN_3 environments compared to BHN_2, suggesting the removal of hydrogen during the heat treatment up to 800°C. However, it is clear that the polymer-to-ceramic conversion is not fully achieved at 800°C as attested by TGA. The residual hydrogen (the existence of BHN_2 units in the structure) is released in the temperature range 800-1450°C. After heat-treatment at 1450°C, only BN_3 environment are identified in the ^{11}B solid-state NMR spectrum. We have analyzed the XRD patterns of the samples prepared at 1000°C (labeled **PB1000**) and 1450°C (labeled **PB1450**)

We have performed X-ray diffraction on the PB-derived BN isolated after heat-treatment of PB at 1000 (**PB1000**) and 1450°C (**PB1450**) under N_2 (Figure III-5).

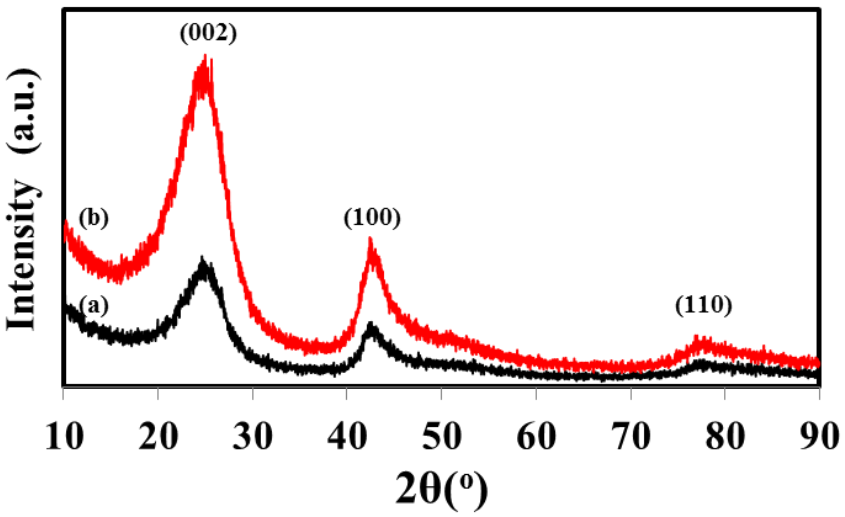

Figure III-5: XRD patterns of (a) **PB1000** and (b) **PB1450**.

The diffuse diffraction peaks of **PB1000** are asymmetric, broad and the 2θ position (2θ =24.3°) is distant from that one in *h*-BN crystal (2θ =26.776°), indicating a high amount of disorder in the structure. In particular, the asymmetric shape of the (002) peak and the absence of the (102) and (112) peaks suggests in a coherent way the presence of turbostratic BN. In comparison, a decrease in the full width at half maximum (FWHM) and an increase in the intensity of the (002) reflections are observed with increasing heat treatment temperatures. This indicated that **PB1450** has a higher relative degree of crystallization than **PB1000**. However, the sample **PB1450** still displays a turbostratic structure.

The increase of the temperature above 1450°C increased the density of BN as well as the crystallinity of samples based on X-ray diffraction investigations (Figure III-6). The samples **PB1600** (heat-treatment at 1600°C) and **PB1800** (heat-treatment at 1800°C) exhibit the (004) and the (112) peaks. In addition the XRD pattern of the sample **PB1800** displays a separation of the (102) peak into the (100) and (101) peaks. This results from a strong improvement in the structural ordering of samples.

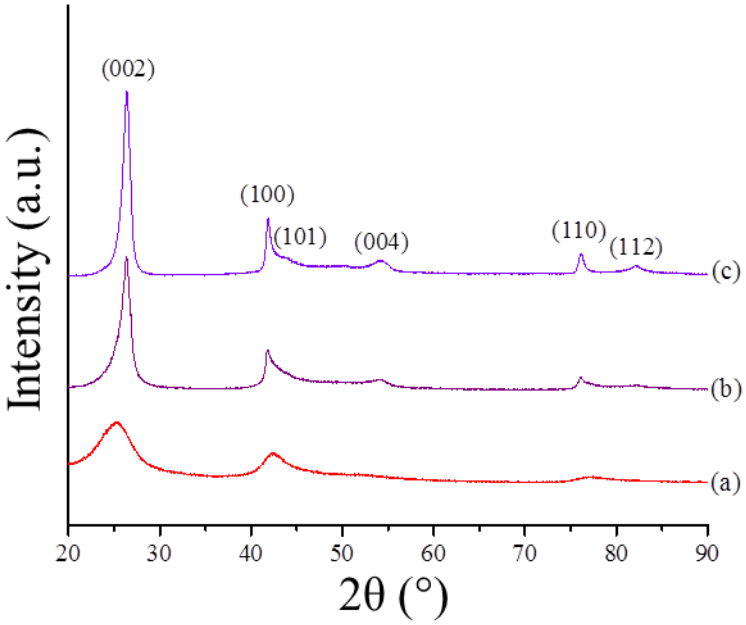

Figure III-6: XRD patterns of (a) **PB1450**, (b) **PB1600** and (c) **PB1800.**

The first part of this chapter allowed us to understand the pyrolysis behavior of PB. The following sections will consist to shape PB through a templated approach and a supercritical CO_2 drying in order to generate after pyrolysis monolithic-type porous BN.

3. MESOPOROUS BN FROM ACTIVATED CARBON

3.1. Experimental part

3.1.1 Materials

PB used as BN precursor was described in the previous section. Activated carbon monoliths were of type NORIT RX3 (purity 97%) and the solvent used for impregnating the monoliths was molecular sieved anhydrous TetraHydroFuran THF (Sigma Aldrich, purity 99%).

Textural parameters of the activated carbon (**AC**) are reported in Table I-1.

Table III-1: Textural properties of Activated Carbon (Norit RX3).

Type	Specific Surface Area ($m^2.g^{-1}$)	Pore Diameter (nm)	Total Volume ($cm^3.g^{-1}$)	Pore
Norit X3	**989**	**4.3**	**0.51**	

3.1.2 Elaboration of mesoporous BN monoliths

220 mg of AC (SSA= 989 $m^2.g^{-1}$; V_p= 0.51 $cm^3.g^{-1}$) are transferred inside a Schlenk tube to be degased under dynamic vacuum at 150°C for 24 h. 165 mg of PB were dissolved in 2 mL of THF (solubility: 25 g of PB in 100 g of THF) which leads to a weight ratio PB:AC= 0.75 (this ratio was considered after optimization where different weight ratios were tested). The solution of PB in THF was injected on the AC under static vacuum at room temperature. Effervescence foam is immediately observed which indicates the impregnation of the solution inside the pores of AC by capillary effect. To further optimize the impregnation process, the tube was then placed in an ultrasonic bath for 30 min. The material is then left under static vacuum for 48 h. After this step, the sample underwent a drying under dynamic vacuum followed by a quick wash with THF to dissolve the PB remaining out of the monolith. Finally, the sample was dried for 48 h under dynamic vacuum. Thus, the sample labeled **PB/AC** is obtained. A series of heat treatment in a nitrogen atmosphere as well as ammonia are crucial to transform the PB/AC into BN; the samples will be labeled as follows BN-T (with T being the final temperature of pyrolysis).

Three samples have been prepared: **mesoBN1000**, **mesoBN1200** and **mesoBN1450**. All the BN samples are stored in the glove box to prevent the adsorption of moisture inside the porosity.

Figure III-7 illustrates the process used to produce porous BN monoliths.

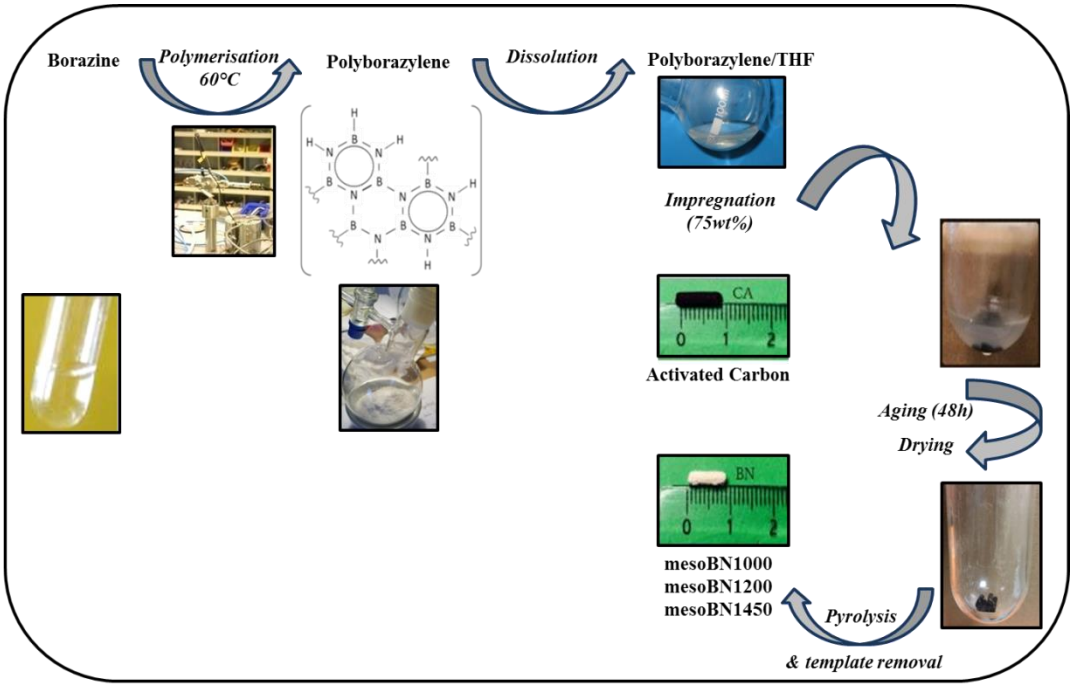

Figure III-7: Overall synthetic pathway for mesoporous BN synthesis.

3.1.3 Experiments

The porous BN materials were characterized by different analyses techniques in order to study their textural parameters, and their eventual evolution with temperature:

BET: N_2 adsorption-desorption isotherms were carried on a Model Sorptomatic 1900 analyser (Fisons). Before adsorption measurements, all samples were outgassed for 4 h at 150°C in the degas port of the adsorption analyzer. The Brunauer.Emmett.Teller (BET) method was used to calculate the specific surface area. The pore-size distribution was derived from the adsorption branches of the isotherms using the Barrett.Joyner.Halenda (BJH) method. The total pore volume (Vp) was estimated from the amount of N_2 adsorbed at a relative pressure of $P/P_0 = 0.99$.

Scanning electron microscopy: SEM pictures were taken with a Hitachi S800 microscope coupled with EDX microanalysis system with IDFix and MaxViwe softwares from SamX. Maximum resolution of 2 nm at 30 kV for a working distance of 5 mm, range of acceleration tension between 1 to 30 kV, sample deplacement from 0 to 25 mm in X and Y axes, from 5 to 30 mm in Z axes. Tilt angle from -5° to +45°, complete rotation of 360°. Samples were mounted on copper tape and sputtered with (10 Å of a Pd/Au mixture) to prevent charging during the observation.

Transmission Electron microscopy: TEM was carried using a Tecnai G² 30 UT operating at 300 kV acceleration voltage with a 0.17 nm point resolution. The images were recorded from a 3-mm diameter specimen mounted on a double tilt holder in a conventional compu-stage that enables a tilting range of ±20-29° (Laboratoire CRISMAT: UMR 6508 mixte CNRS-ENSICAEN). We deliberately selected the samples **mesoBN1000** and **mesoBN1450** to investigate their structure by HR-TEM.

X-ray diffraction: Wide angle XRD patterns were recorded on fibers on a Philips PW 3040/60 X'pert PRO X-ray diffraction system operating at 30 mA and 40 kV from 10 to 90° with a step size of 0.0167, using a Kα1 of copper as source. SA-XRD patterns were recorded using a Philipps PW 3040/60 X'Pert PRO X-ray diffraction system operating at 30 mA and 40 kV, and between 0.7° and 5.0° with a step size of 0.0167.

Density measurements helium pycnometry were performed on the sample **mesoBN1450** with an AccuPyc 1330 Micromeritics device. **Compression tests** (hydraulic MTS apparatus tension\torsion) were carried out at the laboratory MATEIS (Materials Engineering and Science) - UMR 5510 INSA Lyon, on **mesoBN1450**. **Thermal conductivity** measurements were performed in the LCTS-University de Bordeaux.

3.2. Results and discussion

The objective of this study was to replicate the mesoporosity of activated carbon (AC) as well as its monolithic shape using PB as BN precursor. PB infiltrated AC then a pyrolysis was applied to transform PB into BN and remove AC. We selected AC as a porous template due to its high interconnected porosity with a large surface area, its low cost, and practical use of the monolithic form. PB is soluble in toluene or THF, and displays a very high ceramic yield (~ 95%) which is an essential key parameter to retain the monolithic shape during pyrolysis and template removal, hindering in this way any risk of material collapsing or porosity degradation. Impregnation was achieved in toluene by fixing a PB:AC ratio of 0.75. After 2 days of impregnation, washing and drying of the impregnated AC, the composite has been pyrolyzed under N_2 up to 1000°C (dwelling time of 2 h), then under ammonia to 1000°C (dwelling time of 5 h) to deliver the sample labeled **mesoBN1000**. Then the sample **mesoBN1000** is annealed at different temperatures under N_2 up to 1450°C (**mesoBN1450**) to follow the evolution of the porosity *versus* crystallinity

The treatment done at 1000°C for 5 h under ammonia aims to remove the carbon according to the following reaction (Equation III-2) [254]:

$$\mathbf{3C + 4NH_3 \rightarrow 3CH_4 + 2N_2} \qquad \text{(III-2)}$$

Here, in contrast to the preparation of meso-/macroporous AlN, we selected the two-step pyrolysis procedure (similarly to preparation of AlN aerogels) because we observe that a direct pyrolysis under ammonia altered the textural properties of the derived BN).

The TEM images of **mesoBN1000** and **mesoBN1450** samples are presented in Figure III-8. The low-magnification TEM (Figure III-8 a and b) confirms its porous character (disordered porosity) made of voids surrounded by a very thin wall. This is clearly observed in Figure III-8-c. The corresponding SAED pattern which reveal diffuse haloes, as a general feature, has been indexed as the $P6_3/mmc$ space group. In general, diffuse haloes are characteristic of a poorly crystallized structure. Moreover, HR-TEM observations reveal the presence of BN layers with a lack of a long range ordering which surround the voids and therefore develop the porosity. This means that the structure is turbostratic as observed by XRD studies. The average number of layers in the walls is comprised between 5 and 10.

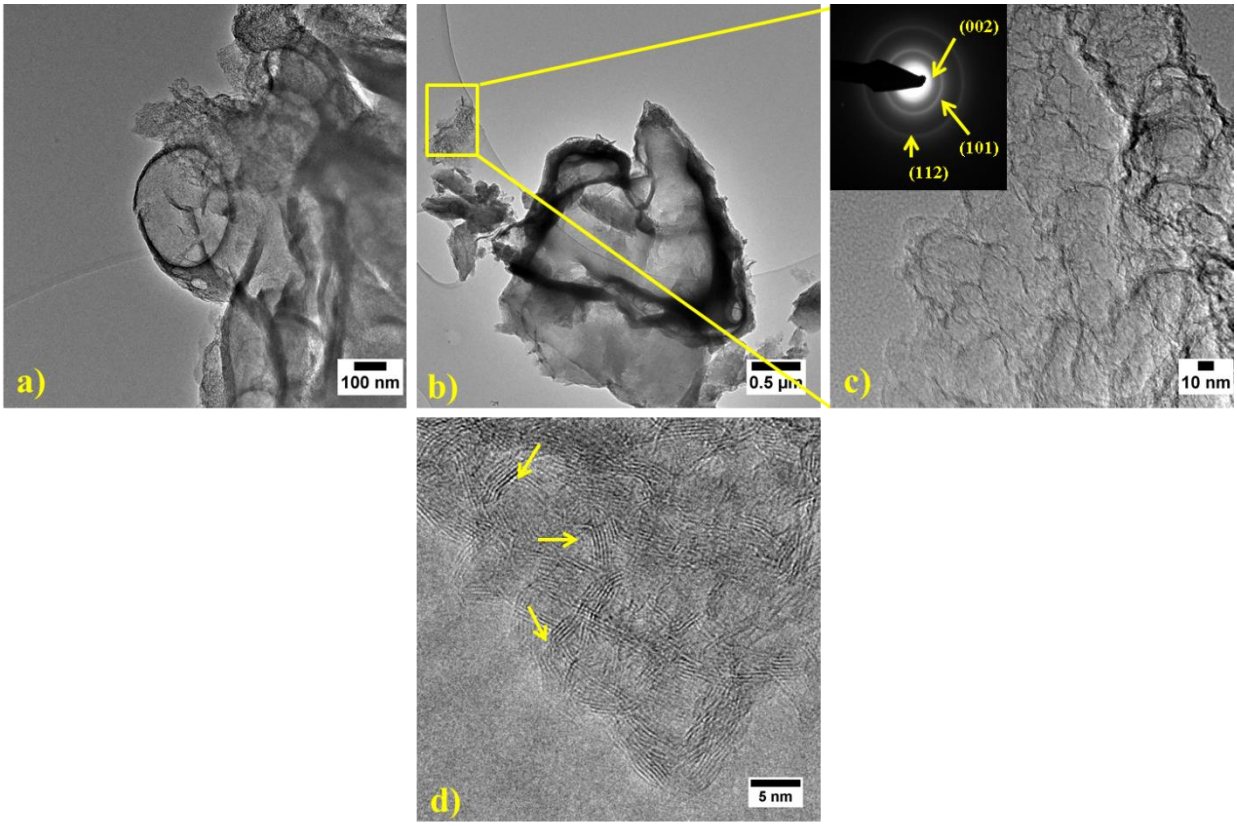

Figure III-8: TEM images of **mesoBN1000**: a) and b) Low magnification, c) High magnification and d) High magnification ROI.

The sample **mesoBN1450** (Figure III-9) also exhibits a relatively high degree of porosity (Figure III-9-a). However, it is made of strongly facetted nanopolyhedral shapes from concentric shells containing voids. The degree of crystallinity of the walls appears to be very high in contrast to the observations of XRD patterns. Figure III-9-b shows that there is a clear continuity between layers of adjacent facets even if locally a discontinuity in the walls and a mismatch within the wall structure can be encountered for this sample (Figure III-9-c). The polyhedron wall thickness has been found to vary from 6 to more than 30 layers. The SAED pattern exhibits spots that indicate the formation of a more crystalline structure. We have encountered structures that exhibited hexagonal BN polyhedra belonging to the $P6_3/mmc$ space group.

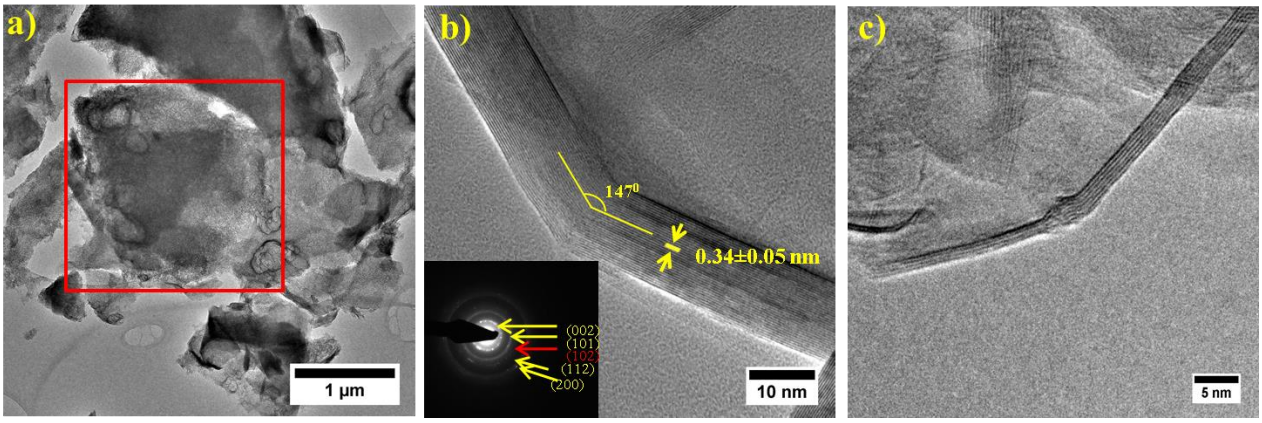

Figure III-9: TEM images of **mesoBN1450**: a) Low magnification, b) and c) High magnification.

TEM investigations showed that the samples display a disordered porosity with pores defined by surrounded BN layers. In order to gain more information on the textural properties of the samples isolated at 1000, 1200 and 1450°C, we studied the porosity at mesoscopic length scale by N_2 physisorption measurements at 77k (Figure III-10-b, Table III-2). For comparison, we have reported the adsorption-desorption isotherm and BET data of AC.

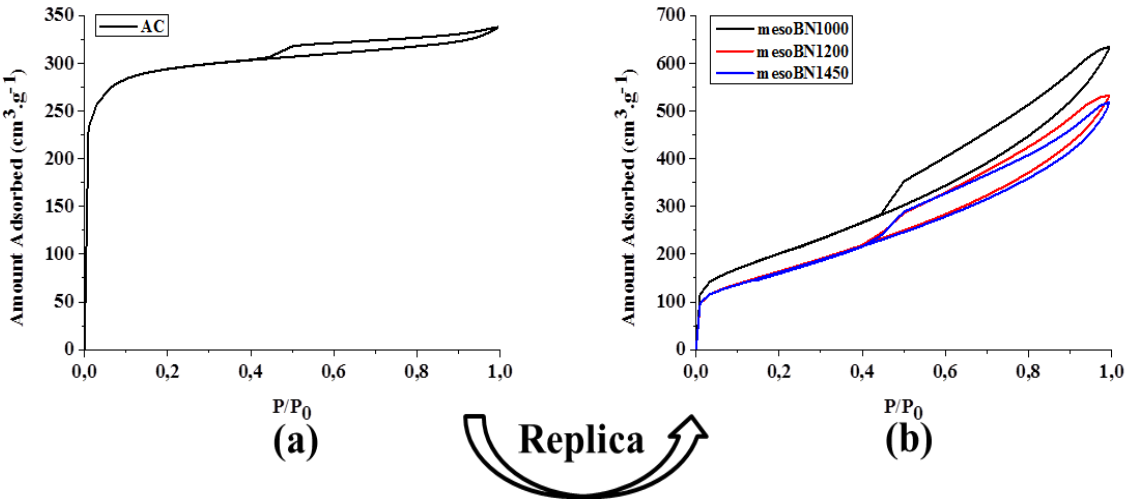

Figure III-10: N_2 sorption isotherms of (a) **AC** and (b) the 3 **mesoporous BN** samples.

We note that the three **BN samples** display similar isotherms which followed the typical behavior of type IV in mesoporous materials. Isotherms of BN samples are close to that of AC except at low relative pressure where AC displays a fast increase of adsorption reflecting a higher presence of micropores. This indicated that micropores disappeared during the replication process. Above a relative pressure P/P_0 of 0.4-0.45 and up to 1, the distinct hysteresis loops observed between the adsorption and desorption curves confirmed the presence of mesopores. It is identifiable to a type H2. According to the IUPAC nomenclature, this indicates that the BN replica consist of

interconnected mesopores which is of interest to the nanoconfinement [271]. The BET data of the BN samples are summarized in Table III-1. The latter is completed with BET data of AC.

Table III-2: BET data of **AC** and the **mesoporous BN samples**.

Sample	SSA ($m^2.g^{-1}$)	Dp (nm)	Vp ($cm^3.g^{-1}$)
AC	989	4.3	0.51
mesoBN1000	728	5.7	0.93
mesoBN1200	593	5.8	0.78
mesoBN1450	584	5.8	0.75

Even if the BET SSA of the three BN samples logically decrease compared to that of AC, we considered that they remain relatively high. In contrast, the pore diameter as well as the pore volume increases in comparison to those of AC. The pore size distribution of the four samples is represented in Figure III-11.

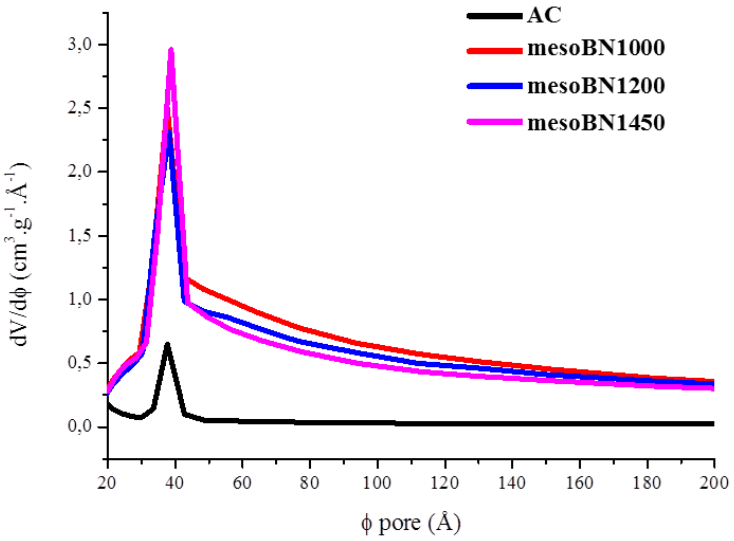

Figure III-11: Pore size distribution of **AC** and the three **mesoporous BN samples**.

The samples exhibit uniform mesopore dimensions according to the N_2 desoprtion determined by the Barrett-Joyner-Halenda (BJH) analysis. The increase of the pore diameter of PDCs in comparison to CMK-3 is usually observed [239]. Surprisingly, the pore volume values increase in BN samples in comparison to AC. If we compare the BET data between the 3 samples, the SSA, pore size and pore volume values decrease with the increase of the temperature due to the crystallization process which affect the textural properties.

In addition to the N_2 adsorption manometry, we investigated density measurements, thermal conductivity measurement and compressive strength tests of the sample **mesoBN1450**. They are reported in Table III-3.

Table III-3: Density, thermal conductivity and compressive strength data of mesoBN1450.

He density	**Heat capacity ($J.g^{-1}.K^{-1}$)**	**Thermal diffusivity ($mm^2.s^{-1}$)**	**Thermal conductivity ($W.m^{-1}.K^{-1}$)**	**Compressive strength (MPa)**
2.03	0.676	0.485	0.2295	3.3

A value of the density was found to be equal to 2.03, which is close to the theoretical value of 2.27. A compressive strength of 3.3 MPa has been found for the sample **mesoBN1450**, which is significantly lower than the values reported for dense commercial BN: 143 MPa in parallel orientation to the pressing direction and 186 MPa in perpendicular orientation to the pressing direction [272]. This is inherently attributed to the porosity level of the sample. The thermal conductivity obtained for this sample (obtained at 1450°C) is clearly not optimized. Firstly, it can be increased by increasing the temperature of pyrolysis (up to 1800°C). Secondly, others parameters such as density, microstructural organization have an effect. Such aspects will be considered in the future investigations.

The textural properties of BN samples should allow the nanoconfinement of hydrogen storage compounds according to its high porosity, the pore volume and the interconnectivity of the pores. This will be achieved in the last part of the present chapter. Before investigating nanoconfinement, we focused on the preparation of BN aerogels derived from PB based on the process described in Chapter II.

4. BN AEROGELS

4.1. Experimental part

4.1.1 Materials

The polyborazylene (PB) has been described above. The cross-linking agent used is the divinylbenzene (DVB) and was purchased from Alfa Aesar (Alfa Aesar, Ward Hill, MA, USA) (technical grade 80%). The solvent was the molecular sieved anhydrous TetraHydroFuran THF

(Sigma Aldrich, purity 99%). The presence of the catalyst is important to stimulate the reaction therefore we used the Platinum(0)-1,3-divinyl-1,1,3,3-tetramethyldisiloxane complex called Karsted Catalyst obtained from Sigma-Aldrich with 2% of Pt in xylene.

4.1.2 Preparation of PB-derived BN aerogels

The synthesis is similar to that one reported and described in the experimental part of AlN aerogels. In a typical reaction, a certain quantity of PB is mixed with DVB in a THF medium. The total volume of the solution was varied between 70 vol% and 90 vol% in the presence of Pt catalyst or not. The reaction mixture was stirred for 1 to 2 minutes and then it was transferred into the pressure reactor. Accordingly, the pressure reactor was transferred to an oven and the temperature was gradually increased from room temperature to the fixed temperature and then held at that temperature for one or several nights. The wet gels were obtained after cooling the oven to RT.

Table III-4 summarizes the experimental parameters varied during the preparation of the wet gels before pyrolysis.

Table III-4: Experimental parameters for the preparation of wet gels before pyrolysis.

	Sample*	**Vol. (%)**	**PB (g)**	**DVB (g)**	**[Pt] Mol.L^{-1}**	**T (°C)**	**Time (h)**	**Observation**
1	90-25-20 **(No catalyst)**	90	0.41	0.17	-	25	20	**No gel**
2	90-40-20 **(No catalyst)**	90	0.41	0.17	-	40	20	**No gel**
3	90-45-20 **(No catalyst)**	90	0.41	0.34	-	45	20	**No gel**
4	90-50-72 **(With catalyst)**	90	0.41	0.34	10^{-5}	50	72	**Gel cracked**
5	90-25-20 **(With catalyst)**	90	0.27	0.11	10^{-5}	25	20	**No gel**
6	90-50-72 **(With catalyst)**	90	0.27	0.11	10^{-5}	50	72	**No gel**
7	90-70-20 **(With catalyst)**	90	0.25	0.21	10^{-5}	70	72	**Gel cracked**
8	70-25-72 **(With catalyst)**	70	0.25	0.21	10^{-5}	25	72	**Viscous**

9	70-70-20 **(With catalyst)**	70	0.25	0.21	10^{-5}	70	20	**Gel**
10	90-150-20 **(With catalyst)**	90	0.4	0.33	10^{-4}	150	20	**Gel**
11	90-100-72 **(With catalyst)**	90	0.4	0.33	10^{-4}	100	72	**Gel**

*The samples are labelled as follows: dilution-temperature-aging time.

The wet gels were then supercritically dried with liquid CO_2. Hereafter we will focus only on the samples (**4**, **7**, **9**, **10** and **11**) that lead to the formation of a gel**: BN_Aero 4, BN_Aero 7, BN_Aero 9, BN_Aero 10, BN_Aero 11** after a two-step pyrolysis to 1000°C in a silica tube inserted in a horizontal furnace (Nabertherm type RS 80/500/11, Germany) which was connected to the glove box to prevent oxygen contamination of the sample. The first thermal treatment under nitrogen up to 1000°C for 2 h, followed by a second treatment under ammonia for 5 h for the carbon removal. The heating rate was 1°C.min^{-1} and the cooling rate 2°C.min^{-1}. A constant flow (120 mL.min^{-1}) of nitrogen/ammonia was passed through the tube during pyrolysis.

4.1.3 Experiments

TGA coupled with DTA was performed to investigate the polymer-to-ceramic conversion of the green aerogels. Structural investigations of the suprecritically dried aerogels were performed by means of FTIR spectroscopy (Nicolet Magna-IR 550 Fourier transform-spectrophotometer 5Nicolet Instrument Co. USA in a KBr matrix).

The porosity of the ceramic aerogels was characterized by:

BET: N_2 adsorption-desorption isotherms were carried on a Model Sorptomatic 1900 analyser (Fisons). Before adsorption measurements, all samples were outgassed for 4 h at 150°C in the degas port of the adsorption analyzer. The Brunauer.Emmett.Teller (BET) method was used to calculate the specific surface area. The pore-size distribution was derived from the adsorption branches of the isotherms using the Barrett.Joyner.Halenda (BJH) method. The total pore volume (V_p) was estimated from the amount of N_2 adsorbed at a relative pressure of $P/P_0 = 0.99$.

Scanning electron microscopy: SEM pictures were taken with a Hitachi S800 microscope coupled with EDX microanalysis system with IDFix and MaxViwe softwares from SamX. Maximum resolution of 2 nm at 30 kV for a working distance of 5 mm, range of acceleration tension between 1 to 30 kV, sample deplacement from 0 to 25 mm in X and Y axes, from 5 to 30 mm in Z axes. Tilt

angle from -5° to +45°, complete rotation of 360°. Samples were mounted on copper tape and sputtered with (10 Å of a Pd/Au mixture) to prevent charging during the observation.

4.2. Results and discussion

The approach to prepare BN aerogels consists in using a Pt-catalyzed reaction between the preceramic polymer (PB) and the cross-linking agent (DVB). This cross-linking is performed in highly diluted conditions.

From the same concept of hydrosilylation (Si-H+ $H_2C=CH_2 \rightarrow Si-CH_2-CH_3$) [273] or hydroalumination (see AlN aerogels, **Al-H+ $H_2C=CH_2 \rightarrow$ Al-CH_2-CH_3**), we expect hydroboration reactions (**B-H+ $H_2C=CH_2 \rightarrow$ B-CH_2-CH_3**) between the reactive B-H bonds of PB and the C=C bonds provided by the DVB. Different compositions were prepared by modifying the quantity of reactants, the amount of solvent in order to study solutions with a volume of solvent in the range 70–97 vol%, the amount of catalyst, the temperature and the time of heating. The samples are labeled as follows: first we indicate the vol% of THF, second the temperature and third the time. From Table III-2, we observed that a reaction (gelation) occurs only in presence of Pt and at temperatures higher than the boiling temperature of the solvent. We noticed for the sample **4** the formation of a powder-like foam instead of a complete gel, therefore, all the polymeric network vanished along with the gel network formation. These results suggest that polymer particles are initially formed by a catalytically activated cross-linking process at a minimal temperature (70°C) with a subsequent growth leading to the final gel formation [273].

Figure III-12 displays the images of the wet gels before drying and of the green aerogels after the CO_2 supercritical drying. No particular shrinkage of the gels was observed after drying.

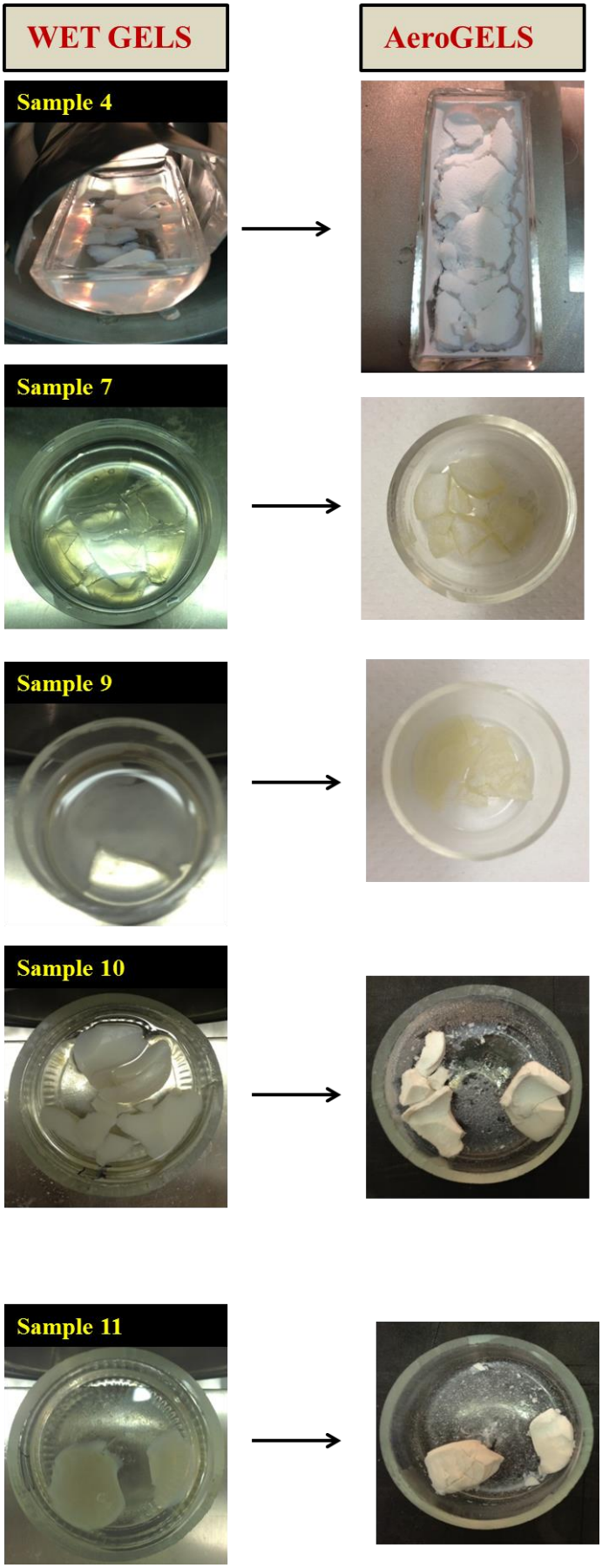

Figure III-12: Images of the wet and corresponding aerogels.

The FTIR spectra (Figure III-13) exhibit the signals attributed to PB: $\nu_{(N-H)}$=3425 cm^{-1}, $\nu_{(B-H)}$=2500 cm^{-1}, $\nu_{(B-N)}$=1435 cm^{-1} and $\delta_{(B-N)}$=890 cm^{-1}. In comparison to PB, the band characteristic to B-H bonds (2500 cm^{-1}) is significantly reduced in derived wet gels (after adding DVB). This confirms the participation of B-H units in the process of gelation. Furthermore, a band around 1180 cm^{-1} appeared. It is attributed to B-C bonds, most probably due to the occurrence of hydroboration reactions between B-H units present in PB and vinyl groups present in DVB. Residual vinyl groups remain in the aerogels. The corresponding band appears at 1600 cm^{-1}. Nevertheless the spectrum of the sample **4** lacks the presence of the B-H bonds this can be due to a reaction between the remaining B-H (that did not cross-link) with moisture which can explain the foaming observed before. It should be mentioned that the reaction occurring at 100 (sample **11**) and 150 °C (sample **10**) inherently involves the self-crosslinking of PB through deshydrocouling between BH and NH units forming B-N bonds. This also can explain the disappearance of the B-H and N-H bond bands.

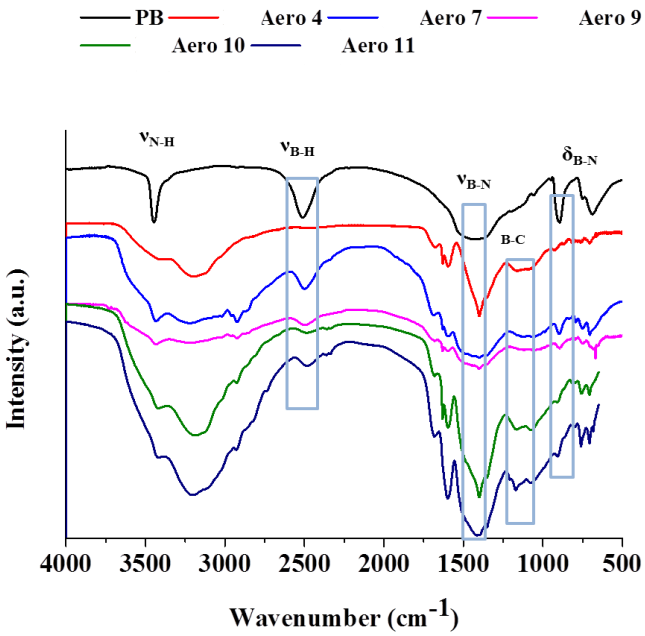

Figure III-13: FTIR spectra of **PB** and samples **4, 7, 9, 10** and **11.**

After characterization of the aerogels, thermogravimetric analyses (TGA) have been performed up to 1450°C under N_2. They have been coupled with differential thermal analyses (DTA). Only the sample **9** is presented here (Figure III-14) as a representative results, since the TGA data from other samples were similar.

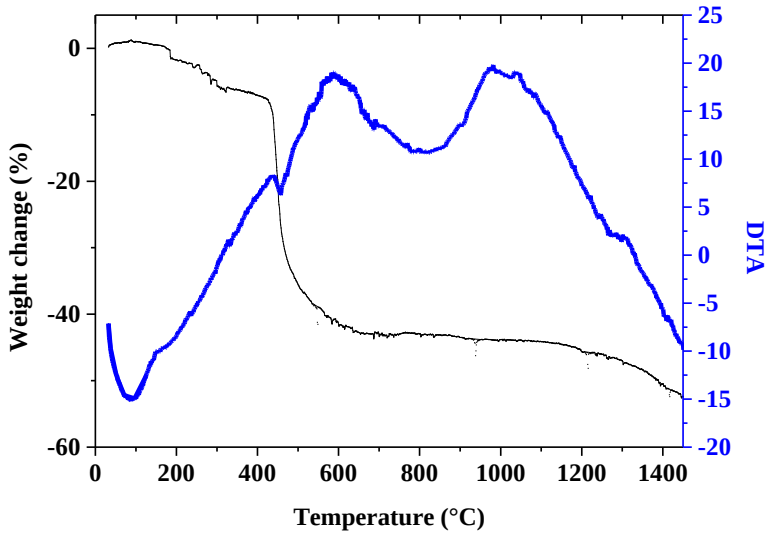

Figure III-14: TGA and DTA curves of **9** up to 1500°C under N_2 with a heating rate of 10°C.min^{-1}.

A weight loss of 55% was measured after TGA at 1500°C for the sample **9.** The majority of the weight loss is associated with the decomposition of DVB from 390 to 500°C. The final weight loss is closely related to the quantity of DVB used during the experiments. After decomposition of DVB, the TG profile is similar the TG profile of PB reported in the first part of the present chapter. Weight losses ranging from 50 to 65% have been measured for all the samples after decomposition at 1450°C. The DTA curve allowed us to distinguish four steps during the transformation of green aerogels into ceramic aerogels.

As already done for AlN aerogels, we deliberately applied a two-step pyrolysis procedure: a first step under nitrogen up to 1000°C then a second step under ammonia up to 1000°C. The evolution of the sample **10** is illustrated in Figure III-15. After pyrolysis to 1000°C under N_2 of green aerogels, black aerogels are obtained. The black color is caused by the presence of carbon in BN which disappears after heat-treatment under ammonia. We can observe that the monolithic form is retained in the final material labeled **BN_Aero-10**.

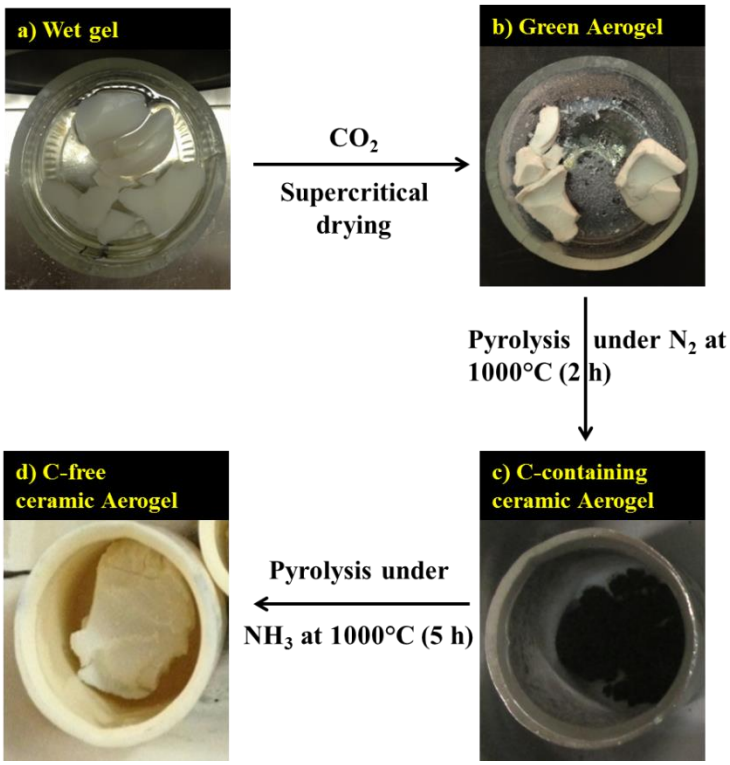

Figure III-15: Photos of the **BN_Aero-10** at the 4 stages: a) Wet gel, b) Green gel, c) C-containing ceramic aerogel and d) C-free ceramic aerogel.

All samples have been characterized by the N_2 adsoprtion-desorption technique.

The N_2 adsorption–desorption isotherms are provided in Figure III-16. The isotherms for the samples display different profiles. This means that we are able to prepare BN aerogels with different textural properties.

The sample **BN_Aero-4** displays a typical isotherm of a poorly porous material with a hysteresis loop of type H3 which is not characteristic of a defined mesoporosity. The sample **BN-Aero-7** displays an isotherm characteristic of mesoporous samples (type IV) with a hysteresis loop in the relative pressure P/P_0 range (0.42 to 1) of the type H2, typically attributed to interconnected pores. The fast increase of the adsorption at low relative pressure is attributed to the presence of relatively large portion of micropores. The sample **BN-Aero-9** displays a more complex isotherm (Type II/IV) with a hysteresis loop of type H2 characteristic of mesoporous material. The isotherm of the sample **BN_Aero-10** is similar to that one of the sample **BN_Aero-9**. This observation was rather speculated from the physical appearance of the foamed sample when recovered from the supercritical drying. The sample **BN_Aero-11** displays an isotherm characteristic of type IV with an hysteresis loop of type H4 characteristic of a microporous compound. This is confirmed by the fast increase of the adsorption at low relative pressure.

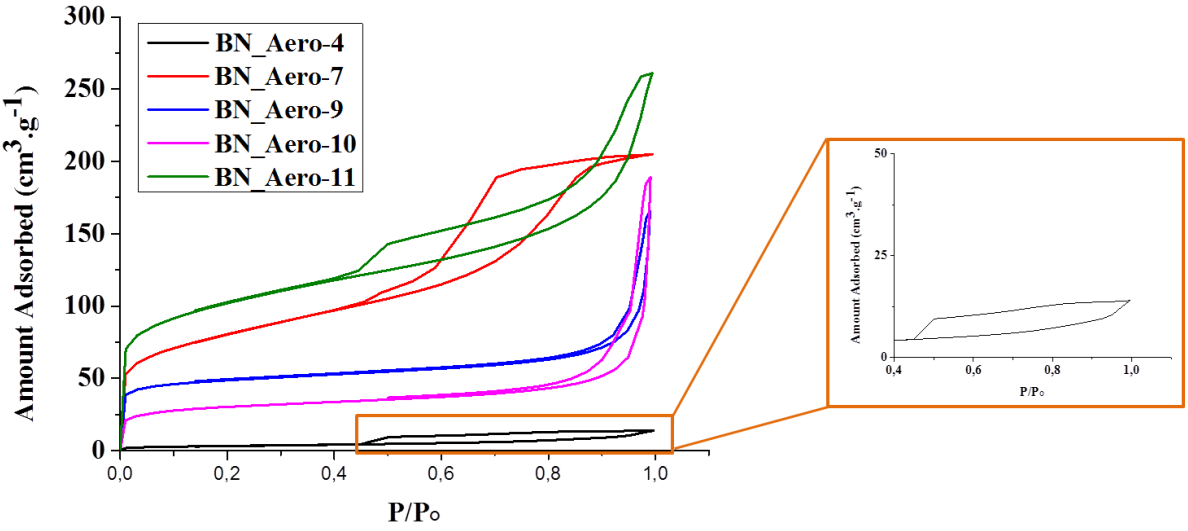

Figure III-16: N_2 adsoption-desorption isotherms of the **BN aerogels**.

Table III-5 reports the BET data calculated from the isotherms represented in Figure III-16.

Table III-5: BET data of the **BN aerogels**.

Sample	SSA ($m^2.g^{-1}$)	Dp (nm)	Vp ($cm^3.g^{-1}$)
BN_Aero-4	12	8	0.02
BN_Aero-7	285	5.9	0.32
BN_Aero-9	166	18	0.15
BN_Aero-10	105	27	0.14
BN_Aero-11	358	7.5	0.36

Let us discuss on the effect of the synthesis parameters. As the percentage of solvent increases from 70 vol% (**BN_Aero-9**) to 90 vol% (**BN_Aero-7**), the hysteresis loops shift towards higher pressure regimes, as a result of mesopores increasing and pore size broadening. Furthermore, the BET SSA as well as the pore volume decreases by 20 and 10%, respectively (Table III-5). The increase of the temperature (**BN_Aero-7 → BN_Aero-10)** has a tendency to increase the size of the mesopores, whereas the BET SSA and the pore volume significantly decreased from 285 to 105 $m^2.g^{-1}$ and from 0.32 to 0.14 $cm^3.g^{-1}$, respectively. It is therefore probable that the increase of the dilution of the PB-DVB-Pt mixture or the temperature have a significant influence on the gelation process. The nucleation rate is reduced resulting in the formation of larger particles and larger pores.

However, these conclusions could not fit for the sample **BN_Aero-4** that displays the lowest BET SSA and pore volume values. This sample has clearly lost all his porosity as discussed earlier.

Among the BN aerogels that have been characterized, we selected the sample **BN_Aero-9** to investigate the effect of the temperature of annealing of BN aerogels on the evolution of the BET parameters. The sample **BN_Aero-9** at 1000°C has been annealed under N_2 at 1450°C to generate the sample **BN_Aero-9-1450**. As we demonstrated with mesoporous BN monoliths, the SSA of **BN_Aero-9-1450** decreased from 166 to 125 $m^2.g^{-1}$ according to the fact that the crystallization of BN occurs leading to a progressive collapse of the porosity. Surprisingly, the pore volume and pore diameter increased at 1450°C (Table III-6).

Table III-6: BET data of **BN_Aero-9** and **BN_Aero-9-1450**.

Sample	SSA ($m^2.g^{-1}$)	Dp (nm)	Vp ($cm^3.g^{-1}$)
BN_Aero-9	166	18	0.15
BN_Aero-9-1450	125	34	0.54

Using the same strategy we have applied to prepare AlN aerogels, we have prepared BN aerogels by combining the PDCs and the aerogels technology using the CO_2 supercritical drying and PB as BN precusor. BN aerogels with relatively high BET SSA could be generated according to an appropriate choice of the synthesis parameters. The BET SSA values are lower (358 $m^2.g^{-1}$) than those obtained with AlN aerogels (511 $m^2.g^{-1}$) but we can propose BN aerogels with a larger panel of porosity including microporous aerogels and mesoporous aerogels. Similarly to mesoporous BN monoliths, we investigated the use of BN aerogels for the nanoconfinement of ammoniaborane.

5. NANOCONFINEMENT OF AMMONIABORANE

5.1. Introduction

We discussed in the literature part (Chapter I) the interest of the nanoconfinement of hydrogen carriers such as ammoniaborane (AB) to increase their kinetics of dehydrogenation through their thermolysis. It has been reported that the reaction mechanism to explain the thermolytic decomposition of AB consists in 3 steps: i) the induction where slow dehydrogenation starts along with some structural modification, ii) the nucleation with the formation of DADB, and iii) the growth step where a reaction between DADB and AB occurs releasing thus all the hydrogen [60]. The solid residue of the thermolysis is composed of PolyAminoBorane PAB, PolyIminoBorane, PIB and PolyBorazylene PB as a result of the evolution of gaseous by-products of the type borazine,

ammonia and hydrogen. Therefore, it seems important to promote the hydrogen evolution without other undesired by-products while polyborazylene is the only residue in order to facilitate the regeneration. We think that the nanoconfinement strategy could be a solution, in particular using BN as host materials. This is demonstrated after.

5.2. Experimental part

5.2.1 *Materials*

The chemicals used during the impregnation of AB inside the porous template are listed below: AB (Sigma Aldrich, purity ~97%); dry THF over molecular sieve (Sigma Aldrich, 99% purity). All products used are stored under controlled atmosphere of argon. As for all the experimental part in this PhD work, the solid precursors are processed and stored in an argon-filled glove-box (MBraun M200B, H_2O <0.1 ppm O_2 <0.1 ppm) and all the synthetic steps are performed in Schlenk-type long tubes under vacuum-argon mixed ramp. All the glassware was first dried overnight in an oven (120°C) and then degassed under vacuum for 30 min before use. The solvents, stored on molecular sieve are collected under argon flux with glass syringes previously conditioned.

5.2.2 Nanoconfinement protocol

Our objectives were firstly to work with a volume of THF equivalent to the pore volume of the support, and secondly to be at the limit of solubility of AB (25 mg of AB in 0.112 mL of THF), and thirdly to prevent any possible decomposition of AB at room temperature. Thus, 200 mg of the porous support were outgassed overnight at 150°C under dynamic vacuum. While cooling to 0°C, a solution of 200 mg of AB in 1 mL of THF is prepared. This solution of 1 mL, by the means of a syringe, is injected into the porous sample under static vacuum (AB:porous host weight ratio =1).. By capillary action, the solution of AB quickly fills the pores of the host material, this being evidenced by a remarkable sign of effervescence. The tube is then placed in an ultrasonic bath at 0° C for 15 min. This step optimizes the impregnation of the AB solution inside the porosity. When effervescence ceases, the sample was dried under dynamic vacuum for 30 min. The impregnated material is then left under static vacuum for 48 h at 0°C. Then the sample is vacuum-dried to remove the solvent and rapidly washed with THF to dissolve the residual AB left outside of the monolith. Finally, the sample at 0°C was dried for 48 h under dynamic vacuum to remove any solvent traces. The sample obtained was stored in a sealed vial under an inert atmosphere in the freezer at 0°C. The composites are labeled as follows: **AB@porous host**.

5.2.3 Experiments

FTIR spectroscopy (Nicolet Magna-IR 550 Fourier transform-spectrophotometer 5Nicolet Instrument Co. USA in a KBr matrix) and X-ray diffraction (Philips PW 3040/60 X'pert PRO X-ray diffraction system operating at 30 mA and 40 kV from 10 to 90° with a step size of 0.0167, using a Kα1 of copper as source) were employed to confirm the successful impregnation of AB inside the pores of the host.

The TGA were performed on a TAG/SDTA 851 Mettler TOLEDO apparatus, under dynamic nitrogen flow (50 mL.min^{-1}). A heating rate of 5 °C.min^{-1} from 25 up to 200 °C was applied. Aluminum crucibles of 100 µL were filled in a glove-box under a controlled atmosphere of argon. Prior to analysis, the cover of the crucible is pierced with a fine needle to allow the discharge of gases generated during the temperature rise. A weight between 9 and 10 mg of the product was analyzed. The exit of the TGA furnace is connected to a µ-chromatograph Agilent µGC M200 having three columns: Molecular Sieve column (length 10m) to separate the hydrogen, OV1column (length 8m) devoted to the analysis of possible secondary gas such as borazine, ammonia and diborane, and Poraplot U (length 8m). The mass spectrometer was connected connected to the OV1. The carrier gas of the sieve column was argon, while for the two other columns we used helium. The pre-column of the molecular sieve column is also a PPU (3m in length); its objective is to slow down the heavy compounds such as H_2O, and to let the light compounds such as H_2 pass through the molecular sieve column. The temperature OV1 column was set at 90 °C while the molecular sieve is set at 70 °C. The analysis time was 75 s, while the injection time was set at 250 ms. The pressure in the molecular sieve column was set at 28 Psi whereas the OV1 column at 30 Psi. Helium and argon were used as carrier gases for the separation of the borazine and hydrogen, respectively. The transfer line between the TGA / µGC inlet is heated to 90 °C and the inlet of µGC at 80°C.

5.3. Results and discussion

In a previous work [274] our group demonstrated the interest of activated carbon to destabilize AB. Based on the same procedure, we investigated the nanoconfinement of AB in the mesoporous BN monoliths and BN aerogels we have described previously.

Firstly, we investigated FTIR and XRD in order to evaluate the efficiency of the impregnation protocol evaluate the quality of the AB in our BN samples. We performed these experiments with the mesoporous BN monoliths prepared at 1000 and 1450°C as well as the BN aerogel. Hereafter, we present the results concerning the composites **AB@mesoBN1450.** For **AB@mesoBN1000** and **AB@BNAero9**, all of the results are given in Annex B.

The FTIR spectra for neat AB and the composite **AB@mesoBN1450** are presented in Figure III-17. The composite exhibits the B-N-B bending around 800 cm^{-1}, and the B-N stretching around 1390 cm^{-1}. The characteristic AB bands are almost absent in the spectrum of this composite suggesting the appropriate impregnation of AB into the pores of the BN sample.

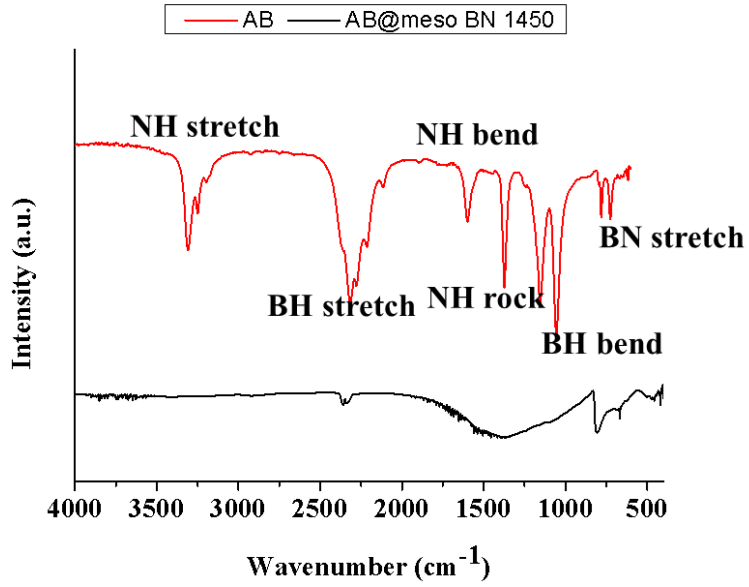

Figure III-17: FTIR spectra of **AB** and **AB@mesoBN1450**.

The XRD patterns of neat AB and the sample **AB@mesoBN1450** are presented in Figure III-18.

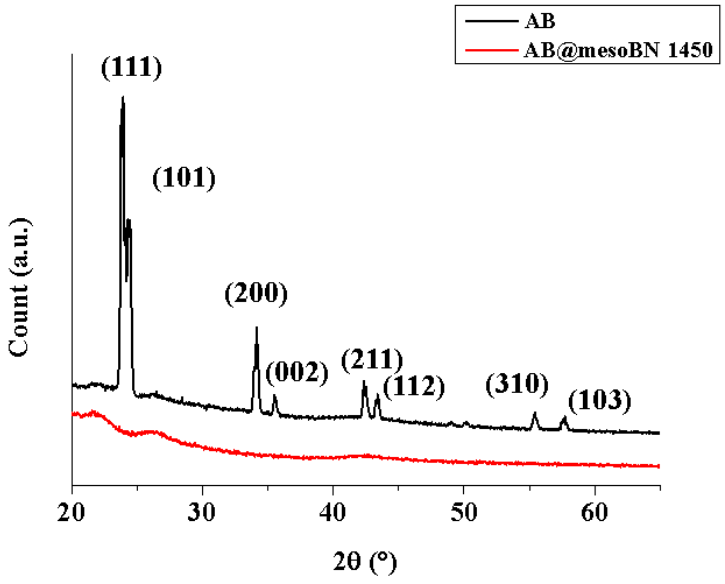

Figure III-18: XRD patterns of neat AB and **AB@mesoBN1450.**

Compared to the XRD pattern of neat AB, that of the composite do not show any characteristic peaks of AB, confirming that the hydride was incorporated into the pores of the support. No residue remained unconfined on the external surface of the host material. Therefore, our procedure consisting in i) impregnating the host material under static vacuum for 48 h, ii) washing the composites to remove all the AB particles at the external surface, and iii) drying the composite, is controlled. This allowed us to discuss on the TG-MS results reported below, without any doubts on the lack of reproducibility of the impregnation procedure.

The decomposition of the composite **AB@mesoBN1450** was investigated by TGA and DSC (Figure III-19-a and b), which are routine techniques in our lab for screening the chemical hydrogen storage materials. The decomposition was compared to the behavior of neat AB under identical experimental conditions (N_2 flow, from room temperature to 200°C, with a heating rate of 5°C.min^{-1}). It is worth mentioning that, unlike neat AB; **AB@mesoBN1450** did not foam during the heat-treatment nor expand.

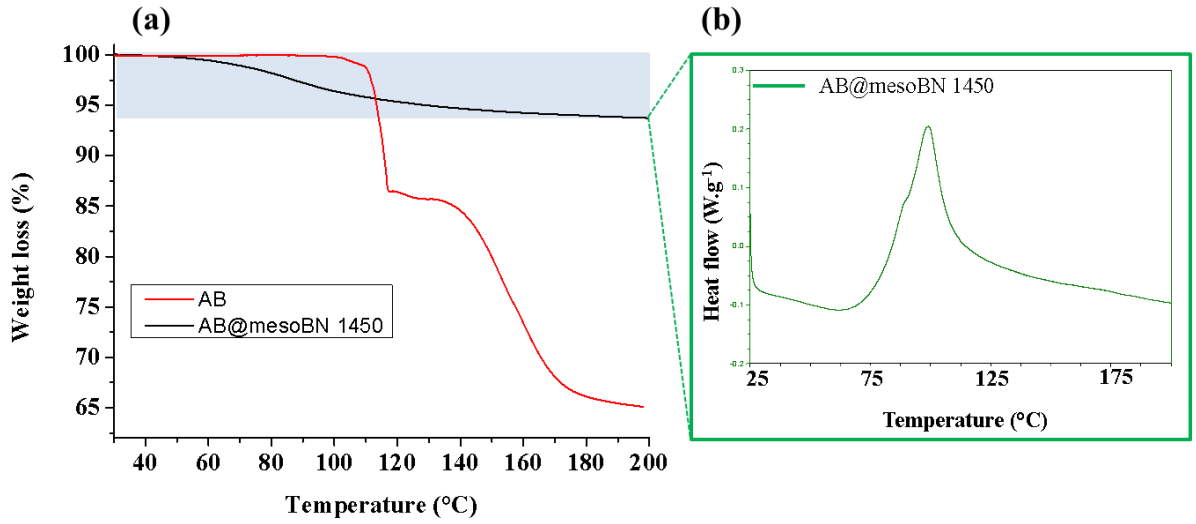

Figure III-19: (a) TGA curves of neat AB and **AB@mesoBN1450** and (b) DSC curve of **AB@mesoBN1450** up to 200°C under N_2 with a heating rate of 5°C.min^{-1}.

We can clearly see that the weight loss of the composite is almost linear. The dehydrogenation starts at around 35-40°C with a total weight loss of 6% at 200°C. In contrast; the neat AB remains stable up to 110°C. The temperature range 25-110°C is a screening criterion as above 110°C the first decomposition of neat AB is almost achieved.

Another important observation from the TGA result is that **AB@mesoBN1450** is stable at RT. Accordingly, the stability of the composite considered here (**AB@mesoBN1450**) is clearly attributed to the absence of surface $H^{\delta+}$ which is not the case in active carbon for example which

contain OH groups that react with BH units in AB [247]. This is not the case of the other porous BN hosts we described earlier in this chapter, namely **mesoBN1000** and **BN_Aero-9.** They are unstable at room temperature. Indeed, they were prepared at 1000°C and they probably still contain reactive groups (NH) on their surface (because the PB-to-BN conversion is not fully achieved at 1000°C as shown through TGA in the first part of the present chapter) which are likely to participate to the dehydrogenation of BH_3 of AB through Lewis acid-base interactions at low temperature. As a consequence, for the composites obtained from these BN hosts, it is no longer an exclusive effect of nanoconfinement that took place but also a contribution of the surface hydrogens of BN. This was particularly true in the case of **AB@mesoBN1000.** In the case of **AB@BN_Aero 9**, a low weight loss is found (1.8 wt%) probably because the porous volume of the aerogel is not high enough to infiltrate high amounts of AB. Studies are in progress to better understand the role of the external and internal surfaces of BN as well as the role of the porosity that is obviously a key property for nanoconfinement. However, it is to mention that the task is arduous by the fact that the BN host and the dehydrogenated product stemmed for thermolyzed AB have similar responses to spectroscopic analyses.

The positive effect of the nanoconfinement in the case of **AB@mesoBN1450** is also confirmed by the DSC curve (Figure III-19-b). Indeed, the peak temperature of the AB decomposition is shifted towards lower values (98°C instead of 110°C for neat AB), which indicates a change in the thermodynamics of the thermolysis [275]. No endothermic melting peak is depicted; this is indicative of the occurrence of a direct solid-state decomposition.

Based on the observations of the µGC results, we did not detect any trace of borazine nor ammonia. Only H_2 was detected in the case of the three composites and in our experimental conditions. In Figure III-20, the MS profile of **AB@mesoBN1450** is presented (see Annex B for the other and aforementioned composites). The MS results confirm the efficiency of the mesoporous BN1450 as nanoscaffold to overcome one of the drawbacks mentioned in the literature, that is, the emission of undesired by-products (like borazine, ammonia, aminoborane) that are harmful to the low-temperature PEMFCs [63, 276].

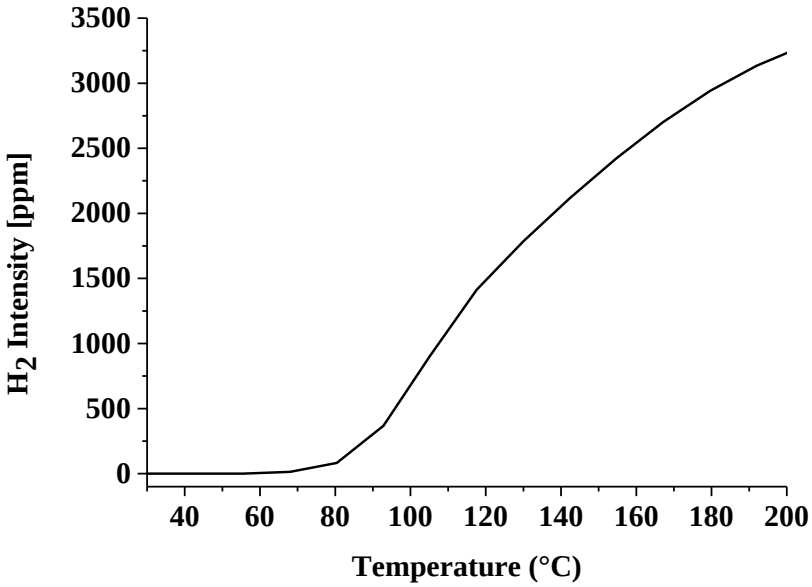

Figure III-20: Cumulative area of the peak of H_2 detected by mass spectrometry for **AB@mesoBN1450.**

Based on Figure III-20, we can clearly see that the dehydrogenation do not occur before 55°C, this goes in line with the observations made from the TGA curve (Figure III-19). To quantify the hydrogen release at 200°C, we should have an exact information regarding the quantity of AB we incorporated in the BN host. Unfortunately, today and in our conditions, we are unable to determine exactly how much AB we have in the composite.[1] Assuming that we infiltrated all the porosity of the BN host, we could expect a weight ratio 1:1 in **AB@mesoBN1450** composite. Then, the quantity of H_2 produced would be approximatively 2 moles of H_2 per mole of AB or 1 mole of H_2 per mol of **AB@mesoBN1450**. We exploited the µGC-MS results to get a quantitative evaluation of the amount of H_2. Calibration was performed with a gas mixture Ar-H_2 (2000 ppm). Almost 1 mole of H_2 per mole of AB was found to evolve at 200°C, which is well below the expected 2 moles. This is in fact an indication of the fact that the AB infiltration did not lead to a weight ratio 1:1. The AB content should be lower. In fact the infiltration was conducted in solution, therefore the amount of AB infiltrated is limited by the presence of the solvent molecules, in addition to the washing and drying steps that, even though are of major importance for recovering a well-impregnated monolith, can be the cause of dissolving some AB particles. Let us assume that the amount of AB is only half of the

[1] The routine techniques are not appropriate to determine the weight of AB really infiltrated into the BN host. Elemental analysis by ICP and EDX are not appropriate as solvation in highly acidic solution is required for the former technique (risk of explosion due to fast H_2 release) and AB evolves under the electron beam for the latter. Works are in progress in our group in order to set up and then optimize a procedure for determining the AB content into a BN-based host.

targeted weight. Hence, the mole number of H_2 per mole of AB was calculated to be 1.65 at 200°C, which is closer to the target. Accordingly, we believe that the infiltration of AB has been inefficient in part. Works are in progress to better quantify the infiltration of AB but also to better understand the fact that the infiltration was less efficient than for a carbonaceous host [274].

Nonetheless, we are more interested in the hydrogen generated between 80 and 100°C for PEMFCs applications. Therefore, as an attempt we record 0.5 equiv. of hydrogen at 100°C. Such result, even though is far from the expectations of DOE, but is still interesting because, the composite was found to i) be stable at RT, ii) decompose at low temperatures, iii) release pure H_2, and iv) avoid expansion and foaming. These improvements are exclusively attributed to the nanoconfinement.

6. CONCLUSION

In this chapter, we presented two methods to obtain porous BN materials.

In the first method we were interested in preparing hexagonal **mesoporous BN monoliths** *via* a **templated synthesis** using **polyborazylene** as BN precursor and **activated carbon monoliths** as hard template. The BN monoliths exhibit a BET SSA ranging from 728 to 584 $m^2.g^{-1}$ and a total pore volume from 0.93 to 0.75 $cm^3.g^{-1}$, depending on the final annealing temperature with a narrow pore size distribution centered at 5.8 nm. These monoliths were used as nanoscaffolds of AB with the objective to improve its dehydrogenation properties. The as-formed composite **AB@mesoBN1450** is able to liberate H_2 at low temperatures (around 50°C), whereas AB confined in carbon mesoporous hosts starts to dehydrogenate immediately. Over the range RT-200°C that we considered in our conditions, the H_2 generated is pure, no traces of by-products were detected. Considering the effective regenerability of AB, these results suggest that our BN-based composite material is a potential safe and practical hydrogen storage material.

In a second method, we used the same protocol we applied in Chapter II for the elaboration of **BN aerogels**. Mixing the polyborazylene as BN precursor with DVB as cross-linking agent in highly diluted solutions in presence of platinum led to porous monolith-like aerogels with SSA as high as 358 $m^2.g^{-1}$ and a porous volume of 0.36 $cm^3.g^{-1}$ After pyrolysis to 1000°C under nitrogen The temperature, the presence of catalyst and the highly diluted medium, were the key parameters to obtaining the most porous BN aerogel. The latter did not show exceptional hydrogen uptake after the nanoconfinement of AB. However, further characterizations are under investigation to optimize the process and generate materials with higher BET SSA.

IV-

ORDERED MESOPOROUS SiAlCN AND Si_3N_4 CERAMICS FOR HYDROGEN GENERATION

IV- Ordered Mesoporous SiAlCN AND Si_3N_4 ceramics for hydrogen generation 140
1. Introduction 144
2. Preparation of Pt supported ordered mesoporous SiAlCN ceramics 149
2.1. Experimental part 149
2.1.1 Materials 149
2.1.2 Preparation and characterization of polyaluminosilazanes 150
2.1.3 Nanocasting and ceramic transformation 151
2.1.4 Preparation of of nanocatalysts 151
2.1.5 Experiments 152
2.2. Results and discussion 152
2.2.1 Synthesis and characterization of polyaluminosilazanes 152
2.2.2 PASZ-to-SiAlCN conversion 154
2.2.3 Characterization of ordered mesoporous SiAlCN 159
2.2.4 Monodispersed Pt nanoparticles supported on ompSiAlCNxy supports 169
2.2.5 H_2 evolution from $NaBH_4$ over Pt/ompSiAlCNxy nanocatalysts 172
3. Preparation of Pt supported ordered mesoporous Si_3N_4 173
3.1. Experimental part 175
3.1.1 Materials 175
3.1.2 Preparation of ordered mesoporous Si_3N_4 175
3.1.3 Preparation of nanocatalysts 176
3.1.4 Experiments 176
3.2. Results and discussion 177
3.2.1 Preparation and characterization of ordered mesoporous Si_3N_4 177
3.2.2 Characterization of Pt/omp-Si_3N_4 nanocatalysts 183
3.2.3 H_2 evolution from $NaBH_4$ over Pt/ompSi_3N_4 nanocatalysts 186
4. Conclusion 188

1. INTRODUCTION

Proton exchange membrane fuel cell-based (**PEMFC**) systems are attractive alternatives to current energy conversion technologies due to their potential to directly convert chemical energy (hydrogen) to electrical energy, their high efficiency, fast responses to loads and potentially zero emissions except water [277]. They consist of three subsystems: fuel cell stack, hydrogen generator, and hybrid power management system (Figure IV-1).

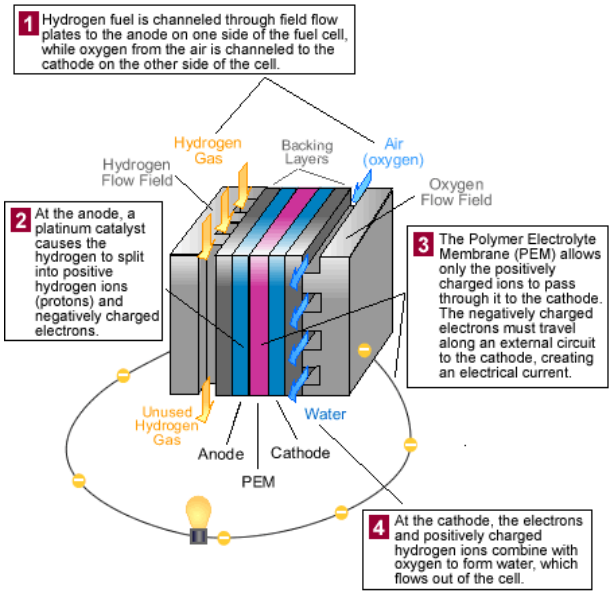

Figure IV-1: PEMFC system [278].

They are stable output power for vehicular and mobile applications. However, despite recent advances, there are still several issues which limit the widespread use of the fuel cell technologies. One of the most crucial issues is the hydrogen source to meet the overall energy requirements for civil vehicle applications such as for small Unmanned Aerial Vehicles (UAVs) commonly known as drones. Actually, ~95% of hydrogen is produced from hydrocarbons such as methane according to the following reaction:

$$CH_4 + 2H_2O = CO_2 + 4H_2 \qquad \Delta H_{298}=165\ KJ.mol^{-1} \quad (IV\text{-}1)$$

This inherently involves the evolution of CO_2. To this purpose, liquid-phase hydrogen carriers are attractive, owing to some very advantageous features [279]: they are in liquid state (especially in aqueous solution), and thus can be easily handled, they can produce hydrogen "on-demand", they are relatively stable in ambient conditions, non-flammable, non-toxic, they are hydrogen-rich compounds and side products are recyclable. A typical and widely-investigated example is the alkaline solution of sodium borohydride **$NaBH_4$** [280].

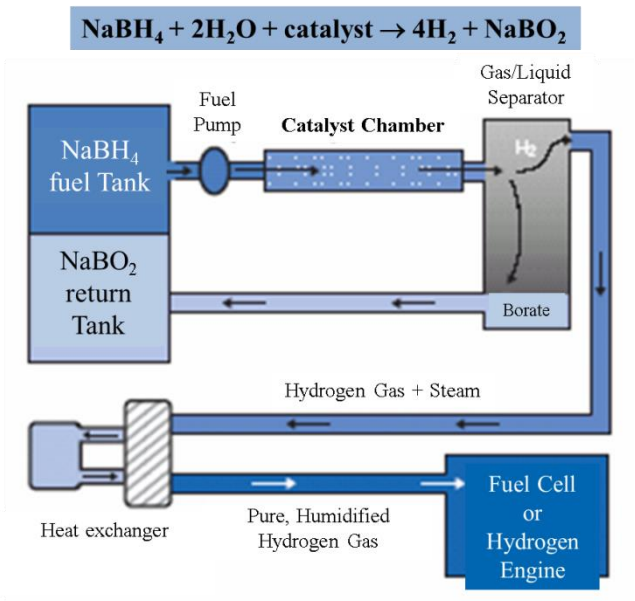

Figure IV-2: $NaBH_4$ as H_2 source.

Sodium borohydride $NaBH_4$ carries 10.8 wt% of hydridic ($H^{\delta-}$) hydrogen. Hydrogen can be easily released by reaction with the protic ($H^{\delta+}$) hydrogen of water. In other words, water provides half of the hydrogen generated. The hydrolysis can take place at temperatures as low as 5-10°C, but has to be accelerated by a metal-based catalyst [281]. In such conditions, the kinetics are low and the storage capacities much limited because of the use of an excess of water. Effective gravimetric hydrogen storage capacities up to 9 wt% can be achieved in the presence of a supported catalyst [282]. However, such attractive performances imply operating conditions such as high temperatures (80-100°C) or high pressures (> 6 bars H_2). It therefore appears that the metal and the support play a key role in the production of H_2 from $NaBH_4$ to withstand these harsh conditions. Various metals as active phases have been employed. Cobalt (Co) has shown to be a cheap solution but it suffers from instability over successive hydrolysis cycles [22]. Late transition metals like Ruthenium (Ru) or Platinum (Pt) are generally more active and stable [283] but the cost issue is a limiting factor. Therefore, application requires significant reduction in the amount of expensive Pt while catalytic performance is expected to be enhanced. It is therefore crucial to use very low amounts of Pt (≤1 wt%) in the form of nanoparticles (NPs) to optimize the catalytic activities. However, the nanoparticle agglomeration is problematic during the long-term catalytic process, bringing a serious issue to the catalyst stability. Consequently, the active surface areas of Pt NPs are continuously destroyed, resulting in continuous catalyst degradation with aging. An efficient solution is the immobilization of the catalyst over a support. The resulting dispersed particles exhibit a much higher total surface area per unit weight than the bulk metal, thus allowing better utilization of the metal as a result of dispersion. In that case, the overall performance of the material can be readily optimized

by suitable control and selection of the support in terms of porosity (order, distribution of the size, shape and volume of the pores), shape (powder, monolith) and composition. Alumina, silica, zeolites and MOFs are generally used as catalyst supports for various catalytic reactions.

In general, the specific surface area, the pore volume, the arrangement and type of the porosity and the Lewis and/or Brønsted acidity of materials are primarily considered when selecting a support for catalysts to be used in H_2 generation. The thermal conductivity, mechanical strength and especially the chemical resistance toward the reaction medium are not always viewed as the most important properties. However, the application of MOFs, zeolites and metal oxides in catalytic hydrolysis is somehow limited because their hydrothermal stability may turn to be poor in harsh environment, leading in general to the collapse of the porous structure. To address the issue of highly stable supports to produce H_2 from the alkaline solution of $NaBH_4$, alternative support materials should be explored.

Carbonaceous supports are an alternative solution. However, silicon carbide (**SiC**) and silicon nitride (**Si_3N_4**) attract much more attention, primarily due to their good mechanical and chemical properties, their high thermal stability and relative high thermal conductivity [284]. However, these materials are usually applied as non-porous materials [285]. To control the size and shape of the particle and avoid the sintering of the metals which inherently occurs on non porous supports, such materials in porous form are required.

In our group, we have along expertise in the preparation of silicoboron carbonitride (**SiBCN**) materials (as dense [211] and mesoporous [107, 251, 286] materials) with the objective to modify the properties of the silicon nitride and silicon carbide phases in many aspects. According to the identification of turbostratic BN(C) around Si_3N_4 crystals, the reaction between free carbon and Si_3N_4 is shifted to T >1484°C. Therefore, they exhibit improved microstructural stability at high temperatures in an inert atmosphere in comparison to boron-free SiCN systems [286]. Despite this advantage, their stability in harsh conditions remains an open question. The exceptionally low oxidation rates of SiBCN, as initially reported [208, 287] have been underestimated for several reasons, for example the low oxide/ceramic volume ratio, the B_2O_3 volatilization, the water-sensitive borosilicate formation and its viscous flow. Within this context, their use as catalytic support for reactions occurring in harsh conditions such as in presence of the alkaline solution of $NaBH_4$ could be problematic.

The addition of aluminum to silicon-based ceramics contributes to the improvement of their hydrothermal stability. As an illustration, it has been shown that the addition of Al to SiNO systems

forming SiAlON ceramics results in an improved thermal and chemical stability in oxidizing atmosphere, in particular in the presence of corrosive species and water vapor, in comparison to aluminum-free SiNO systems [191]. Similarly, the addition of aluminum to SiCN(O) results into a non parabolic oxidation curve (at T ≥1000°C), which decreases more rapidly with time, down to a negligible level. This has been well-demonstrated by An and coworkers [192]. At 1400°C, a stationary parabolic rate is observed after 20 h, with parabolic constants ~10 times lower than those of the Al-free SiCN(O) systems. Authors suggested that the remarkably low oxidation rates of these materials were attributed to the lower permeability of the formed oxide layer to molecular oxygen, which resulted from the incorporation of Al in the silica network. This passivating SiOAl layer is shown to hinder diffusion controlled oxidation in the bulk. Besides, the presence of 1−10% AlN in SiC results in materials having reduced grain size and improved microstructural uniformity, in comparison to monolithic SiC. It was also shown that **SiAlCN** ceramics possess superior creep resistance, high fracture toughness, enhanced oxidation, corrosion resistance, and improved thermal conductivity, in comparison to SiC [288, 289]. Such results, as we also concluded in the literature review, clearly prove the potentialities of the **Si/Al/C/N systems for harsh environment**.

The preparation of SiAlCN with tailored porosity and modifying them with metal NPs is of high scientific and technological interest, because of the wide range of applications potentially offered by these materials in sorption, separation and catalysis to form efficient and active supported metal-based catalysts for reactions in harsh conditions.

There are two strategies to prepare metal modified porous PDCs. The basis of the first strategy (Figure IV-3) is to mix in a controlled molar ratio a metal-containing molecule with a polymeric precursor to generate a metallopolymer. The synthesis is directed to produce metal-ceramic nanocomposites after pyrolysis during which *in-situ* controlled growth of metal occurs in the matrix [290].

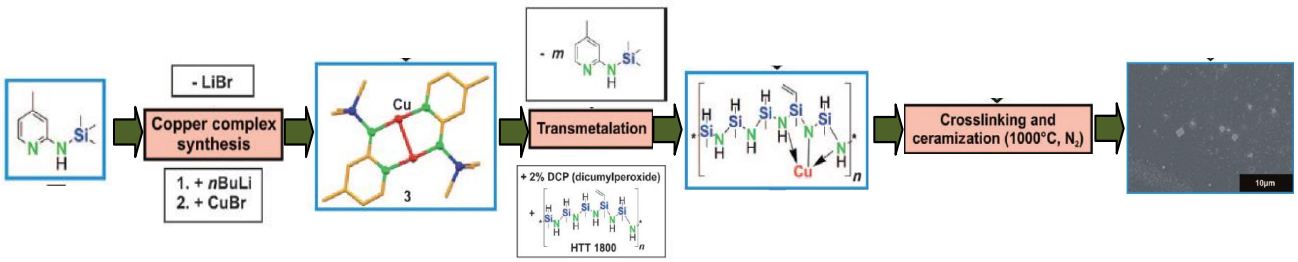

Figure IV-3: One-step procedure to prepare metal-supported PDCs [291].

By this strategy different compositions of nanocomposites can be produced. This molecular approach is advantageous, owing to the dispersion of the metal at an atomic level, and the broad

applicability (coordination compounds of many metals can be used). However, most of the generated metal nanoparticles are not accessible for catalysis since they are deeply embedded in the ceramic support material and the porosity is in general difficult to tune [292].

The second strategy (Figure IV-4) consists in replicating the porous structure of templates such as SBA-15 and CMK-3 by polymer nanocasting [223]. Then, as-obtained materials with tailored porosity are impregnated with the metal precursor to be chemically reduced.

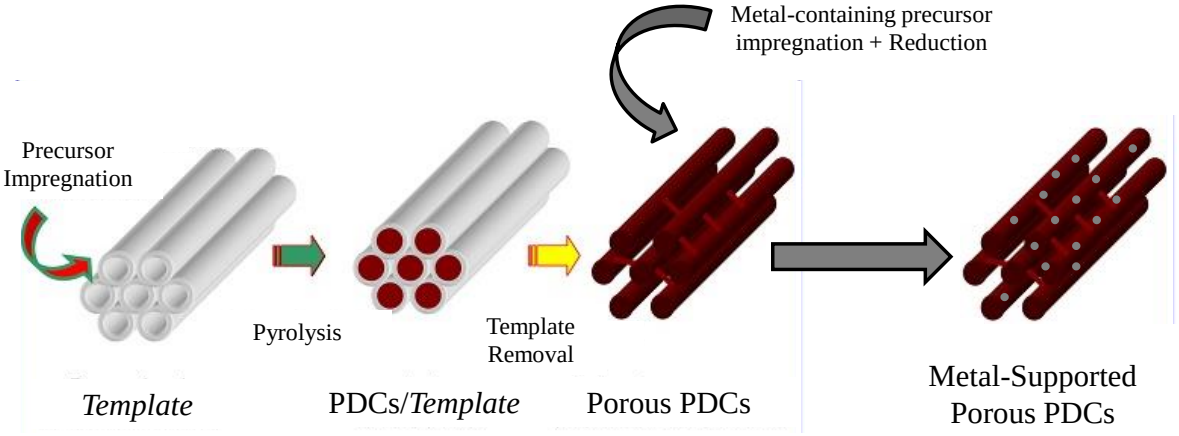

Figure IV-4: Two-step procedure to prepare metal-supported PDCs [223, 225].

This is the strategy we adopt to prepare **Pt-supported SiAlCN ceramics**. In this chapter, we propose, in the first part, the synthesis and characterization of ordered mesoporous SiAlCN to be then modified by platinum nanoparticles. These nanocatalysts have been tested for **H_2 generation by hydrolysis of $NaBH_4$** as summarized in Figure IV-5.

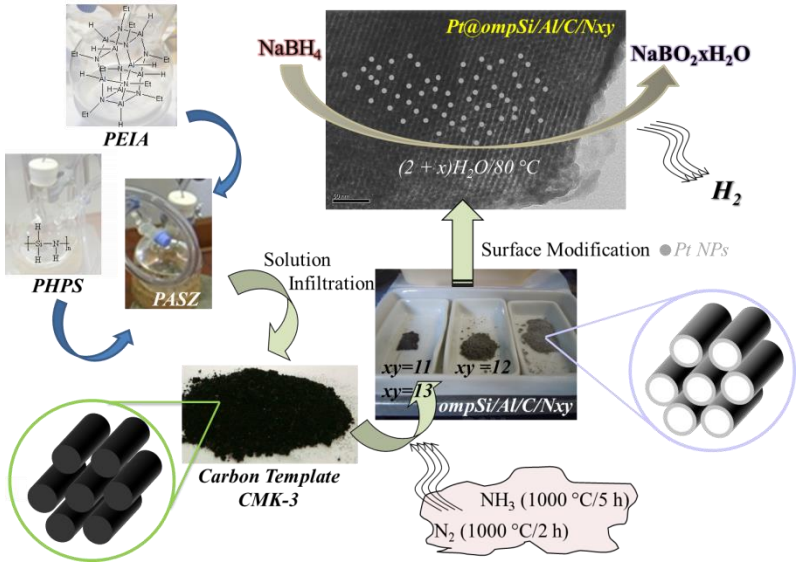

Figure IV-5: Overall synthetic path employed to generate periodic mesoporous SiAlCN ceramics.

Their performance has been compared to that obtained from **Pt/Si_3N_4** nanocatalysts which are the focus of the second part of the present chapter, as well as to **Pt/CMK-3** nanocatalysts to extrapolate and highlight the significant enhancement of the catalytic activity of the new **nitride nanocatalysts** in comparison to carbonaceous supports.

2. PREPARATION OF Pt SUPPORTED ORDERED MESOPOROUS SiAlCN CERAMICS

Using a **co-pyrolysis** strategy (in other terms the "**molecular building block strategy**" [293] since we are building a final material by blending two or more molecular blocks) has the advantage of being a relatively simple and easy process. However, some characteristics are quite mandatory in order to satisfy the conditions required by this approach to prepare ordered mesoporous PDCs: i) solubility of the precursors in a common solvent for processability, ii) occurrence of the polymer-to-ceramic conversion at the lowest possible temperature, iii) similarity of the decomposition temperature of the precursors, iv) expected reaction between precursors during pyrolysis avoiding thus the collapsing of the structure, v) segregation of one of the individual component ceramic phases at the highest temperature for stability of the amorphous network.

Templated synthesis (=polymer nanocasting) has been combined with the molecular building block strategy to develop **ordered mesoporous SiAlCN** materials.

2.1. Experimental part

2.1.1 Materials

The molecular and polymeric precursors are unstable in air. Therefore, all manipulations were carried out under inert conditions. All ceramic products were handled in an argon-filled glove box (MBraun MB200B) where the O_2 and H_2O concentrations were kept <0.1ppm, because of their high surface area and affinity for moisture before characterization. Argon (>99.995%) was purified by passing through successive columns of phosphorus pentoxide, siccapent, and BTS catalysts. Schlenks were dried at 120°C overnight before pumping under vacuum and filling them with argon for synthesis. Manipulation of the chemical products was made inside the glove box. Toluene (99.85%, extra dry over molecular sieve, AcroSeal®) was obtained from Acros Organics. Triblock poly(ethylene oxide)-bpoly(propylene oxide)-b-poly(ethylene oxide) copolymer Pluronic P123 (Mw = 5800 $g.mol^{-1}$, EO20PO70EO20) was purchased from Sigma−Aldrich and used without additional purification. For the preparation of the Pt supported catalysts and the hydrogen generation experiments, chloroplatinic acid hexahydrate ($H_2PtCl_6 \cdot 6H_2O$, Sigma− Aldrich), sodium borohydride

($NaBH_4$, Acros Organics), sodium hydroxide (NaOH, Carlo Erba) and degassed deionized water (resistivity >18 MΩ cm) were used. Poly(perhydropolysilazane) PHPS, AQUAMICA NN-310, average molecular weight of 974) was provided by Mitsuya Boeki, Ltd., Japan.

The Poly(perhydropolysilazane) PHPS is a commercial polymer with the following data:
Elemental analysis (wt %): Si, 65.1; N, 26.2; H, 8.3; O, 0.4.
FTIR (KBr/cm^{-1}): $\nu_{(N-H)}$ = 3374 (m), $\nu_{(Si-H)}$ = 2125 (s), $\nu_{(N-H)}$ = 1180 (s), $\nu_{(Si-N)}$ = 840−1020 (s).
^{1}H NMR (500 MHz, C6D6, δ/ppm):1.0 (NH), 4.96 (SiH).
^{29}Si NMR (79.43 MHz, C_6D_6, δ/ppm): −39.0 ppm ($HSiN_3/H_2SiN_2$).

The synthesis and characterization of poly[N-(ethylimino)alane] (PEIA, $[HAlNEt]_8$) have been already described in chapter II of this manuscript.

SBA-15 was prepared by hydrothermal synthesis and then was used as a hard template to prepare CMK-3 via impregnation with sucrose, according to established procedures [294-296].

2.1.2 Preparation and characterization of polyaluminosilazanes

The reaction is conducted in a three-necked round-bottom flask equipped with a gas inlet tube and a glass stopper. The flask was charged with a precise quantity of **PEIA** (Table IV-1) and toluene (100 L). Depending on the Al (x):Si (y) ratios (x:y =1:1, 1:2, 1:3) based on the monomeric unit of each polymer ratio targeted, a precise quantity of **PHPS** (Table IV-1) was added dropwise to this solution. After stirring at 30°C until complete dissolution and getting a clear solution, the solvent was removed *via* an ether bridge at a reduced pressure to yield a white solid (= polyaluminosilazane, labeled **PASZ*xy*** (**PASZ*11***, **PASZ*12***, and **PASZ*13***). We focused on this restricted ratio range because, outside this range, the effect of the polymer in the lowest proportion is negligible.

Table IV-1: Experimental parameters (synthesis of blended polymers).

Sample	PEIA (g)	PHPS (g)
PASZ*11*	0.180	0.113
PASZ*12*	0.111	0.140
PASZ*13*	0.173	0.327

For the three blended polymers **PASZ*xy***, we performed chemical analysis to obtain information on the elemental composition of the material. We also investigated structural characterization by using liquid state NMR (recorded in C_6D_6 on a Brucker AVANCE-300) and

FTIR spectroscopy (Nicolet Magna 550 Fourier transform-infrared spectrometer in a KBr matrix (dried at 120°C in air)).

2.1.3 Nanocasting and ceramic transformation

0.226 g of **PASZ*xy*** was dissolved in 1.5 mL of toluene under stirring and added to 0.160 g of CMK-3 that was previously dehydrated at 150°C overnight. The mixture was then stirred at room temperature (RT) for 48 h under static vacuum.

In order to study the polymer-to-ceramic conversion, the thermogravimetric analyses (TGAs) were recorded on a Setaram system (Model TGA 92 16.18). The experiments were performed at 5 °C.min^{-1} up to 1000°C in flowing nitrogen for the polymer-to-ceramic conversion using silica crucibles (sample weight of ~ 40 mg) at ambient atmospheric pressure. The CMK-3 removal step was monitored by TGA at 5°C.min^{-1} up to 1000 °C in a mixture of ammonia and nitrogen (75:25 in flow ratio) using silica crucibles (sample weight of ~ 20 mg) at ambient atmospheric pressure.
The composites (**PASZ*xy*/CMK-3**) are transferred into a silica tube inserted in a horizontal tube furnace (Nabertherm type RS 80/500/11, Germany). Subsequently, the samples were subjected to a N_2 cycle of ramping of 1°C.min^{-1} to 1000 °C, dwelling at that temperature for 2 h, and then cooling to RT at a rate of 2°C.min^{-1}. A constant nitrogen volumetric flow of 0.039 mL.s^{-1} was passed through the tube. After the ceramisation process, the composite underwent a final thermal treatment under a mixture of nitrogen and ammonia atmospheres in the same horizontal tube furnace from RT to 1000°C and kept at this temperature for 5 h to remove CMK-3, while generating the mesoporous samples ordered ompSi/Al/C/N*xy* (with x = Al = 1 and y = Si = 1-3). A constant volumetric flow of 0.039 mL.s^{-1} for each gas was passed through the tube.

2.1.4 Preparation of of nanocatalysts

Typically, 43 mg of ***omp*-SiAlCN** was milled, transferred in 2.5 mL of water, and ultrasonicated for 1 h in ambient conditions. Then, 1 mL of an aqueous solution of $H_2PtCl_6.6H_2O$ (2.44×10^{-3} M) was added to the dispersion of ***omp*-SiAlCN** in order to load the target of 1 wt% Pt over the support. The mixture was further ultrasonicated for 1 h. Meanwhile, the reducing solution (*i.e.* alkaline aqueous solution of $NaBH_4$, with the concentrations of NaOH and $NaBH_4$ being of 3 M and 0.14 M, respectively) was prepared. It was added dropwise to the mixture $Pt^{2+}_{(aq)}$+*omp*-Si_3N_4 while the solution was vigorously shaken; the total time of addition was fixed to 30 min. As a final step, the solution was filtrated, and the solid washed twice with deionized water, washed with ethanol, and dried at 60°C to generate **Pt/*omp*-SiAlCN**.

2.1.5 Experiments

The mesoporous materials were observed by SEM (Hitachi, Model S800) equipped with energy-dispersive spectroscopy analysis (EDX). TEM images were taken with a transmission electron microscope (Philips, Model CM 200FEG) operated at 200 kV. All powders were dispersed on carbon-film-covered copper grids for analysis. N_2 adsorption-desorption isotherms were measured on a Model Sorptomatic 1900 analyzer (Fisons). Before adsorption measurements, all samples were outgassed for 4 h at 150°C in the degas port of the adsorption analyzer. The chemical formula of the samples was calculated by coupling EDX (for Si, Al and C contents) and Carrier Gas Heat Extraction (LECO TC-600, for N and O contents). Small-angle powder X-ray diffraction patterns (SA-XRD) were recorded using a Philips Model PW 3040/60 XPert PRO XRD system operating at 30 mA and 40 kV, and between 0.7° and 5.0° with a step size of 0.0167°. High-temperature TGA measurements were performed under N_2 up to 1700°C with a heating rate of 5°C.min^{-1} using tungsten carbide crucibles (HT-TGA, Setaram Setsys 2400 CS evolution equipment) and under static air with a moisture level of 35 % (measured every hour, then averaged) from 25°C to 1000°C with a dwelling time of 5 h) at a heating rate of 5°C.min^{-1}, using silica crucibles (Setaram, Model TGA 9216.18).

2.2. Results and discussion

2.2.1 Synthesis and characterization of polyaluminosilazanes

As mentioned earlier we used two polymeric precursors, both satisfying the aforementioned criteria: Poly(perhydropolysilazane) (**PHPS**, [SiH_2−NH]n) and Poly[N-(ethylimino)alane] (**PEIA**, [HAl-NEt]$_n$). PHPS is a soluble thermoset polymer containing only silicon, nitrogen, and hydrogen. [255]). PHPS leads to a composite material composed of a majority of Si_3N_4 and around 13 wt% of silicium (Si). As PHPS is only available in solution (in xylene in the present case) and is highly reactive even at RT, the precise measurement of its ceramic yield is difficult. It is clear that no weight loss occurs above 800°C under nitrogen but the measured weight loss at 1000°C varies from 16% to 24.7%. PEIA (fully described in chapter II) yields AlN by pyrolysis under ammonia at 1000°C, then under nitrogen at 1800°C. Using nitrogen as the atmosphere from RT to 1800°C results in a carbon-containing AlN with ∼20 wt% carbon [134]. The mixing of PEIA and PHPS in solution, according to different PEIA(x):PHPS(y) ratio (therefore Al:Si), delivered polymers we called polyaluminosilazane with different Al:Si ratios (with Al=1 and Si=1→3). The polymers have been labeled **PASZ*11***, **PASZ*12*** and **PASZ*13***.

The spectra of **PASZ*xy*** of ^{1}H NMR (500 MHz) recorded in C_6D_6 displayed broad signals that are characteristic of PEIA (presence of a broad singlet at δ= 4.45 ppm indicating the presence of Al-**H** bonds) and PHPS (presence of a broad signal in the range δ= 4.86-4.9 ppm indicating the presence of Si-**H** bonds). The protons in C**H₂** groups linked to nitrogen atoms were represented by a triplet signal at δ= 3.24-3.4 ppm, and the protons in C**H₃** groups were identified by the appearance of two sets of signals in the range δ= 1.2-1.6 ppm. Finally, the signal at δ= 0.8-0.9 ppm was assigned to protons in NH units. On the other hand, ^{27}Al NMR (130.20 MHz) and ^{29}Si NMR (79.43 MHz) spectra showed the same peak positions observed respectively in PEIA (135 ppm assigned to H**Al**N_3) and PHPS (-37.2 ppm assigned to H**Si**N_3/H_2**Si**N_2.

The FTIR spectra (Figure IV-6) shows the characteristic stretching and deformation bands of PEIA and PHPS: $\nu_{(N-H)}$= 3425 cm^{-1}, ν_{C-H}= 2956-2803 cm^{-1}, ν_{Si-H}= 2125 cm^{-1}, ν_{Al-H}= 1860-1840 cm^{-1}, $\delta_{asy\ CH3}$= 1463 cm^{-1}, $\delta_{s\ CH3}$= 1378 cm^{-1}, $\delta_{(N-H)}$= 1173-1171 cm^{-1}, $\delta_{(C-N)}$= 1110-1080 cm^{-1}, $\delta_{(N-Si-N)}$= 840-1020 $cm^{-1}$and $\nu_{(Al-N)}$= 720 cm^{-1}.

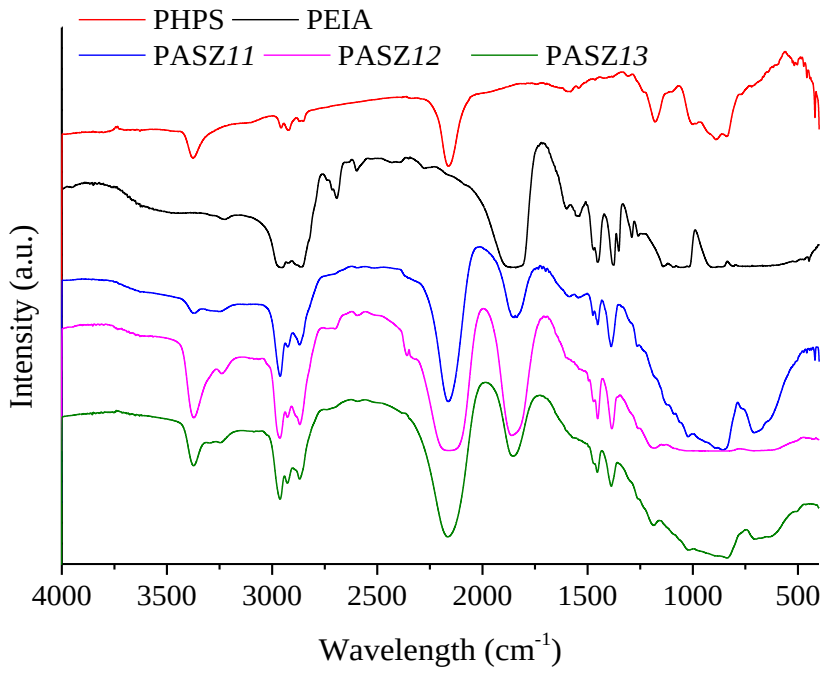

Figure IV-6: FTIR spectra of **PHPS**, **PEIA** and blended polymers **PASZ*xy***.

The data relative to the chemical analyses of the three samples are resumed in Table IV-2.

Table IV-2: Chemical formula of the blended polymers.

PASZ*xy*	**Elemental analysis (wt%)**					**Chemical Formula**
	Si	**Al**	**N**	**H**	**C**	
PASZ*11*	24.7	23.8	21.0	8.3	22.2	$[Si_{1.0}Al_{1.0}N_{1.7}H_{9.3}C_{2.1}]_n$
PASZ*12*	35.9	17.3	22.4	8.2	16.1	$[Si_{1.0}Al_{0.5}N_{1.3}H_{6.4}C_{1.1}]_n$
PASZ*13*	43.3	12.5	23.7	7.5	13.0	$[Si_{1.0}Al_{0.3}N_{1.1}H_{4.8}C_{0.7}]_n$

The chemical formula changes in terms of the fixed Al:Si ratio, from $[Si_{1.0}Al_{1.0}N_{1.7}H_{9.3}C_{2.1}]_n$ for **PASZ*11*** to $[Si_{1.0}Al_{0.3}N_{1.1}H_{4.8}C_{0.7}]_n$ for **PASZ*13***. The proportion of carbon and hydrogen gradually decreases from **PASZ*11*** to **PASZ*13*** which is in agreement with the decrease in the Al:Si ratio and therefore the PEIA:PHPS ratio. Moreover, the Al:Si ratio measured by elemental analysis is similar to the one fixed during the polymer synthesis.

Based on the pervious observations, the results tend to confirm the absence of reaction between both precursors: **PEIA** and **PHPS** prior to their use for the nanocasting and pyrolysis processes.

2.2.2 PASZ-to-SiAlCN conversion

The direct solution infiltration of CMK-3 with the blended polymers **PASZ*11***, **PASZ*12*** and **PASZ*13*** is a very effective method to fully infiltrate the pores of the template. The nanocasting of the samples was carried out through an impregnation process in a Schlenk-type flask according to the process described in the experimental part. It should be mentioned that there are four important parameters to control: First, the polymer:template weight ratio is optimized at 1.4, this is roughly corresponding to the impregnation of the total porosity of the CMK-3. Second, after absorption of the polymer into the pores of the template during the impregnation step, the filtration is applied to selectively remove the precursor molecules that are deposited outside, while the capillary forces keep the precursor molecules effectively inside the pores. Third, the solvent is slowly evaporated at low pressure ($5*10^{-2}$ mbar) at 40°C to generate a black powder. Another important parameter would be the subsequent pyrolysis since the ceramic yield must be as high as possible to keep the maximum of the product confined inside the porosity of the template after the ceramic transformation and obtain after the template removal step, an ordered mesoporous component (replica of the ordered mesoporous CMK-3) without non-expected porosity.

The ceramic yield depends strongly on several factors such as the polymer structure, the molecular weight and the cross-linking degree (that can be affected by the presence of functional groups attached to the polymer backbone: nitrogen, silicon and aluminum). An additional important issue therein is the decomposition chemistry of the precursors involving their capacity to further cross-link during the pyrolysis.

Figure IV-7 presents the TG curves recorded during the decomposition of **PHPS**, **PEIA** (the sources of Si, N and Al) and the blended polymers **PASZ*xy*** performed in a N_2 atmosphere (1000°C, 5°C.min^{-1}) with a dwelling time of 10 min at 1000°C.

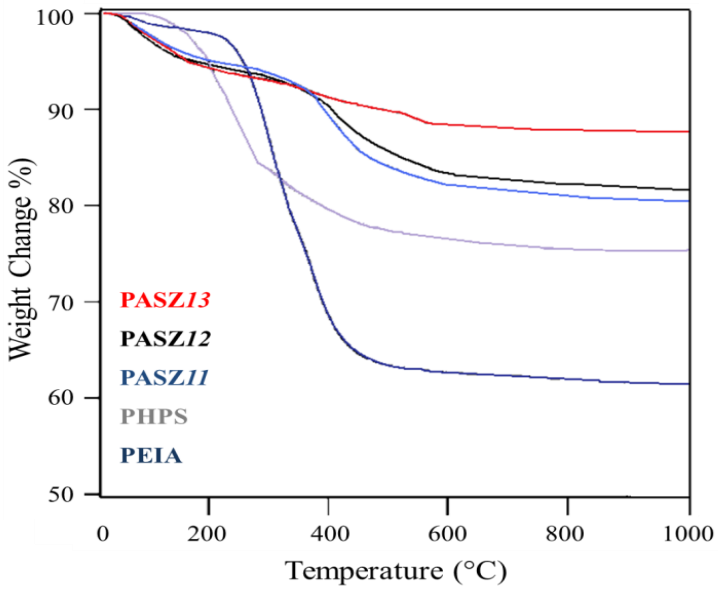

Figure IV-7: TG curves of **PHPS**, **PEIA** and blended polymers **PASZ*xy*** at 1000°C under N_2 with a heating rate of 5°C.min^{-1}).

We can clearly see that the ceramic yield substantially increases for the blended polymers from 80.3% (**PASZ*11***) to 87.5% (**PASZ*13***), compared to that of the two individual precursors (75.3% for **PHPS** and 61.7% for **PEIA**) under the same conditions. This fact suggests that the blended polymers reacted during the heat treatment. In order to understand the exact nature of the mechanistic reactions occurring between **PHPS** and **PEIA** in the porous structure of the template during the polymer-to-ceramic conversion, we isolated intermediates at selected temperatures during the pyrolysis (300, 500, 700 and 1000°C) to perform FTIR characterization of these materials. We only present the results from the sample **PASZ*12*** (Figure IV-8).

Based on the FTIR spectra, it is evident that the signals associated to Al-H (1867-1823 cm^{-1}), Si-H (2170 cm^{-1}) and N-H (3390 cm^{-1}) decreases as the temperature increases, especially between

500 and 1000°C. This can be explained by dehydrocoupling reactions between Si-H and N-H units forming Si-N, or between Al-H and N-H forming Al-N bonds (see **reactions 1 and 2** hereafter) [297, 298].

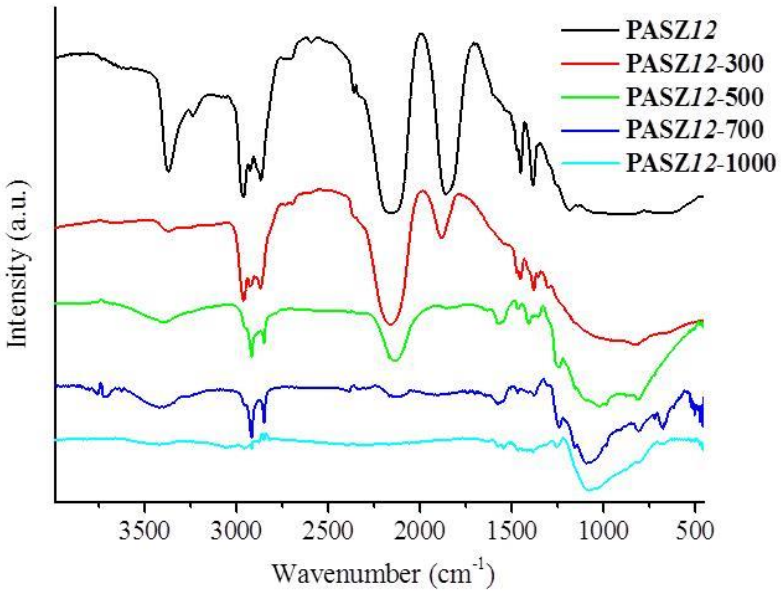

Figure IV-8: FTIR spectra of **PASZ*12*** and **N_2-treated intermediates** isolated at different temperatures during the polymer-to-ceramic conversion.

Based on the FTIR data and solid-state NMR reported by Sugahara and co-workers [293], ten reactions can be considered to represent the mechanism that takes place during the conversion of **PASZ*xy*** pre-ceramic polymers into **SiAlCN** ceramics:

$$1)\quad Si_2N\text{-}H + H\text{-}Si \rightarrow Si_2\text{-}N\text{-}Si + H_2$$

$$2)\quad Si_2N\text{-}H + H\text{-}Al \rightarrow Si_2\text{-}N\text{-}Al + H_2$$

$$3)\quad Al\text{-}NCH_2CH_3 \rightarrow Al^{\bullet} + {}^{\bullet}NCH_2CH_3$$

$$4)\quad Si\text{-}H \rightarrow Si^{\bullet} + H^{\bullet}$$

$$5)\quad Si^{\bullet} + {}^{\bullet}NCH_2CH_3 \rightarrow Si\text{-}NCH_2CH_3$$

$$6)\quad H^{\bullet} + {}^{\bullet}NCH_2CH_3 \rightarrow H\,NCH_2CH_3$$

$$7)\quad Al_2N\text{-}CH_2CH_3 \rightarrow Al_2N^{\bullet} + {}^{\bullet}CH_2CH_3$$

$$8)\quad Si^{\bullet} + Al_2N^{\bullet} \rightarrow Al_2N\text{-}Si$$

$$9)\quad Si^{\bullet} + {}^{\bullet}CH_2CH_3 \rightarrow Si\text{-}\,CH_2CH_3$$

$$10)\quad H^{\bullet} + {}^{\bullet}CH_2CH_3 \rightarrow CH_3CH_3$$

The heterolytic cleavage of Al-N bonds (**reaction 3**) leading to the formation of nitrogen terminals (=N$^{\bullet}$) may involve the attack of silicon and hydrogen radicals (**reaction 4**) to form Si-N bonds (**reaction 5**) and ethylamine (**reaction 6**). Furthermore, the homolytic cleavage of C-N bonds (**reaction 7**) is expected to involve the formation of Si-N bonds (**reaction 8**), Si-C bonds (**reaction 9**) and alkanes (**reaction 10**). Disappearance of the bands characteristic of alkyl groups confirmed the occurrence of these reactions. After heat-treatment to 1000°C, only a broad band in the wavenumber range 1200-700 cm^{-1} is present. It indicates the presence of Al-N, Si-C and Si-N bonds in the material labelled **SiAlCN@CMK-3**. The chemical interaction between both precursors from the polymer state to the ceramic state under nitrogen to 1000°C (dwelling time of 2 h) is not only a way of preventing the appearance of an unexpected porosity but it also finds a great interest in limiting the degree of phase separation in the ceramics at high temperature.

After the polymer conversion into ceramic that occurred at 1000°C under N_2, the following step consists in removing CMK-3 from the samples **SiAlCN@CMK-3** in order to generate the replica of CMK-3. CMK-3 removal has been performed under ammonia. Decomposition under ammonia results in an incomplete weight loss which is intently related to the polymer:CMK-3 ratio that is fixed before the nanocasting process. Figure IV-9 illustrates a typical example of the weight loss occurring during the decomposition of CMK-3. Around 55 wt% is lost by the composite **PDCs@CMK-3** to form ordered **mesoporous PDCs.**

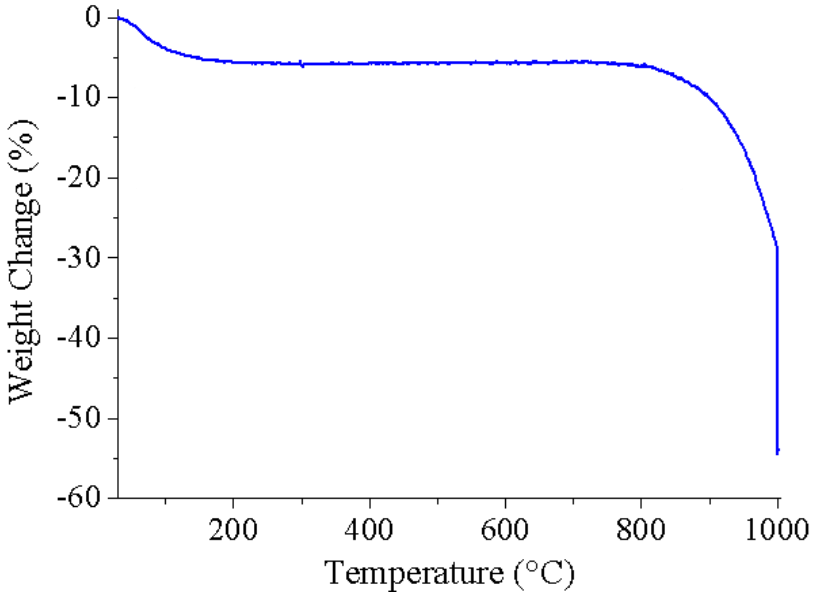

Figure IV-9: TGA curve of a typical example of **PDCs@CMK-3** recorded during decomposition under ammonia at 1000°C (heating rate 5°C.min^{-1}).

It should be mentioned that we investigated TGA of the samples **PASZ*12*-derived SiAlCN** as a test sample (obtained by pyrolysis under nitrogen at 1000°C without infiltration) under ammonia up to

1000°C to follow the behavior of the SiAlCN phase under ammonia: The TGA curve of the Figure IV-10 does not show fundamental weight change after this treatment. Chemical analyses performed before ($Si_{1.0}Al_{0.5}O_{0.2}C_{1.0}N_{1.4}$; Si, 36.7 wt%; Al, 19.3 wt%; C, 15.5 wt%; N, 24.7 wt%; O, 3.8 wt%) and after ($Si_{1.0}Al_{0.5}C_{0.9}N_{1.3}$; Si, 39.9 wt%; Al, 20.9 wt%; C, 14.0 wt%; N, 24.8 wt%; O, 0.4 wt%) ammonia-treatment were similar. This allows us to say that the **SiAlCN** phase is stable under these conditions. Therefore, we considered this protocol (heat-treatment at 1000°C with a dwelling time of 5 h in a nitrogen/ammonia atmosphere) for the removal of CMK-3 template.

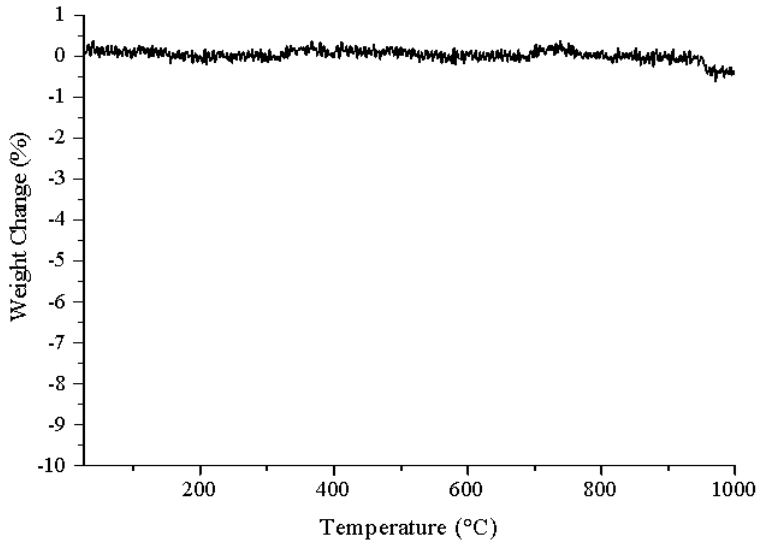

Figure IV-10 : TGA curve under ammonia of **PASZ*12*** pyrolyzed under N_2 at 1000°C (heating rate 5°C.min^{-1}).

After the two-step heat-treatment, grey samples going from dark (***omp*SiAlCN*11***) to light (***omp*SiAlCN*13***) are obtained as shown below Figure IV-11. Samples were labelled *omp*SiAlCN*xy* (with *omp* meaning ordered mesoporous and *xy* the Al:Si ratio fixed during the mixing of **PHPS** and **PEIA**).

Figure IV-11: *omp*SiAlCN*xy* samples after template removal.

2.2.3 Characterization of ordered mesoporous SiAlCN

The chemical formula of the samples changed with the Al:Si ratio from $Si_{1.0}Al_{0.9}O_{0.6}C_{1.1}N_{1.6}$ (***omp*SiAlCN*11***, Si, 29.0 wt%; Al, 24.1 wt%; C, 14.0 wt%; N, 23,1 wt%; O, 9.8 wt%) to $Si_{1.0}Al_{0.3}O_{0.2}C_{0.4}N_{1.0}$ (***omp*SiAlCN*13***, Si, 46.9 wt%; Al, 15.6 wt%; C, 9.0 wt%; N, 23.0 wt%; O, 5.5 wt%). For the ***omp*Si/Al/C/N*12*** sample, a chemical formula of $Si_{1.0}Al_{0.4}O_{0.1}C_{1.1}N_{1.2}$ was calculated based on the weight percent of the elements that compose the materials (Si, 39.4 wt%; Al, 17.5 wt%; C, 14.6 wt%; N, 24,7 wt%; O, 3.8 wt%). Firstly, we suggest that the oxygen content level of the samples is mainly due to physisorbed/chemisorbed water confined in the porous structure of the material despite extreme precaution to protect samples against moisture. The reason why O content is higher for the ***omp*SiAlCN*11*** sample can be explained by its high sensitivity to oxidation, since this sample has the highest proportion of PEIA thus of AlN which is known to be extremely sensible to O and moisture. Secondly, if we compare the composition of the polymers and the ceramic materials we note that the Al:Si ratio stays constant during pyrolysis. This points out the absence of evolution of Si- and Al-based gaseous species as by-products during the pyrolysis confirming thereby the chemical interaction of both polymers during heat-treatment. Moreover, the Si:N ratio remains almost unchanged. The most apparent difference (excepted for hydrogen) in the chemical compositions is the different carbon content of the precursors and the ceramics which proved the evolution of C-based units during the pyrolysis.

The samples were generated as micron-sized plate-like powders clearly displaying an excellent order after the template removal as shown in the SEM and TEM images of the representative *omp*SiAlCN*12* sample (Figure IV-12). When viewed down the [100] direction of the sample (Figure IV-12-b), the HRTEM image shows one-dimensional channels that represent hexagonally ordered pores arranged in a linear array. The distance between the centers of the adjacent channels is approximately 7.5 nm, which is in good agreement with the value of the lattice parameter a_{100} mentioned previously. This is also close to the value measured for the CMK-3 template (8.2 nm) indicating that the mixed polymer framework is sufficiently rigid and cross-linked to withstand pore collapse and deterioration of the nanoscale order of the CMK-3 hard template. As for the cross-section HRTEM image (Figure IV-12-c) it clearly displays a hexagonal (honeycomb-like) arrangement of the mesopores with regular diameters around 7 nm. Based on these observations, it can be assumed that the sample exhibits a structure with an ordered hexagonal arrangement of cylindrical channels similar to that observed in silica template SBA-15.

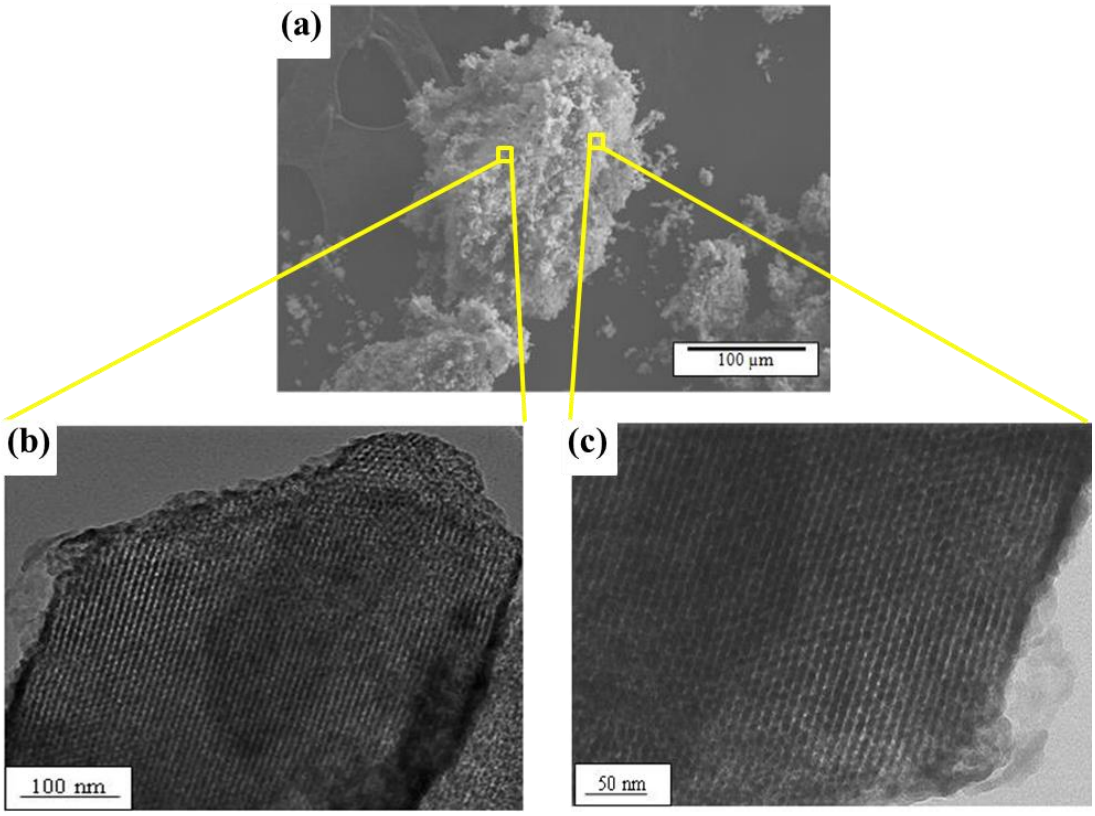

Figure IV-12: (a) SEM image of ***omp*SiAlCN*12*** and HRTEM images of ***omp*SiAlCN*12*** (b) longitudinal projection and (c) cross-sectional projection.

Figure IV-13 presents the SA-XRD patterns of the ***omp*SiAlCN*xy*** (with x = Al = 1 and y = Si = 1 → 3) samples. They confirmed the ordered structure of the specimens with an improvement of the ordering from ***omp*SiAlCN*11*** to ***omp*SiAlCN*13*** in line with the increase of the ceramic yield of the corresponding polymers from **PASZ*11*** to **PASZ*13***.

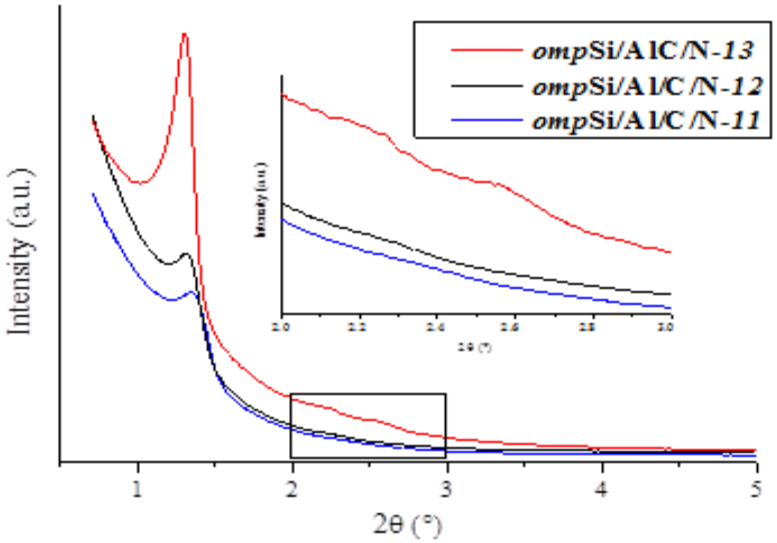

Figure IV-13: SA-XRD patterns (Cu Kα radtion) of the ***omp*SiAlCN*xy*.**

This clearly demonstrated the strong correlation between the ceramic yield of preceramic polymers and the retention of the ordered porosity of the derived ceramics. A clear diffraction peak with d = 6.8 nm (2θ = 1.30°) and two weak peaks at 3.96 (2θ = 2.23°) and 3.45 nm (2θ = 2.56°) were observed for ***omp*SiAlCN*13*** whereas the SA-XRD patterns of ***omp*SiAlCN*11*** and ***omp*SiAlCN*12*** samples exhibited a slight loss of order as illustrated with the gradual decrease in both intensity of the (100) and higher orders of reflections. These peaks can be assigned to the (100), (110) and (200) reflections of the 2D hexagonal lattice (space group *P6mm*) with a lattice parameter a_{100} = 7.5-7.8 nm.

Table IV-3 reports the structural XRD properties of all specimens as well as those of SBA-15 and the CMK-3, from which we replicated our porous samples. The values 7.5-7.8 nm are slightly smaller than that measured for CMK-3 (8.5 nm) suggesting a limited framework shrinkage occurring during the polymer-to-ceramic conversion.

Table IV-3: SA-XRD data of **SAB-15**, **CMK-3** and ***omp*SiAlCN*xy*.**

Sample	**SA-XRD data**	
	D100 spacing (nm)	Cell parameter, a (nm)
SAB-15	9.4	10.8
CMK-3	8.5	9.8
omp*SiAlCN*11	6.5	7.5
omp*SiAlCN*12	6.7	7.7
omp*SiAlCN*13	6.8	7.8

In addition, powder XRD was applied in a wider range: from 20° to 80° to identify the global structure of the SiAlCN phase. In Figure IV-14 we show a particular example of ***omp*SiAlCN*xy*** which is the ***omp*SiAlCN*12*** treated under N_2 at three different temperatures: 1000, 1400 and 1700°C.

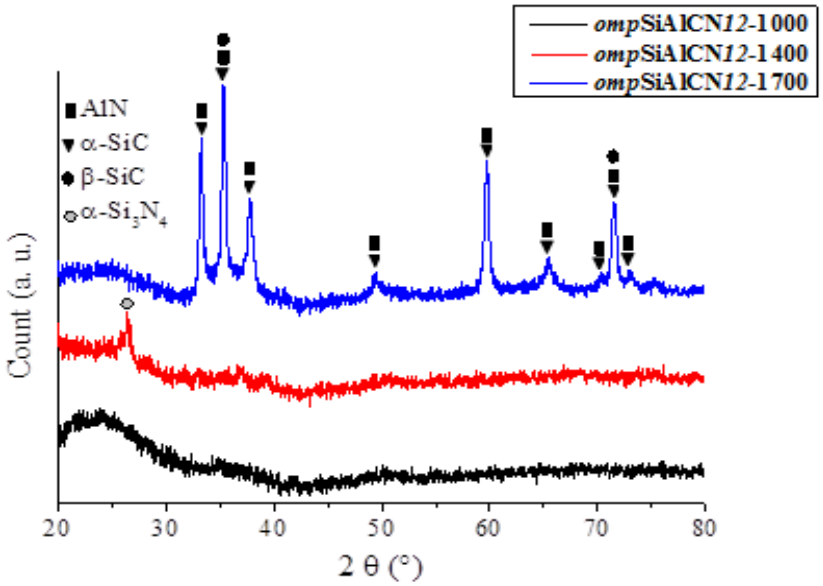

Figure IV-14: XRD patterns of ***omp*SiAlCN*12*** at different temperatures.

The absence of diffraction peaks in the wider angle XRD patterns of the ***omp*SiAlCN*12*** at 1000°C (***omp*SiAlCN*12*-1000**) demonstrates that the channel walls of the samples are amorphous in nature. The amorphous state is globally retained after heat-treatment to 1400°C (***omp*SiAlCN*12*-1400**) with only the appearance of a diffuse α-Si_3N_4 peak emerging around 26°. Crystallization of these frameworks only occurs at prolonged reaction times at 1700°C (***omp*SiAlCN*12*-1700**) into the *2H* solid solution (AlN, SiC). The other ***omp*SiAlCN*xy*** samples proceed in a similar way regarding to crystalisation. The structural evolution in the temperature range 1000-1700°C can be understood through high temperature TGA (HT-TGA) investigations.

The high-temperature behavior of Si-based PDCs is related to the chemistry and structure of the preceramic polymer, the form of the material (powders, coatings, fibers…), the texture (porous or dense) and of the atmosphere of pyrolysis (reactive or inert). Since it has been shown that the porosity had a great influence on the high-temperature stability of the ceramics [200], we investigated TGA measurements under N_2 up to 1700°C at a heating rate of 5°C.min^{-1}. The HT-TGA curves of the three samples are shown in Figure IV-15.

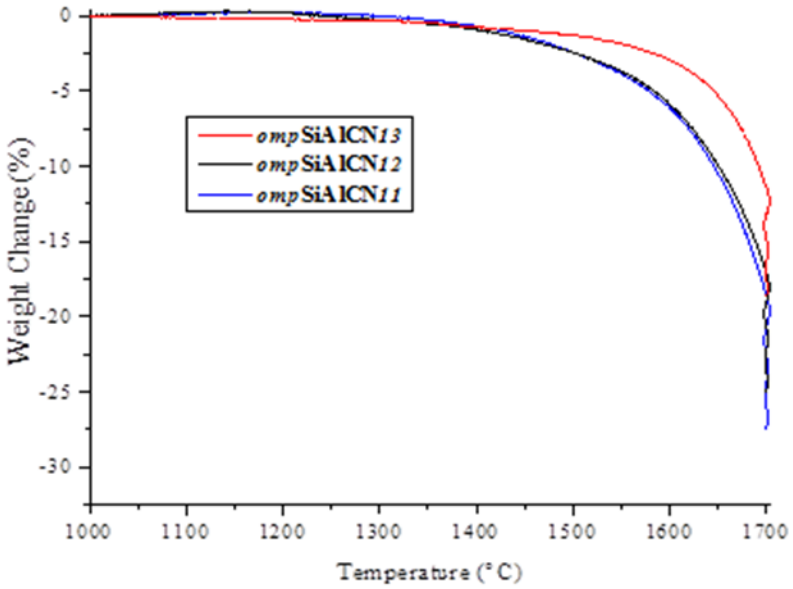

Figure IV-15: HT-TGA up to 1700°C under N_2 of ***omp*SiAlCN*xy*** (heating rate 5°C.min^{-1}).

For the three samples, almost no weight change is noticeable up to 1470°C, demonstrating the excellent stability of the amorphous channel walls. Further heating at higher temperatures (up to 1700°C) results in a decomposition step accompanied with a continuous mass loss. The sample ***omp*SiAlCN*13*** is the most stable with a decomposition shifted to higher temperature by ~70°C and associated with the lowest final weight loss measured at 1700°C (18.7 wt%). The weight loss measured after heat-treatment at 1700°C gradually increased from ***omp*SiAlCN*13*** to ***omp*SiAlCN*11*** (27.5 wt%). Based on the fact that *i)* AlN does not thermodynamically decompose below 1700 °C, *ii)* Si_3N_4 and C are in contact during sintering and *iii)* a *2H* solid solution (AlN, SiC) is identified after heat-treatment to 1700°C (see XRD Figure IV-14), the reaction depicted in the equation IV-2 below, which is known to proceed under standard conditions at 1484°C, mainly occurred in the materials.

$$Si_3N_4 + 3C \rightarrow 3SiC + 2N_2 \quad \text{(IV-2)}$$

Accordingly, the total mass of the ceramic should decrease due to the loss of gaseous nitrogen. Consequently, the difference in the final weight loss can be directly linked to the proportion of free carbon and silicon nitride in the final ceramics. The better stability associated with a lower final weight loss of the sample ***omp*SiAlCN*13*** is clearly a consequence of the low carbon content in the ceramic material.

The nitrogen-adsorption isotherms of the samples ***omp*SiAlCN*xy*** are shown in Figure IV-16. The Brunauer.Emmett.Teller (BET) method was used to calculate the specific surface area. The pore-size distribution was derived from the adsorption branches of the isotherms using the

Barrett.Joyner.Halenda (BJH) method. The total pore volume (V_p) was estimated from the amount of N_2 adsorbed at a relative pressure of $P/P_0 = 0.99$.

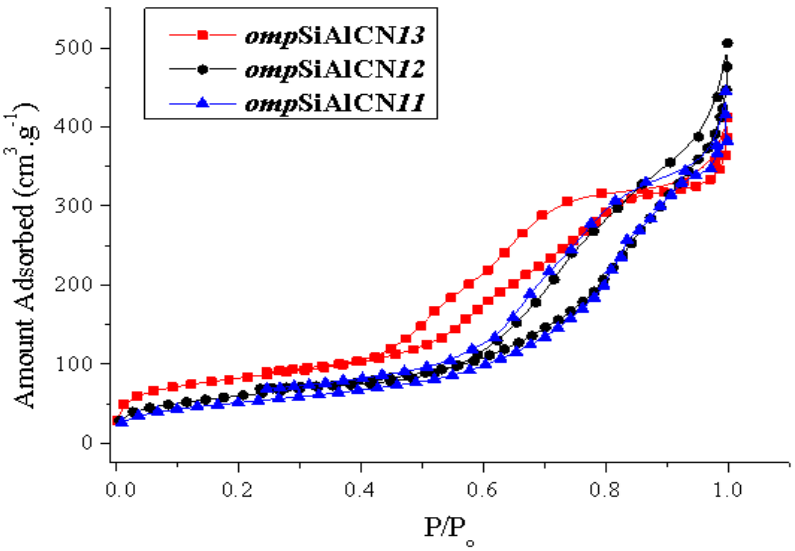

Figure IV-16: N_2 adsorption-desorption isotherms of ***omp*SiAlCN*xy*.**

The isotherms show curves of type IV typical for mesoporous adsorbents with a distinct capillary condensation, which suggests that the materials have uniform mesoporous channels (IUPAC classification. The three samples exhibit a hysteresis loop with a capillary condensation at P/P_0 ranging between 0.45 and 1. A H2 hysteresis loop is observed for the ***omp*SiAlCN*13*** sample, whereas a superposition of H1 and H2 hysteresis loops is rather observed for the other two samples (the H1 hysteresis loop suggesting the presence of cylindrical mesopores and the H2 loop of ink-bottle-shaped mesopores. The samples exhibit specific BET surface areas ranging from 182 to 326 $m^2.g^{-1}$ associated with uniform mesopores dimensions according to the nitrogen desorption determined by the *Barett-Joyner-Halenda* analysis (Figure IV-17). The pore-size distributions are in the range of 4.1-5.9 nm and pore volumes varies from 0.51 to 0.65 $cm^3.g^{-1}$. By comparison, close mesopore volumes are observed for the ***omp*SiAlCN*11*** and ***omp*SiAlCN*13*** samples. This is in agreement with SA-XRD observations and emphasizes the necessity of an optimal filling of the hard template with a high ceramic yield precursor. Based on the cell parameters and the mesopores diameter, the wall thickness was found to be in range of 1.8-3.7 nm.

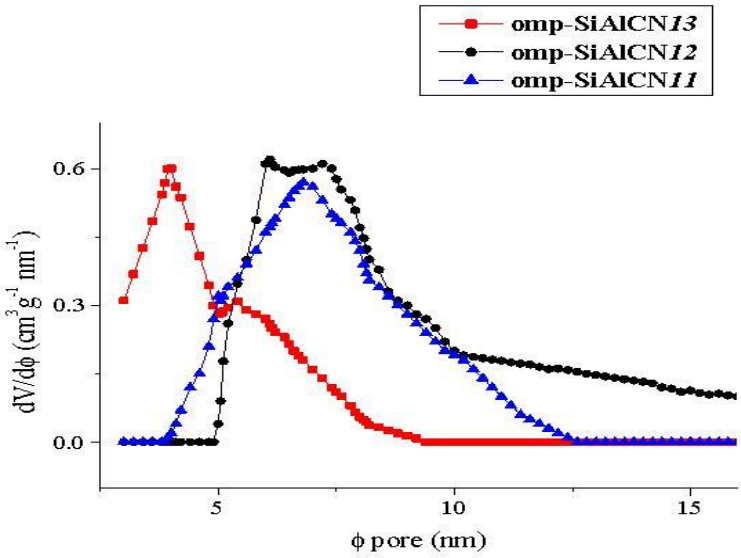

Figure IV-17: Pore size distribution of ***omp*SiAlCN*xy*.**

Table IV-4 reports the BET data of **SBA-15** and **CMK-3** templates and of the ***omp*SiAlCN*xy*** samples. For SBA-15 and CMK-3 we reported the values from literature [294, 295].

Table IV-4: BET Data of SAB-15, CMK-3 and ***omp*SiAlCN*xy*.**

Sample	**BET Data**				
	SSA ($m^2.g^{-1}$)	Dp (nm)	Vp ($cm^3.g^{-1}$)	Wall (nm)	thickness
SAB-15	545	6.9	0.75	3.9	
CMK-3	1355	3.5	1.00		
omp*SiAlCN*11	182	5.1	0.51	2.4	
omp*SiAlCN*12	214	5.9	0.65	1.8	
omp*SiAlCN*13	326	4.1	0.61	3.7	

Chemical, structural and textural properties of the samples ***omp*SiAlCN*xy*** have been performed previously. Based on such properties, it clearly appears that these materials are potential candidates to be used as catalyst support. Before investigating this potential, we decided to test the stability of ***omp*SiAlCN*xy*** samples in air up to 1000°C because it is known that the introduction of Al in the SiCN system tends to stabilize the amorphous network.

According to Figure IV-18, the materials, depending on the Al:Si ratio, showed different behaviors when heat-treated in air up to 1000°C with only a small detectable weight change.

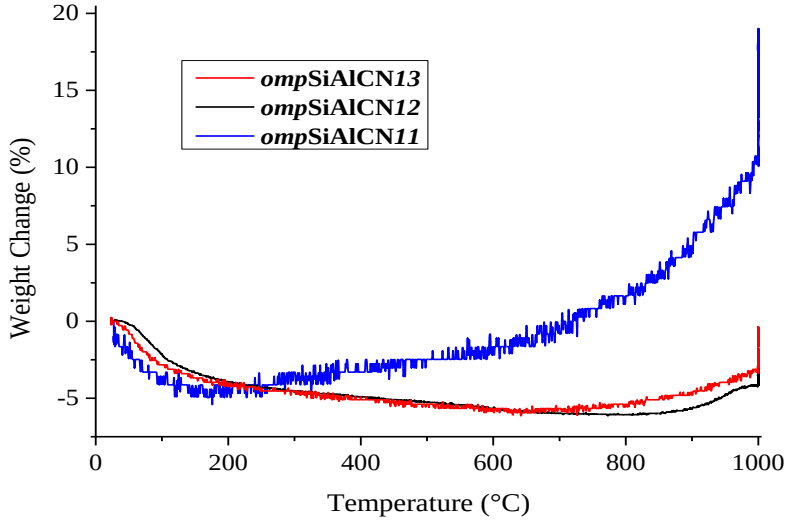

Figure IV-18: HT-TGA under air of ***omp*SiAlCN*xy*** (heating rate 5°C.min^{-1}).

For the sample ***omp*SiAlCN*11***, a continuous increase of the weight is measured in the temperature range 150-1000°C to reach finally 17.5%. For the sample ***omp*SiAlCN*12***, the TGA curve can be shared into four temperature ranges. A first weight loss is detected from RT to 200°C (4 wt%) caused by the evolution of water confined in the porous structure of the sample. Then, a second step from 200 to 870°C in which almost no weight changes are recorded. A third range, from 870 to 1000°C corresponds to a small weight increase (2.50 wt%). In a fourth range during the plateau at 1000°C, oxidation in air proceeds with a continuous weight gain (1.40 wt% measured after a dwelling time of 5 h). The behavior is similar for the sample ***omp*SiAlCN*13*** in the temperature range RT–700°C. Above 700°C, the weight increased faster (5%) up to 1000°C.

Based on the phases which are formed (AlN, Si_3N_4, SiC) we can try to understand the different oxidation mechanisms that can occur. In air, surface oxidation of AlN takes place above 700°C, and even at RT according to the following reaction:

$$4AlN\ (s) + 3O_2\ (g) \rightarrow 2Al_2O_3\ (s) + 2N_2\ (g) \quad \text{(IV-3) [299, 300]}$$

Bowen *et al* reported that the initial reaction product of AlN in water was found to be a porous amorphous AlOOH and then changed to a crystalline $Al(OH)_3$ at RT which melts around 300°C.

$$AlN\ (s) + 3H_2O\ (g) \rightarrow Al(OH)_3\ (s) + NH_3\ (g) \quad \text{(IV-4) [301]}$$

In air, Si_3N_4 and SiC are known to form a dense and continuous SiO_2 layer according to the following equations without bubbles nor cracks and with a sharp oxide/ceramic interface at T ≥ 1000°C [302].

$$Si_3N_4\ (s) + 3O_2\ (g) \rightarrow 3SiO_2\ (s) + 2N_2\ (g) \qquad (IV\text{-}5)$$

$$2SiC\ (s) + 3O_2\ (g) \rightarrow 2SiO_2\ (s) + 2CO\ (g) \qquad (IV\text{-}6)$$

Both SiC and Si_3N_4 react with water vapor to form SiO_2. This is also the case for Si. As an illustration, the oxidation reactions of Si_3N_4 and Si progress as follows [303]:

$$Si_3N_4\ (s) + 6H_2O\ (g) \rightarrow 3SiO_2\ (s) + 4NH_3\ (g) \qquad (IV\text{-}7)$$

$$Si\ (s) + 2H_2O\ (g) \rightarrow SiO_2\ (s) + H_2\ (g) \qquad (IV\text{-}8)$$

Normally the SiO_2 layer acts as a protective layer and decreases the reaction rate in high-temperature and high-pressure water, however, this layer is believed to be unstable and dissolved into water through the reaction (IV-9):

$$SiO_2\ (s) + 2H_2O\ (g) \rightarrow SiO(OH)_3^-\ + H^+ \qquad (IV\text{-}9)\ [304].$$

Firstly, we postulated that oxidation in *omp*SiAlCN*xy* (with x = Al = 1 and y = Si = 1 → 3) samples occurred by inward diffusion of oxygen due to the presence of nanochannels resulting in a higher sensitivity of the material against oxygen in comparison to the bulk analog. Secondly, the weight increase measured on the three samples is caused by the formation of Al_2O_3 and/or SiO_2 which, depending on the ratio between both, are known to form mullite at high temperatures based on the equilibrium diagram for the system Al_2O_3-SiO_2. Mullite is defined as a solid solution with the composition $Al_2[Al_{2+2x}Si_{2-2x}]O_{10-x}$ with $0.17 \leq x \leq 0.5$ that is extremely stable in air up to 1725°C [305].

The large increase of the weight of the sample ***omp*SiAlCN*11*** is clearly attributed to the high proportion of AlN forming alumina in air. After heat-treatment in air we found a chemical composition of $Si_{1.0}Al_{0.7}O_{1.7}C_{0.4}$ with no detectable nitrogen. In addition, a SSA value of 21.04 $m^2.g^{-1}$ has been measured which means that sintering occurred in this particular sample indicating that it is not attractive in harsh environments. As for the samples ***omp*SiAlCN*12*** and ***omp*SiAlCN*13***, the increased proportion of Si considerably decreased the weight gain after heat-treatment in air. The resistance of the sample ***omp*SiAlCN*12*** against oxidation is even excellent which is confirmed by the

absence of changes in the morphological (SEM image in Figure IV-19), structural (XRD pattern in Figure IV-20) and textural properties (SSA of 171 $m^2.g^{-1}$) for the sample ***omp*SiAlCN*12***.

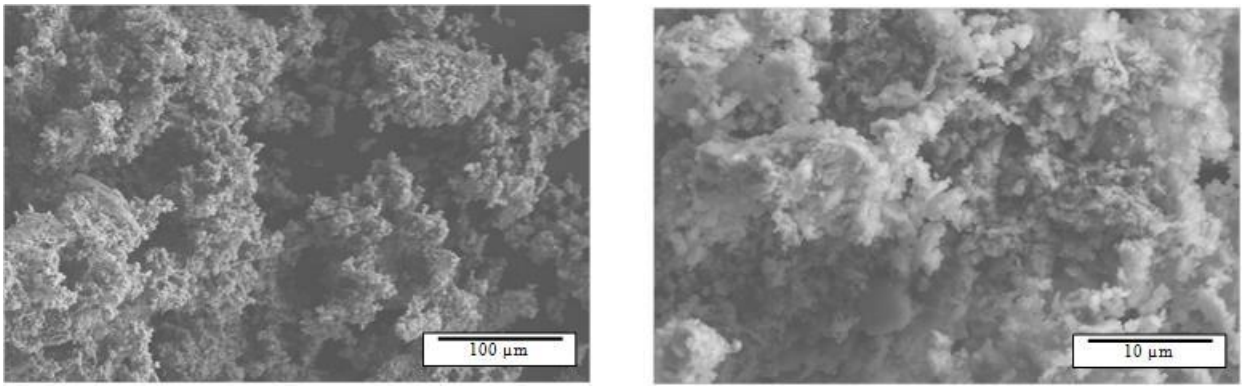

Figure IV-19: SEM images of ***omp*SiAlCN*12*** after heat-treatment in air at 1000°C for 5 h.

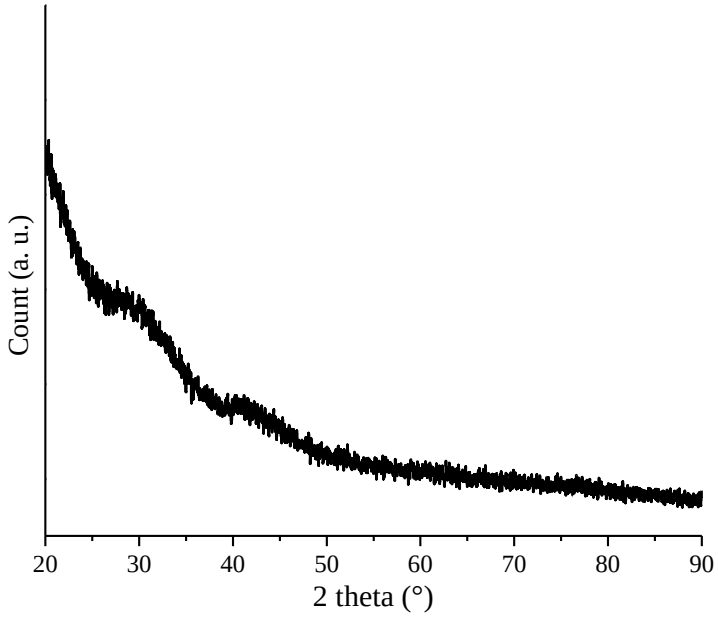

Figure IV-20: XRD pattern of ***omp*SiAlCN*12*** after heat-treatment in air at 1000°C for 5h.

After oxidation, the ***omp*SiAlCN*12*** sample displayed a chemical formula of $Si_{1.0}Al_{0.5}O_{0.6}C_{0.5}N_{0.8.}$ Although the sample ***omp*SiAlCN*13*** displays a similar behavior with a TG profile closer to ordered mesoporous ceramics derived from pure PHPS, a SSA value of 29.6 $m^2.g^{-1}$ is measured after heat-treatment in air at 1000°C. Reproducibility of the experiments confirmed this tendency. These studies highlight the fact that the role of Al is one of the key parameters which affects the stability of SiAlCN materials.

2.2.4 Monodispersed Pt nanoparticles supported on ompSiAlCNxy supports

In this section, our goal is to illustrate one of the principal application which can be performed on ordered mesoporous PDCs according to their potential thermal and chemical stability: the catalytic hydrogen generation from a potential hydride described in the literature review: the **sodium borohydride**. We used **ordered mesoporous SiAlCN** frameworks to support nanoparticles of platinum with the intention of investigating the hydrolysis of an **alkaline solution of $NaBH_4$ at 80°C.** This probe reaction is advantageous to assess the robustness of the support because it offers harsh experimental conditions, in terms of alkalinity, very high rates of H_2 production over the catalytic sites, presence of water and temperature.

2.2.4.1 Preparation of Pt/ompSiAlCNxy nanocatalysts

Platinum nanoparticles (Pt NPs) are deposited on the ***omp*SiAlCN*xy*** supports using hexahydrated chloroplatinic acid as precursor by wet impregnation followed by chemical reduction in alkaline medium. Sodium hydroxide and sodium borohydride were used as received, the latter being handled in the argon-filled glove box. Platinum nanoparticles synthesized from the precursor $H_2PtCl_6.6H_2O$ were supported over the supports by wet impregnation followed by sodium hydroxide-assisted chemical reduction using aqueous $NaBH_4$. Pt supported *omp*SiAlCN*xy* nanocatalysts are obtained (denoted Pt/*omp*SiAlCN*xy*) (with x = Al = 1 and y = Si = 1 → 3).

2.2.4.2 Chacarterization of Pt/ompSiAlCNxy nanocatalysts

EDX analyses revealed that the presence of Pt is in good agreement with the target 1wt%. Values of 1.0, 0.8 and 0.8 wt% were measured for **Pt/*omp*SiAlCN*11*, Pt/*omp*SiAlCN*12*** and **Pt/*omp*SiAlCN*13***, respectively. When coupled with the elemental map overlapping, EDX analyses characterized even better the relatively homogeneous repartition of the Pt nanoparticles represented qualitatively in yellow in Figure IV-21 for the three supported samples. Elemental mapping revealed that the Pt atoms are uniformly distributed in the samples.

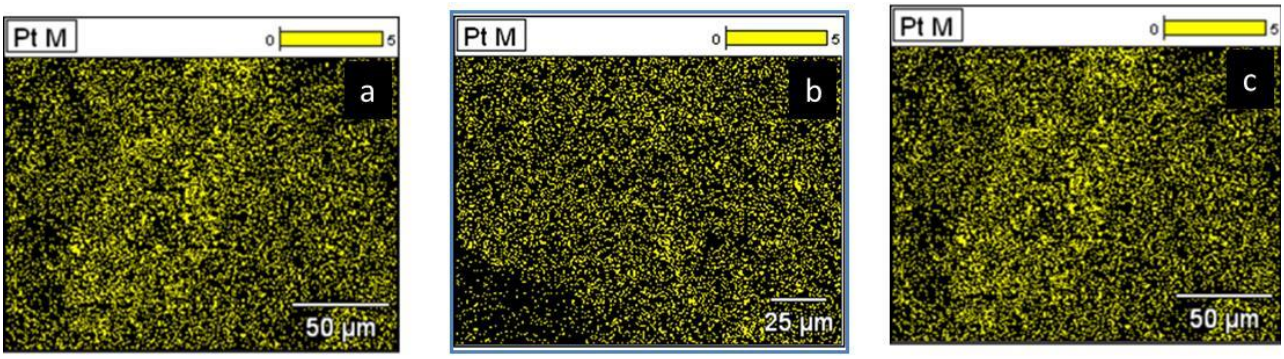

Figure IV-21: EDX elemental map overlapping Pt (yellow) a) **Pt/*omp*SiAlCN*11***, b) **Pt/*omp*SiAlCN*12***, c) **Pt/*omp*SiAlCN*13***.

The morphology of **Pt/*omp*SiAlCN*xy*** was investigated by TEM (Figure IV-22). The presence of Pt in the form of (nano)particles is confirmed. The size of the (nano)particles was measured and the size dispersion plotted. With **Pt/*omp*SiAlCN*12***, the size is centered to 7 nm. These results reveal the pore-size-controlled growth of the (nano)particles using mesoporous SiAlCN samples. Similar results were obtained with **Pt/*omp*SiAlCN*11*** even though very few large particles (up to 40 nm) are observed. However, with **Pt/*omp*SiAlCN*13***, the particles size is heterogeneous, with many particles of 20-40 nm.

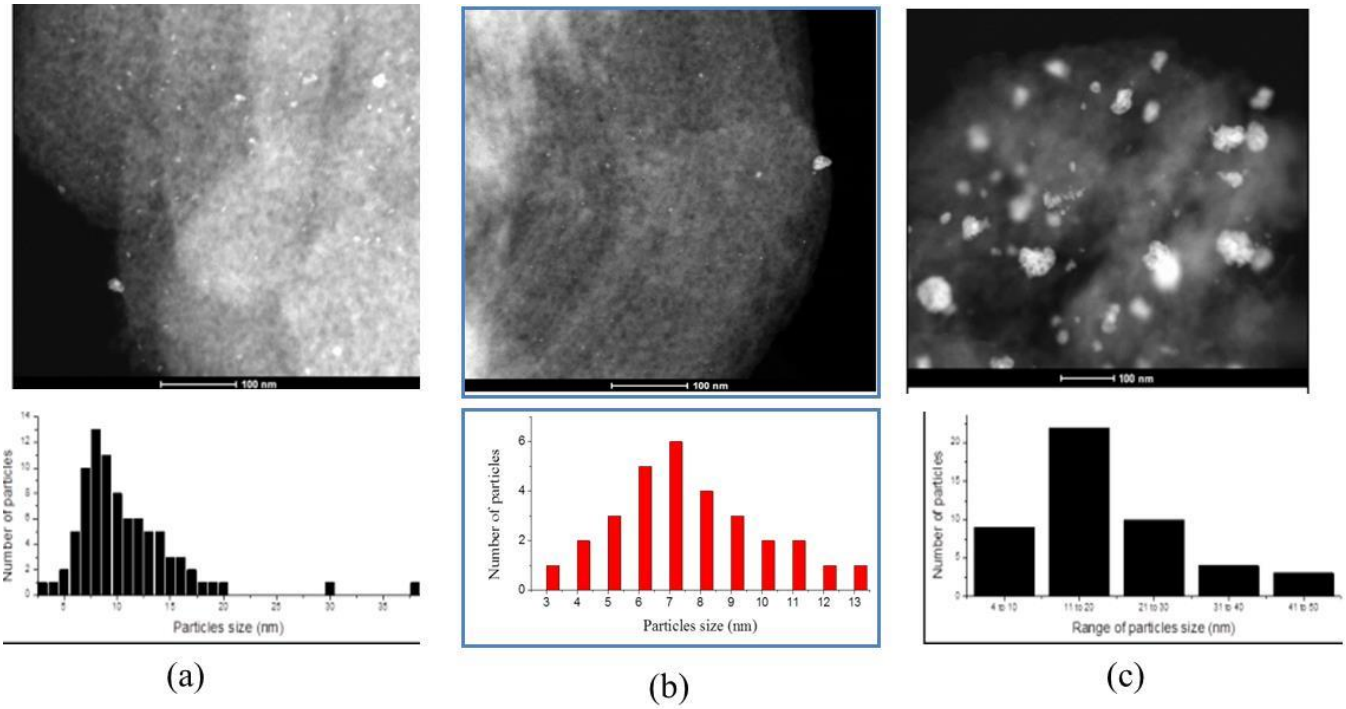

Figure IV-22: TEM image & corresponding size histogram for the dispersion of Pt in a) **Pt/*omp*SiAlCN*11***, b) **Pt/*omp*SiAlCN*12***, c) **Pt/*omp*SiAlCN*13***.

Henceforth, we will consider only the sample ***omp*SiAlCN*12***.

The SA-XRD pattern of **Pt/*omp*SiAlCN*12*** (Figure IV-23-a) shows a small decrease in the intensity of the lowest angle most probably due to the filling of a part of the pores with Pt (nano)particles. Peaks are broad and weak suggesting the formation of small crystallites. Using the Scherrer's formula, an average crystallite size of 16 nm was calculated based on the (111) peak.

The powder XRD pattern shows (Figure IV-23-b) the characteristic peaks of Pt (ICDD 004-0802) at 2θ = 26° (111), 28° (200) and 40° (220).

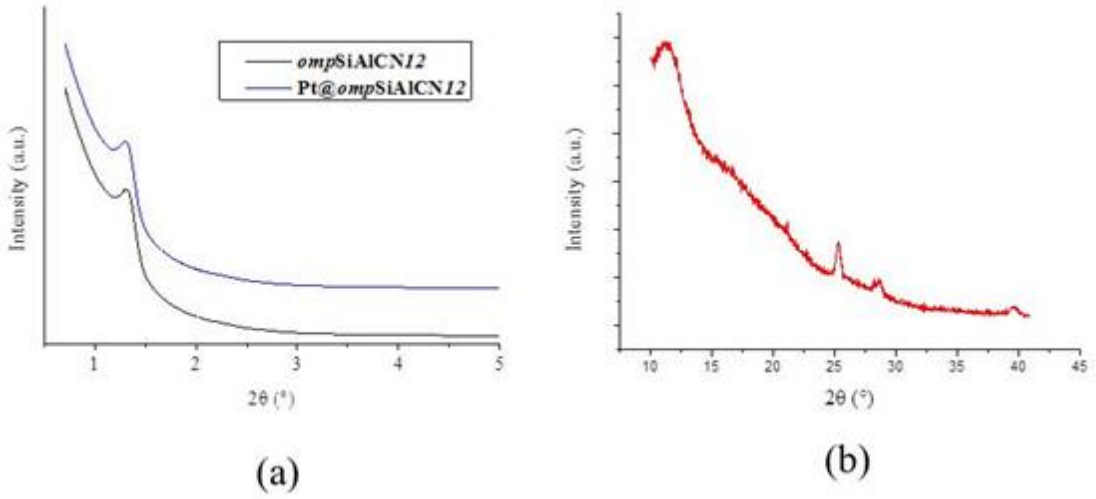

Figure IV-23: Pt@*omp*SiAlCN*12*: a) SA-XRD and b) Wide angle XRD.

In fact, these results are consistent with the pore distribution found for the support. With the sample ***omp*SiAlCN*13***, the pore distribution is 4.1 nm. Such small pores do not probably enable the incorporation of Pt (nano)particles as well as their stabilization. Most of the (nano)particles are formed on the external surface of the **Pt/*omp*SiAlCN*13***. These results indicate the great interest of *omp*SiAlCN*12* in preventing the aggregation of (nano)particles and stabilizing the formed (nano)particles, some of them being probably inside the mesoporous channels.

After surface modification, the shape of the isotherm and the hysteresis loop of **Pt/*omp*SiAlCN*12*** are almost identical to the isotherm of the parent ***omp*SiAlCN*12*** (Figure IV-24). The hysteresis loop extends over a lower relative pressure range (0.60 to 0.90) revealing that the highly ordered structure is maintained even after surface modification or encapsulation of the Pt (nano)particles. The specific BET surface was found to decrease from 214 $m^2.g^{-1}$ for ***omp*SiAlCN*12*** to 102 $m^2.g^{-1}$ for **Pt/*omp*SiAlCN*12*** and the specific pore volume decreased from 0.65 $cm^3.g^{-1}$ to 0.51 $cm^3.g^{-1}$. These results are due to the formation of the (nano)particles inside the pore channels. The absence of an abrupt change in the pore volume and surface area of the support after the Pt deposition further proves that the pores of the support are not blocked by Pt (nano)particles larger than the pore size of the support, revealing that this support hinders the agglomeration or migration of the (nano)particles.

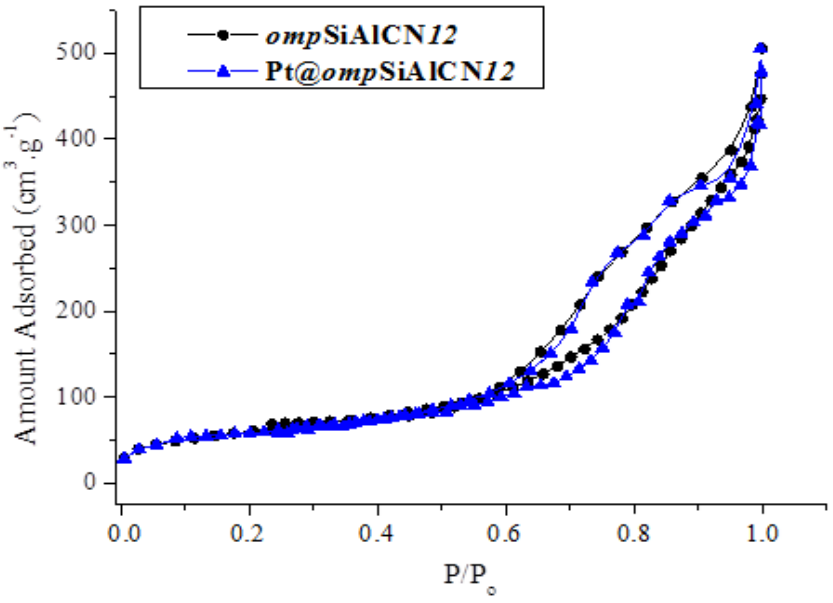

Figure IV-24: N_2 adsorption-desoprtion isotherms of **Pt/*omp*SiAlCN*12***.

2.2.5 H_2 evolution from $NaBH_4$ over Pt/ompSiAlCNxy nanocatalysts

The activity of **Pt/*omp*SiAlCN*xy*** (with x = Al = 1 and y = Si = 1 → 3) for the hydrolysis of **sodium borohydride** at **80°C** was investigated. Hydrolysis is an interesting probe reaction because the experimental conditions can be considered as being severe. In our laboratory, the mechanical stability is generally assessed in hydrolysis at 80°C, because the process offers the following features: very high rates of H_2 production on the catalytic sites, very alkaline solution (>10), and presence of water [306]. In other words, a catalyst that passes this test can then be considered for reactions requiring harsher conditions (water-gas-shift reaction, Fisher-Tropsch synthesis, or thermochemical water splitting).

It should be noticed that the catalytic ability of the Pt-free supports ***omp*SiAlCN*xy*** (with x = Al = 1 and y = Si = 1 → 3) was assessed and, as expected, they were found to be inactive in hydrolysis of $NaBH_4$.

The hydrogen generation results for **Pt/*omp*SiAlCN*xy*** (with x = Al = 1 and y = Si = 1 → 3) are presented in Figure IV-25. The hydrolysis starts immediately; no induction period is observed. This is in agreement with the metallic state of Pt as the occurrence of an induction period is generally observed with oxidized metals. Hydrogen generation rates (slope of the curves) of 1, 1 and 0.7 $mL.min^{-1}$ were measured for **Pt/*omp*SiAlCN*13***, **Pt/*omp*SiAlCN*12*** and **Pt/*omp*SiAlCN*11***, respectively. Such rates are consistent with the very low amount (1 wt%) of Pt. Expressed per gram of Pt, the rates are 6.7, 6.7 and 4.7 $L.min^{-1}.g_{Pt}^{-1}$ respectively, which is therefore an attractive performance. Accordingly, the **Pt/*omp*SiAlCN*xy*** catalysts have passed our first catalytic test and

thus, the SiAlCN ceramics are potential supports for catalytic applications taking place in severe experimental conditions.

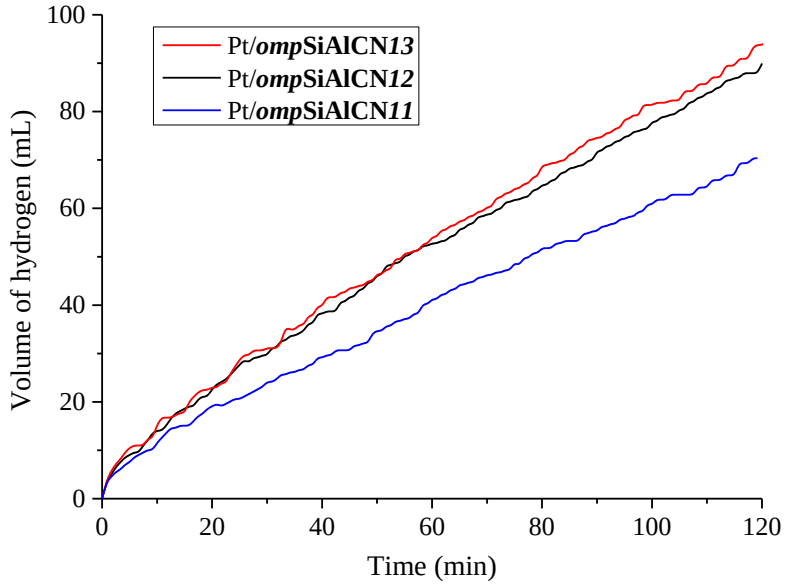

Figure IV-25: H_2 evolution by hydrolysis of **$NaBH_4$** in the presence of **Pt/*omp*SiAlCN*xy*** supported catalysts at 80°C.

Relatively high values of H_2 are generated from **$NaBH_4$** in the presence of **Pt/*omp*SiAlCN*xy*** which seems directly related to its textural properties. However, there is a lack of direct comparison on the catalytic performance among mesoporous PDCs. As a consequence, we decided to prepare PHPS-derived (ordered mesoporous) Si_3N_4 to be used as supports for Pt nanoparticles. Furthermore, we have synthesized Pt-supported CMK-3 to extrapolate and highlight the significant enhancement of the catalytic activity of the new Si_3N_4-based nanocatalysts.

3. PREPARATION OF Pt SUPPORTED ORDERED MESOPOROUS Si_3N_4

The design of silicon carbide/nitride (SiC/Si_3N_4) *via* the PDCs route offers a number of advantages [103], **among them** controlling the ceramic compositions and micro-/nanostructures (amorphous, crystalline or nanocomposite) and processing materials, in particular shape and morphology (dense or porous). **As shown in the first part of this chapter,** the PDCs route is particularly adapted to the preparation of periodic mesoporous inorganic materials in a large variety of composition. In the first part of this chapter, we used blended polymers: PEIA (Al(C)N precursor) and PHPS (Si_3N_4/Si precursor) to form ordered mesoporous SiAlCN materials. However, there is usually a lack of direct comparison on the catalytic performance among mesoporous supports. As a consequence, we decided to compare the performances of ordered mesoporous SiAlCN materials as

a support of platinum nanoparticles and of the derived nanocatalysts for the catalytic hydrolysis of $NaBH_4$ with those of the materials obtained separately from PEIA and PHPS. The use of PEIA did not allow preparing ordered mesoporous AlN as shown in Chapter II. Meso-/macroporous AlN are generated. Therefore, we did not consider this material. In contrast, we propose in the following part the use of PHPS to synthesize ordered mesoporous Si_3N_4. The latter was used as a support to grow Pt nanoparticles leading to the generation of nanocatalysts labelled Pt/*omp*-Si_3N_4. As previously seen in the first part of this chapter, these nanocatalysts have been tested for H_2 generation by hydrolysis of $NaBH_4$. The process scheme is illustrated in Figure IV-26. The performances are also compared to those obtained from Pt/CMK-3 nanocatalysts. The comparison allows to understand the behavior of ordered mesoporous PDCs-based nanocatalysts and highlight the efficiency (superior H_2 rate) and stability (easily recovered after H_2 generation) of the new proposed nanocatalyst in comparison to carbonaceous-based nanocatalysts.

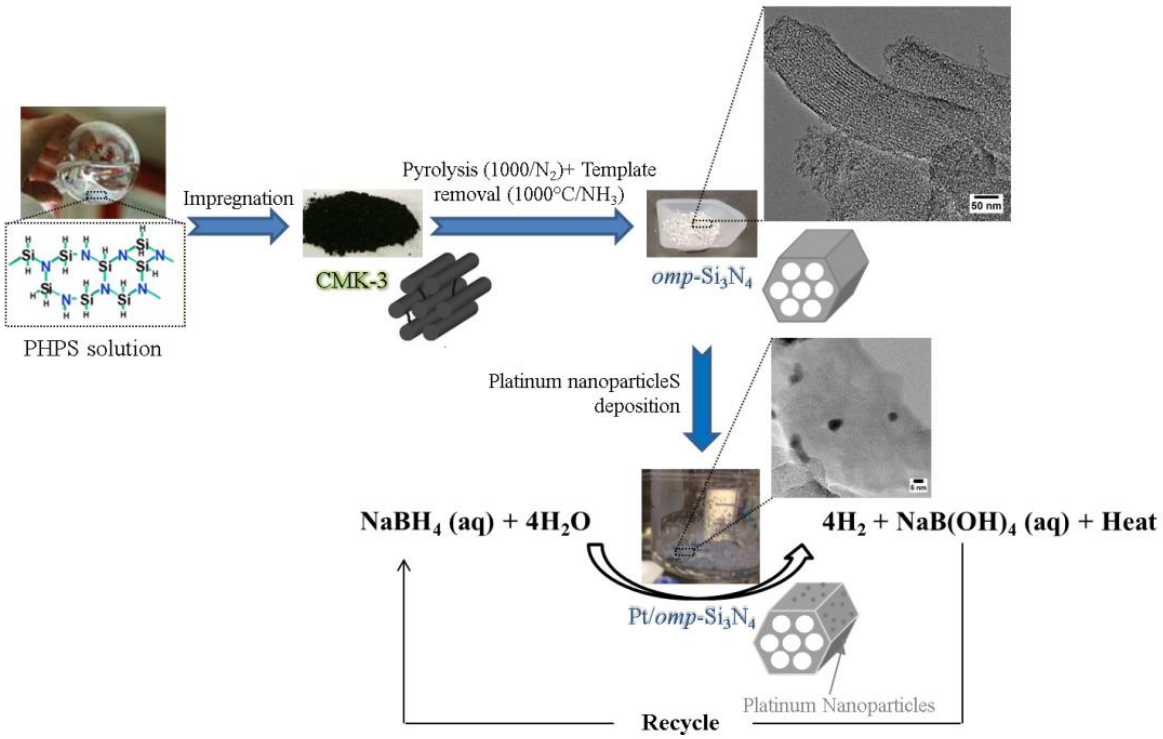

Figure IV-26: Overall synthetic path employed to generate Pt supported periodic mesoporous Si_3N_4 ceramics.

3.1. Experimental part

3.1.1 Materials

The polymeric precursor is unstable in air. Therefore, all manipulations are carried out under inert conditions. All ceramic products are handled in an argon-filled glove box (MBraun MB200B; O_2 and H_2O concentrations kept at <0.1 ppm) due to their high surface area and affinity for moisture before characterization. Argon (>99.995 %) is purified by passing through successive columns of phosphorus pentoxide, siccapent™, and BTS catalysts. Schlenk tubes are dried at 120°C overnight before pumping under vacuum and filling them with argon for synthesis. The chemical products are handled inside the argon-filled glove box. Toluene (99.85%, Extra Dry over Molecular Sieve, AcroSeal(R)) is obtained from Acros Organics. CMK-3 was purchased from ACS Materials®. Textural and structural parameters are reported in the first part of this chapter. Perhydropolysilazane in xylene (20 wt%) (PHPS, AQUAMICA NN-310) is provided by Mitsuya Boeki Ltd., Japan. The data of PHPS are reported in the first part of this chapter. For the preparation of the Pt supported catalysts and the hydrogen generation experiments, chloroplatinic acid hexahydrate ($H_2PtCl_6 \cdot 6H_2O$, Sigma-Aldrich), sodium borohydride ($NaBH_4$, Acros Organics), sodium hydroxide (NaOH, Carlo Erba) and deionized ultra-pure water (Milli-Q grade; resistivity > 18 MΩ cm) are used.

3.1.2 Preparation of ordered mesoporous Si_3N_4

Nanocasting of PHPS was carried out through an impregnation process in a Schlenk-type flask. 4.5 mL of the PHPS dissolved in xylene under stirring and added to 0.63 g of the CMK-3 template previously dehydrated at 150°C overnight at reduced pressure. The mixture was then stirred at 10°C for 48 h under static vacuum. After absorption of the polymer into the pores of the template, a filtration step was performed to selectively remove the PHPS molecules deposited outside while the capillary forces kept the PHPS molecules effectively inside the pores and then the solvent was slowly evaporated at low pressure at 30°C while PHPS crosslinks to generate a black powder labeled PHPS@CMK-3.

The polymeric composite was transferred into a silica tube inserted in a horizontal tube furnace (Nabertherm type RS 80/500/11, Germany). Subsequently, the sample was subjected to a N_2 cycle of ramping of 1°C.min^{-1} to 1000°C, dwelling there for 2 h, and then cooling to RT at 2°C.min^{-1} to convert the PHPS into a composite Si_3N_4/Si. After the polymer-to-ceramic conversion process, the composite underwent a final thermal treatment under NH_3 to remove the carbon template through a cycle of ramping of 2°C min^{-1} to 1000°C, dwelling there for 5 h, and then cooling to RT at 5°C.min^{-1} to generate slightly grey samples ***omp*-Si_3N_4.**

3.1.3 Preparation of nanocatalysts

Here we exactly replicated the process described in the first part to deposit Pt nanoparticles on the **Si_3N_4** support. The successful loading of Pt on *omp*-Si_3N_4 giving the sample **Pt/*omp*-Si_3N_4** is verified by HRTEM, EDX and elemental mapping as will be discussed in section 3.2. For comparison, Pt-supported CMK-3 (SSA = 983 $cm^2.g^{-1}$) has been also prepared through the same process. In details, 103 mg of CMK-3 was milled, transferred in 3.5 mL of distilled water, and ultrasonicated for 1 h in ambient conditions. Then, 1 mL of an aqueous solution of $H_2PtCl_6.6H_2O$ (2.44×10^{-3} M) was added to the dispersion of CMK-3.

3.1.4 Experiments

Thermogravimetric analyses (TGA) of the polymer-to-ceramic conversion are recorded on a Setaram TGA 92 16.18. Experiments are performed at 2°C min^{-1} up to 1000°C (dwelling time of 5 h) under ammonia using silica crucibles (sample weight of ~40 mg) at ambient atmospheric pressure.

Fourier transform infrared (FT-IR) data of PHPS are obtained from a Nicolet Magna 550 Fourier transform-infrared spectrometer in a KBr matrix (dried at 120°C in air).

The small-angle powder X-ray diffraction pattern (SA-XRD) is recorded using a Philipps PW 3040/60 X'Pert PRO X-ray diffraction system operating at 30 mA and 40 kV, and between 0.7° and 5.0° with a step size of 0.0167°. In addition, powder X-ray diffraction is applied from 20° to 80° to identify the global structure of the Si_3N_4 phase.

SAXS experiments were performed with an in-house setup of the *Laboratoire Charles Coulomb, "Réseau X et gamma", Université Montpellier 2, France*. A high brightness low power X-ray tube, coupled with aspheric multilayer optic (GeniX^{3D} from Xenocs) was employed. It delivers an ultralow divergent beam (0.5mrad). Scatterless slits were used to give a clean 0.8mm beam diameter (35 Mphotons/s) at the sample. We worked in a transmission configuration and scattered intensity was measured by a Schneider 2D imageplate detector prototype, at a distance of 1,9m from the sample for SAXS configuration, 0.2m from the sample for WAXS configuration. All Intensities were corrected by transmission and the empty cell contribution was substracted. The SA-XRD pattern recorded using a Philipps PW 3040/60 X'Pert PRO X-ray diffraction system operating at 30 mA and 40 kV, and between 0.7° and 5.0° with a step size of 0.0167°.

The mesoporous materials are observed by SEM (Hitachi S800) equipped with energy-dispersive spectroscopy analysis (EDX). The Brunauer–Emmett–Teller (BET) method was used to calculate the specific surface area. The pore-size distribution is derived from the desorption branches of the isotherms using the *Barrett–Joyner–Halenda* (BJH) method. The total pore volume (Vp) is estimated from the amount of N_2 adsorbed at a relative pressure of (P/P_0) 0.97. Samples for TEM are

ground under ethanol and the resulted dispersion was transferred to a lacey or holey carbon film fixed on a 3 mm nickel grid. High-resolution TEM (HRTEM) and electron diffraction (ED) studies are performed using a FEI Tecnai G^2 30 UT (LaB_6) microscope operating at 300 kV with a 0.17 nm point resolution.

The catalytic ability of Pt/*omp*-Si_3N_4 is assessed in hydrogen production by hydrolysis of sodium borohydride in our 'harsh' conditions, and the hydrogen generation measurement is performed according to the general procedure we reported in the first part of this chapter. Typically, the catalyst (16 mg) is milled and sieved, and then transferred into a reactor (glass tube) that is sealed with a silicon septum. The reactor is connected to a water-filled inverted burette (water colored in blue), *via* a cold trap for steam, maintained at 0°C. Then, it is immersed in an oil bath kept at 80°C. To start the hydrogen generation, 1 mL of a stabilized (2 wt% NaOH) aqueous solution of $NaBH_4$ (120 mg) is injected over the catalyst. Hydrogen starts to evolve rapidly and the evolution is video-recorded for 2 h, to be then computationally analyzed post-hydrolysis.

3.2. Results and discussion

3.2.1 Preparation and characterization of ordered mesoporous Si_3N_4

Ordered mesoporous Si_3N_4 with a cubic lattice, a specific surface area of 384 $m^2.g^{-1}$ and a pore volume of 0.71 $cm^3.g^{-1}$ have been reported from polycarbosilane in one paper [307]. Here, we used poly(perhydropolysilazane) (PHPS, $[SiH_2\text{-}NH]_n$) to form ordered mesoporous Si_3N_4. We have replicated the process that allowed us to produce ordered mesoporous SiAlCN materials.

Nanocasting provides access to mesopores by replicating the nanostructure of CMK-3 into a locally ordered pore system through (i) the impregnation of the pore template with PHPS solution (20 wt% in xylene) at 10°C for 48 h under static vacuum, (ii) the subsequent filtration step that consists to selectively remove the PHPS molecules deposited outside while the capillary forces kept the PHPS molecules effectively inside the pores, (iii) the post-treatment of the infiltrated template at low pressure and 30°C in order to slowly remove the solvent while PHPS crosslinks, (iv) the pyrolysis under nitrogen at 1000°C (dwelling time of 2 h) of the composite PHPS/CMK-3 to convert the PHPS confined in the porosity of CMK-3 into a composite Si_3N_4/Si, and (v) the heat-treatment under ammonia (dwelling time of 5 h) to remove CMK-3 involving a weight loss of 54.5% while the title sample is generated.

They display a typical chemical formula determined by Energy Dispersive X-ray Spectroscopy (EDXS) of $Si_{3.0}O_{0.1}N_{4.4}$. The relatively low O content is related to the precautions which are taken to analyse the material: samples are kept in an argon-filled glove box to avoid

moisture adsorption. Furthermore, CMK-3 was heat-treated under vacuum to remove moisture before impregnation of PHPS. Here, there is no residual carbon and no excess of Si: the Si:N ratio is almost that one found in Si_3N_4. This is probably related to the second treatment under ammonia which is achieved to remove CMK-3. Nitridation of the silicon present in the material after thermal conversion of PHPS under nitrogen at 1000°C probably occurs during this step to form near-stoichiometric **Si_3N_4** after heat-treatment under ammonia [308, 309]. The absence of carbon is confirmed by the heat-treatment in air of the sample which does not exhibit any weight change in the temperature domain where CMK-3 is oxidized (350-550°C) (Figure IV-27).

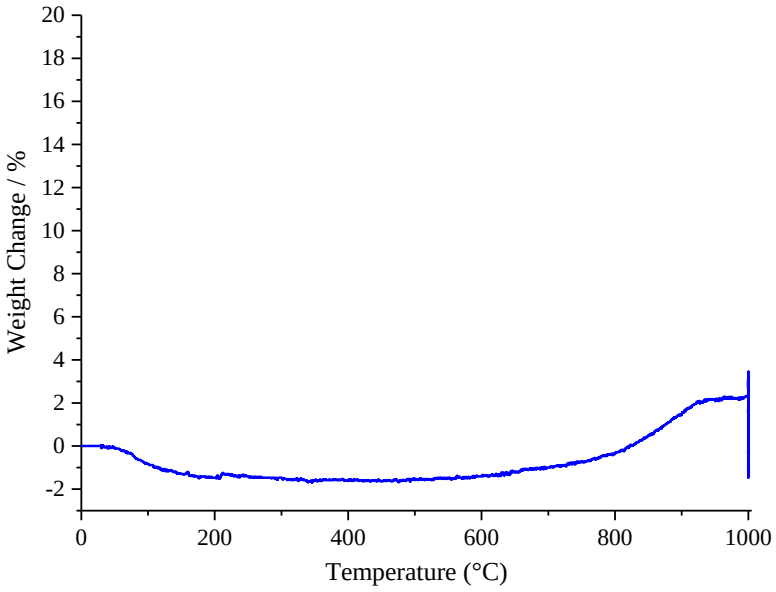

Figure IV-27: TGA curve of ***omp*-Si_3N_4** recorded under static air up to 1000°C (moisture level: 36%).

The morphology and structure of the sample ***omp*-Si_3N_4** are characterized using Scanning Electron Microscopy (SEM) as illustrated in Figure IV-28. The sample is generated as highly porous powder that is composed of agglomerated and elongated blocks.

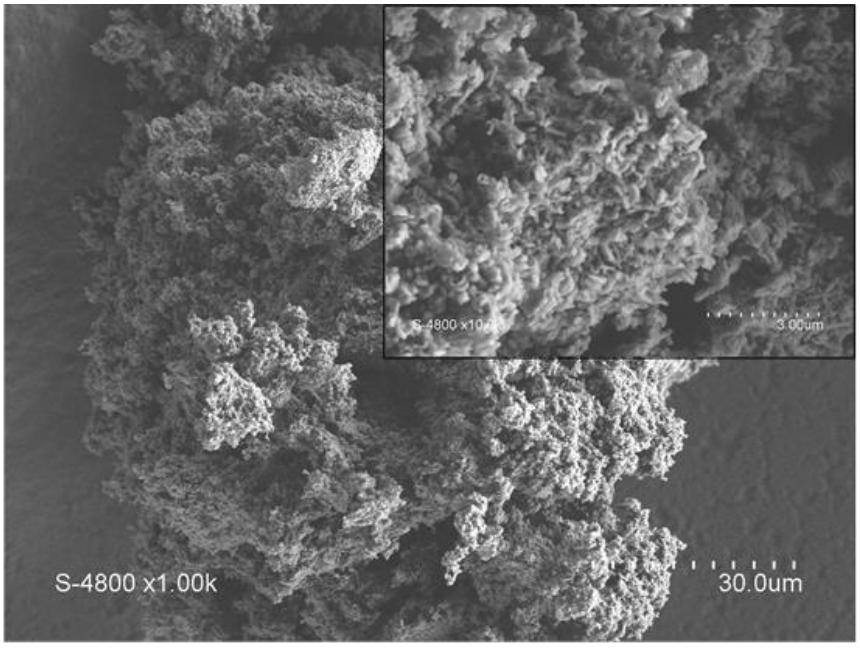

Figure IV-28: SEM image of *omp*-Si_3N_4.

As-obtained samples are amorphous based on the absence of diffraction peaks in their powder X-Ray Diffraction (XRD) pattern (Figure IV-29). Crystallization into α-Si_3N_4 occurs by heat-treatment under N_2 at 1700°C as revealed with the XRD pattern of the sample heat-treated at 1700°C and labeled ***omp*-Si_3N_4_1700** (Figure IV-29). Crystallization is associated with the appearance of whiskers, as shown by the SEM image in the inset of Figure IV-29, which indicates the occurrence of vapor phase reactions at high temperature as generally reported for PHPS-derived ceramics [310].

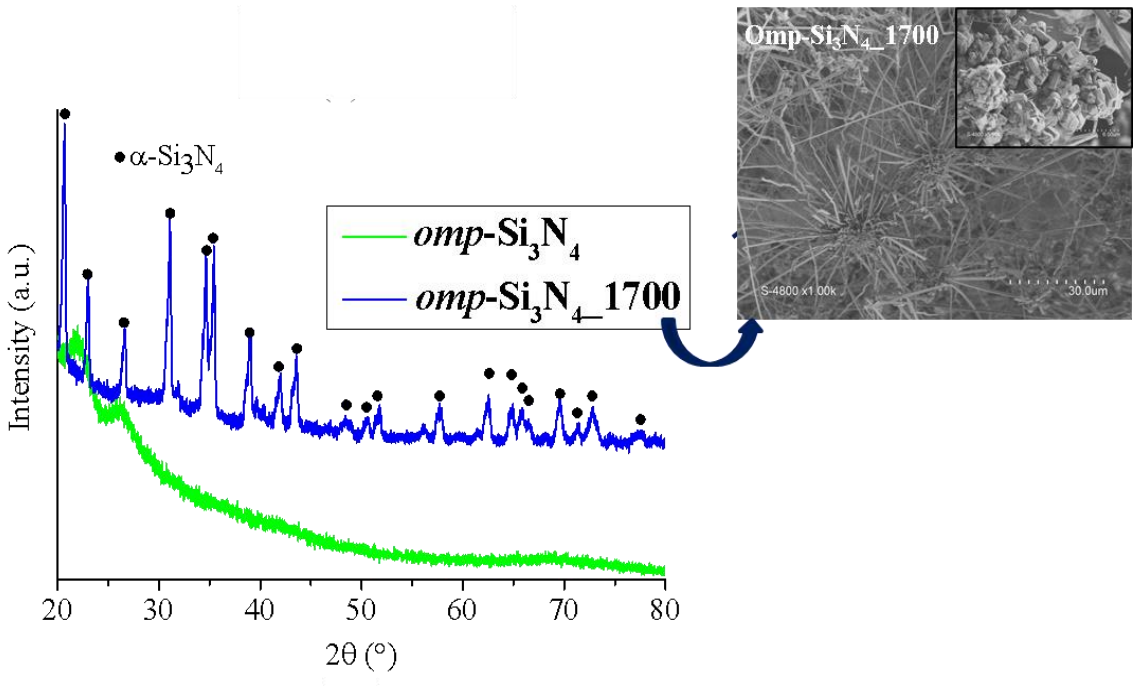

Figure IV-29: XRD patterns of ***omp*-Si_3N_4** and ***omp*Si_3N_4_1700**.

Figure IV-30 depicts the corresponding low and high magnification Transmission Electron Microscope (TEM) images of ***omp*-Si_3N_4**. Figure IV-30-a shows that the sample is an assembly of elongated cylinders with a length of ~500 nm and a majority of cylinders with diameter less than 100 nm. We called these cylinders nanoblocks. In 2D projection (Figure IV-30-b), the sample shows channels that are arranged in a linear array similarly to ordered mesoporous materials with hexagonal symmetry. The distance between the centers of the adjacent channels is ~5 nm. To confirm the TEM observations, the samples have been analyzed by Small-Angle X-ray Diffraction (SA-XRD), Small-Angle X-ray Scattering (SAXS) and nitrogen gas adsorption-desorption measurements.

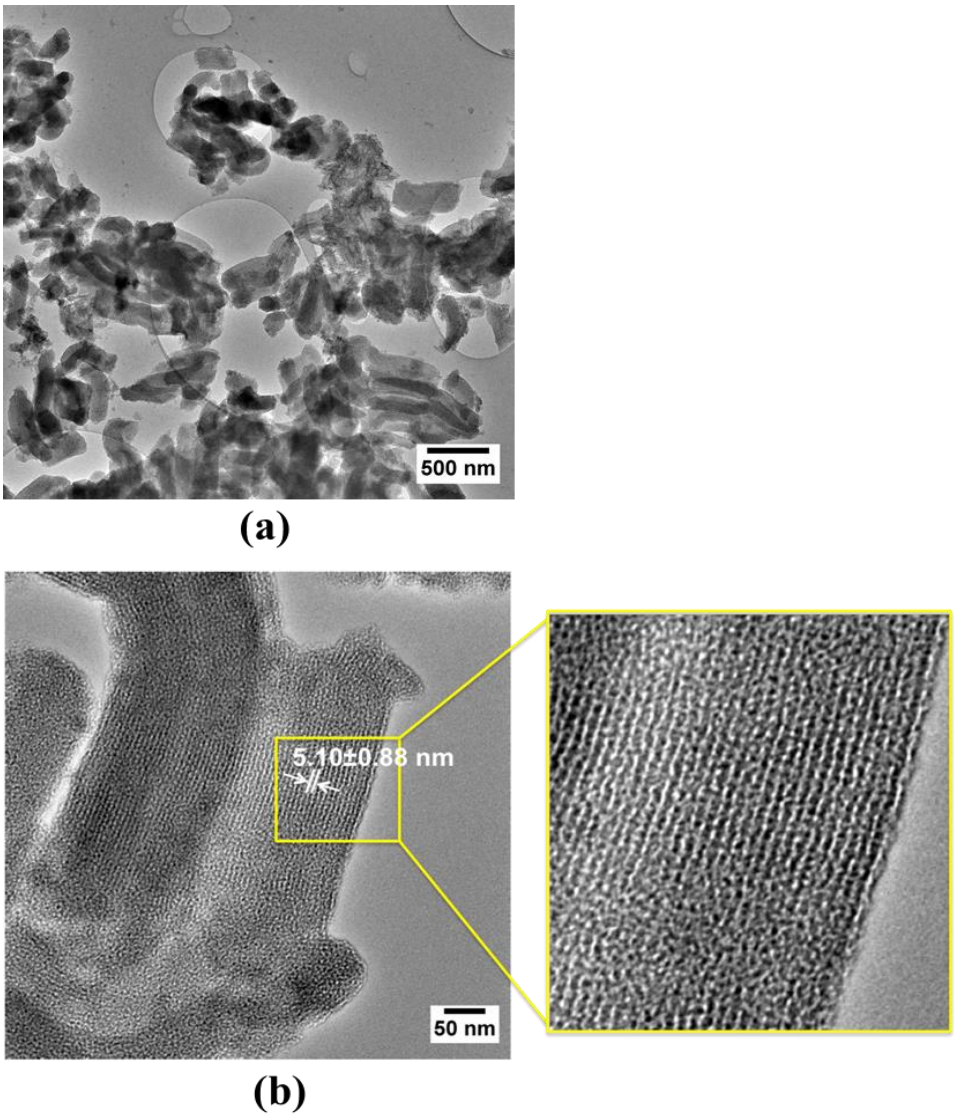

Figure IV-30: (a) Low and (b) high magnification TEM images of ***omp*-Si_3N_4**.

The SA-XRD pattern confirms the ordered structure of the specimens (Figure IV-31). A clear diffraction peak at $2\theta = 1.39°$ corresponding to d = 6.35 nm is observed. This peak is assigned to the (100) reflection of the 2D hexagonal lattice (space group *P6mm*) with a lattice parameter a_{100} = 7.3

nm. Other peaks characteristic of the hexagonal structure and observed in CMK-3 do not appear because of a partial loss of the order in ***omp*-Si_3N_4** due to the impregnation-heat-treatment cycle which inherently involves loss of matter. The SAXS pattern of ***omp*-Si_3N_4** (Figure IV-31 as inset) that displays a well-resolved (100) peak at the *q* vector of 0.99 also demonstrates the presence of ordered hexagonal pore arrays with mesoporous structure.

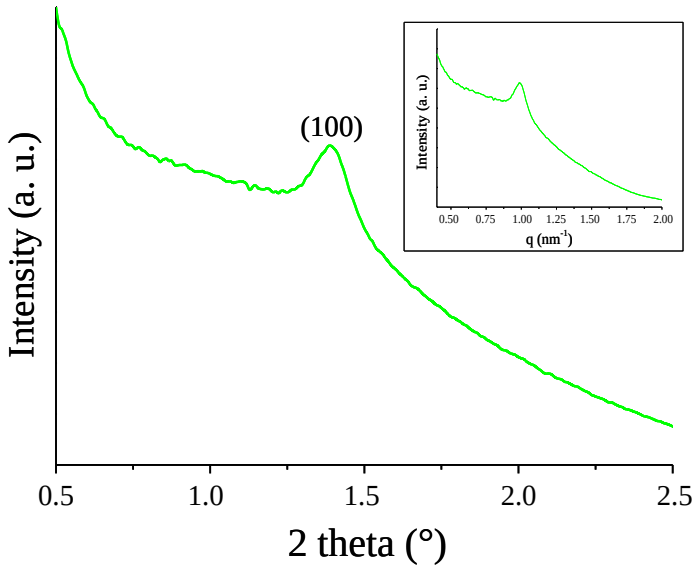

Figure IV-31: SA-XRD and SAXS patterns (as inset), (Cu Kα radiation) of ***omp*-Si_3N_4**.

The analysis of the N_2 adsorption-desorption isotherms of ***omp*-Si_3N_4** (Figure IV-32) allows to estimate the pore-network dimension and structure of nanoblocks. The isotherms show IV type-curves in which the adsorption and desorption isotherms do not coincide over the region of relative pressure *P/Po*= 0.4-0.72. The IV-type isotherms suggest that the samples have uniform mesoporous channels [262, 271]. At relative pressure below 0.1, the relatively high uptake implies the presence of micropores. The type of the adsorption hysteresis is relatively complex and usually speculative. We can suggest that it represents a mixture of H1 type (typical for SBA-15 [311]) and H2-type which is due to the interconnectivity of the pores [312]. Therefore, we can consider that ***omp*-Si_3N_4** samples are mesoporous materials with interconnected pores. A specific BET surface area as high as 772.4 $m^2.g^{-1}$ is measured. The total pore volume determined from the amount of nitrogen adsorbed at *P/Po* = 0.97 is as high as 1.19 $cm^3.g^{-1}$. The pore size distribution (PSD) was calculated from the desorption branch by means of the *Barett-Joyner-Halenda* method. A uniform diameter of 4.83 nm is found (Figure IV-32 as inset). In comparison to the textural properties of CMK-3, the values are logically lower but they are in the range of the highest values reported for PDCs to our knowledge. This means that PHPS solution is efficiency infiltrated in the porosity of CMK-3 most probably due

its low viscosity and the good wettability. The high BET surface area, tailored mesoporous structure and large pore volume of ***omp*-Si_3N_4** are positive features for heterogeneous catalysis. Such advantage is of course beneficial to catalytic hydrolysis of $NaBH_4$.

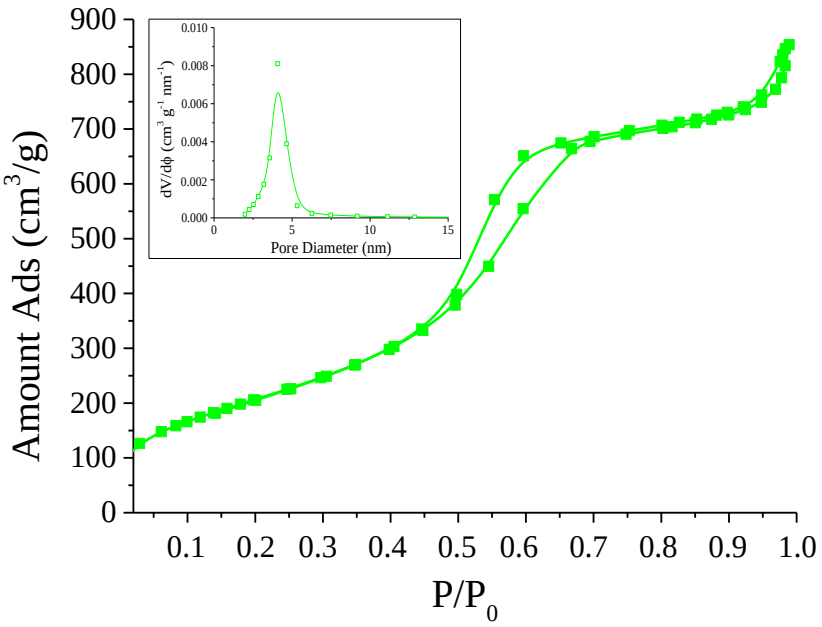

Figure IV-32: N_2 adsorption-desorption isotherms recorded at 77K of ***omp*-Si_3N_4.** Pore size distribution as inset.

The TGA profile presented in Figure IV-9 shows that CMK-3 is eliminated at high temperature above 800°C under NH_3. At this temperature, the ceramic conversion of PHPS is almost achieved. Therefore, we tentatively performed the heat-treatment of the composite PHPS/CMK-3 obtained after nanocasting directly under NH_3 (dwelling time of 5 h) to convert PHPS into a ceramic while the template was removed. This allowed us to suppress one step in the process. In that case, a hydrogenated compound with composition close to Si_3N_4 is obtained [313]. We obtained a N_2 adsorption-desorption isotherms of IV-type similarly to mesoporous materials with a specific surface of 715.8 $m^2.g^{-1}$, a mean pore size of 4.85 nm (with a certain proportion of macropores) and a pore volume of 0.94 $cm^3.g^{-1}$ (Figure IV-33). Because of values slightly lower than those obtained with the two-step heat-treatment and the presence of macropores, we used the sample labelled ***omp*-Si_3N_4** obtained with the two-step heat-treatment as a support to synthesize Pt nanoparticles.

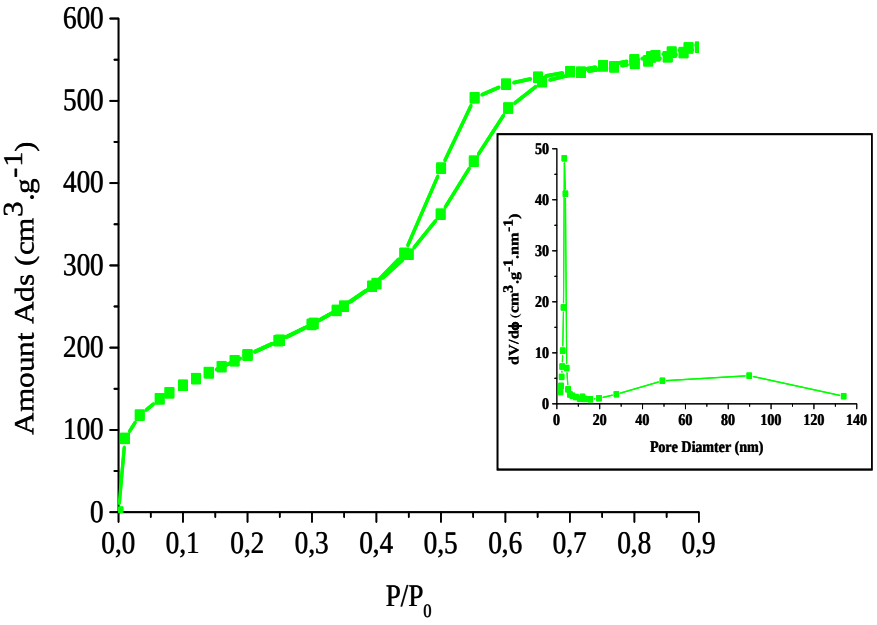

Figure IV-33: N_2 adsorption-desorption isotherms recorded at 77K of ***omp*-Si_3N_4** by direct heat-treatment under ammonia of **PHPS@CMK-3** composite. Pore size distribution as inset.

3.2.2 Characterization of Pt/omp-Si_3N_4 nanocatalysts

TEM images of **Pt/*omp*-Si_3N_4** are shown in Figure IV-34 and the corresponding histogram of metal nanoparticles is presented in Figure IV-35. The presence of Pt in the form of circular nanoparticles is confirmed by TEM analyses. We clearly observe a majority of homogeneously dispersed Pt NPs with a circular shape on the surface of the Si_3N_4 nanoblocks (Figure IV-34-a and white arrows in Figure IV-34-b) and a few ones that tend to agglomerate are found. Figure IV-34-c shows one Pt nanoparticle supported on the surface of the nanoblocks. Lattice fringes are clearly distinguishable, emphasizing a lattice spacing of 0.24±0.03 nm, which corresponds to the (111) crystalline planes of Pt.

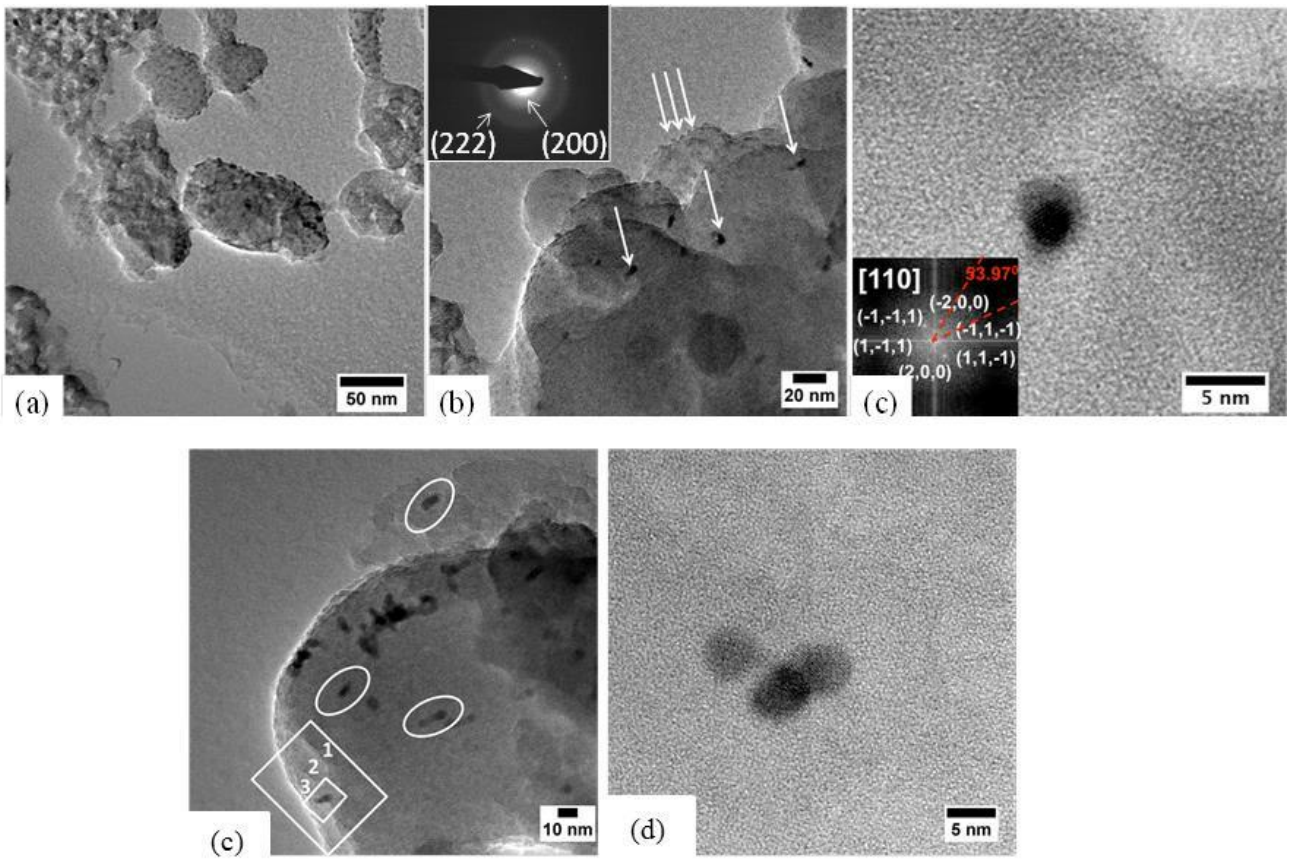

Figure IV-34: TEM images of **Pt/*omp*-Si_3N_4.**

The mean size of the Pt nanoparticles distributed on the surface of ***omp*-Si_3N_4** has been found to be 7.06±1.07 nm, as shown in the histogram of the nanoparticles diameters (Figure IV-35), for which we have considered 100 nanoparticles. The histogram emphasizes the low size distribution of the NPs (comprised between 5-9.5 nm), which confirms that the support contains a homogeneous size distribution of mesopores.

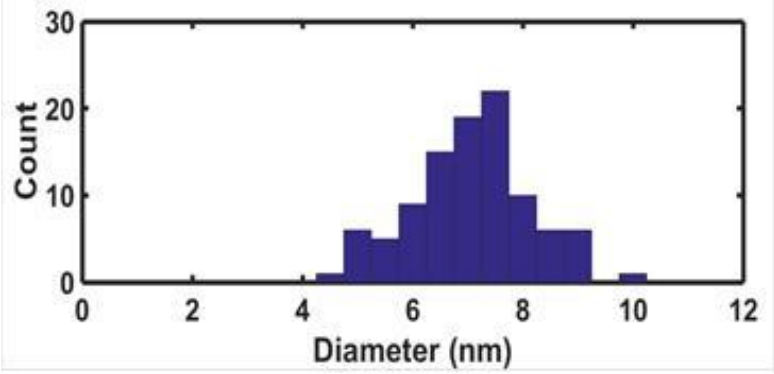

Figure IV-35: Particle size distribution.

Elemental mapping (Figure IV-36) reveals the presence of silicon and nitrogen from the support as well as the uniform distribution of Pt on ***omp*-Si_3N_4**. EDX spectroscopy indicates the presence of 0.06 at% of Pt (0.61 wt. %).

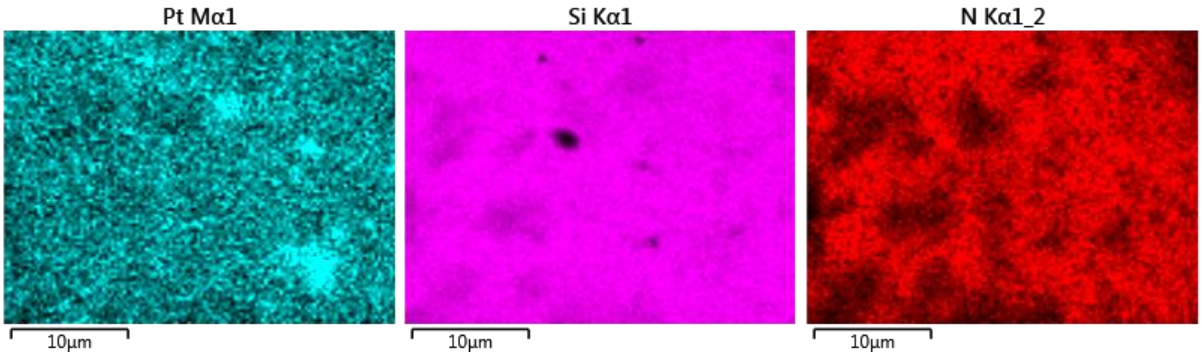

Figure IV-36: Elemental mapping of Pt@*omp*-Si_3N_4.

More TEM images of **Pt/*omp*-Si_3N_4** are displayed in Figure IV-37 where we have observed a very high mobility of the nanoparticles on the surface. Indeed, the particles are extremely sensitive to the electron beam. In the series of images presented, some Pt NPs undergo a process of crystallization under the electron beam (particle A). We have also observed that, under irradiation with the electron beam, a process of amorphization is also possible (particle B). The 'neck' growth occurs to reduce the chemical potential at the particle contact points [314]. A 'neck' formation mechanism is also formed between particles B and C, who undergo through a process of further crystallization under the electron beam.

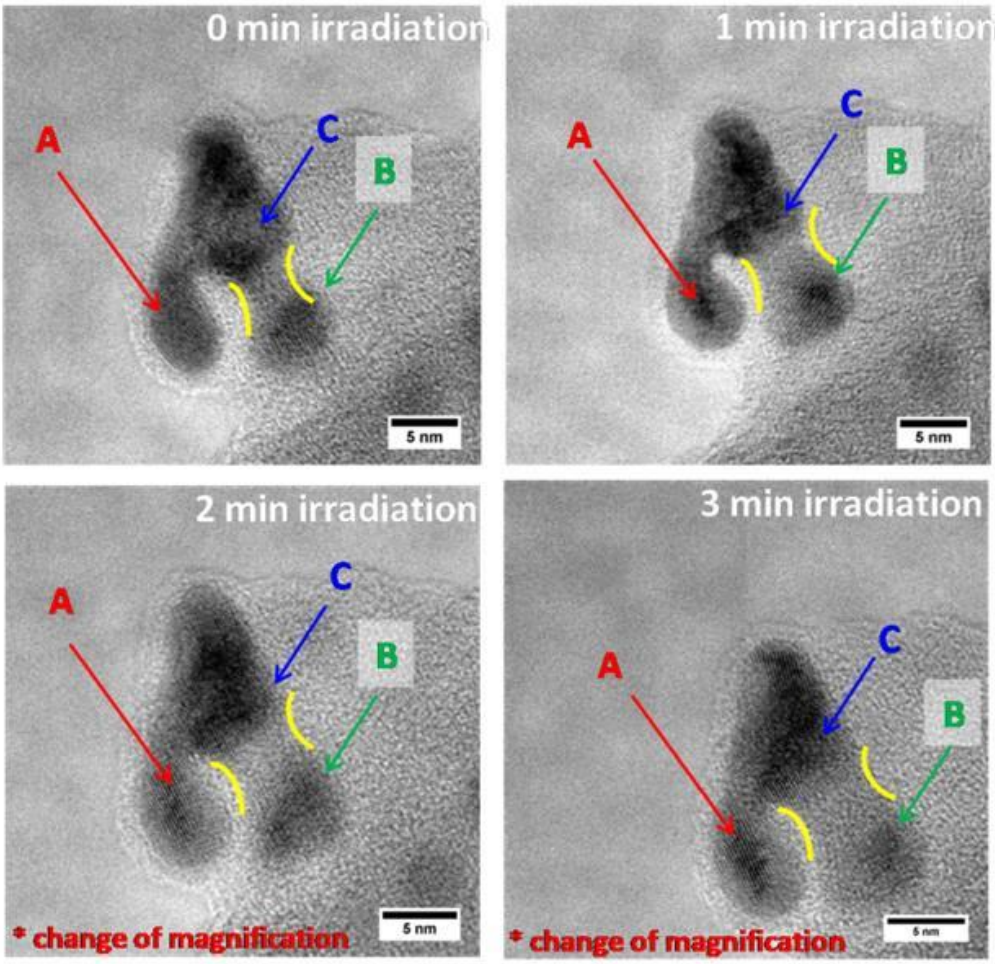

Figure IV-37: Evolution of the nanostructure of **Pt NPs** under electron irradiation with TEM.

3.2.3 H_2 evolution from $NaBH_4$ over Pt/ompSi_3N_4 nanocatalysts

The activity of **Pt/*omp*-Si_3N_4** for the hydrolysis of sodium borohydride was investigated at 80°C, in a very alkaline solution (pH>10), and with the presence of water. It is important to mention that the catalytic ability of the Pt-free supports ***omp*-Si_3N_4** was assessed and, as expected, they were found to be inactive. The hydrogen generation results for Pt/*omp*-Si_3N_4 are presented in Figure IV-38.

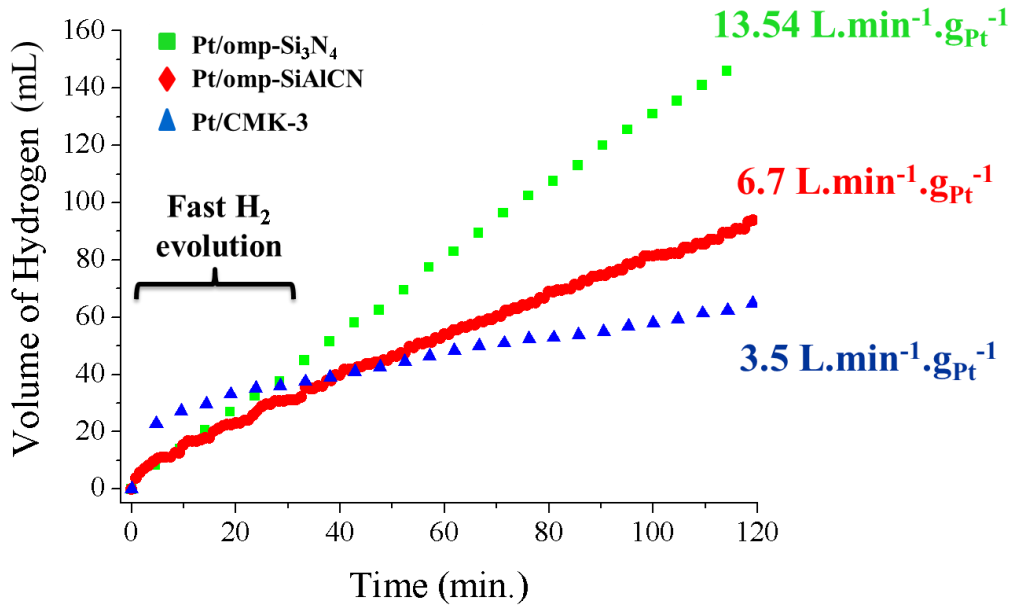

Figure IV-38: Catalyzed hydrogen generation by hydrolysis of sodium borohydride at 80°C over **Pt/*omp*-Si_3N_4, Pt/*omp*-SiAlCN** and **Pt/CMK-3**.

The hydrolysis starts immediately; no induction period is observed, which is in agreement with the metallic state of Pt as the occurrence of an induction period is generally observed with oxidized metals [22]. A hydrogen generation rate (slope of the curves at a conversion <50%) of 1.3 mL.min^{-1} was measured. Expressed per gram of Pt, the rate is 13.54 L.min^{-1}.g_{Pt}^{-1}, which is a high performance, especially when compared to many of the supported platinum catalysts reviewed elsewhere [16]. A direct comparison to the literature is somehow complicated because of the discrepancies in the experimental conditions, but it may give a good idea about the aforementioned performance. For example, hydrogen generation rates of 0.2, 0.7 and 1.6 L.min^{-1}.g_{Pt}^{-1} in the presence of 1 wt% Pt/γAl_2O_3, 1 wt% Pt/C and 1 wt% Pt/TiO_2, respectively, were reported at 40°C for diluted $NaBH_4$ solutions [315]. We have also compared with the catalytic hydrolysis of ammoniaborane. First, Zhou *et al.* reported activation energy of 31.6 kJ.mol^{-1} over Ni nanoparticles supported on carbon [316] which is indicative of a hydrogen generation rate around 5.6 L.min^{-1}.g_{Ni}^{-1} at 80°C. Second, Metin *et al.* reported similar activation energy (34 kJ.mol^{-1}) for Ni/SiO_2 nanocatalysts [317] which supposes a hydrogen generation rate of about 5 L.min^{-1}.g_{Ni}^{-1} at 80°C.

Moreover, we have compared the performance of **Pt/*omp*-Si_3N_4** to that of **Pt/CMK-3** with 0.09 at% of Pt as measured by EDX. Indeed, Pt/CMK-3 was tested in the same conditions (Figure IV-38). The hydrogen evolution is markedly different from that observed with the Si_3N_4-based nanocatalyst. During the first minutes, the hydrogen release is fast: this is explained by the catalytic

activity of the Pt nanoparticles as well as some contribution of the acid groups available on the surface of the carbonaceous support. However, this fast step is soon followed by a process with slow kinetics. Visual inspection of the reactor showed that the carbonaceous support favorably adsorbs water and significantly swells. The consequence is that the diffusion of the anions BH_4^- and $B(OH)_4^-$ is negatively affected; accordingly, the surface reactions are restricted, the borates desorption is hindered (leading to a catalyst surface "poisoning") and the hydrolysis kinetics are decreased. Expressed per gram of Pt, the hydrogen evolution rate is 3.5 $L.min^{-1}.g_{Pt}^{-1}$. In other words, the adsorption/swelling ability of carbon is a drawback in our experimental conditions (excess of water and high temperature) as it leads to harsh experimental conditions in the vicinity of the platinum nanoparticles, which makes then the catalytic reaction more challenging. In contrast, these phenomena do not appear with the **Pt/*omp*-Si_3N_4** nanocatalysts. As a matter of fact, *omp*-Si_3N_4 is a most suitable support for the aforementioned reaction. Considering the recyclability of the borate, the proposed nanocatalyst may be viewed as an effective hydrogen source to meet the overall energy requirements for civil vehicles applications such as for small Unmanned Aerial Vehicles (UAVs). However, these nanoblocks have necessary some difficulties in practical use, *i.e.* in the scale of the demonstrator reactor. Within this context, further investigations are under progress to prepare monolithic Si_3N_4 with tailored porosity and to study their catalytic performances as well as their reusability in operating conditions.

4. CONCLUSION

Periodic mesoporous silicon-aluminum-carbon-nitrogen frameworks have been prepared and characterized to be used as catalytic support of metal (nano)particles. Samples displaying *P6mm* hexagonal symmetry were synthesized by a solvent **nanocasting** route using mesoporous carbon (**CMK-3**) as hard template and blended polymers with various and controlled Al:Si ratios prepared through a simple and cost-effective procedure from poly(perhydridosilazane) and poly(ethyliminoalane) as silicon nitride (Si_3N_4) and aluminium carbonitride (Al/C/N) precursors, respectively. The solution infiltration-ceramic conversion-template removal cycle performed under nitrogen at 1000°C (2 h, ceramic conversion) then in NH_3 atmosphere at 1000°C (5 h, template removal) resulted in the formation of periodic mesoporous Si/Al/C/N frameworks with surface areas of 182 to 326 $m^2.g^{-1}$, a pore size distribution of 4.1-5.9 nm and pore volumes varying from 0.51 to 0.65 $cm^3.g^{-1}$. By characterization using electron microscopy, X-ray diffraction, N_2 sorption, chemical analyses, and high temperature thermogravimetric analysis, it was demonstrated that the amorphous micron-size powders display excellent mesopores uniformity and periodicity depending on the ceramic yield and therefore on the Al:Si ratio fixed during the polymer preparation. The materials

show almost no mass change up to 1400 - 1470°C in flowing N_2 and the behavior in air up to 1000°C is closely dependent on the Al:Si ratio.

Moreover, using the same protocol we synthesized highly **ordered mesoporous silicon nitride** in the form of nanoblocks. They displayed a surface area as high as 772.4 $m^2.g^{-1}$, a pore size distribution of 4.85 nm and a pore volume of 1.19 $cm^3.g^{-1}$.

The as-obtained ***omp*SiAlCN** and ***omp*Si_3N_4** ceramic powders were then considered as potential **catalyst supports** to synthesize and disperse **Pt (nano)particles**. Such highly stable mesoporous materials allowed acting as a pore-size-controlling support. The Pt (nano)particles were thus supported by powder impregnation and successfully assessed in our probe reaction, *i.e.*, **hydrolysis of alkaline aqueous solution of sodium borohydride at 80°C**.

High hydrogen rates have been measured for these materials. The performance is even significantly superior than that obtained with CMK-3 supported Pt NPs which are, in addition, difficult to recover after reaction. Based only on the H_2 evolution, the sample ***omp*-Si_3N_4** is clearly the best candidate for the catalytic hydrolysis of **$NaBH_4$**. However, several points have to be highlighted:

1) The evolution of the textural properties of the support after H2 production has to be studied
2) The behavior of platinum nanoparticles, their sinterability and growth is not known.
3) H2 production after successive cycles must be investigated
4) There is a limited practical use of powders if we target the production of **civil vehicle applications such as for small Unmanned Aerial Vehicles (UAVs)**. Monoliths are required.

Such studies are under investigation.

V-

SiAlCN AND SiBCN:FROM ELABORATION TO APPLICATION

V- SiAlCN and SiBCN:from elaboration to application....190
1. Introduction....194
2. Synthesis and characterization of “home-made” Al-modified polycarbosilazanes....195
2.1. Experimental part....195
2.1.1 Materials....195
2.1.2 Synthesis of polyaluminosilazanes-derived SiAlCN ceramics....195
2.1.3 Experiments....197
2.2. Results and discussions....197
2.2.1 Synthesis and characterization of polyaluminosilazanes....197
2.2.2 Polyaluminosilazanes-to-SiAlCN conversion....207
2.2.3 PMVAZ structure evolution: RT→ 1000°C....211
2.2.4 Characterization of SiAlCN: 1000→ 1800°C....214
3. Microcellular foams elaboration....223
3.1. Introduction....223
3.2. Experimental part....223
3.2.1 Materials....223
3.2.2 Preparation of foams....223
3.2.3 Experiments....224
3.3. Results and discussion....225
3.3.1 Preparation of SiAlCN microcellular foams....225
3.3.2 Characterization of SiAlCN microcellular foams....227
4. Synthesis and characterization of Al- and B-modified commercial polysilazanes....235
4.1. Experimental part....235
4.1.1 Materials....235
4.1.2 Synthesis of Al- and B-modified polycarbosilazanes....235
4.1.3 Polymer-to-ceramic conversion....236
4.2. Results and discussion....237
4.2.1 Preparation and characterization of Al- and B-modified polycarbosilazanes....237
4.2.2 PAZ/PBZ-to-SiAlCN/SiBCN conversion....240
5. Conclusion....250

1. INTRODUCTION

In Chapter IV, we have demonstrated the potentialities of using SiAlCN ceramics as catalyst support. Through this study, we also demonstrated the excellent stability of their amorphous network against heat-treatment and oxidation. Such materials are obtained from a **building block approach** consisting of mixing homogeneous organoaluminum and organosilicon precursors. This approach is very simple in terms of chemistry. However, it presents some **drawbacks.** In particular, **shaping processes, including plastic forming, are difficult to achieve**. In addition, **phase segregation** occurs early in the elaboration process (~1400°C). In this chapter, we investigate the preparation of **SiAlCN** ceramics from **single-source precursors** and we demonstrate that the latter can be shaped by plastic forming and deliver ceramics with an amorphous network stable at high temperature. This "**single-source precursor**" approach is very interesting because of the ability to: i) **control the composition** of polymers and derived ceramics at the atomic scale, ii) introduce attached functional groups or substituents which **are beneficial for** the **shaping ability** of the polymer processing properties as well as their pyrolysis behavior, and iii) determine the **functionality of the derived ceramics**. For example, **SiCH=CH$_2$**, **SiH** and **NH** groups offer the opportunity to attach supplementary elements to the polymer structure. Aluminum, for example, may be introduced by hydroalumination of CH=CH$_2$ groups, using alane Lewis-base adducts. Accordingly, the molecular weights for polymers may be increased *via* hydrosilylation (SiH + SiCHCH$_2$). Reactions may involve dehydrocoupling with formation of Si-N units (SiH + NH). In contrast, Si- and N- bounded substituents, such as methyl or ethyl, are chemically inert and are usually introduced to adjust the needed physical and chemical properties. Therefore we have a quasi-infinite latitude to tailor the structure of polymers; therefore the ceramics because **properties of PDCs** are strongly related to their **molecular origin**. The **Si/Al/C/N system** represents a ceramic material with an **amorphous structure** made of covalent bonds that is stable at high temperatures. Only one paper reports the development of the **Si/Al/C/N system from single-source precursors** [197].

In the first part of our work, individual steps of the procedure to prepare polymer-derived SiAlCN ceramics were carefully investigated. In particular, we describe the synthesis of a series of polyaluminosilazanes by reaction of ammonia (=network building agent) with dichlorosilanes followed by a reaction with an alane complex. As-obtained polyaluminosilazanes were chemically and structurally characterized then pyrolyzed at 1000°C under N_2 to deliver amorphous SiAlCN materials. A systematic mechanistic study of the polymer-to-ceramic conversion of the polyaluminosilazanes in N_2 atmosphere is provided. The individual chemical processing steps and the related structural and chemical changes occurring during the polymer-to-ceramic conversion are

investigated in details using a combination of *in-situ* thermo-analytical experiments coupled with *ex-situ* solid-state NMR and FT-IR spectroscopy. Then, more structural investigations are reported to follow the evolution of the **amorphous SiAlCN network** into a multiphase component made of **SiC**, **Si_3N_4**, **AlN** and **free carbon**. As a proof of concept, **microcellular SiAlCN foams** were elaborated.

Because we observed in this part that alanes exhibited a different selectivity with polycarbosilazanes in comparison of boranes based on former studies, we have conducted a comparative study, in terms of chemistry, structure and thermal behavior between **SiAlCN and SiBCN ceramics** in the second part of the present chapter. We will investigate the influence of the **substitution of aluminum** with its lower homologue: **boron** on the **structure** of commercial polycarbosilazanes, on the **pyrolysis behavior** and on the **structural/thermal properties** of the derived materials. In contrast to AlN which forms a wurtzite type lattice, BN can dissolve graphite because of close lattice parameters. Consequently, very different thermal stability and phase evolution are expected.

2. SYNTHESIS AND CHARACTERIZATION OF "HOME-MADE" Al-MODIFIED POLYCARBOSILAZANES

2.1. Experimental part

2.1.1 Materials

All the synthesis procedures have been performed using the Schlenk technique operating with an Argon/vacuum line in order to prevent contamination with oxygen and moisture of the synthesized products. All the Schlenks and glassware were dried at 120°C before the use.

Dichloromethylvinylsilane, dicholoromethylsilane were purchased from Sigma-Aldrich, whereas dichloroallylsilane, dichloroallylmethylsilane, dichlorodivinylsilane were purchased from ABCR chemicals. Toluene (99.85%, extra-dry over molecular sieve, AcroSeal®) was obtained from Acros Organics. N,N dimethylethylaminealane complex 0.5 M in toluene was provided from Sigma-Aldrich.

2.1.2 Synthesis of polyaluminosilazanes-derived SiAlCN ceramics

The dichlorocarbosilanes were freshly distilled with magnesium powders. Dichloromethylvinylsilane was freshly distilled at 110-115°C, dichloromethylsilane at 45-50°C, dichloroallylsilane at 110-115°C, dichloroallylmethylsilane at 150°C at and dichlorodivinylsilane at 120-150°C.

The preparation of poly(methylvinyl)aluminosilazane is described below as a representative procedure, since the other precursors (Table V.1) were prepared in a similar manner.

In details, a three necked Schlenk was equipped with a water cooled reflux condenser and a gas inlet tube. 35 g (0.25 mol) of dichloromethylvinylsilane were dissolved in 500 mL of toluene. The system was cooled at 0°C and ammonia (at -40°C) was slowly added. After the addition was finished, the solution was warmed naturally to room temperature and the by-products were separated through filtration. Once a clear solution was obtained, the solvent was removed under vacuum (RT/10^{-2} mbar). Polymethyvinylsilazane was obtained as a transparent visqueous liquid. The quantity of the ammonia is not a key point in the control of the polycarbosilazane, we are working in an excess of ammonia and the quantity is controlled through the condensation of ammonia in the condenser after bubbling into the chlorosilane solution. 40 mL (20 mmol) of solution of $AlH_3.N(Me)_2Et$ in toluene were added at 0°C to 5 g (58.7 mmol) of polymethylvinylsilazane in solution with 200 mL of toluene. After three days of stirring, the solvent and the by-products were separated by distillation at (RT°C/10^{-2}) and 3.5g (70% yield) of Al-modified polymethyvinylsilazane was obtained, it will be named **PMVAZ**. In Table V-1, we report the details concerning the synthesis of the polyaluminosilazanes **(PASZ)**.

Table V-1: Synthesis data of the polyaluminosilazanes.

Samples	**Dichloro-silane**	**M polycarbosilazane g (mmol)**	**V $AlH_3.N(Me)_2Et$ (mL)**	**M polyaluminosilazane (g)**	**Synthesis yield (%)**
PMVAZ	A	5 (58.7)	40	3.5	70
PAAZ	B	8 (94)	65	8	100
PMAAZ	C	2 (20.2)	14	1.2	60
PDVAZ	D	8 (82)	60	5.28	66
PMAZ	E	6.5 (109)	75	5	77

As-synthesized polymers were all in form of white glass-like powders very sensitive to air and moisture. The structure of the different polymers was investigated by FT-IR and NMR spectroscopies, and their chemical composition was studied by elemental analysis. For each thermolysis experiments, **PASZs** are introduced into a nitrogen-filled glovebox connected to a horizontal tube furnace (Nabertherm type RS 80/500/11, Germany). Samples of typically are filled into an alumina boat and then introduced into the furnace. The tube is evacuated (10^{-3} mbar) and

refilled with ammonia (99.995 %). Subsequently, samples are subjected to a cycle of ramping of 5°C.min^{-1} to to 1000 °C (1°C.min^{-1}) and annealed at this temperature for 2 h in flowing nitrogen (120 mL.min^{-1}). Samples are finally cooled to RT at 5°C.min^{-1}. Nitrogen-treated materials were further pyrolyzed in a nitrogen atmosphere up to 1800°C (5°C.min^{-1}) and held 2 h at the final temperature in the range 1200-1800°C in a graphitic furnace (Gero, Model HTK8).

2.1.3 Experiments

FTIR was performed on a Nicolet Magna-IR 550 Fourier transform-spectrophotometer 5Nicolet Instrument Co. USA) using KBr window in case of liquid polymer and KBr pellets in case of solid polymer (2 wt% of polymer mixed with KBr powder followed by a compaction into a dense pellet). Preparation of samples for analyses has been done in a glove box filled with argon. This spectrophotometer is coupled with the ATTenuated Total Reflectance (ATR) accessory.

Investigation on the thermolysis of one example of the Al-modified polysilazanes that is the poly(methylvinyl)aluminosilazane **PMVAZ** from RT up to 1000°C was carried on by performing (^{13}C, ^{29}Si, ^{27}Al, ^{15}N) solid-state NMR spectroscopy.

Thermogravimetric analyses were performed on the polymers under nitrogen up to 1000°C with a heating rate of 5°C.min^{-1} and a dwelling time of 10 min (sample weight ~80 mg).

As-pyrolyzed samples are characterized by X-ray diffraction (Philips PW 3040/60 X'pert PRO X-ray diffraction system operating at 30 mA and 40 kV from 10 to 90° with a step size of 0.0167, using a Kα1 of copper as source), Raman spectroscopy (A Renishaw model RM 1000 Raman microscope operating at λ~ 514.5 nm), and we investigated the microstructural evolution of **SiAlCN** derived from **PMVAZ (PMVAZ-d-SiAlCN)** by TEM measurements (FEI Tecnai G^2 30 UT operating at 300 kV). The chemical composition of the SiAlCN materials was obtained by EDX (microanalysis system with IDFix and MaxViwe softwares from SamX coupled to a Hitashi S800 microscope). High temperature TGA was performed on the **PMVAZ-d-SiAlCN** under N_2 up to 1800°C and under air up to 1000°C.

2.2. Results and discussions

2.2.1 Synthesis and characterization of polyaluminosilazanes

The Al-modified polycarbosilazanes, also called polyaluminosilazanes **(PASZ)**, were prepared via a "polymer" route according to a procedure described for the synthesis of boron-modified poly(vinylsilazanes) [212]. Precursor synthesis was performed by ammonolysis of commercial dichlorocarbosilanes, followed by a reaction with the alane complex in toluene solution. Figure V-1 presents the structure of the different dichlorosilanes we used to prepare the

polyaluminosilazanes. It should be mentioned that Müller et al. only considered the dichlorosilanes A and B [197].

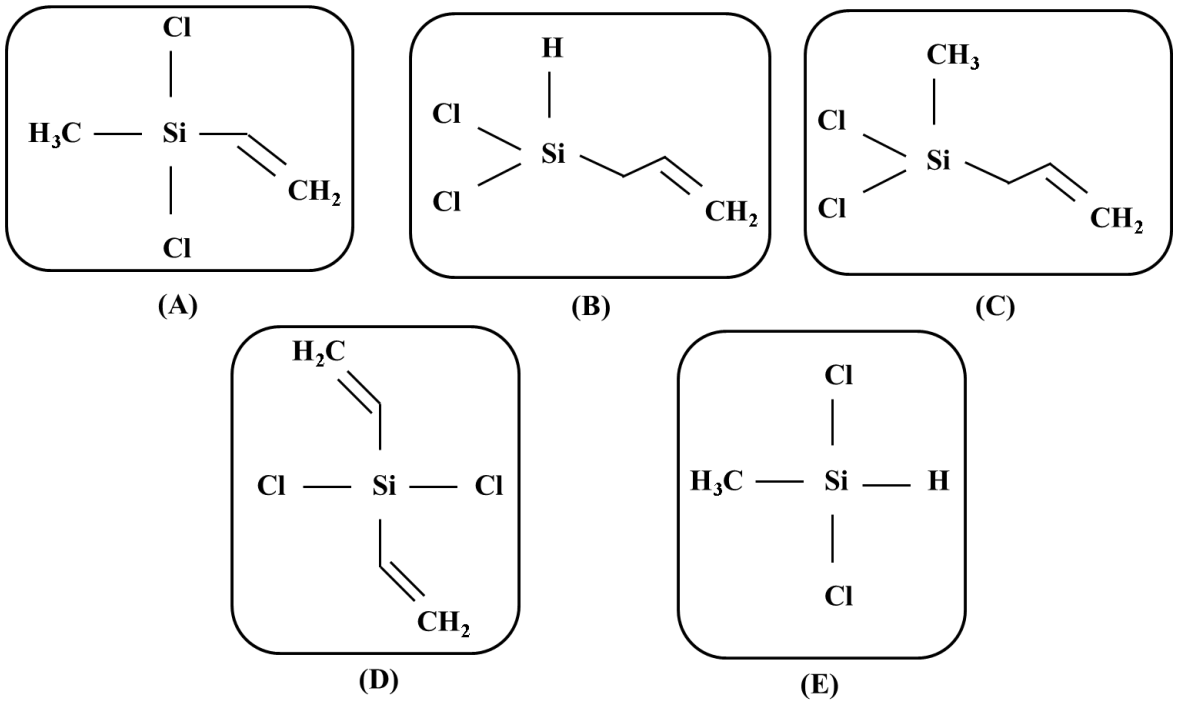

Figure V-1: Molecular structures of (A) dichloromethylvinylsilane, (B) dichloroallylsilane, (C) dichloromethylallylsilane, (D) dichlorodivinylsilane and (E)dichloromethylsilane .

During the first step (ammonolysis), a maximum degree of transformation of Si-Cl groups into Si-NH_2 is reached by reaction of dichlorosilanes with excess of ammonia. The resulting Si-NH_2 groups polycondense at RT to build up the polycarbosilazane network through Si-NH-Si units, according to the ideal synthesis pathway depicted in Figure V-2 releasing ammonium chloride.

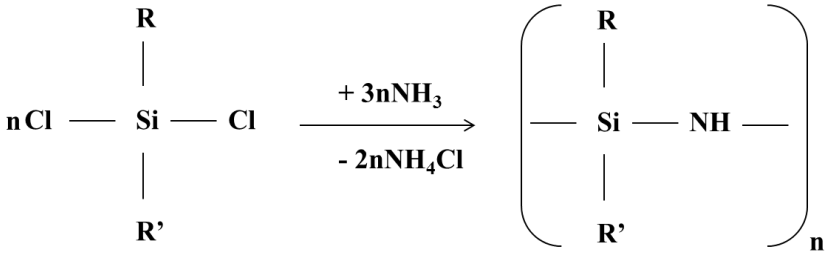

R=R'=H, CH_3, CH=CH_2, CH_2-CH=CH_2

Figure V-2: Ammonolysis of dichlorosilanes.

In a second step, addition of the alane complex $AlH_3.N(Me)_2Et$ occurs on the polycarbosilazanes. Based on the synthesis of boron-modified polycarbosilazanes for which hydroboration is reported, we expect hydroalumination reactions between the vinyl/allyl groups in the polycarbosilazane obtained from dichlorosilanes A → D and the Al-H units of the alane complex. According to the presence of 3 Al-H bonds in the alane, 3 vinyl or allyl groups should react with the alane complex ($3\ CH_2$=CH-Si + AlH_3 → Al $(C_2H_4Si)_3$). This corresponds, ideally, to a Si:Al ratio of 3. This is why we used this ratio in our experimental protocol. However, Müller *et al.* [197] reported that hydroalumination reactions were accompanied by dehydrocoupling reactions as depicted in Figure V-3. Therefore, we have considered a last sample prepared without vinyl/allyl groups from the dichloromethylsilane E to identify this reaction.

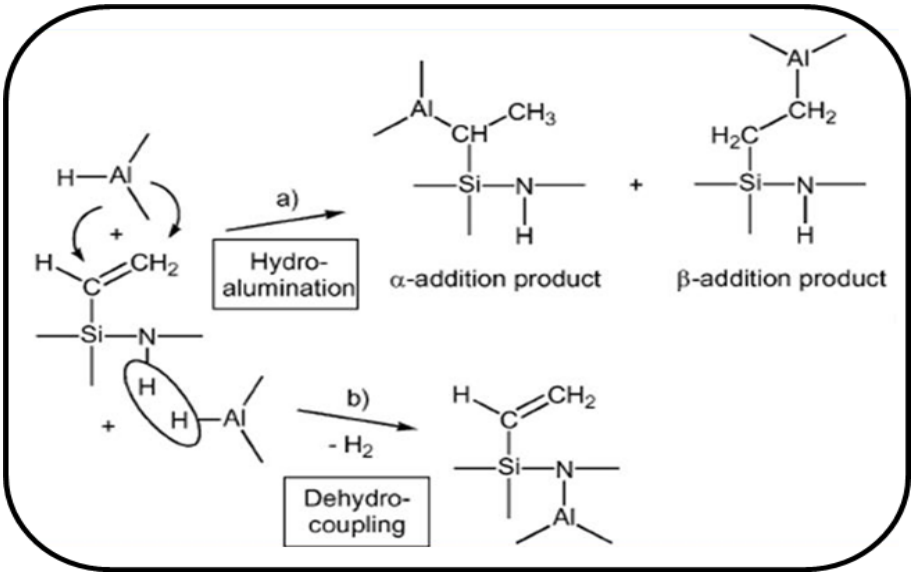

Figure V-3: Expected reactional mechanism between polyvinylsilazane and $AlH_3.NMe_3$ complex [197].

The pictures presented in Figure V-4 give an example of the evolution of the synthesis process going from the molecular precursor dichloromethylvinylsilane (A) to the Al-modified polymethylvinylsilazane (**PMVAZ**). The latter turns out to be a white glass-like solid.

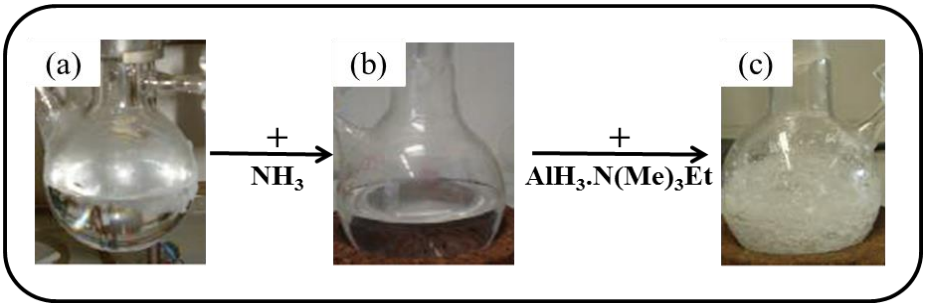

Figure V-4: Pictures of (a) dichloromethylvinylsilane, (b) polymethylvinylsilazane and (c) polymethylvinylaluminosilazane.

Elemental analysis data of the polyaluminosilazanes (Table V-2) confirm the Si:Al atomic ratio we fixed during the synthesis of PASZs: it is close to 3. Surprisingly, this is not the case for **PDVAZ** for which we do not know the reason. We can notice that the proportion of C, N, and H increases from samples **PMAZ** to **PMAAZ** in relation with the increase of the alkyl groups (*i.e.* presence of 1C in methyl, 3C in methylvinyl, 4C in divinyl and 4C in methylallyl groups). We observe a relatively high proportion of oxygen we never observed in our previous polymers. This is probably related to a new procedure we adopted at the University of Rennes to analyze N and O elements which includes a short contact of the samples with air.

Table V-2 : Elemental composition of the as-synthesized polyaluminosilazanes.

Samples	Si (wt%)	Al (wt%)	C (wt%)	H (wt%)	N (wt%)	O (wt%)	Empirical formula
PMAZ	38.09	13.7	20.4	8.9	11.0	7.1	$Si_{3.0}Al_{1.1}C_{3.7}N_{1.7}H_{19.3}O_{1.0}$
PMVAZ	27.6	9.7	32.7	9.9	12.5	7.6	$Si_{3.0}Al_{1.08}C_{8.3}N_{2.7}H_{30.0}O_{1.4}$
PDVAZ	23.2	10.3	34.5	9.5	11.5	11	$Si_{3.0}Al_{1.3}C_{10.3}N_{2.9}H_{35.4}O_{2.4}$
PMAAZ	23.5	8.5	39.00	9.2	13.1	6.7	$Si_{3.0}Al_{1.1}C_{11.6}N_{3.4}H_{32.9}O_{1.4}$

Then, we analyzed the structure of the polymers using infrared spectroscopy. Figure V-5-a reports the FT-IR spectra of the polymethylvinylsilazane (**PMVZ**) and its polyaluminosilazane derivative (**PMVAZ**). Figure V-5-b shows the spectra for all the synthesized polyaluminosilazanes.

First of all, by considering the FTIR spectra of PMVZ and **PMVAZ**, the band characteristic of N-H bonds (ν_{N-H}= 3450 cm^{-1}) decreases in intensity indicating a possible dehydrocoupling reaction involving NH groups in PMVZ and AlH units in the alane complex forming Al-N bonds. This is confirmed through the appearance of the band around 1753 cm^{-1} which is attributed to the vibration of Al-N bonds. The bands in the wavenumber range 3365-3385 cm^{-1} and 1375 (δ_{sCH_3})-1450

(δ_{asCH_3}) cm^{-1} are broader which is due to the incorporation of carbon-based groups in **PMVAZ**. The band attributed to vinyl groups (1650-1600 cm^{-1}) also decreases in intensity from PMVZ to **PMVAZ** which tends to demonstrate the occurrence of hydroalumination reactions. The region 1200 – 500 cm^{-1} is difficult to interpret in **PMVAZ**.

All the polyaluminosilazanes display the weak absorption signal in the 3365-3385 cm^{-1} region, and the series of bands in the wavenumber range 2750-3100 cm^{-1}, which confirms the presence of N-H and C-H vibrational bands, respectively. In addition, they exhibit the bands around 1753 cm^{-1} caused by the vibration of Al-N bonds and the bands ascribed to Si-N vibrations that appear in the 1190-1200 cm^{-1} range. We can also observe the band at 1650 cm^{-1} which is present in the vinyl-/allyl- containing polycarbosilazanes. This means that hydroalumination occurs but is not total. Particularly, in the **PMAZ** and **PAAZ** spectra we can detect the vibrational Si-H band at 2159 and 2124 cm^{-1}, respectively. Deformation bands of CH_3 appear for all samples: δ_{sCH3} =1375 cm^{-1} and δ_{asCH3}=1450 cm^{-1}. Based on the infrared spectroscopy, we can suggest that hydroalumination of the vinyl/allyl groups takes place but, according to the identification of Al-N bonds, dehydrocoupling reactions proceed as reported by Müller *et al*. [197]. For all polymers, we can detect a small band around 2100 cm^{-1} attributed to Al-H units from the alane complex.

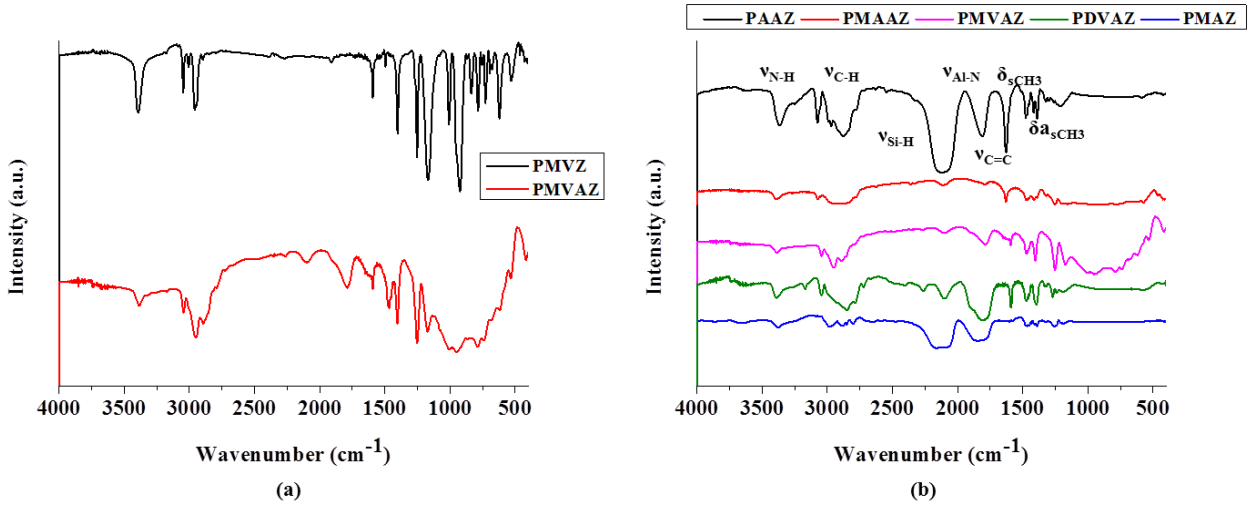

Figure V-5: FTIR spectra of (a) **PMVZ** and **PMVAZ** and (b) **PMAZ**, **PMVAZ**, **PAAZ**, **PMAAZ** and **PDAZ**.

Solid-state NMR was used as a complementary tool to confirm all these predictions. This technic is of particular interest for complex systems such as ternary (Si/C/N) and quaternary ceramic systems (Si/B/C/N, Si/Al/C/N), not only to establish the chemical environment in the polymeric

precursor containing various NMR-active nuclei, such as ^{13}C, ^{29}Si, ^{1}H, ^{10}B or ^{27}Al, but also on the pyrolyzed intermediates to follow the structural evolution from the polymer to the ceramic.

Unlike the case of Si/C/N and Si/B/C/N, so far only little has been investigated concerning the structural evolution of Si/Al/C/N quaternary systems [197]. Multinuclear (^{13}C, ^{29}Si, ^{27}Al, ^{15}N, ^{1}H) solid-state NMR spectroscopy experiments are employed here to investigate the structure of aluminum-modified polysilazanes, from which SiAlCN ceramics can be formed.

It should be emphasized that the two-step polymer synthesis (ammonolysis and alane reaction) is expected to give rise to a large variety of structural components which are not all explicitly shown in the idealized structures/reactions illustrated previously. In this part, we try to give a detailed representation of the structure of polyaluminosilazanes described in Table V-1 based on the local carbon, silicon, aluminum and nitrogen environments. ^{13}C, ^{29}Si and ^{27}Al are sufficiently abundant to be studied without isotopic enrichment. Nevertheless, ^{13}C spectra were recorded using the cross-polarisation (CP) technique to obtain spectra with reasonable signal-to-noise ratio.

The experimental and simulated ^{13}C CP MAS NMR spectra of the five polyaluminosilazane samples are given in Figure V-6 and V-7.

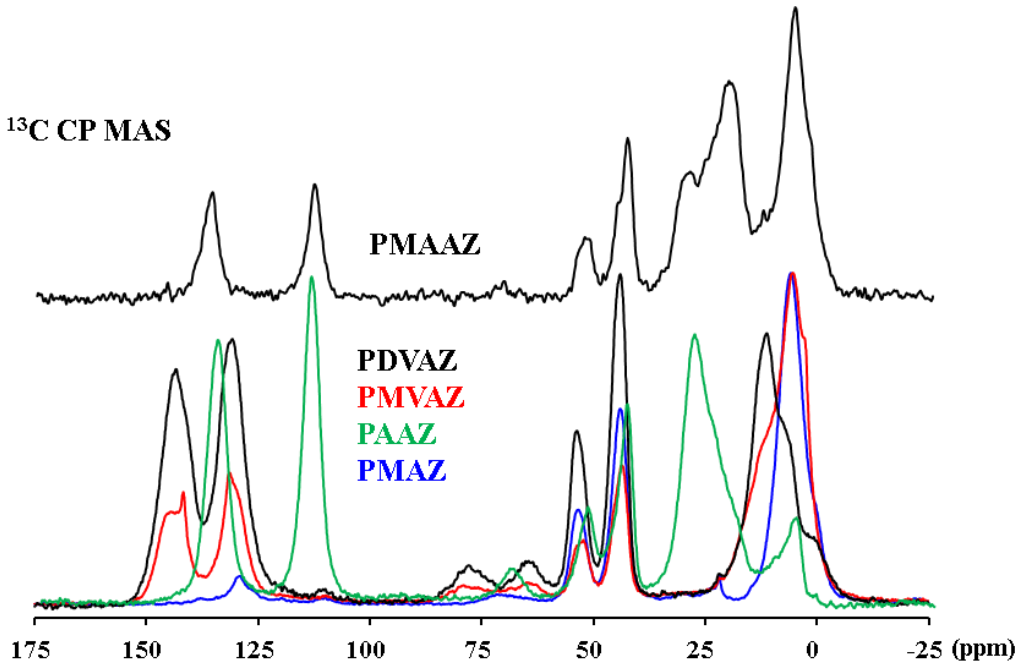

Figure V-6: ^{13}C CP MAS spectra of **PMAZ**, **PMVAZ**, **PAAZ**, **PMAAZ** and **PDVAZ**.

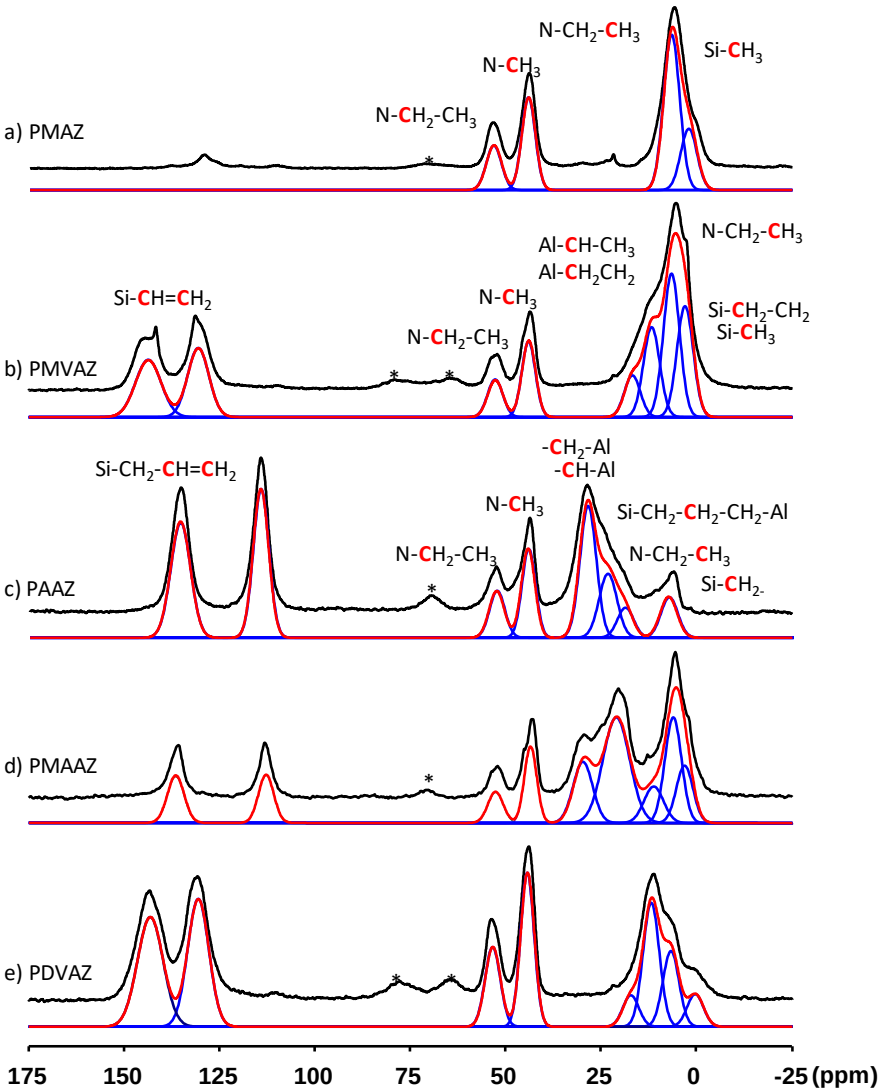

Figure V-7: ^{13}C CP MAS NMR experimental and simulated spectra of **PMAZ**, **PMVAZ**, **PAAZ**, **PMAAZ** and **PDVAZ**.

First of all, we can clearly identify the signals in the range 115-150 ppm corresponding to sp^2 carbons which are attributed to the vinyl (131, 145 ppm) and allyl (115, 137 ppm) groups [318] that did not react during the addition of aluminum in **PMVAZ**, **PAAZ**, **PMAAZ** and **PDVAZ**. This confirms that hydroalumination is not the only reaction that occurs during the synthesis of polyaluminosilazanes. These signals are logically absent in the sample **PMAZ** which does not contain allyl and/or vinyl groups.

All samples exhibit two signals at ~53 and ~46 ppm which are attributed to N-***C***H_2-CH_3 and N***C***H_3 groups coming from the alane (the signal at ~46 ppm is tentatively attributed to N***C***H_3 since it is twice as intense as the signal at ~46 ppm while there are two methyl groups and one ethyl group in the alane). This reflected FTIR observations which demonstrated the incorporation of carbon-based groups in the sample **PMVAZ** prepared from PMVZ.

The **PMAZ** spectrum shows two other overlapping signals around 3 and 7 ppm that can be assigned to Si-***C***H_3 and N-CH_2-***C***H_3 environments respectively. For the other samples, additional signals are present between 10 and 30 ppm. They arise from hydroalumination reactions leading to the formation of Si-CH(CH_3)-Al and Si-CH_2-CH_2-Al units. According to previous work [197], signals around 20 ppm could correspond to Al-***C***H_2 and Al-***C***H environments while Si-CH(***C***H_3)-Al is expected to be around 10 ppm. Si-***C***H_2 probably resonates in the same area as Si-***C***H_3, that is at a small chemical shift value around 5 ppm as previously observed in Si/B/C/N systems [109].

The ^{29}Si MAS and CP MAS spectra of the polymeric precursors shown in Figure V-8 are not very sensitive to the reactions which occur during the addition of alane but mainly depend on the conformation of the polysilazane which is used before the reaction with alane. However, addition of Al can slightly shift the signal position, especially when Al is added by hydroalumination.

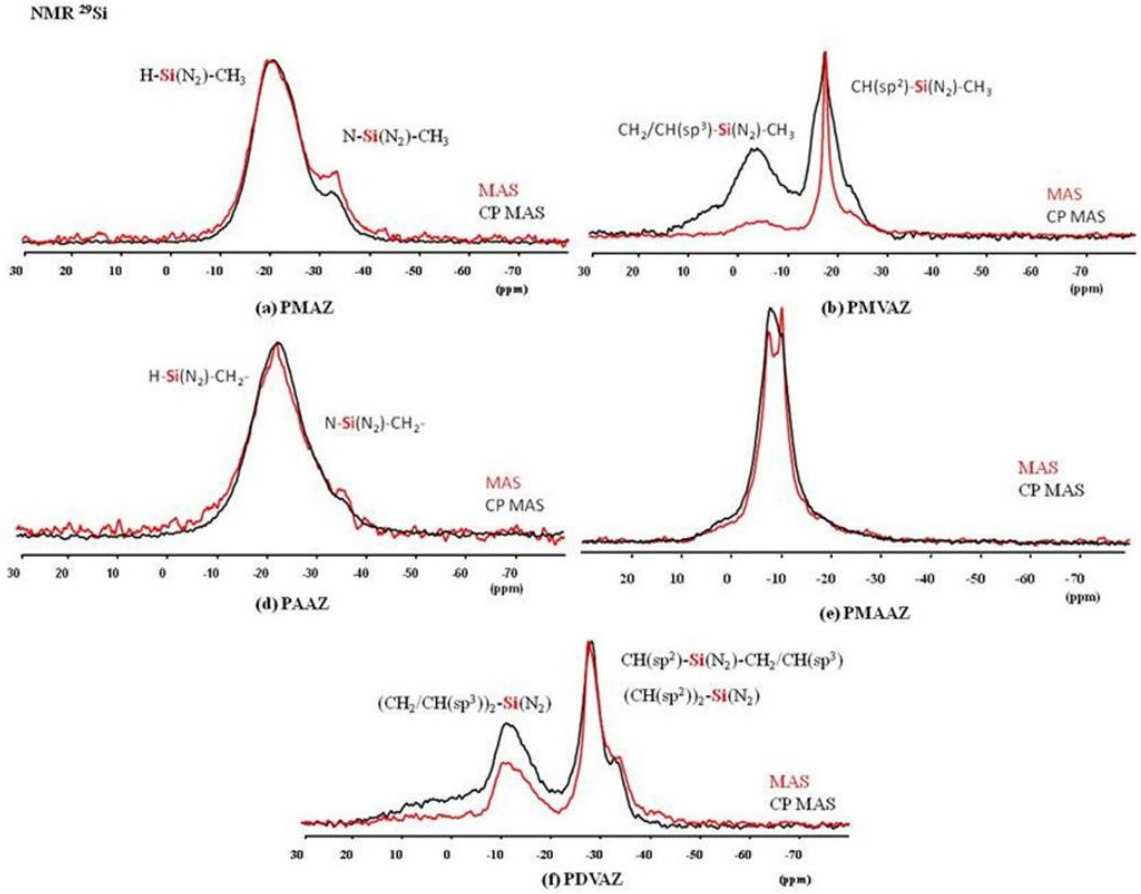

Figure V-8: ^{29}Si MAS and CP MAS spectra of **PMAZ**, **PMVAZ**, **PAAZ**, **PMAAZ** and **PDVAZ**.

On the **PMAZ** spectrum, the main signal observed at -21 ppm can be assigned to the expected *Si*HCN_2 environment from the ammonolysis. Indeed, signals attributed to *Si*HC(sp^3)N_2 groups are usually observed at -18 ppm [319, 320]. Nonetheless, an additional signal is observed at

~ -32 ppm that corresponds to *Si*N_3C environment based on former studies [321] suggesting that there is ending groups. These two signals are also observed for the **PAAZ**.

An SiC_2N_2 environment (~ -10 ppm) is as expected present in **PMVAZ**, **PMAAZ** and **PDVAZ** as classically observed in boron-modified polysilazane with *sp3* carbons [109, 211]. Moreover, after Al addition to vinyl-containing polysilazanes **PMVAZ** and **PDVAZ**, two signals are identified suggesting that SiC_2N_2 chemical shift depends on the type of hybridization of the carbon in α and β position. The peaks at -2 ppm (PMVAZ) and -12 ppm (**PDVAZ**) correspond to $(CH_2/CH(sp^3))_xSiN_2$ (x= 1 (**PMVAZ**), 2(**PDVAZ**)). The presence of a C(sp^3) in α position of Si, means that hydroalumination occurs in such samples. However, the reaction is not total as attested by the presence of the second signals centered at -18 ppm (**PMVAZ**) and -28 ppm (**PDVAZ**). In **PDVAZ**, the shoulder at -32 ppm is attributed to a CH(sp^2)-SiN_2-CH_2/CH(sp^3) units which means that hydroalumination occurs on one vinyl group. It is interesting to mention that we do not identify the SiC_3N environment that is observed in boron-modified polysilazanes [322]. The environment results from the structural rearrangement occurring during the polymer synthesis as follows (Equation V-1):

$$SiC_2N_2 + BC_3 \rightarrow SiC_3N + BC_2N \qquad (V\text{-}1)$$

This can be due to the absence of AlC_3 units in the polymers containing vinyl/allyl groups. Figure V-9 shows the ^{27}Al MAS NMR spectra of the samples. They can help us to identify the environment around aluminum.

Spectra are composed of broad signals suggesting the presence of overlapping components due to the mixed local chemical environment of the aluminum nuclei. Tetrahedrally coordinated aluminium resonates between 140 and 40 ppm to low field [323]. Therefore, the major broad signal centered at 40 ppm can be attributed to $AlN_{3-x}C_x$ suggesting that the N_2AlR, $NAlR_2$, and AlR_3 units expected according to Figure V-3 are also coordinated by $NEtMe_2$ groups as suggested by the ^{13}C NMR experiments. According to the chemical shift range that is covered, Al nuclei can also display 5- and 6-fold coordination assigned to AlN_5 and AlN_6. It was reported that AlN_5 and AlN_6 appears at 50 and 0 ppm, respectively [197]. Such environments are possibly present in all samples. In the case of **PMAAZ**, a new signal appears at 120 ppm that can be attributed to a tetracoordinated AlN_4 [197]. This clearly confirms the strong affinity of aluminum to nitrogen along with the dehydrocoupling reactions, *i.e.,* Al atoms in pentagonal and octahedral coordination with nitrogen atoms.

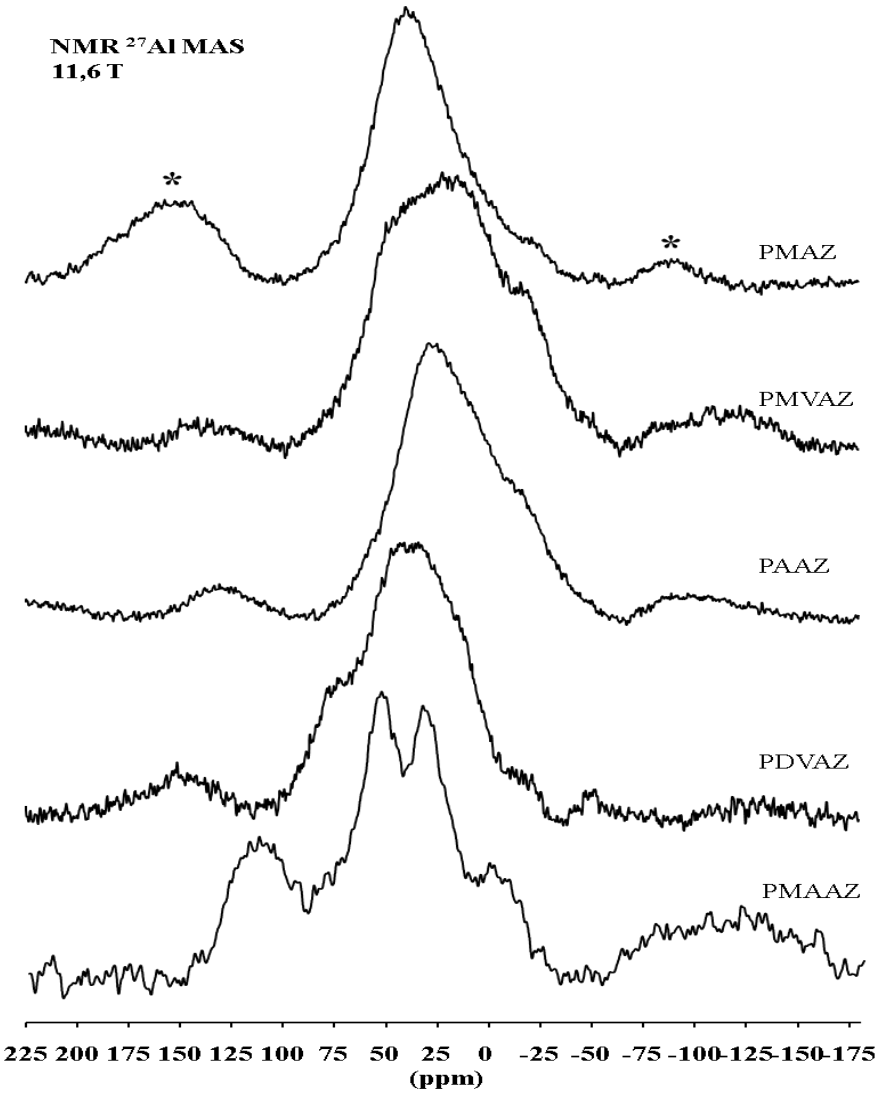

Figure V-9: ^{27}Al MAS spectra of **PMAZ**, **PMVAZ**, **PAAZ**, **PMAAZ** and **PDVAZ**. Asteriks indicate spinning side bands.

^{15}N CP MAS NMR spectra (Figure V-10) highlight the results obtained from the ^{27}Al NMR spectra. The spectra of the five samples exhibit a broad signal around -350 ppm depicting the Si-N unit of the silazane backbone. The signal at -320 ppm indicates the Al-N bonds. It appears mostly in the case of **PMAZ** since the latter do not possess in his chain reactive sites other than the N-H and Si-H, and Al is more likely to react with N-H. This confirms the dehydrocoupling reactions.

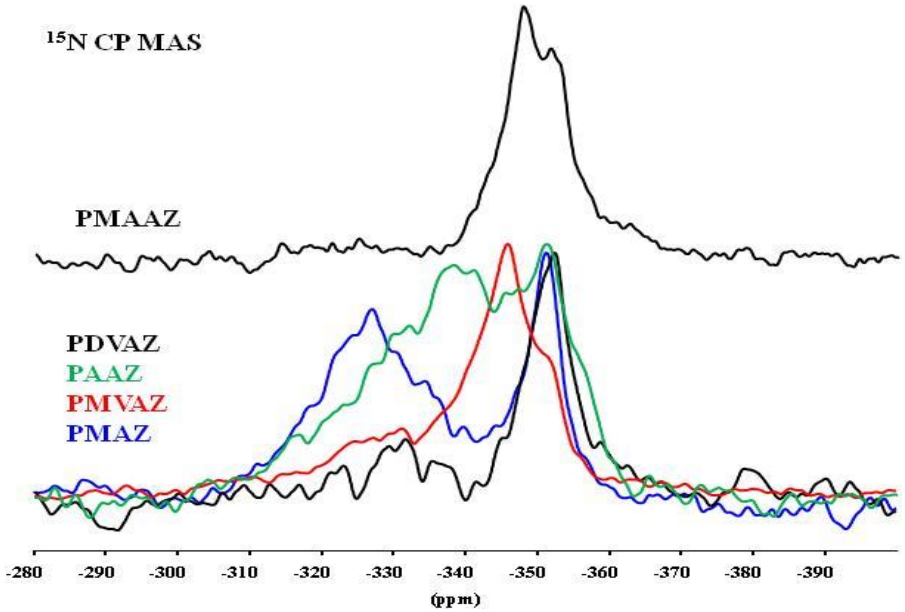

Figure V-10: ^{15}N MAS NMR spectra of **PMAZ**, **PMVAZ**, **PAAZ**, **PMAAZ** and **PDVAZ**.

Based on solid-state NMR, we identified the two possible reactions that occur during the synthesis of the polyaluminosilazanes: hydroalumination and dehydrocoupling. This indicated the strong difference in the reactivity of aluminum in comparison to boron. In boron-modified polysilazanes, it is usually reported that hydroboration is the only mechanism that occur during the synthesis of these polymers. Such a reaction is total and no residual vinyl groups are found in boron-modified polysilazanes. The differences in the selectivity of reaction of AlH_3 and BH_3 with the polycarbosilazanes can be due to the different reactivity of AlH_3 and BH_3 towards C=C groups and N-H functions, which can be explained by their different Lewis base acidity. Because aluminum organyles exhibits a distinguished Lewis acidity, reactions of alanes with vinyl-containing polysilazanes are therefore not restricted to the hydroalumination of olefenic groups. Rather, dehydrocoupling along with the formation of Al-N units is preferable. According to these differences, the polymer-to-ceramic conversion is expected to be extremely complex in the case of SiAlCN materials. It is studied in the following section.

2.2.2 Polyaluminosilazanes-to-SiAlCN conversion

Once polymers are synthesized and characterized, their pyrolysis behavior has been investigated. Pyrolysis is performed under N_2 up to 1000°C. The pyrolysis behavior of the preceramic polymer is intimately linked to its cross-linking degree and also to the presence of groups with a latent reactivity. Aluminum, added by hydroalumination and dehydrocoupling, contributes to increase the cross-linking degree of polycarbosilazanes (=PSZs) leading to polyaluminocarbonsilazanes (=**PASZs**). The thermal conversion of preceramic polymers into

ceramics is accompanied by the formation of gaseous by-products and therefore weight loss occurs during the polymer-to-ceramic conversion. The ceramic yields for the **PASZs** are determined by TGA (Figure V-11).

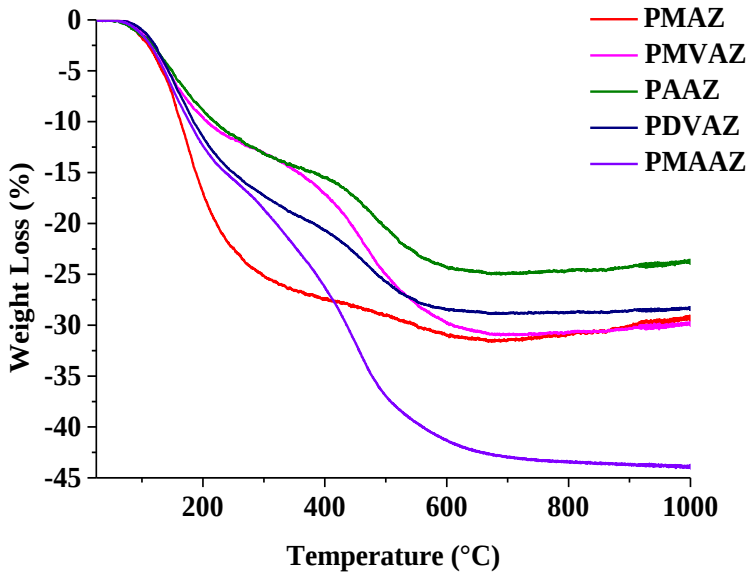

Figure V-11: TGA curves of **PMAZ**, **PMVAZ**, **PAAZ**, **PMAAZ** and **PDVAZ** under N_2 up to 1000°C (5°C.min^{-1}).

All the samples exhibit a two-step weight loss which is intimately related to the latent thermal reactivity of the specific groups that are linked to Si. As an illustration, **PAAZ** exhibits Si-H, remaining allyl groups and N-H units (because they do not react totally with the alane) as identified by FTIR and solid-state NMR. Desirable cross-linking reactions are either *trans*-amination followed by ammonia elimination, dehydrocoupling or hydrosilylation or polymerization of vinyl/allyl groups as detailed in the following equations.

$$2\ \text{Si-NH-Si} \rightarrow (\text{Si})_3\text{N} + \text{Si-NH}_2;\ \text{Si-NH-Si} + \text{Si-NH}_2 \rightarrow (\text{Si})_3\text{N} + \text{NH}_3 \quad \text{(V-2)}$$

$$2\ \text{Si-H} \rightarrow \text{Si-Si} + \text{H}_2 \quad \text{(V-3)}$$

$$\text{Si-H} + \text{CH}_2\text{=CH-CH}_2\text{-} \rightarrow \text{Si-CH}_2\text{-CH}_2\text{-CH}_2\text{-} \quad \text{(V-4)}$$

$$\text{Si-H} + \text{N-H} \rightarrow \text{Si-N} + \text{H}_2 \quad \text{(V-5)}$$

$$n\ \text{CH}_2\text{=CH-Si} \rightarrow (\text{CH}_2\text{-CH})_n\text{-Si} \quad \text{(V-6)}$$

Based on these reactions, **PAAZ** cross-links during the pyrolysis only by removing only NH_3 and H_2. Logically, the weight loss measured at 1000°C is the lowest (23%). This indicates that **PAAZ** has a ceramic yield of 77%. At the opposite, the sample **PMAAZ** displays the highest weight loss whereas the only difference between both samples is the presence of $SiCH_3$ groups (**PMAAZ**)

instead of SiH units (**PAAZ**). Therefore, other reactions or additional reactions that those depicted above occur as proposed by Corriu *et al.* 20 years ago [324].

Authors studied the pyrolytic behavior of a variety of polycarbosilazanes such as PMZ (polymethylsilazane) and PVZ (polyvinylsilazane) and discussed on the possible mechanisms and temperature ranges at which they occurred. Hydrocarbons were escaped during their pyrolysis as methane (from PMZ) and ethylene (from PVZ). The mechanism of mineralization reactions of these polymers is likely radical, in view of the high temperatures involved (400-800°C) [325]. The large escape of methane, in the case of PMZ showed that the most probable reaction is the abstraction of a hydrogen atom from Si-H, N-H or C-H bonds according to equations V-7 and V-8.

$$Si\text{-}CH_3 \rightarrow Si^{\bullet} + {}^{\bullet}CH_3 \quad (V\text{-}7)$$

$${}^{\bullet}CH_3 + Si\text{-}H/N\text{-}H \rightarrow CH_4 + Si^{\bullet}/N^{\bullet} \quad (V\text{-}8)$$

This clearly occurs in **PMAAZ** but this cannot explain its high weight loss because samples **PMAZ** and **PMVAZ** also display $SiCH_3$ groups and their pyrolytic conversion occurs with lower weight losses. The vinyl/allyl groups, either unreacted should lead *via* Si-C bond cleavage to vinyl/allyl radicals; these vinyl/allyl radicals would lead to an escape of ethylene/propylene (by H abstraction due to H-X (X = Si, N) $\rightarrow {}^{\bullet}H + X^{\bullet}$) according to equations V-9 and V-10.

$$Si\text{-}CH_2\text{-}CH{=}CH_2 \rightarrow Si^{\bullet} + {}^{\bullet}CH_2\text{-}CH{=}CH_2 \quad (V\text{-}9)$$

$${}^{\bullet}CH_2\text{-}CH{=}CH_2 + {}^{\bullet}H \rightarrow CH_3\text{-}CH{=}CH_2 \quad (V\text{-}10)$$

However, as already noticed by Burns *et al.* [326] elemental analysis of the PVZ showed that only a small part of the carbon arising from vinyl groups is lost as hydrocarbons; rather, the vinyl groups are consumed *via* addition reactions, such as polyaddition or hydrosilation. This is confirmed through our study because the behavior of samples **PMVAZ** and **PDVAZ** during the pyrolysis is similar: they exhibit a two-step weight loss 1) from RT to 300°C and 2) from 300°C to 1000°C with a close final weight loss whereas **PDVAZ** was expected to be decomposed *via* a large quantity of ethylene through equations V-9 and V-10. This is not the case and this tends to confirm the polymerization of vinyl groups according to equation V-6.

This discussion leads to us to consider that the only reason of the lower weight loss for **PMAAZ** is the evaporation of low-weight oligomers possibly due to depolymerization of the precursor. This process takes place in the 300-500°C temperature range. A similar result was obtained for the boron-modified polycarbosilazanes prepared from PMAZ by Müller *et al.* [327]. A weight loss of 78.4 % was measured after thermal decomposition. This comparison tends to

demonstrated that the pyrolytic behavior of boron- and aluminum-modified polycarbosilazanes using a same polycarbosilazane (PMAZ) significantly differs. To support this observation, we have compared the behavior of the sample **PMVAZ** with that one of the boron-modified polysilazane of the type **(**$B[C_2H_4SiCH_3NH)]_3)_n$ (C_2H_4=$CHCH_3$, CH_2CH_2) which is obtained from the same dichloromethylvinylsilane (Figure V-12).

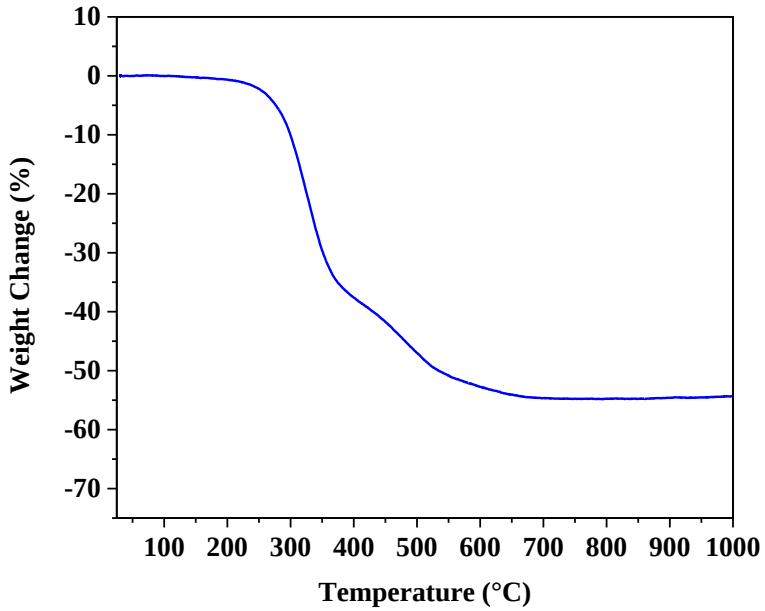

Figure V-12: TGA curve of boron-modified polysilazane of the type $(B[C_2H_4SiCH_3NH)]_3)_n$ under N_2 up to 1000°C with a heating rate of 5°C.min^{-1}.

The boron-modified polysilazane of the type **(**$B[C_2H_4SiCH_3NH)]_3)_n$ (C_2H_4=$CHCH_3$, CH_2CH_2) does not exhibit any weight change up to 250°C, temperature at which a two-step weight loss occurs leading to a weight loss of 44.6%. **PMVAZ** is less stable at low temperature but it displays a lower weight loss of 28%. Because Si-H units are absent in these polymers (which are know to react during pyrolysis with vinyl/allyl and NH groups), this clearly emphasize that PASZs display high cross-linking degree than their boron analogues confirming the different reactivity of AlH_3 and BH_3 during the polymer synthesis towards C=C groups and N-H functions.

Structural changes occurring during the pyrolysis up to 1000°C were monitored by solid-state NMR of intermediates isolated at 200, 450, 700 and 1000°C. We selected the sample **PMVAZ** to observe the evolution of the vinyl groups during the pyrolysis according to the absence of Si-H units,

and to follow the evolution of the chemical environment around Al since it is expected to be bonded to C and N elements.

2.2.3 PMVAZ structure evolution: RT→1000°C

Figure V-13 exhibits the ^{29}Si NMR spectra of **PMVAZ** and of the derived N_2-treated intermediates between 200 and 1000°C. We previously discussed on the ^{29}Si NMR spectrum of PMVAZ. It contains broad signals corresponding to SiC_2N_2 environments with a signal at -10 ppm and another one at -2 ppm due to the presence of two sp^3 or one sp^2/one sp^3 carbons linked to Si. The lack of protons in the sample heat-treated at 1000°C prevents the application of CP and thus a single pulse ^{29}Si MAS of the sample is recorded.

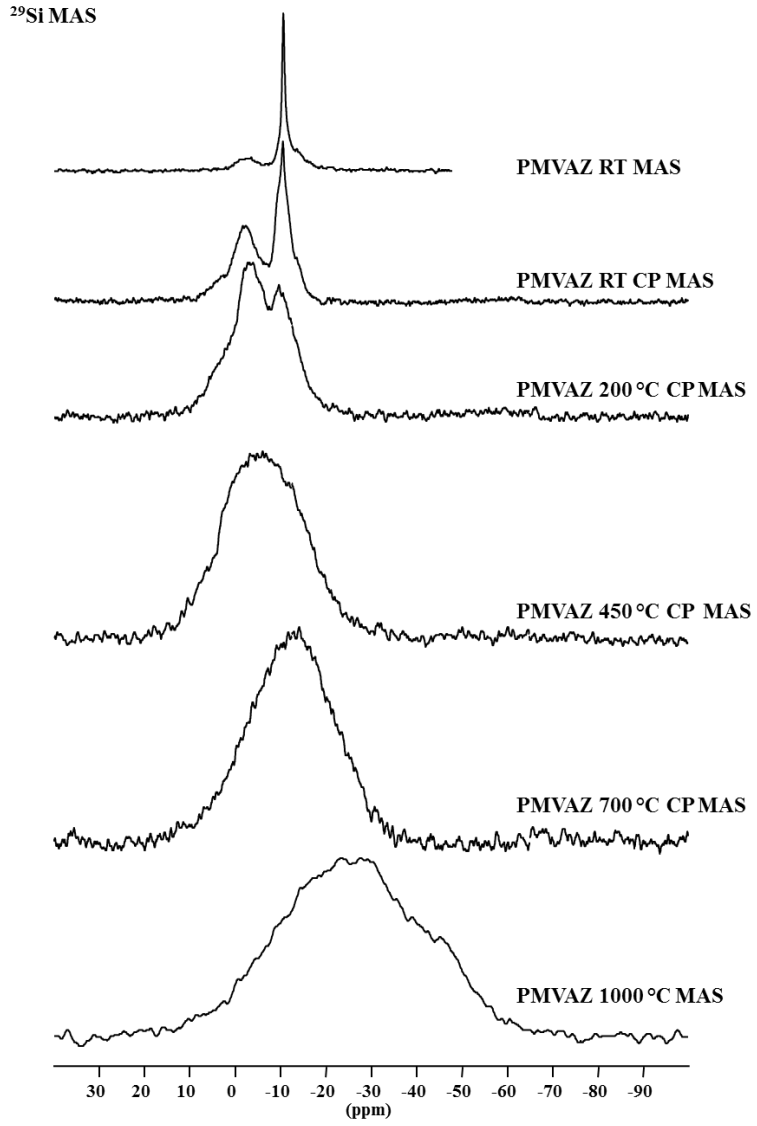

Figure V-13: Solid-state ^{29}Si MAS and CP MAS spectra of **PMVAZ** and **N_2-treated intermediates** at 200, 450, 700 and 1000°C.

With the increase of the temperature signals broaden and the spectra become featureless. After calcination at 450°C under N_2, this broad signal is centered at -5 ppm. Above 450°C, the peak progressively tends to shift to lower positions while the signal is still characterized by overlapping resonances. The signal is centered at -13 ppm at 700°C and -25 ppm at 1000°C. The appearance of these broadened signals is typical for amorphous Si-based PDCs [328, 329] and it is in general caused by overlapping resonances of SiC_xN_{4-x} units (with x=0, 1, 2, 3 and 4). Moreover, it occurs here that SiC_3N are not identified in PMVAZ-derived SiAlCN ceramics (since they are expected at positive chemical shift values) in contrast to polymer-derived SiBCN ceramics [211]. The sample heat-treated at 1000°C is composed of SiC_2N_2, $SiCN_3$ and SiN_4 environments.

Experimental ^{27}Al MAS NMR spectra recorded at 11.6 T are presented in Figure V-14. Only minor changes occur during the heat-treatment from RT to 1000°C, reflected by the slight sharpening of the broad signal identified in PMVAZ around 25 ppm. According to the chemical shift range that is covered, the Al nuclei possess 4-, 5- and 6- fold coordination. For example, ^{27}Al resonance signals of AlN_4, AlN_5 and AlN_6 are reported to appear at 100, 50 and 0 ppm, respectively [323, 330, 331].

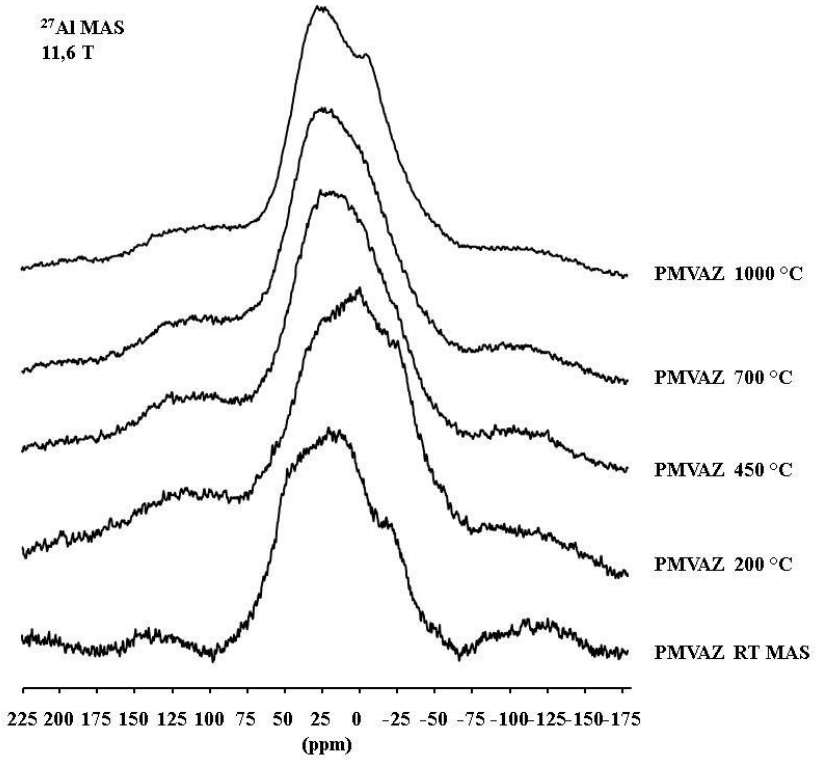

Figure V-14: Solid-state ^{27}Al MAS spectra of **PMVAZ** and **PMVAZ-derived samples** pyrolyzed at 200, 450, 700 and 1000°C under N_2.

Experimental ^{13}C CP MAS NMR spectra are given in Figure V-15.

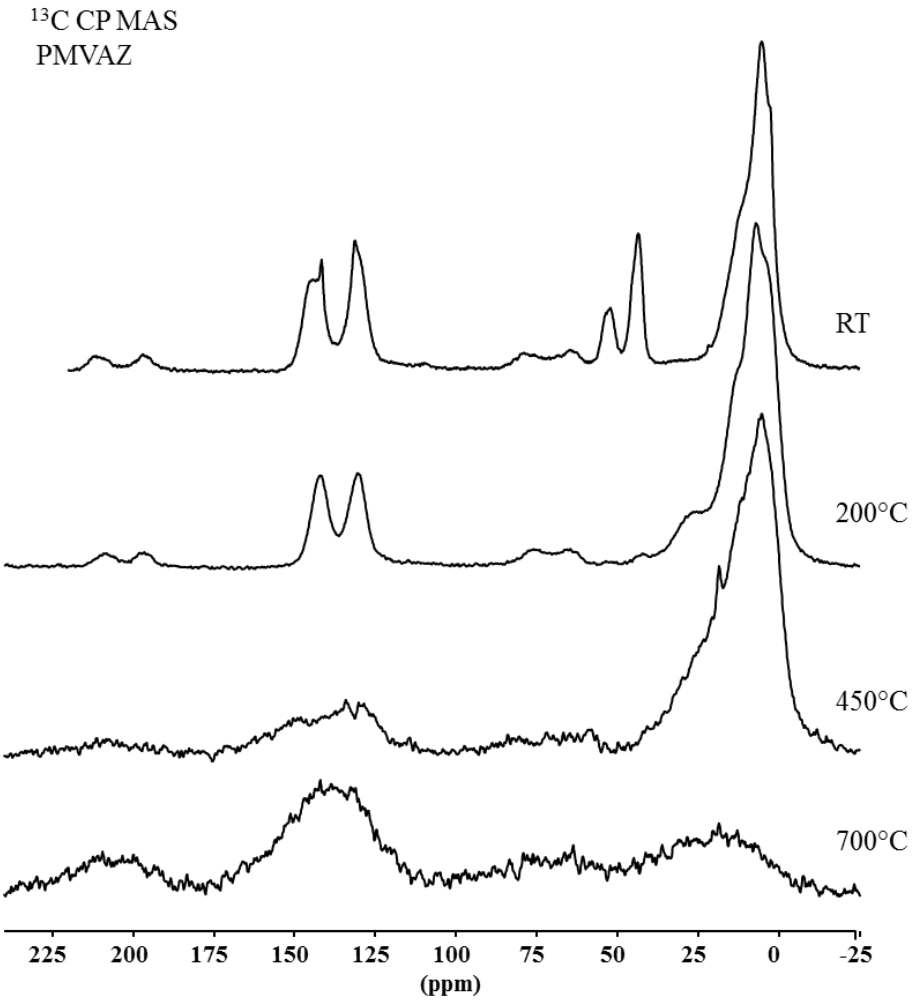

Figure V-15: ^{13}C CP MAS NMR spectra of **PMVAZ** and **N_2-treated intermediates** at 200, 450 and 700°C.

The samples heat-treated at 1000°C could not be recorded with CP due to the absence of protons. As previously discussed, the **PMVAZ** exhibits a set of signals attributed to the vinyl groups (133 and 141 ppm) that did not react during the hydroalumination, ethylamine groups (53, 46 ppm) and aliphatic groups linked to Si and Al (in the range 2-20 ppm) resulting from hydroalumination in α and β position of the carbon. Heat-treatment at 200°C induces the disappearance of the signal in the 40-58 ppm region, confirming that they are ending groups such as amine-based units. The signal intensity corresponding to vinyl groups decreases pointing to a thermally induced polymerization of the Si-bonded vinyl groups and their conversion into aliphatic hydrocarbons $(-CH_2-CH_2)_n$ and/or the escape of ethylene/acetylene. These reactions are significant in the temperature range 200-450°C. The signal centered at 10 ppm does not change in intensity but has a tendency to broaden. That can be assigned to CH_xSi_{4-x} units (with x=0, 1, 2) [319, 328]. The broad signal in the low-field region at

130-140 ppm which is more intense in the sample heat-treated at 700°C indicates the formation of amorphous (graphite-like) carbon during the thermal degradation.

We have seen that the PASZ-to-SiAlCN conversion is achieved at 1000°C. The chemistry involved during the polymer-to-ceramic conversion is intimately linked to the chemistry of the polymer, including the structural rearrangements at the atomic scale. In particular, the chemistry involved during the polymer-to-ceramic conversion includes a complex sequence of structural and chemical changes based on molecular rearrangements and the release of gaseous by-products including weight loss which are inherently related to the molecular structure and chemistry of preceramic polymers. In the following part, the amorphous-to-crystalline transformation is investigated. The introduction of boron into silicocarbonitride ceramics can lead to materials possessing excellent high-temperature stability and resistance to crystallization which was explained by the formation of a turbostratic B-C-N phase retarding the possible decomposition reactions between Si_3N_4 and free carbon [332]. We do not know the effect of the substitution of boron by aluminum. This is studied in the following part.

2.2.4 Characterization of SiAlCN: 1000 → 1800°C

The main purpose of producing polymers with different structural units is to tailor the composition and properties of the derived PDCs. The latter have a molecular origin, *i.e.*, their properties are affected by the intrinsic architecture of the starting polymer. After heat-treatment to 1000°C, PASZ-derived SiAlCN ceramics labeled **PASZX** (with X the temperature at which PASZs have been annealed) are amorphous. The amorphous state of polymer-derived Si(E)CN (with E=B, Al) ceramics at 1000°C can be associated to a continuous network of mixed $Si(E)C_xN_y$ environments combined with a free carbon phase [208]. Further annealing to temperatures exceeding 1000°C promotes rearrangements within the amorphous matrix. Based on TEM studies, Monthioux and Delverdier [333] reported that the nucleation of the free C, commonly present in organosilicon polymer-based PDCs, is always the first crystallization phenomenon that takes place. A nucleation of the SiC phase follows this first event whatever the number of constituents within the system. This point aims at the characterization of the chemical evolution as well as the phase evolution and crystallization of the amorphous PASZ-derived SiAlCN ceramics. In particular, the effect of the polymer and the influence of its chemistry are examined.

The elemental compositions gained by EDX of the PASZ-derived SiAlCN ceramics (five samples) obtained after pyrolysis to 1000°C, are given in Table V-3. As expected, the samples are composed of Si, Al, C and N with a small amount of O.

Table V-3: Chemical composition of **SiAlCN** ceramics.

Sample	Si (wt%)	Al (wt%)	C (wt%)	N (wt%)	O (wt%)	Chemical composition
PMAZ1000	39	18	15	23	5	$Si_{3.0}Al_{1.3}C_{2.8}N_{3.6}O_{0.6}$
PMVAZ1000	24	16	23	29	8	$Si_{3.0}Al_{2.0}C_{6.0}N_{7.0}O_{1.6}$
PAAZ1000	32	12	29	19	8	$Si_{3.0}Al_{1.05}C_{6.3}N_{3.7}O_{1.3}$
PMAAZ1000	35	14	22	19	10	$Si_{3.0}Al_{1.3}C_{4.5}N_{3.4}O_{1.5}$
PDVAZ1000	32	16	30	17	5	$Si_{3.0}Al_{1.6}C_{6.6}N_{3.2}O_{0.7}$

On the basis of our experience with the synthesis of a variety of nitrides and carbonitrides, and the severe problems associated with the elemental analysis of such materials, we believe that an oxygen content level below 10 wt% is mainly associated with the presence of surface oxides on otherwise phase-pure nitride/carbonitrides. We can observe that the Si:Al ratio is almost constant with a low difference in comparison to the Si:Al ratio calculations in the polymers from which SiAlCN ceramics are obtained. The low carbon content in **PMAZ1000** is related to the low carbon content of the polymer (1 CH_3Si unit in the monomeric structure). For the other samples, the carbon content is similar. It is seen that the total nitrogen content remains nearly constant in all of the samples (excepted for **PMVAZ1000**) which was expected according to the fact that all polymers contain 1 NH unit in the monomeric structure.

XRD plots of SiAlCN materials annealed at temperatures going from 1000 to 1800°C with an isothermal hold of 2 h at each temperature are reported in Figure V-16. Phase identification is achieved by locating the characteristic diffraction peaks of the respective phases in the XRD patterns.

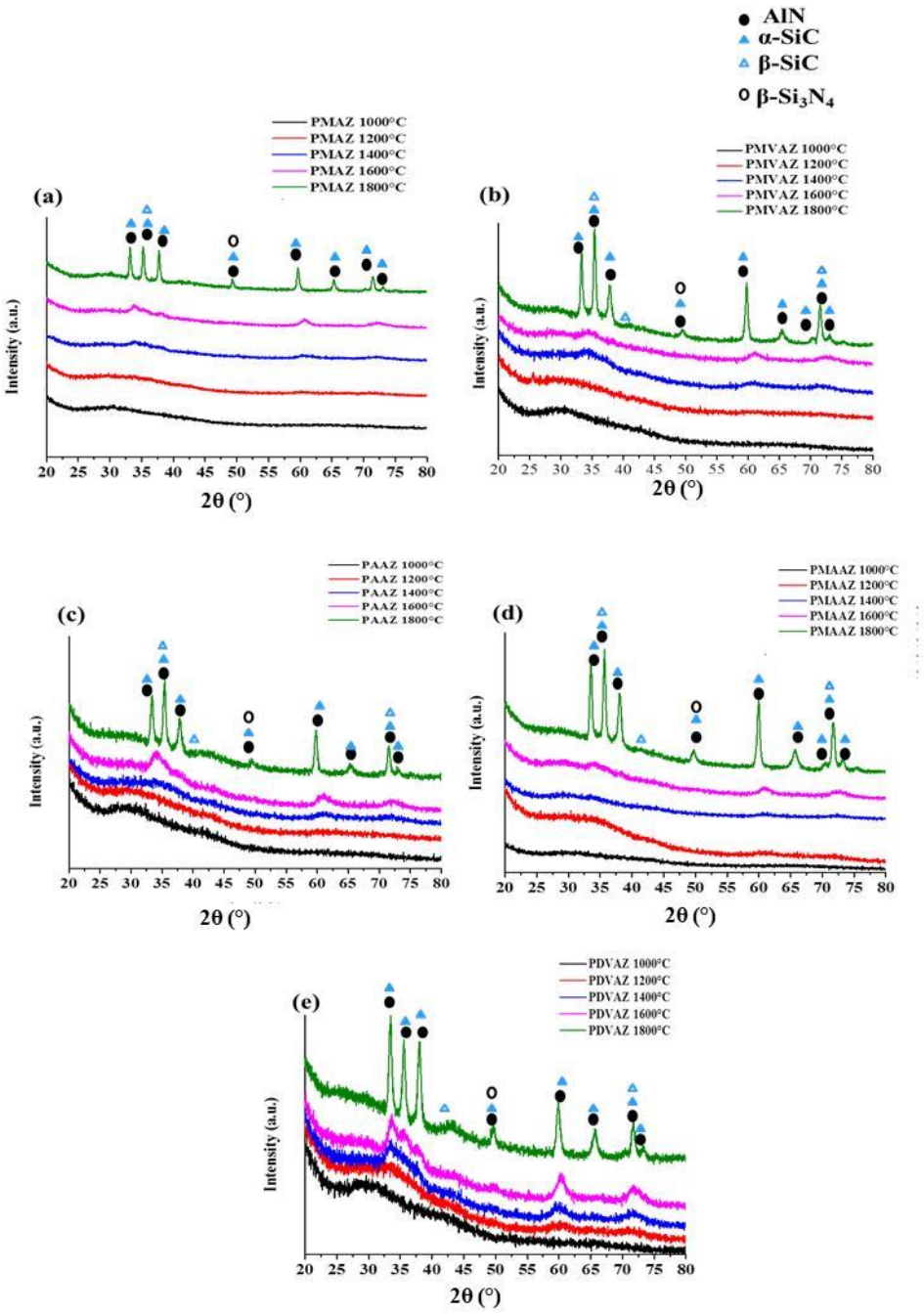

Figure V-16: XRD patterns of SiAlCN materials at 1000, 1200, 1400, 1600 and 1800°C under N_2 derived from (a) **PMAZ**, (b**) PMVAZ**, (c) **PAAZ**, (d) **PMAAZ** and (e) **PDVAZ**.

As previously discussed, PASZ-derived SiAlCN ceramics, independently from the nature of the preceramic polymer, are amorphous at 1000°C and remain in this state up to 1200°C. At 1400°C, the degree of crystallinity seems to be affected by the type of the polymeric precursor. In particular, the XRD pattern of **PDVAZ1400** shows broad peaks corresponding to nanosized β-SiC crystals. This observation points to the fact that SiC nucleation already occurs at 1400°C if the starting polymer contains relatively high carbon content. It is interesting to observe that, at the opposite,

SiAlCN ceramics derived from PMAZ (without olefin), *i.e.*, **PMAZ1400**, do not show any diffraction peaks. Riedel and co-workers studied the effect of carbon content and the precursor chemistry on the crystallization of amorphous SiCN ceramics [334]. Authors showed that the C:Si atomic ratio had an effect on the crystallization of Si_3N_4 and no relationship with the crystallization of SiC. In our case, it seems that the C:Si ratio measured in PASZ-derived SiAlCN ceramics has a clear effect on the structural evolution of the samples: the lowest C:Si ratio attributed to **PMAZ1000** (Table V-3) corresponds to the lowest degree of crystallization after annealing to 1800°C (**PMAZ1800)**. This is clear based on the XRD patterns of the samples derived from **PAAZ1000** and **PMAAZ1000**. The former (C:Si=2.1) crystallizes earlier than the latter (C:Si=1.5) upon heating to 1800°C. As mentioned above, the sample **PMAZ1000** (C:Si=0.9) is the most stable against crystallization through annealing to 1800°C. There is, therefore, a clear evidence that the C:Si ratio governs the crystallization of SiAlCN ceramics. After heat-treatment to 1800°C, all the samples exhibit the reflections characteristic of a 2H wurtzite-type compound [335]. The similarity in the basal plane lattice parameters between AlN and SiC suggests that AlN may seed SiC crystallization [336, 337]. Most interesting is the absence of silicon nitride (Si_3N_4) even if some XRD peaks attributed to SiC could be assigned to β-Si_3N_4 (whereas Si_3N_4 is identified in SiBCN ceramics). This probably means, based on XRD, that Si_3N_4 decomposed by the carbon leading to SiC according to the reaction depicted in equation V-11.

$$Si_3N_4 + 3C \rightarrow 3SiC + 2N_2 \qquad \text{(V-11)}$$

This reaction usually occurs at 1484°C (P_{N2}= 1 bar) [338].

Raman spectroscopy is an important non-destructive tool for investigating the structural evolution of the free carbon phase in these materials. Free carbon appears in the Raman spectra of PDCs in the form of disordered-induced D and D' bands at ~1350 and 1620 cm^{-1}, the G band at ~1582 cm^{-1} due to the band stretching of sp^2 carbon, as well as the G' band that is overtone of the D band at ~2700 cm^{-1}, characteristic of defect-free samples [339, 340]. Raman spectra of the samples annealed under N_2 at 1000, 1200, 1400, 1600 and 1800°C are presented in Figure V-17.

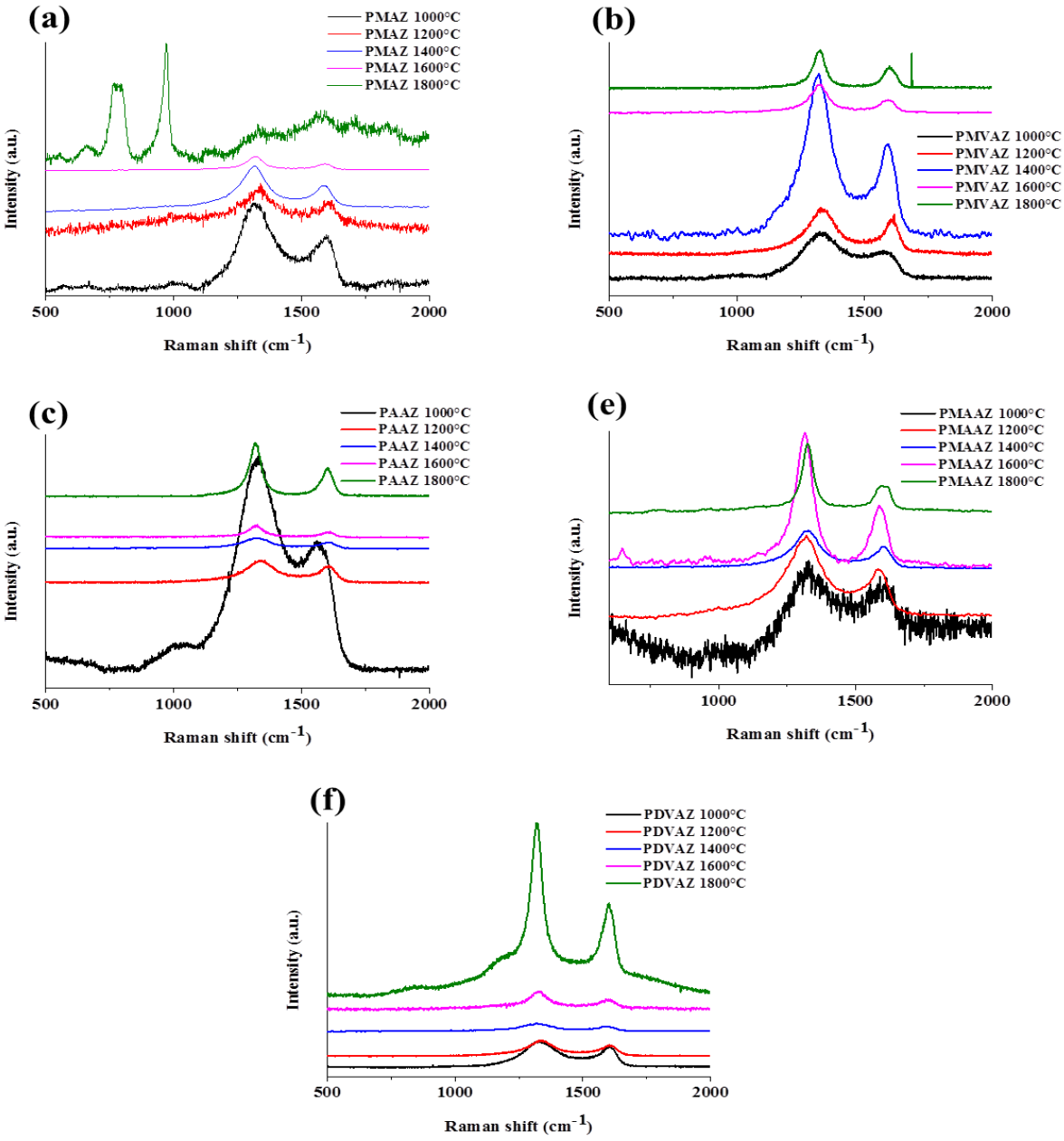

Figure V-17: Raman spectra of SiAlCN materials at 1000, 1200, 1400, 1600 and 1800°C under N_2 derived from (a) **PMAZ**, (b) **PMVAZ**, (c) **PAAZ**, (d) **PMAAZ** and (e) **PDVAZ**.

The samples exhibit the characteristic broad D and G signals and strong overlaps at each temperature from 1000 to 1700°C as a consequence of the pronounced structural disorder of the carbon phase. At 1800°C, these bands almost disappear in the sample **PMAZ1800** while new bands appear at 830 and 920 cm^{-1}. They are attributed to SiC as reflected by XRD. Also the AlN phase appears around 650 cm^{-1} in this sample at 1800°C. Finally, we can observe, in the sample **PMAZ1800,** all the peaks characteristic of the crystalline phases (AlN, SiC) whereas it appears the lower crystallized by XRD.

TEM studies were used to examine details of the crystallization process. Typical results obtained on the samples derived from **PMVAZ** at different temperatures are shown in Figure V-18, 19, 20, 21). The bright field TEM image of the sample **PMVAZ1000** in Figure V-18-a is characterized by extended amorphous regions (predominant feature of the sample). The corresponding selected area electron diffraction (SAED) pattern supports the amorphous state of the sample. It displays diffuse haloes, indicating the amorphous microstructure of the sample heat-treated at 1000°C. However, in some local part of the sample, fine crystallites have been observed which suggests that the sample is not a pure amorphous material (a fact that we could not presume based on XRD and Raman). The corresponding SAED (inset in Figure V-18-b) is identical to β-Si_3N_4.

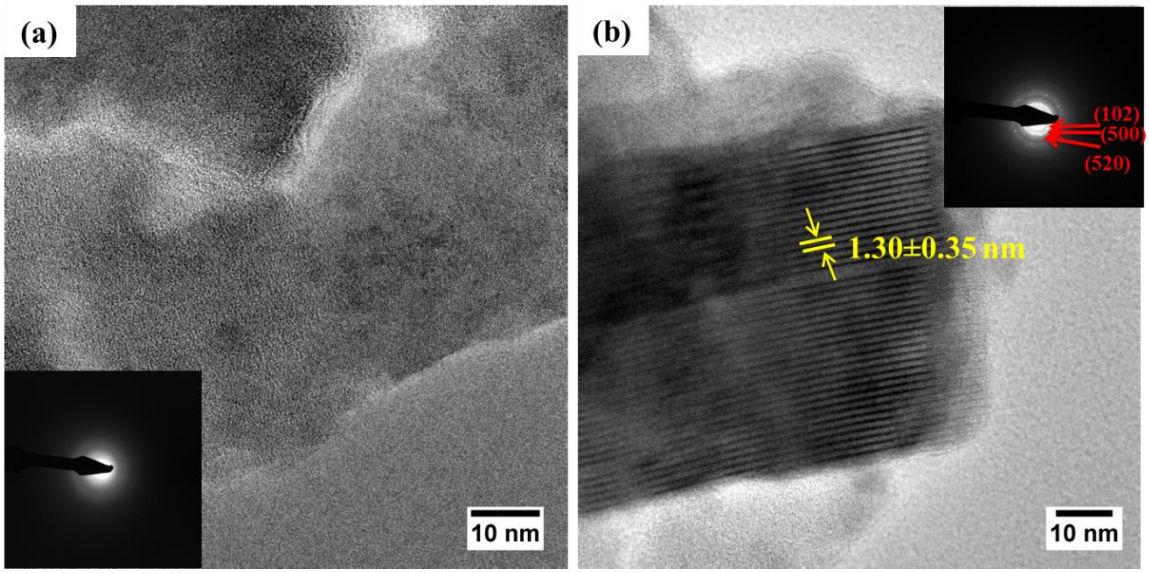

Fi**gure V-18:** TEM images of **PMVAZ1000** : (a) low magnification and (b) High Resolution with in inset the corresponding SAED pattern indexed with the hexagonal phase of β-Si_3N_4.

As shown in Figure V-19, the TEM observation results of the sample **PMVAZ1400** shows a more crystallized state. This is emphasized in the SAED patterns where distinct rings and spots are clearly observed. The sample exhibits rich nanosheets of β-Si_3N_4 (with a $P6_3/m$ space group) and some α- Si_3N_4 regions as a secondary phase (Figure V-19-a). No SiC-regions have been observed yet at this temperature, however, we could detect AlN nanocrystalline phases (Figure V-19-b), with a $P6_3mc$ space group that starts to appear at 1400°C, as confirmed through the SAED pattern (inset Figure V-19-b). The size of the AlN crystallites varies from 7 to 12 nm (diameters have been measured as average on long and short axis). It should be mentioned that we concluded by XRD and Raman spectroscopy that the sample was amorphous.

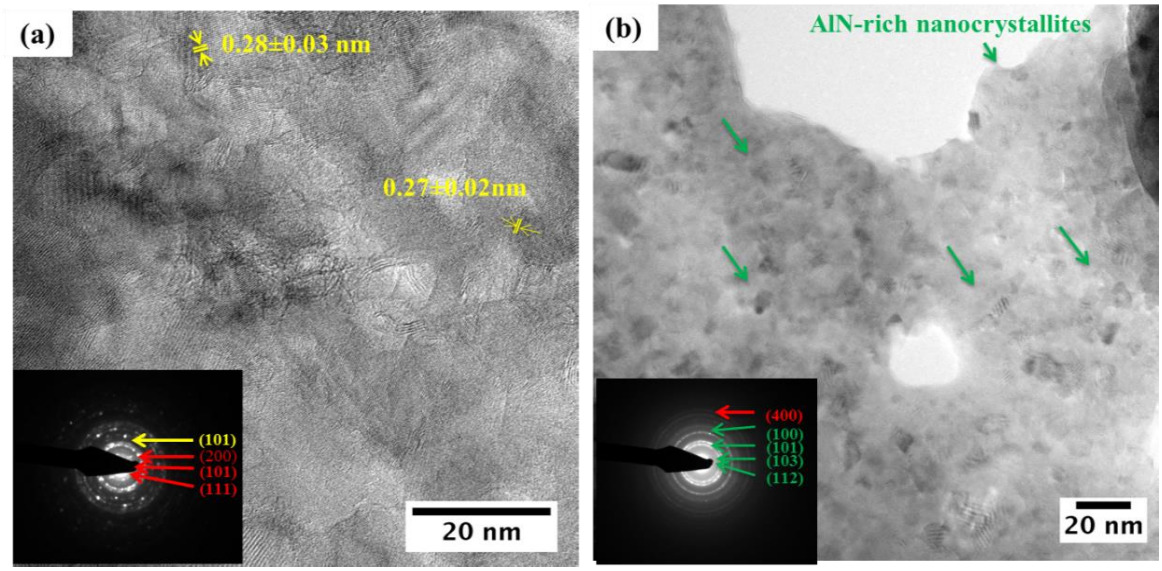

Figure V-19: TEM images of **PMVAZ1400** with in inset the corresponding SAED pattern in which the red indices refer to the β-Si_3N_4 phase, the green ones to the hexagonal AlN phase and the yellow ones to the α-Si_3N_4 phase.

The characterization of the sample **PMVAZ1600** under nitrogen has resulted in a much more crystalline material.

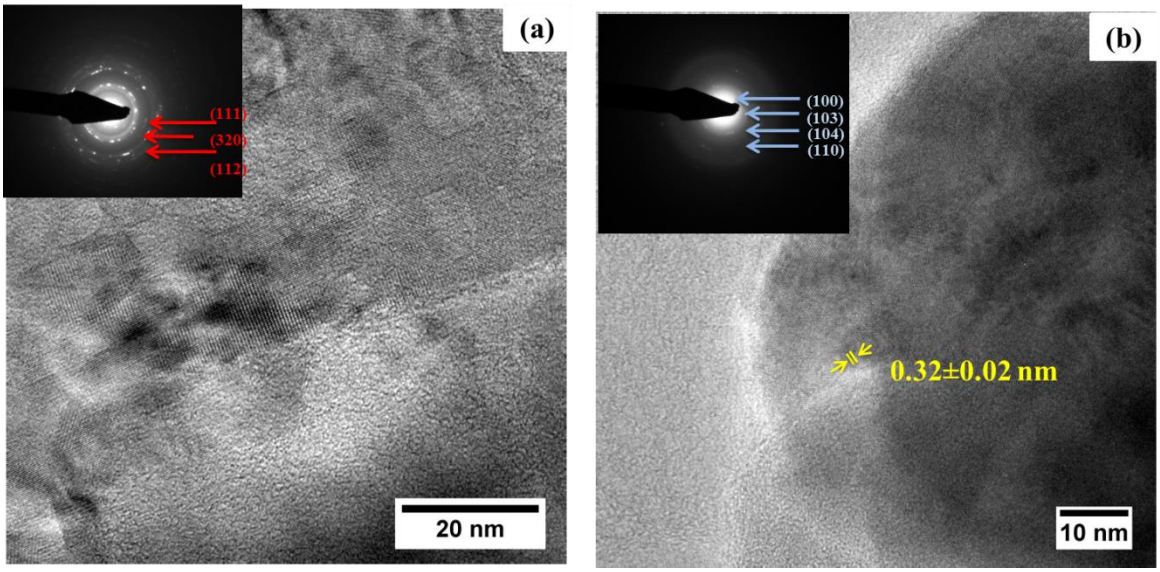

Figure V-20: TEM images of **PMVAZ-d-SiAlCN** at 1600°C in N_2 atmosphere.

The HRTEM and SAED patterns emphasize the presence of β-Si_3N_4 (Figure V-20-a) and α-SiC regions (Figure V-20-b). The nanosized SiC crystallites are more frequent than the Si_3N_4 crystallites which tend to prove that SiC is formed to the detriment of Si_3N_4 (Equation V-1). SiC phases encounter a space group of *$P6_3mc$* that is identical to the AlN phase depicted at 1400°C. Since we could not depict AlN, at 1600°C, as a single crystalline phase, we can imagine that it is merged

with the SiC since they crystallize in the same space group forming a solid-solution rather than a mixture of both separate phases of SiC and AlN.At 1800°C (**PMVAZ1800**) a polycrystalline nature of the **SiAlCN** ceramic is obviously encountered with the presence of a SiC-AlN compound and SiC phases (Figure V-21). Fine β-Si_3N_4 crystallites are still present which was identified also by XRD.

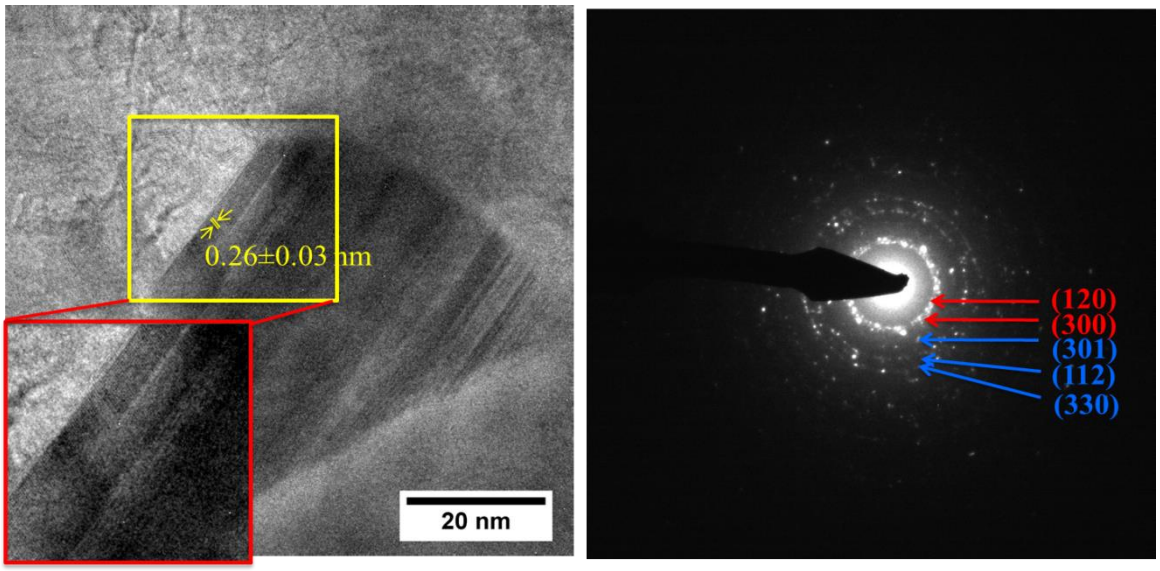

Figure V-21: TEM images of **PMVAZ1800** with in inset the corresponding SAED pattern in which the red indices refer to the β-Si_3N_4 phase and the blue ones to the SiC phase.

Before concluding, we have performed TGA experiments at high temperature on the sample **PMVAZ1000**. The high temperature behavior of **PMVAZ1000**was investigated by TGA in N_2 from RT to 1800°C (Figure V-22-a), compared with their SiBCN analog published by our group [107] and discussed based on XRD, Raman and HRTEM results. Preliminary investigations of the resistance of **PMVAZ1000** towards oxidation and hydrolysis at 1000°C was performed by recording the high temperature TGA in air (35% moisture) up to 1000°C with a dwelling time of 5 h (Figure V-22-b).

Under nitrogen, **PMVAZ1000** is decomposed through two steps with a neglected first weight loss (around 0.7 %) most probably due to evaporation of surface oxide-based compounds. The second weight loss occurs at 1650°C and corresponds to the crystallization of the materials as seen through XRD investigations and probably to the major decomposition reaction occurring, i.e., the solid-state carbothermal reduction of Si_3N_4 with “free” carbon that leads to the major formation of the SiC phase. It should be mentioned that the SiBCN analog is stable over the temperature range investigated here which tends to indicate that SiAlCN materials are less stable than SiBCN materials with regard to crystallization.

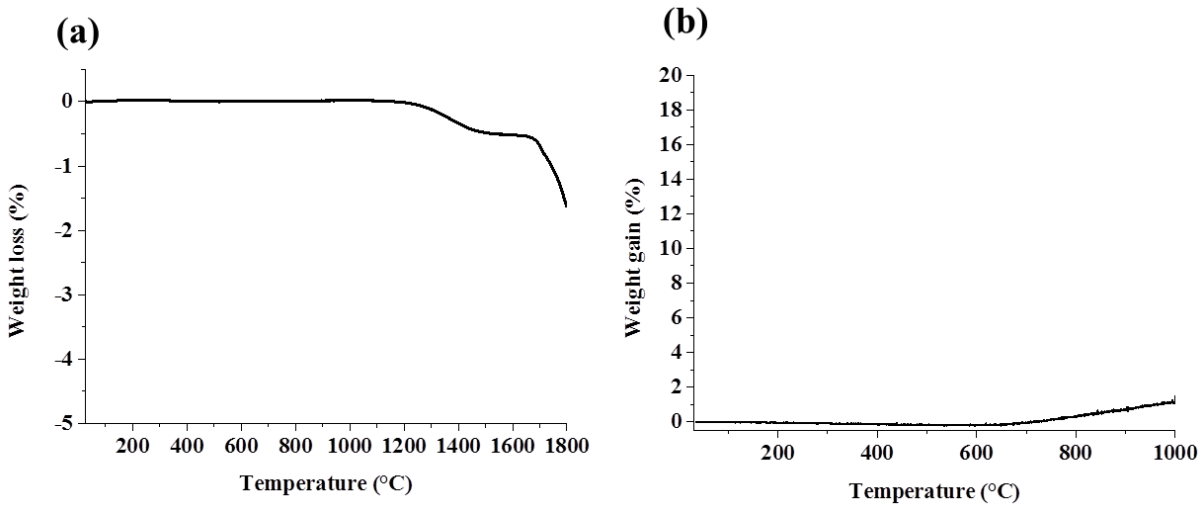

Figure V-22: TGA of **PMVAZ-d-SiAlCN** (a) under N_2 up to 1800°C and (b) under air (35% moisture) up to 1000°C. Heating rate 5°C.min^{-1}.

Under air, the material remains stable up to 700°C. In the temperature range 700-1000°C, a slight increase in the weight corresponding to 1% is observed which is comparable to their SiBCN analogs [212]. However, further investigations are required to discuss on this behavior.

In this study, X-ray amorphous SiAlCN ceramics with various carbon contents and C:Si atomic ratio have been obtained from a series of polyaluminosilazanes. The crystallization behavior under N_2 atmosphere was investigated by XRD, Raman spectroscopy and TEM. By XRD, the crystallization of the ceramic samples increased with the increase of C:Si atomic ratio going from a global amorphous state to a SiC/AlN solid solution. Raman spectroscopy allowed us to identify the presence of the free carbon in all the samples and it remained in the samples heat-treated at 1800°C. By TEM, on a selected sample, we could confirm the structural evolution of the amorphous SiAlCN phase toward a SiC/AlN solid solution. Si_3N_4 detected by XRD, is identified at each temperature in the SiAlCN sample in the temperature range 1000-1800°C.

In the introduction, we mentioned that the interest of the "single-source precursor" approach is to extend the possibility of shaping of the polymers using plastic forming-based processes. As a proof of concept, we demonstrate in the second part of the present chapter the preparation of SiAlCN foams. This work is done in collaboration with the University of Padova (Prof. Paolo Colombo).

3. MICROCELLULAR FOAMS ELABORATION

3.1. Introduction

(Carbo)nitrides are gaining considerable interest with the aim of further exploiting their properties in industrial and technological applications (metallurgy, catalyst supports, filters, membranes…). Elaboration of **polymer-derived oams** has been a matter of research owing to the advantage of preceramic polymers to form monolith-type ceramics with relatively good control of the dimensional charges which occur during the polymer-to-ceramic conversion. It has been recently demonstrated that preceramic polymers can be used to produce porous foams with variable composition essentially based on silicon such as SiCN [233, 341] and SiCO [220] compositions. Our group was interested in SiBCN microcellular systems mixing the SiBCN precursor polymethylvinylborosilazane with sacrificial fillers [342]. Here, the focus will be on the preparation of microcellular **SiAlCN foams** consisting of a 3D array of open cells. The process includes two major steps:

i) Shaping the SiAlCN precursor homogeneously mixed with the sacrificial fillers in the solid state, in their plastic domain, by warm-pressing

ii) Pyrolysis of the green compact to convert the polymer into ceramic while the sacrificial fillers are decomposed leaving voids.

Porosity, pore size and distribution, occurrence of open or closed cells are parameters that can be tailored by controlling the amount of the sacrificial fillers and the conditions of pressing, which make this process, a very versatile one to produce foams.

3.2. Experimental part

3.2.1 Materials

We used polymethymetacrylate (PMMA) microspheres as sacrificial fillers with an average diameter of 25 µm. These were provided from Padova University within collaboration with Prof. Paolo COLOMBO. PolyAllylAluminosilazane (PAAZ) was used as SiAlCN precursor.

3.2.2 Preparation of foams

First of all, we dry-mixed the preceramic polymer with the microspheres of PMMA-25 µm according to a precise weight ratio in order to obtain a homogeneous mixture of two phases (~ 250 mg). It should be noted that we considered milling the polymer+PMMA using a ball milling type IKA ULTRA-TURRAX® Tube drive, using steel balls (Ika BMT-20S) respecting a weight ratio balls: (polymer+PMMA) of 20. The milling was conducted with a rotation speed of 2500 $tr.min^{-1}$ for

10 min. Then the mixture was sieved through an 80 μm screen in a glove box full of argon to recover fine grained powder. However the results turned out to be quite similar to only mixing manually the preceramic polymer with the PMMA in an agate mortar for 5 min so we considered this quicker alternative for obtaining well homogenized and fine polymeric mixture. For producing a cylindrical piece, the polymeric mixture is placed in a mold related to uniaxial press (Atlas Auto T8 model from Sepac) setup in a nitrogen filled glove box, subject to controllable pressure and temperature for the rearrangement of the grains. The samples were slowly de-loaded during cooling down to room temperature within 30 min and the cylindrical green bodies taken the form and dimensions of the mold that is of 13 mm are obtained. The height of the cylinder is limited to 3 mm, because above this value cracks are likely to be formed in the materials. The green bodies were subsequently placed in an alumina boat and transferred into a silica tube inserted in a horizontal tube furnace (Nabertherm type RS 80/500/11, Germany) directly connected to the glove box where the pressing took place to prevent any oxygen contamination. The tube was held under dynamic vacuum for 30 min and refilled with nitrogen (99.99%). A constant flow of 120 $mL.min^{-1}$ of nitrogen was passed through the tube where the samples were subjected to a cycle of ramping of 0.5°$C.min^{-1}$ up to 1000°C, dwelling there for 2 hours, and then cooling down to room temperature at 1°$C.min^{-1}$. The samples are labeled as follows: weigh ratio between the polymer and the PMMA, temperature of pressing, pressure. For example PAAZ20/PMMA80-80-74 stands for a mixture of 20/80 weight ratio between PAAZ and PMMA, which was hot-pressed at 80°C at 74 MPa. Furthermore we were interested in studying the evolution of the foams, if obtained, with the increase of the curing temperature; therefore the previously pyrolyzed samples were transferred in a graphitic furnace (Gero Model HTK8). The furnace was vacuum pumped for 30 min then filled with nitrogen to undergo a heating program through a cycle of ramping of 1°$C.min^{-1}$ up to 1400°C, dwelling there for 2 h and then cooling down to room temperature at 2°$C.min^{-1}$. A constant flow of N_2 was fixed to 200 $mL.min^{-1}$.

3.2.3 Experiments

The TGA-DSC measurements were carried on a Setaram TGA 16.1892 equipment. Before the measurements, the samples, loaded in alumina crucibles, are always purged with a vacuum cycle, then the chamber is filled with nitrogen and measurements start up to 1000°C with 5°$C.min^{-1}$ as heating rate and 10 min as dwelling time. High temperature TGA (Netzsch STA 501 equipment) was performed under N_2 up to 1800°C with a heating rate of 10°$C.min^{-1}$ and a dwelling time of 10 min.

The textural properties of the foams were investigated by means of mercury porosimetry using a Micromeritics Autopore IV 9500 penetrometer. This type of measurements provides

information on the macroporosity, the pore size, the volume as well as the pore distribution by the mercury impregnation that connects two adjacent macropores thus the diameters in question concern the void spaces and not the cells themselves. XRD (Philips PW 3040/60 X'pert PRO X-ray diffraction system operating at 30 mA and 40 kV from 10 to 90° with a step size of 0.0167, using a Kα1 of copper as source) and SEM (Hitashi S4800, operating with a acceleration voltage between 0.1 kV and 30 kV) were employed in order to investigate the structural evolution.

3.3. Results and discussion

3.3.1 *Preparation of SiAlCN microcellular foams*

First of all, we should mention that selecting the PMMA-50 µm as sacrificial fillers in producing the **SiAlCN foams** was not successful. The composite piece did not survive to the pyrolysis step and got directly blown due to the large size of the spheres that, in our case, were not adequate to consolidate the final material after burning out the sacrificial fillers. Based on the study presented in the first part of this chapter, we deliberately chose the **PAAZ** with a ceramic yield corresponding to 76% to avoid collapsing during the foaming procedure. This is an important point to consider because, due to the gas release during curing and elimination of the **PMMA**, the material must be sufficiently consolidated and avoid a too important volume shrinkage during the pyrolysis to prevent the foam from collapsing. Therefore, selecting a preceramic polymer with a high ceramic yield such as **PAAZ** seemed to us judicious but this is not a sufficient condition: it must exhibit plastic forming to be warm-pressed leading to a consolidated piece.

Figure V-23 illustrates the pathway we used to produce **SiAlCN microcellular foams**.

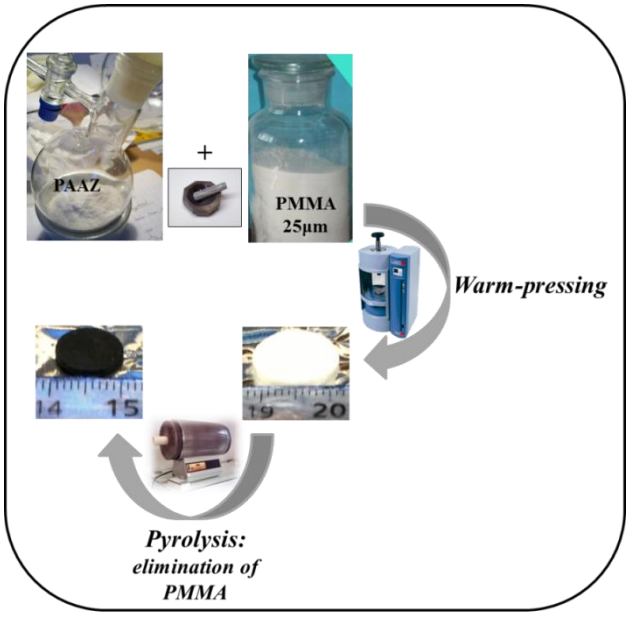

Figure V-23: Experimental protocol of the warm-pressing.

The control of the weight ratio influences both the retention of the integrity of the piece during the pyrolysis and the final porosity of the material. It is the first parameter to study therefore we chose to study two weight ratio Polymer/PMMA 20/80 and 30/70 based on the literature [220]. Depending on the preceramic polymer, the pressing can be carried out at low temperatures (cold-pressing) or at high temperatures (hot or warm-pressing). In our case, as an example and based on the DSC investigations, the **PAAZ** reflect a plastic deformation from 80 to 200°C. Above 150°C the polymer swells and softens probably due to the polymer decomposition (Figure V-24-a). For the PMMA microspheres we can identify the glass transition from 100°C to 115°C with an average temperature of 111°C (Figure V-24-b). Considering the results, the pressing temperature, our second parameter to change, has been tested in the range of 60-150°C with a particular focus on the range 60-100°C to avoid deformation of the PMMA sphere during pressing. It should be mentioned that we did not precrosslink the preceramic polymer before pressing as the majority of papers mention. The third parameter that we changed was the pressure (74 to 370 MPa).

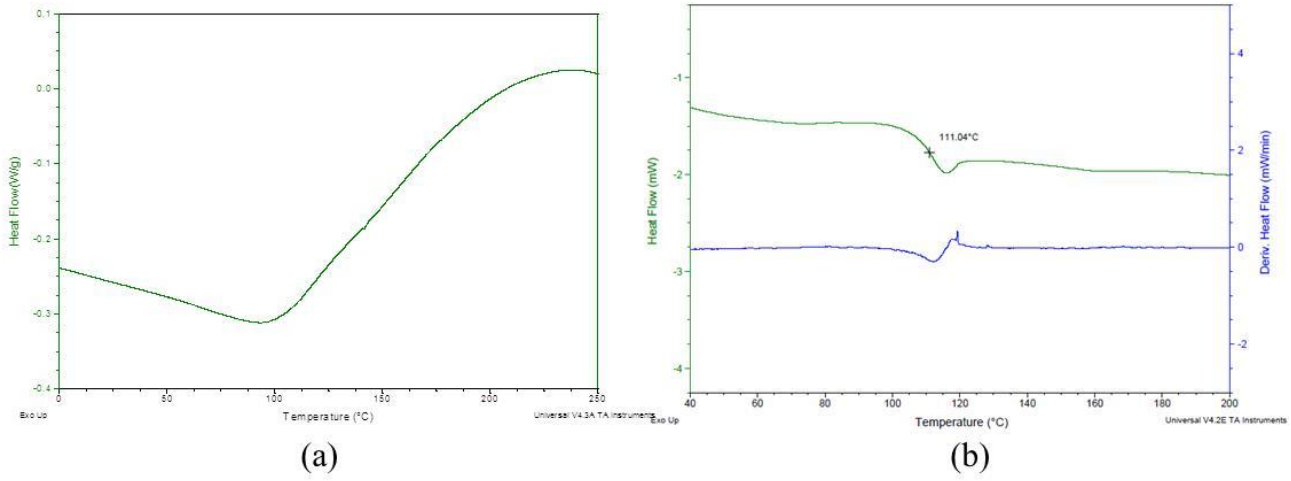

Figure V-24: DSC curves for (a) **PAAZ** and (b) **PMMA-25 µm** under N_2 with 5°C.min^{-1} as heating rate.

We selected a slow heating rate of the pyrolysis step is to avoid the collapsing during the template burning-out process. In fact, the PMMA-25 µm starts decomposing around 277°C and finishes at 400°C, as depicted in the Figure V-25.

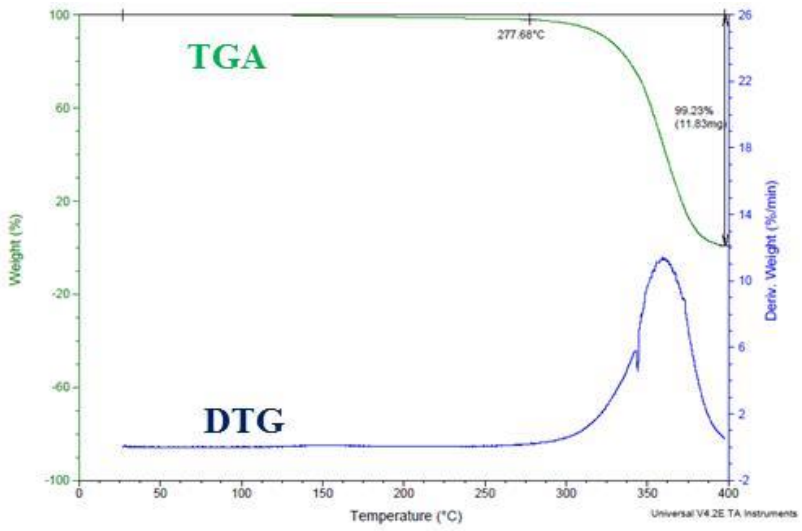

Figure V-25: TGA and DTG curves for PMMA-25 µm under N_2 with 5°C.min^{-1} as heating rate.

As-obtained samples are then characterized using different techniques to select the parameters that allow us obtaining foams responding to our specifications that are interconnected porosity with a relatively homogeneous distribution of pores.

3.3.2 Characterization of SiAlCN microcellular foams

A typical example of **PAAZ-derived foam** is presented in Figure V-26.

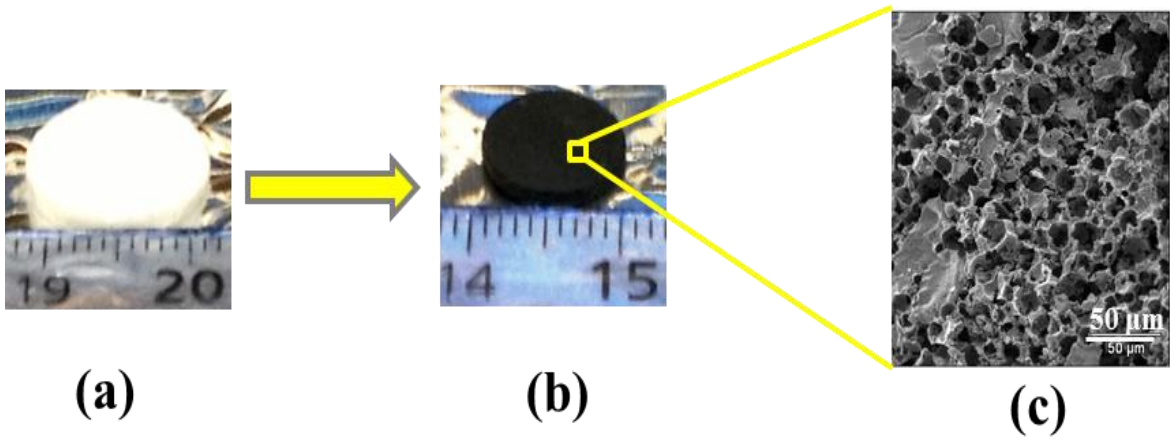

Figure V-26: Typical example of SiAlCN foams (a) polymeric green body, (b) SiAlCN ceramic and (c) the corresponding SEM image.

No cracks were found in these monoliths by the naked eye. They have a pellet-like appearance and they replicated the cylindrical shape of the die used during the warm pressing. Shrinkage is relatively well controlled (~20%). However, even though the materials can he handled, they are relatively brittle under load. Table V-4 summarizes the parameters we applied during the warm-pressing (WP) process.

Table V-4: Warm pressing (WP) conditions of PAAZ/PMMA-25 μm mixtures.

Sample name	PAAZ/PMMA ratio	WP temperature (°C)	WP pressure (MPa)	Observation After WP (green body)	Observation After pyrolysis (foam)
PAAZ20/PMMA80-60-74	20/80	60	74	Compact	Brittle
PAAZ20/PMMA80-80-74	20/80	80	74	Compact	Brittle
PAAZ20/PMMA80-100-74	20/80	100	74	Compact	Compact
PAAZ20/PMMA80-120-74	20/80	120	74	Compact	Compact
PAAZ30/PMMA70-60-74	30/70	60	74	Compact	Brittle
PAAZ30/PMMA70-80-74	30/70	80	74	Compact	Compact
PAAZ30/PMMA70-100-74	30/70	100	74	Compact	Compact
PAAZ30/PMMA70-120-74	30/70	120	74	Compact	Brittle
PAAZ30/PMMA70-150-74	30/70	150	74	Compact	Brittle
PAAZ30/PMMA70-80-222	30/70	80	222	Compact	Brittle
PAAZ30/PMMA70-80-370	30/70	80	370	Compact	Brittle
PAAZ30/PMMA70-100-370	30/70	100	370	Compact	Brittle

Our first objective was to select the parameters in terms of Polymer:PMMA ratio, temperature and pressure which allowed us to obtain foams with an homogeneous distribution of the pores and pore interconnectivity. First of all, the elaboration of foams using 80% of PMMA in the polymer mixture was not successful because the pores were not homogeneously distributed and the porosity was not interconnected. As a consequence, we focused on the use of a mixture of 30:70 (PAAZ:PMMA). We have compared some of the samples listed in Table V-4 by SEM). Figure V-27 presents the SEM images of the 30:70 foams prepared at temperatures ranging from 60 to 150°C at different pressures.

We can observe that the samples prepared using a pressure of 74 MPa displays spherical interconnected cells with an average size of 20 μm (Figure V-27-a,b,e) close to the diameter of the PMMA beads with an interconnectivity mainly induced by the contact of the spheres with each other during the pressing process. The homogeneity and interconnectivity are two basic parameters for the application we have in mind; that is catalytic support for hydrogen generation. In fact this particular sample after pyrolysis retained the shape of the green sample without any fracture and with limited volume shrinkage (~20%). By using high pressures (Figure V-27-c,d,f), we obtained dense samples with no apparent porosity. At this stage, it is difficult to conclude on the effect of the temperature fixed during the warm pressing even if it seems that a too high temperature (150°C, Figure V-27-h) does not lead to apparent porosity.

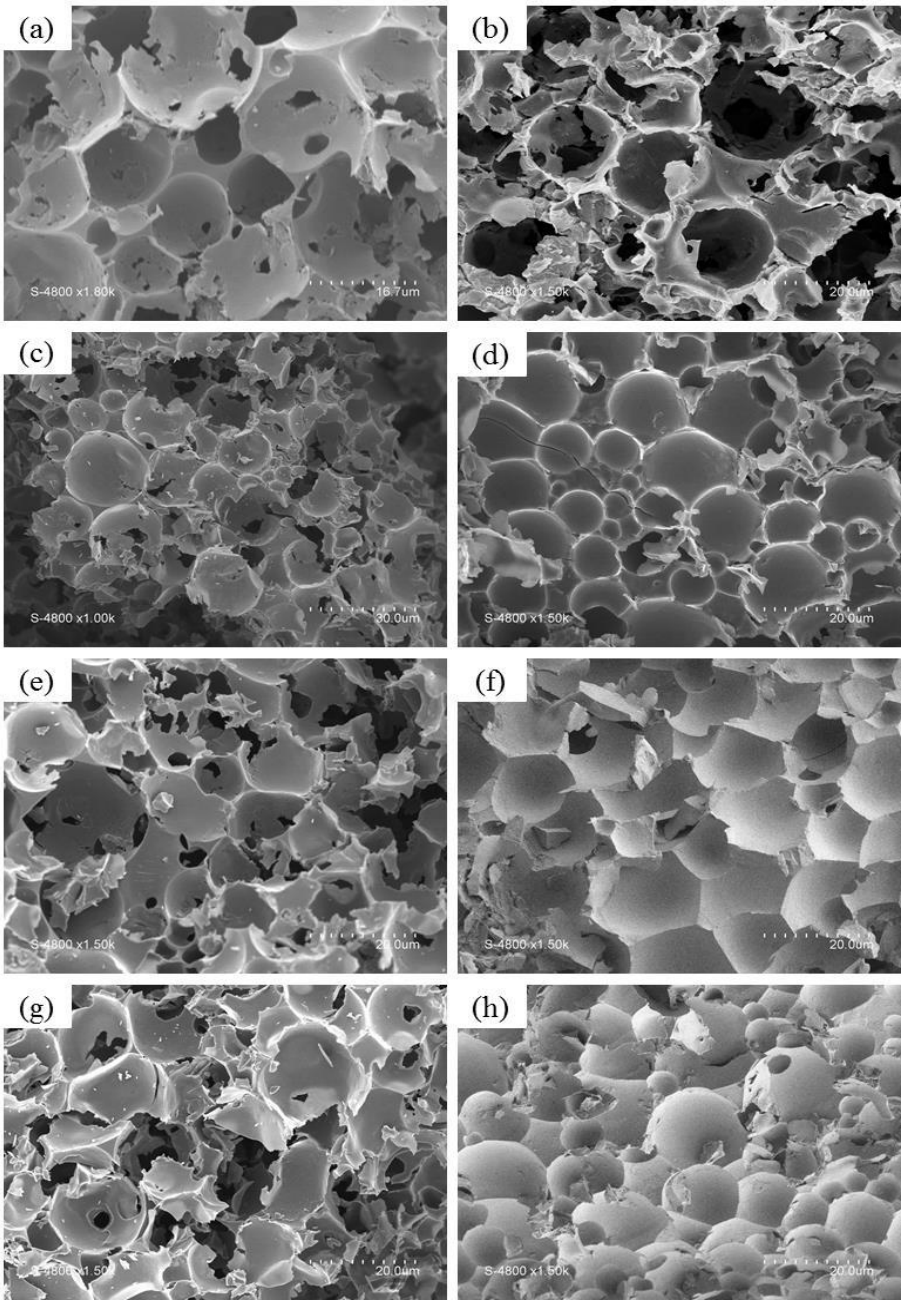

Figure V-27: SEM images of (a) **PAAZ30/PMMA70-60-74** (b) **PAAZ30/PMMA70-80-74**, (c) **PAAZ30/PMMA70-80-222**, (d) **PAAZ30/PMMA70-80-370**, (e) **PAAZ30/PMMA70-100-74**, (f) **PAAZ30/PMMA70-100-370**, (g) **PAAZ30/PMMA70-120-74** and (h) **PAAZ30/PMMA70-150-74**.

As mentioned in the first part of the present chapter, the precursors are air- and moisture-sensitive. Here, it is shown that the oxygen level in the derived ceramics as foam can be as high as 11wt%. The oxygen intake in the present study could be attributed to the PMMA beads $(C_5H_80_2)_n$, despite the fact that drastic precautions are taken concerning the manipulation of the products, the use of the glove box to do the warm pressing and the absence of contact with air of the sample during the transfer between the glove box and the furnace for achieving the pyrolysis. In our case, EDX

analysis revealed characteristic peaks with a weight percentage of 48.7 wt% silicon, 15.3 wt% aluminum, 19.7 wt% carbon, 5.1 wt% nitrogen and 11.2 wt% oxygen leading to an empirical formula of $Si_{3.0}Al_{1.0}C_{2.8}N_{0.6}O_{1.2}$.

In order to better qualify and quantify the macroporosity of the samples prepared using a WP pressure of 74 MPa, mercury intrusion porosimetry investigations were performed. The first important feature is that these monoliths are robust enough to endure mercury impregnation without collapsing. The results are reported in Figure V-28 and Table V-5 for the samples obtained using a warm pressing pressure of 74 MPa.

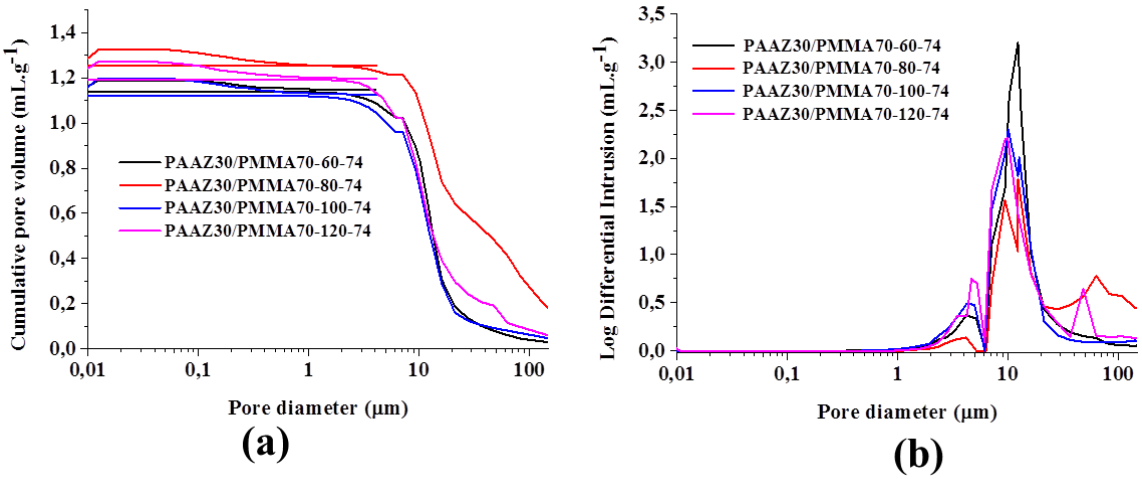

Figure V-28: Mercury porosimetry (a) cumulative intrusion and (b) log differential cumulative intrusion *vs* pore size diameter

Table V-5: Mercury-intrusion porosimetry properties of SiAlCN foams elaborated from PAAZ.

Sample	Total intrusion volume ($cm^3.g^{-1}$)	Median pore diameter (µm)	Bulk density at 0.52psia ($g.cm^3$)	Apparent skeletal density ($g.cm^3$)	Porosity (%)
PAAZ30/PMMA70-60-74	1.16	12.7	0.59	1.8	68
PAAZ30/PMMA70-80-74	1.3	21.4	0.59	2.35	75
PAAZ30/PMMA70-100-74	1.15	11.6	0.62	2.15	72
PAAZ30/PMMA70-120-74	1.24	11.5	0.53	1.6	66

The pore volume and size distribution of samples revealed a single intrusion step in the domain of large macropores from 5 to 80 µm. The curve of cumulative pore volume versus pore diameter showed a continuous increase in mercury uptake with a decrease in pore diameter (*i.e.*, increase of Hg intrusion pressure). It is clear that the monoliths display a cell window with a relatively large polydispersity in size which corresponds to the size of the larger interstices. The total pore volume measured by this method is high (>1.1 $cm^3.g^{-1}$), whereas the average pore diameter varies from 11.5 to 21.4 µm. Especially, we confirmed for the sample **PAAZ30/PMMA70-80-74** that the average pore diameter fits the average diameter of the PMMA spheres. From the cumulative pore volume, the porosities of the samples are calculated to be in the range 66-75%. According to the Table V-5, we selected the sample **PAAZ30/PMMA70-80-74** for further characterization, because it is the most porous sample with the highest pore volume. Helium pycnometry allowed us to determine the bulk density of the sample. A helium density of 2.1 was obtained. It is close to that obtained from the same sample without induced porosity (=powder) (d=2.3). Compression tests have been performed in collaboration with Prof. Fantozzi from INSA, Lyon. The foams display a linear behavior up to 70 N. Then, an inflection point is obtained similarly to a densification process up to 200 N. This indicated that the material is poorly consolidated. Therefore, the warm pressing process has to be optimized.

After elaboration, the XRD patterns of the sample **PAAZ30/PMMA70-80-74** exhibit peaks indicating the amorphous state of the samples as seen in the first part of the present chapter. The main interest of **PAAZ-derived SiAlCN** ceramics is the stability of their "disordered" long range structure up to 1600°C. An important issue which affects the high temperature stability of the ceramics is their textural properties. This has been demonstrated by our group for SiBCN [107]. The thermal stability of **PAAZ30/PMMA70-80-74** has been therefore investigated by TG experiments up to 1800°C in a N_2 atmosphere (Figure V-29-a).

The sample shows no weight change up to 1400°C, demonstrating the excellent stability of the amorphous channel walls. This offers the interest to deposit or infiltrate materials in gas phase by CVD or CVI without any change of the structure. Heat-treatment above 1400°C resulted in a relatively rapid decomposition step associated with a continuous weight loss up to 1800°C (25 wt%). This behavior is clearly attributed to the high amount of porosity in this material because a significantly smaller weight loss is measured in the analog dense sample obtained by direct pyrolysis under nitrogen at 1000°C **PAAZ** (Figure V-29-b).

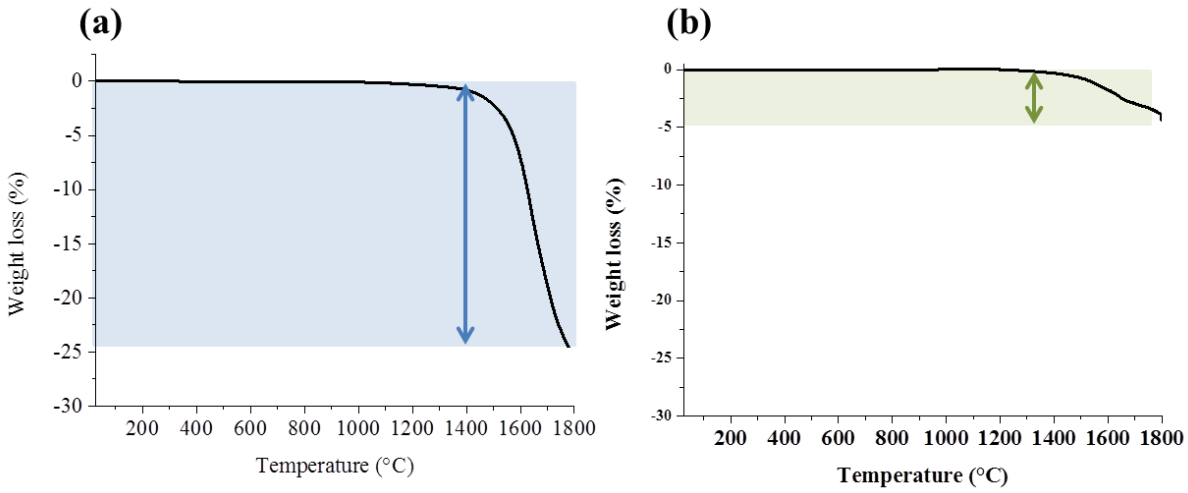

Figure V-29: HTTGA curve of (a) **PAAZ30/PMMA70-80-74-1000°C** and (b) **PAAZ-1000°C** under N_2 up to 1800°C with a heating rate of 5°C.min^{-1}.

At 1800°C, α-SiC phase seems to be present in majority as observed on the XRD patterns in Figure V-30. This confirmed the carbothermal reduction of Si_3N_4 into crystalline SiC.

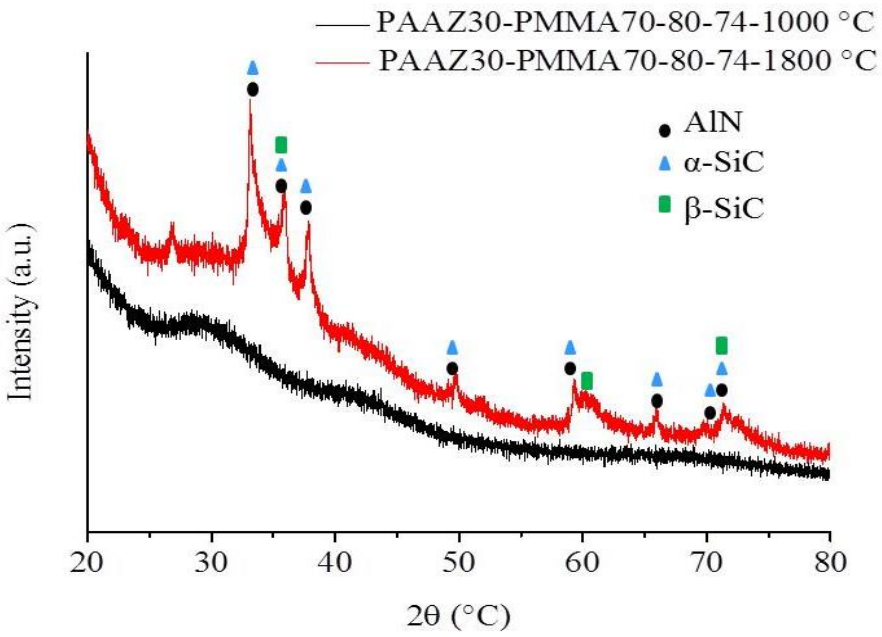

Figure V-30: XRD patterns of **PAAZ30/PMMA70-80-74** at 1000°C (black) and at 1800°C (red).

After heat-treatment to 1800°C, SEM images of the sample **PAAZ30/PMMA70-80-74-1800°C** have identified the presence of white fibers or whiskers emerging from the cells of the material (Figure V-31).

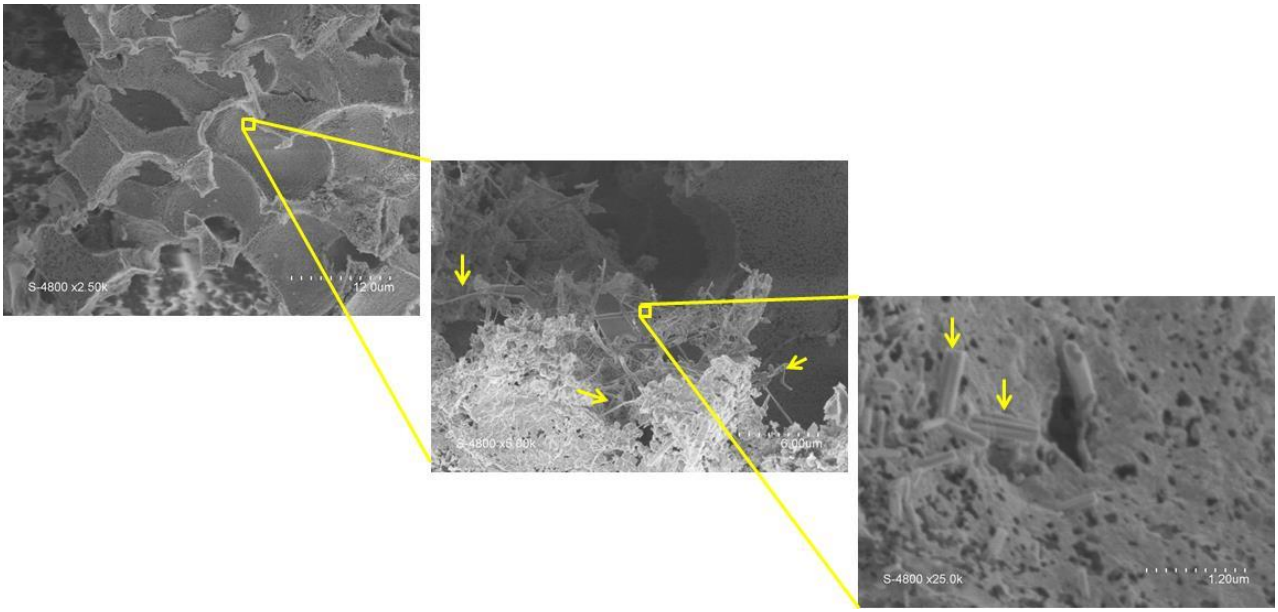

Figure V-31: SEM images of the HTTGA residue (**PAAZ30/PMMA70-80-74-1800°C**).

These observations show that reactions, rather in the vapor phase, take place in the temperature range (1000-1800°C) in which the material decomposes as we saw on the HTTGA curve and the XRD patterns. In fact in such porous materials vapor-phase reactions and in particular the reduction between the free carbon and the silicon nitride are accelerated. Therefore the diffusion paths of nitrogen are facilitated byte interconnectivity of the porosity which kinetically favorites this reaction and therefore the decomposition of the porous materials. The presence of the whiskers that we evidence on the SEM images is quite important and is a clear sign of the decomposition of the material, showing the influence of the high porosity and its interconnectivity on the thermal stability of the SiAlCN material.

To sum up, warm pressing of a mixture of polyallylaluminosilazane (PAAZ) and polyl(methylmethacrylate) PMMA microbeads, followed by pyrolysis were investigated with the aim to produce porous SiAlCN foams. Microcellular SiAlCN foams were obtained with a porosity of 75%. Such high porosity resulted from i) applying a PAAZ/PMMA ratio of 30/70 (with PMMA microbead size of 25 μm), ii) warm pressing the mixture under 74 MPa at 80°C, and iii) pyrolyzing the green compact at 1000°C under N_2 atmosphere. SEM and mercury porosimetry studies revealed that the pores in the material were homogeneously distributed with an average pore diameter of ~22 μm which means a good replication of the pore diameter of PMMA (25 μm). When it comes to the application of such materials, preliminary studies have been done on modifying these SiAlCN foams by tantalum nitride (Dr. Franck Tessier, Rennes) in order to assess the photocatalytic ability of such modified porous SiAlCN for a wide range of applications including H_2 generation (water splitting), water treatment (photodegradation of the organic dye molecules by UV- or visible-light illumination

of the metal nitride incorporated in the foams) …In the first part of the chapter, multi-nuclear solid-state NMR has been mainly used to follow the polymer synthesis and pyrolysis of a series of Al-modified polycarbosilazanes. It has been shown that aluminum exhibits a strong affinity to nitrogen through dehydrocoupling reactions. It seems that hydroalumination reactions are minor. In this part, as we already mentioned we refer also to the analogue Si/B/C/N system. However, the polymer synthesis is exclusively reported to proceed by hydroboration. It should be mentioned that Al-modified polycarbosilazanes are synthesized through a polymer route which consists to prepare, in the first place the polycarbosilazane, then in the second step to synthesize the Al-modified polycarbosilazane. Boron-modified polycarbosilazanes can be prepared through this way [212], but in the majority of the case, boron-modified polycarbosilazanes are prepared by borane addition leading to a monomer tris-(dichloromethylsilylethyl)borane of the type $B(C_2H_4SiCH_3Cl_2)_3$ (C_2H_4= $CHCH_3$, CH_2CH_2) called TDSB, followed by subsequent ammonolysis/aminolysis yielding the polyborosilazane $[B(C_2H_4SiCH_3NH)_3]_n$ which is cross-linked *via* the C-B-C bridge. This route is called "monomer route". In the following part of this chapter, we investigate the addition of alane and borane on commercially available polycarbosilazanes. Therefore, we focus on the "polymer route".

4. SYNTHESIS AND CHARACTERIZATION OF Al- AND B-MODIFIED COMMERCIAL POLYSILAZANES

4.1. Experimental part

4.1.1 Materials

KiON Ceraset Polysilazane 20 and KiON Ceraset Polyureasilazane were purchased from KiON Ceraset. N,N diethylmethylaminealane complex 0.5 M in toluene and dimethyle sulfide borane complex 2 M in toluene were provided from Sigma-Aldrich. Toluene (99.85%, extra-dry over molecular sieve, AcroSeal®) was obtained from Acros Organics.

4.1.2 Synthesis of Al- and B-modified polycarbosilazanes

In a typical reaction, a certain amount of the polycarbosilazane was reacted with the corresponding amount of the alane/borane complex in a toluene medium (250 mL) (depending on the functional groups considered-see Table V-6) to form polyaluminosilazane (PAZ) and polyborosilazanes (PBZ). In the case of PAZ, we considered three different ratios according to the presence of different reactive groups, whereas in the case of PBZ we only considered the vinyl groups since it is known that only hydroboration occurs in such polymers. The preparation of PBZ1(1.2) is described below as a representative procedure, since the other precursors (Table V-6)

were prepared in a similar manner. In details, 5 g (76 mmol) of HTT1800 were added to 250 mL of toluene inside a three necked Schlenk. The system was cooled at 0°C. After, 14 mL (25 mmol) of solution of BH_3•$S(CH_3)_2$in toluene were added at 0°C. After the addition was completed, the mixture is left warm up to RT and left three days under stirring, the solvent was separated by distillation at (RT°C/10^{-2}) and 4.3g (86% yield) of B-modified HTT1800 was obtained.

In Table V-6, we report the details of the preparation of the Al-and B-modified HTT1800 and Ceraset.

Table V-6: Synthesis data of Al-/B-modified commercial polycarbosilazanes.

Samples	**M polycarbosilazane g (mmol)**	**V AlH_3•$N(Me)_2Et$/BH_3•$S(CH_3)_2$ (mL)**	**M Polymer (g)**	**Synthesis yield (%)**
PAZ1(0.2)	3 (46)	6.5	2	67
PAZ1(1.2)	2.3 (35)	30	2.1	91
PAZ1(2.0)	1 (15)	21	0.9	90
PAZ2(0.2)	1.9 (29)	5.3	1.3	68
PAZ2(1.2)	0.98 (14.9)	16	0.8	82
PAZ2(2.0)	1 (15)	26	0.9	90
PBZ1(1.2)	5 (76)	14	4.3	86
PBZ2(1.2)	5 (76)	14	4.2	84

The Al- and B- modified polysilzanes were characterized by means of FT-IR and solid-state NMR spectroscopy. Elemental analysis was performed to investigate the chemical composition of the polymers.

4.1.3 Polymer-to-ceramic conversion

The ceramic samples were prepared by the pyrolysis of the obtained polymer powders in a quartz tube under a steady flow of nitrogen (N_2) in a tube furnace. The following heating cycle was used: (i) an initial 5°C.min^{-1} ramp up to the desired temperature up to 1000°C, (ii) a 2 h dwelling time, (iii) a cooling of samples to room temperature at a cooling rate of 5°C.min^{-1}.

High temperature TGA (Netzsch STA 501 equipment) was performed on the sample PBZ1(1.2) under N_2 up to 1700°C with 5°C.min^{-1} as heating rate and 10 min as dwelling time. XRD (Philips PW 3040/60 X'pert PRO X-ray diffraction system operating at 30 mA and 40 kV from 10 to 90° with a step size of 0.0167, using a Kα1 of copper as source) and Raman spectroscopy (A

Renishaw model RM 1000 Raman microscope operating at λ~ 514.5 nm) were employed in order to study the structural evolution.

4.2. Results and discussion

4.2.1 Preparation and characterization of Al- and B-modified polycarbosilazanes

The synthesis of the aluminum- and boron-modified polycarbosilazanes is performed through a reaction of alane N,N dimethylethylamine and borane dimethylsulfide complexes with KiON Polysilazane 20 (labeled HTT1800®) and KiON Polyureasilazane (labeled Ceraset®). The molecular structures of HTT1800 and Ceraset are shown is Figure V-32.

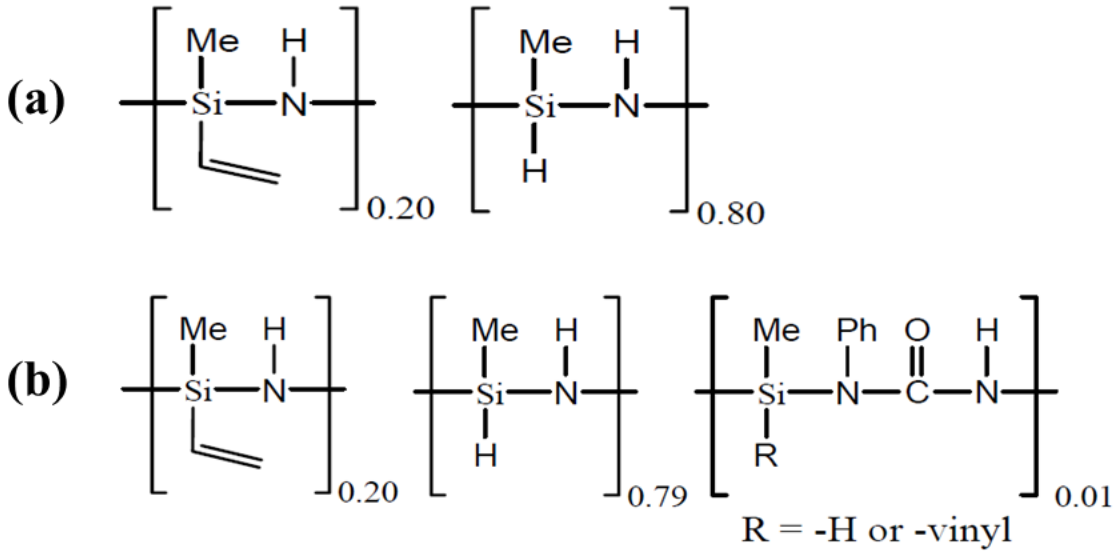

Figure V-32: Molecular structures of (a) HTT1800 and (b) Ceraset.

From here onwards, the synthesized polymers which are obtained starting from HTT1800 and Ceraset are denoted as **poly(alumino/boro)silazane 1 (PAZ1/PBZ1)** and **poly(alumino/boro)silazane 2 (PAZ2/PBZ2)**, respectively. Regarding the alane/borane complex, the reactive units are restricted to Al-H/B-H units. HTT1800 and Ceraset display three reactive groups: -CH=CH_2, N-H and Si-H (Figure V-32). Therefore three possible reactions could be considered:

i) Only hydroalumination/hydroboration of the vinyl groups (the samples are called **PAZ1/PBZ1(0.2)** and **PAZ2/PBZ2(0.2)** (n=0.2 since we are considering only the vinyl groups),

ii) considering hydroalumination/hydroboration of the vinyl groups and dehydrocoupling between Al-H/B-H and N-H (the samples in this case are **PAZ1/PBZ1(1.2)** and **PAZ2/PBZ2(1.2)**),

iii) considering the three functional units (vinyl, Si-H and N-H) capable of reacting with the alane/borane complex therefore the samples will be named **PAZ1/PBZ1(2)** and **PAZ2/PBZ2(2)**.

We have considered all ratios for **PAZ1/2** whereas we only considered the ratio 1.2 for **PBZ1/2** (=**PBZ1/2(1.2)**)

Figure V-33 illustrates a picture of the experimental process to prepare the series of PAZs and PBZs.

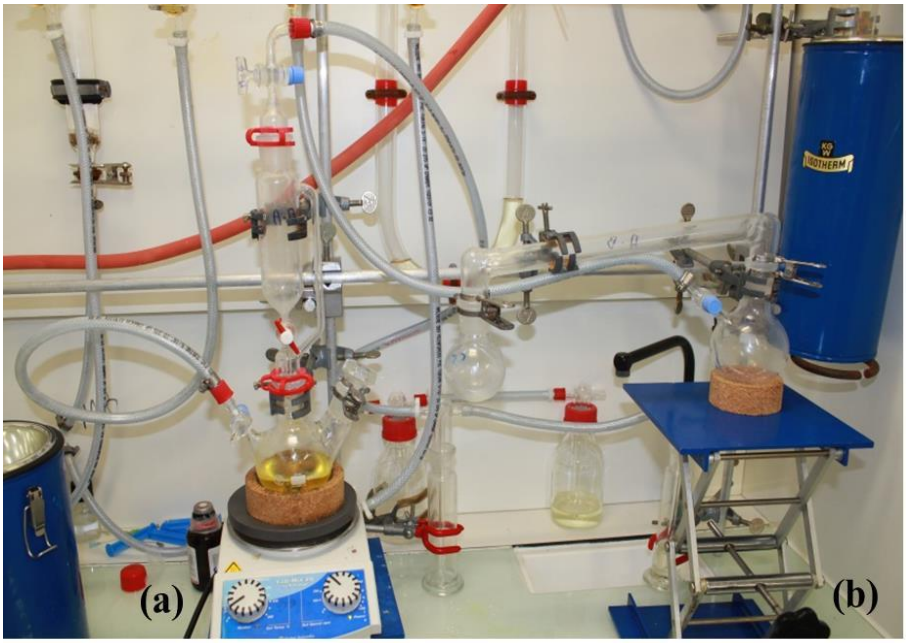

Figure V-33: Photo of the experimental process for synthesizing **PAZ** and **PBZ**: (a) addition of the alane/borane, (b) solvent removal.

The synthesis process is based on two steps, the first being the addition of the alane/borane over the polycarbosilazane diluted in toluene at 0°C, followed by a distillation step to remove the solvent and recover the final polyaluminosilazanes. Here we take advantage of using commercial polycarbosilazanes since we economize time and material to prepare preceramic polymers in comparison with the process described in the first part of this chapter. Except for **PAZ1(0.2)** and **PAZ2(0.2)** that were viscous, all the other **PAZ** were recovered as solid products. This difference in the physical state is *a priori* due to a difference in the mechanism occurring during the addition of alane. The more we take into consideration functional entities, the more the products tend to form a solid; but these presumptions cannot be stated as facts until we investigate the structure and composition of these polymers. **PBZ1/2(1.2)** are solids.

Figure V-34 presents the FTIR spectra of the samples.

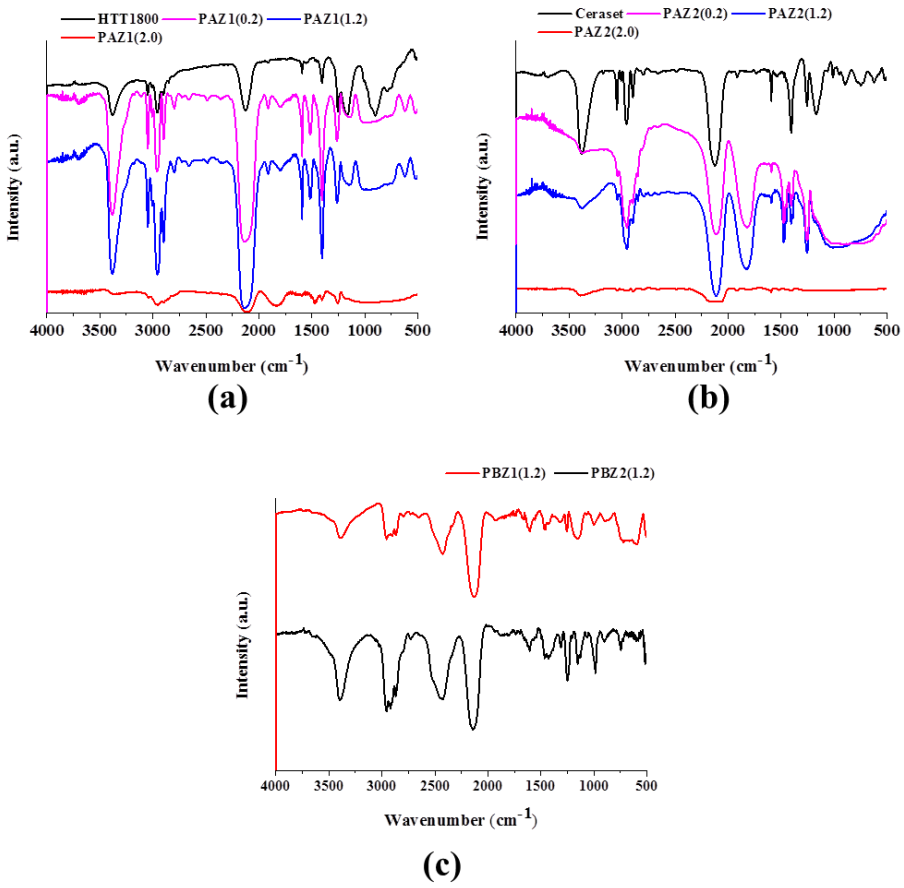

Figure V-34: FTIR spectra of (a) **HTT1800, PAZ1(0.2), PAZ1(1.2), PAZ1(2.0),** (b) **Ceraset, PAZ2(0.2), PAZ2(1.2), PAZ2**(2.0) and (c) **PBZ1(1.2)** and **PBZ2(1.2)**.

For **PAZ1/2(0.2)**, the bands related to the vinyl groups (H_2C=CHSi) appear in the wavenumber range 3045 - 3000 cm^{-1}. The C=C stretching bond appears at 1590 cm^{-1}. A strong Si-H bond appears at 2130 cm^{-1}. The bands ascribed to Si-NH-Si groups include N-H stretching at 3380 cm^{-1} and Si-N vibrations at 1170 cm^{-1}. Si-CH_3 was associated with its characteristic band at 1255 cm^{-1} whereas C-H vibrations in methyl groups appear at 2900 and 2950 cm^{-1}. A broad signal around 800 cm^{-1} that can be attributed to Al-N units starts to appear in the samples PAZ1 and 2 with a ratio of 1.2, and the bands related to C=C drastically decrease. Therefore, we can assume that the more the ratio increases the more the polymer cross-links promoting the dehydrocoupling reactions and thus the formation of Al-N units. No major difference could be detected between the polymers with ratio 1.2 and 2.

For the sample **PBZ1/2(1.2),** the bands related to N-H are depicted at 3420 cm^{-1} (stretching) and at 1170 cm^{-1} (deformation). A stretching vibration for Si-N appears at 860 cm^{-1}. The bands ascribed to vinyl groups appear at 1580 cm^{-1} is absent. The Si-H vibration band appears intensely at 2100 cm^{-1}. The band located at 1250 cm^{-1} is characteristic of Si-CH_3 groups. C-H stretching and CH_3

deformation vibrations are shown at 2950 and 1400 cm^{-1}, respectively. The absorption band at 2415 cm^{-1} clearly confirms the presence of B-H vibrations which indicates that are in excess which was expected because we used a large excess in comparison to the proportion of vinyl groups. This tends to demonstrate that BH groups did not react with NH units. These groups can act as active functional sites for the hydroboration reaction between B-H and CH_2=CH. To support this result, the absorption band at 1180 cm^{-1} assigned to C-B-C groups suggests that the hydroboration reaction is favorable.

We investigated the elemental composition of the **PAZ1(1.2)** and **PAZ2(1.2)** as well as **PBZ1(1.2)** and **PBZ2(1.2)** and as it shown in the empirical formula, the two Al-modified polymers have a similar composition $Si_{3.0}Al_{1.4}C_{4.8}N_{2.4}H_{22.2}O_{0.9}$ for **PAZ1(1.2)** and $Si_{3.0}Al_{1.7}C_{4.3}N_{1.5}H_{20.0}O_{1.0}$ for **PAZ2(1.2)**. This confirms that aluminum does not only react by hydroalumination because the expected Si:Al ratio is in that case 3. Here, dehydrocoupling occurs. In contrast, hydroboration seems to be the only mechanism in **PBZ1** ($Si_{3.0}B_{1.0}C_{1.4}N_{0.8}H_{13.3}O_{0.8}$) and **PBZ2** ($Si_{3.0}B_{1.2}C_{1.5}N_{1.2}H_{14.0}O_{0.9}$).

Based on FTIR, elemental analyses, we have a relatively good representation of the differences of the mechanisms which govern the synthesis of PAZ and PBZ. However, solid-state NMR is more useful in the identification of the local environment around carbon, aluminum/boron and nitrogen in the polymer and also in the determination of the changes in the local environment during the polymer-to-ceramic conversion. Here, we investigated the structure of PBZ by solid-state NMR to be sure that dehydrocoupling is not involved during polymer synthesis in contrast to PAZ. This study was also performed on the derived pyrolysis intermediates obtained during pyrolysis under nitrogen in the temperature range 200-1000°C. Solid-state NMR is presented in the following section. TGA as well further annealing under nitrogen was performed on PAZ and PBZ in the temperature range 1000-1800°C. XRD and Raman spectroscopy was investigated.

4.2.2 PAZ/PBZ-to-SiAlCN/SiBCN conversion

In this part and similarly to the first part of the chapter 2, we have distinguished two temperature ranges: RT $\rightarrow$ 1000°C and 1000 $\rightarrow$ 1800°C. The purpose of this section is to investigate the first temperature region of the polymer-to-ceramic conversion (up to 1000°C under nitrogen) by TGA for all samples as well as solid-state NMR and FTIR for sample PBZ in order to identify the related structural changes which occur during pyrolysis. Then, we investigated the second temperature region (1000-1800°C under nitrogen) of the polymer-to-ceramic conversion by XRD and Raman spectroscopy to follow the evolution of the structure of SiAlCN and SiBCN ceramics.

- *Temperature range: RT $\rightarrow$ 1000°C*

As shown in the TGA curves (Figure V-35), the addition of aluminum and especially boron to HTT1800 decreased the weight loss of the derived polymers (**PAZ1/PBZ1**) and thus increased their ceramic yields (from 67% for HTT1800 to 77% for the three **PAZ1** and 85.2% for **PBZ1(1.2)**) as a crosslinking agent proceeds. Regarding the ceramic yields of samples PAZ1, there is no effect of the ratio fixed during the synthesis on the ceramic yield. This tends to indicate that either no further reactions occur above a ratio of 0.2 during the polymerization leading to PAZ1 with the same degree of crosslinking and the same portion of groups with latent reactivity or PAZ1 release high gaseous by-products such as H_2, NH_3 or CH_4 so that they have a limited influence on the final weight loss.

Interestingly, in the first part of the present chapter, we demonstrated that aluminum-modified polycarbosilazanes systematically displayed higher ceramic yields than their boron-modified polycarbosilazane analogs. Here, this is not the case and the TGA curve of **PBZ1(1.2)** shows 2 distinct stages of weight losses: i) 6.1% from 25 to 370°C, ii) 8.7% from 370 to 1000°C. By FTIR, we have identify B-H/Si-H bonds in **PBZ1(1.2)**. We suggest that these groups condense with the NH units of HTT1800 to form B-N/Si-N bonds while releasing only H_2. However, the presence of $SiCH_3$ units is expected to release CH_4 during the pyrolysis.

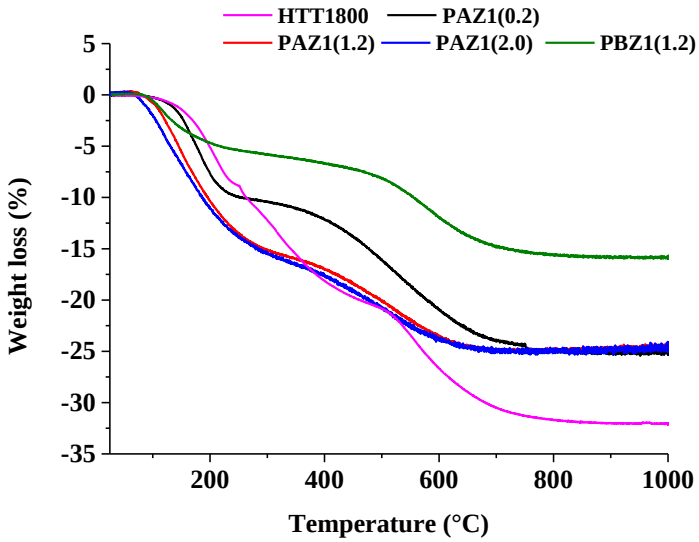

Figure V-35: TGA curves of **HTT1800** and the derived Al- and B- modified polymers (**PAZ1(0.2), PAZ1(1.2), PAZ1(2.0)** and **PBZ1(1.2)**).

We isolated, at different pyrolysis temperatures under N_2 atmosphere, the sample **PBZ1(1.2)** in order to follow the structural evolution by means of FTIR and solid-state NMR. As a first perspective, we observed color changes of the powder from white (RT-200°C), yellow (450°C), brown (700°C) to black at 1000°C (typical color of Si(E)CN ceramics).

Figure V-36 shows the FTIR spectra of the N_2-treated **PBZ1(1.2)** at different temperatures.

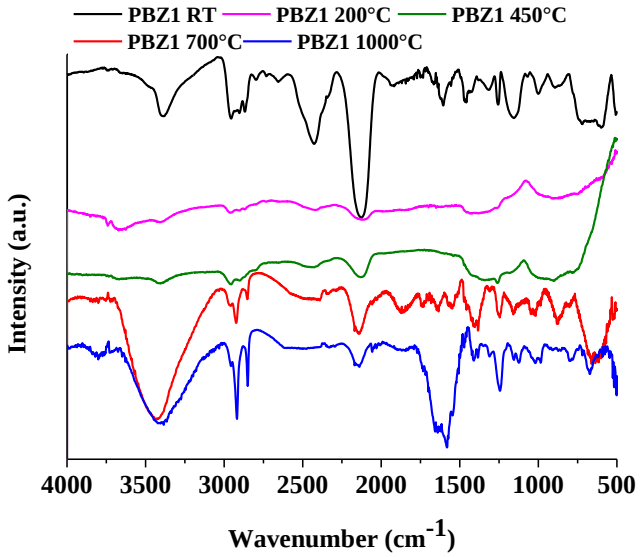

Figure V-36: FTIR spectra of **PBZ1** at RT, 200, 450, 700 and 1000°C.

We can recognize the absorption bands around 3380 cm^{-1} and 1600 cm^{-1} corresponding to the stretching and vibration mode of N-H bonds. We can also see the classical bands for boron-modified polysilazanes in the range 2950-2800 cm^{-1} due to the vibration of C-H bonds. The deformation of Si-CH_3 bonds appears at 1250 cm^{-1} and of B-C-B units at 1180 cm^{-1}. We can identify the stretching of N-Si-N bonds at 890 cm^{-1}. When increasing the temperature up to 450°C, the intensity of the band centered at 2450 and 2250 cm^{-1} and in the wavenumber range 2950-2850 cm^{-1} decreases suggesting the participation of these groups to crosslinking reactions. The band attributed to B-H bonds even disappears after heat-treatment at 450°C. When the sample is exposed to higher temperatures (between 700 and 1000°C) we can distinguish the decrease of the intensity of the band associated to Si-H units at 2100 cm^{-1} and N-H bonds (3450 cm^{-1}). This probably indicates the condensation reaction between N-H and Si-H forming Si-N units. These findings show that the transformation of the original polymeric components into the amorphous preceramic network is completed at 1000°C.

Solid-state NMR is a useful tool to investigate the changes in the polymer structure through the pyrolysis temperature. By observing the chemical environment around B, C, N and Si, we were able to identify the structural rearrangements that occur upon curing under nitrogen, and therefore conclude if the final structure of the material is that expected based on the previous characterization technique.

Figure V-37 reports the ^{13}C CP MAS NMR spectra of **PBZ1(1.2)** and **PBZ1(1.2)** pyrolyzed at 200°C. We can clearly see that the polymer displays two signals in the aliphatic region: a main

composite signal centered around 12 ppm that can be assigned to the superposition of ***C***H_3Si (~ -2 ppm) B-CH_2***C***H_2Si (~6 ppm), B-(CH_3)***C***HSi (~11 ppm) and B-***C***H_2CH_2Si (~16 ppm) [109] obtained from the addition of borane on the α- and β- vinyl carbon atoms (Equation V-12). An additional small signal is observed at 28 ppm and can be attributed to the B-(***C***H_3)CHSi units. Moreover, a very weak signal is depicted at 130 ppm. The latter refers to the remaining vinyl groups that did not react during the hydroboration step.

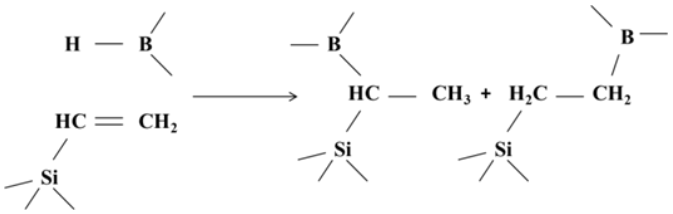

(V-12)

The signal at 130 ppm is no longer present at 200°C.

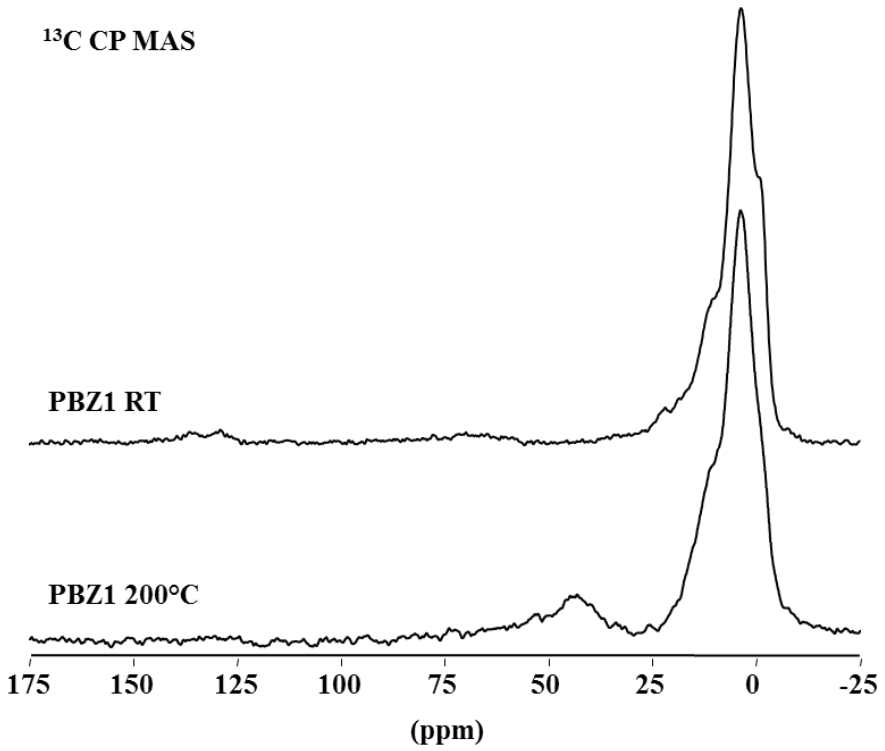

Figure V-37: ^{13}C MAS NMR spectra of **PBZ1(1.2)** and **N_2-treated intermediate** at 200°C.

In Figure V-38, we report the ^{29}Si MAS NMR spectra as well as the CP MAS spectra of **PBZ1(1.2)** and N_2-treated intermediates from 200 to 1000°C. The objective of comparing MAS and CP MAS spectra is to identify Si-H groups that will be overestimated when using the Cross Polarization sequence.

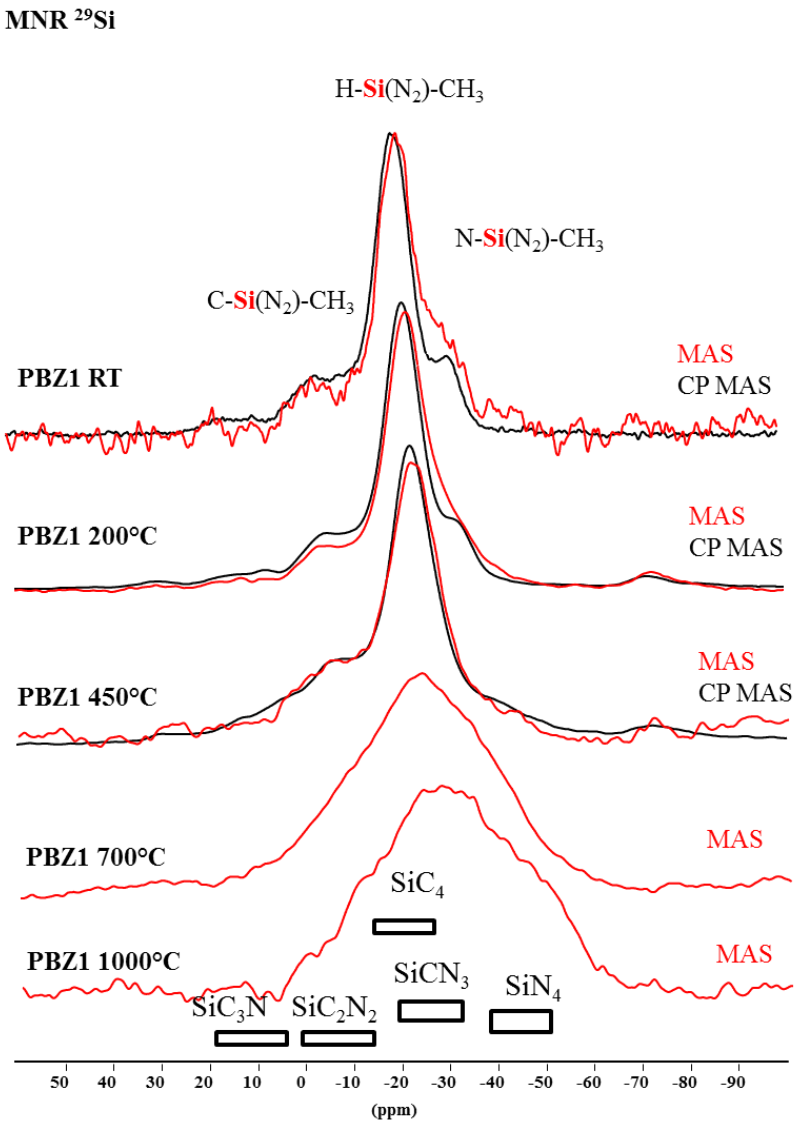

Figure V-38: ^{29}Si MAS (red) and CP MAS (black) NMR spectra of **PBZ1** from RT to 1000°C.

The as-prepared polymer (**PBZ1(1.2)**) have a complex distribution of SiN_xC_{4-x} units with a predominance of H-***Si***N_2-CH_3 units centered around -20 [321]. Two other peaks are observed around -5 and -30 ppm and may correspond to ***Si***C_2N_2 around -5 ppm and ***Si***CN_3 environments, respectively. Upon heating between 200 and 450°C, broad signals characterize the amorphous intermediates along with a reduced signal/noise ratio. On the basis of former NMR studies [254], the broad resonance most likely stems from overlapping signals due to SiC_2N_2, $SiCN_3$ and SiN_4 units. This refers to the presence of silicon with nitrogen-enriched coordination spheres at intermediate temperatures. It should be noted that starting from 450°C, the thermolysis intermediates are characterized by a decrease of the ***Si***HN_2CH_3. This corroborates the FTIR observations that in the same temperature range a considerable decrease of the Si-H and N-H band intensities is displayed. Both results are explained by dehydrocoupling reactions between Si-H and N-H groups at such elevated

temperatures. They allow thus the formation of nitrogen-enriched silicon coordination spheres as we said before.

We have investigated ^{11}B MAS NMR in order to have complementary information on structural rearrangements which occur during the curing and the pyrolysis (Figure V-39).

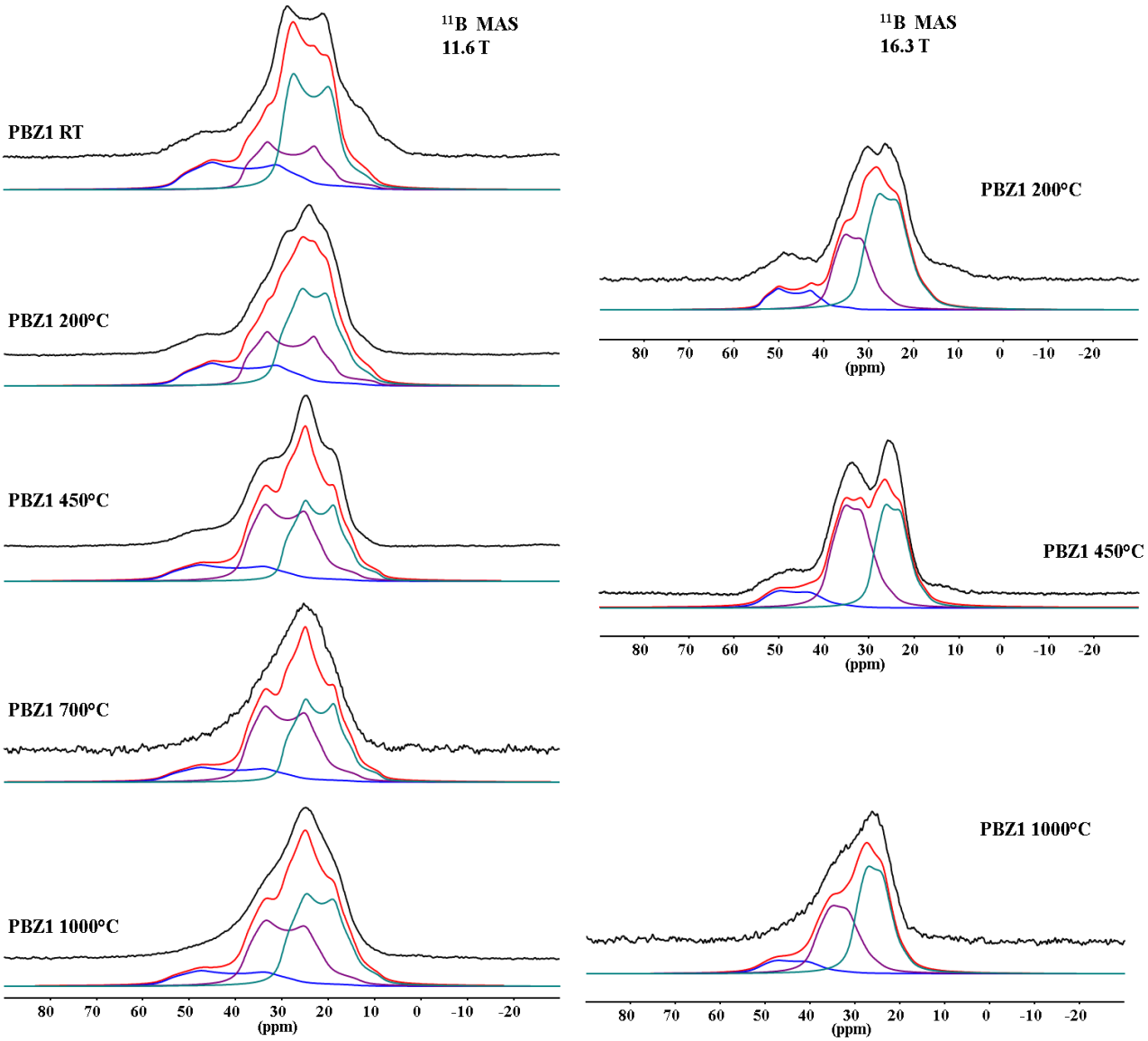

Figure V-39: ^{11}B MAS spectra of **PBZ1(1.2)** and **N_2-treated intermediates** from 200 to 1000°C.

The spectra of the polymeric precursor and of the thermolysis intermediates are found to be broad due to the heterogeneity in the local chemical environment of the boron nuclei and the presence of quadrupolar interactions since ^{11}B is a spin 3/2. We can clearly see the strong presence of tri-coordinated B. Based on the synthesis conditions and the ratio Si:B fixed (=3), BC_3-coordination environments are expected [319]. However, the results are more complex than expected: simulations

of the spectra recorded at two magnetic fields suggest the presence of ***B***N_3 (or BN_2H since B-H bonds are observed by IR [343]), ***B***CN_2, and ***B***C_3 environments at 30, 40, 60 ppm, respectively [167]. ***B***N_3 and ***B***N_2H sites could result from a dehydrocoupling reaction between B-H and N-H, forming B-N instead of B-C. When we increase the temperature, the ***B***C_3 groups disappears which refers to their instability and BC_xN_{3-x} groups are identified. A mixed phase of ***B***CN_2 and ***B***N_3 units arises at 1000°C. It should be mentioned that the formation of BN layers is considered to be a prerequisite for the high-temperature stability of SiBCN ceramics since they serve as diffusion barrier inhibiting decomposition reactions at higher temperatures [344].

The ^{15}N CP MAS NMR spectra of **PBZ1(1.2)** polymer and the sample treated at 200°C are shown in Figure V-40. The spectra of the other pyrolysis intermediates are missing since the decrease of protons quantities at high temperatures enables the use of the CP sequence which is necessary to obtain a reasonable S/N ratio considering the very low natural abundance of ^{15}N. The three spectra are similar depicting a strong line at -352 ppm arising from the ***N***HSi_2 and possibly ***N***HBSi structural unit. An additional broad signal appears in the downfield region at about -280 ppm, which could be attributed to ***N***HB_2 units in borazine-like rings [171]. This is consistent with the data presented earlier.

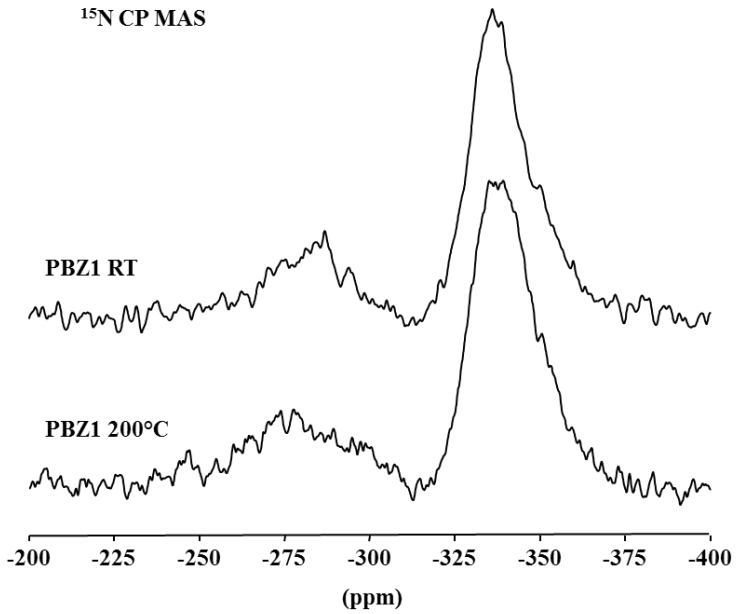

Figure V-40: ^{15}N CP MAS NMR spectra of **PBZ1(1.2) and N_2-treated intermediate at 200°C**.

From the combined analyses of multinuclear solid state NMR and FTIR of sample **PBZ1(1.2)** particularly, we collected interesting information on the structural evolution of this type of polymers during the polymer-to-ceramic conversion between RT and 1000°C. The transformation of the polymeric precursor is completed at about 450°C at which a preceramic network is formed. Boron is

found to have a strong affinity to nitrogen, which results in a reduction of nitrogen in the neighborhood of silicon below 450°C. The amorphous ceramic at 1000°C displays a SiC_xN_{4-x} matrix (with x=0, 1, 2) with graphite-like carbon and BN planar domains. It is argued weather the high-thermal stability of SiBCN results from the presence of separate amorphous carbon and BN domains or from a homogeneous B-C-N phase build up by intercalated carbon and BN layers.

After the heat-treatment to 1000°C under nitrogen, the structure of PDCs is in general amorphous. The second temperature regime from 1000 to 1800°C is associated with structural changes and ceramic crystallization. Therefore, we investigated XRD and Raman spectroscopy.

- *Temperature range: 1000 → 1800°C*

For this study, we selected the samples **PAZ1(1.2)** and **PBZ1(1.2)** heat-treated at 1000°C to perform annealing treatment in the temperature range 1000-1800°C.

The pyrolysis residues obtained at 1000, 1400, 1600 and 1800°C from **PAZ1(1.2)** and **PBZ1(1.2)** are characterized by X-ray diffraction. Phase identification is achieved by locating the characteristic diffraction peaks of the respective phases in the XRD plots.

The XRD patterns (Figure V-41) show that the material remains quite amorphous up to 1400°C for samples derived from **PAZ1(1.2)** (**PAZ1(1.2)1400**). As we observed in the case of the SiAlCN materials studied in the first part of the present chapter, to the samples heat-treated at 1600°C (**PAZ1(1.2)1600**) under nitrogen mainly possess overlapping reflections assigned to AlN, α-SiC and β-SiC. The sharpening of the peaks is clearly observed at 1800°C.

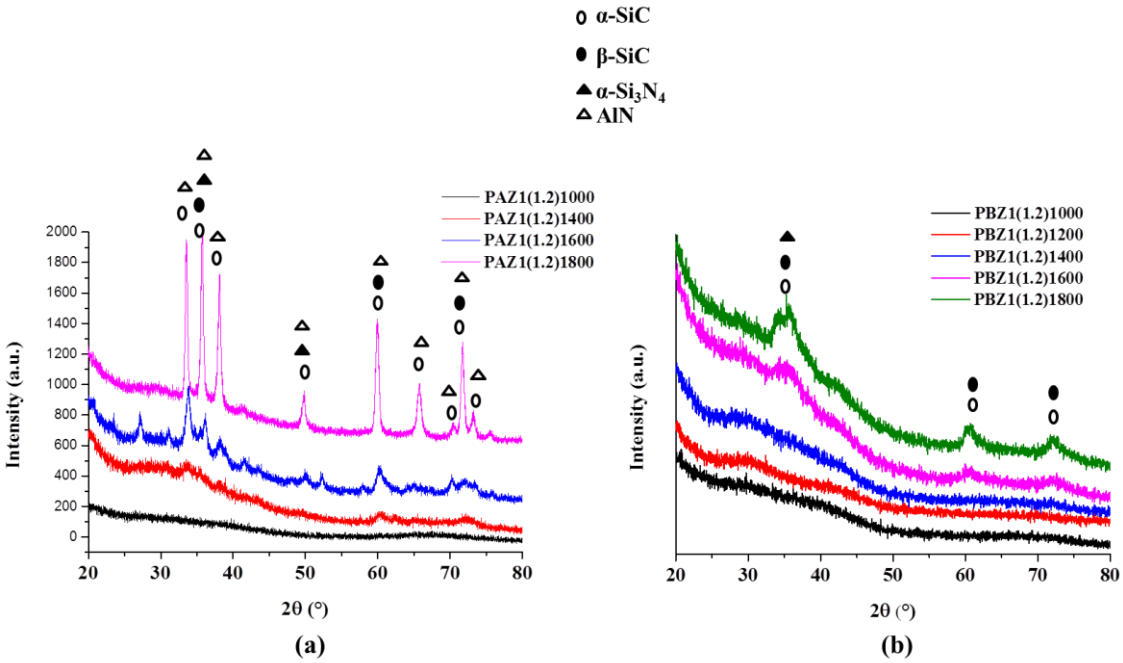

Figure V-41: XRD patterns of (a) **PAZ1(1.2)** and (b) **PBZ1(1.2)** heat-treated at 1000, 1400, 1600 and 1800°C.

The as-pyrolyzed **SiBCN** powders are amorphous and retain their amorphous character up to 1600°C in spite of the appearance at this temperature of broad peaks at 35.65° (d=2.516 Å) and at 60.1° (d=1.540 Å) and 71.78° (311) corresponding to nanosized β-SiC crystals which represents the low temperature form of SiC Nucleation of Si_3N_4 is not detected in any of the samples annealed below 1600°C. Therefore, it is evident here than SiBCN ceramics appear more stable than their SiAlCN analogs at high temperature. By increasing the annealing temperature up to 1800°C, the presence of hexagonal polytypes of SiC (6H, 2H, and 4H) is identified by the two additional peaks at 33.58° (101). The peak emerging at 41.40 correspond to a mixture of β- and α-SiC phases. However, it should be mentioned that peaks emerging at 33.58 and 41.40° could be also attributed to β-Si_3N_4. After heat-treatment to 1800°C, SiBCN materials appear significantly less crystallized than their SiAlCN analogs.

In addition, Raman spectroscopy has been investigated to follow the evolution of free carbon in the SiBCN materials during annealing to 1800°C. Figure V-42 present the spectra of the samples derived from **PBZ1(1.2).**

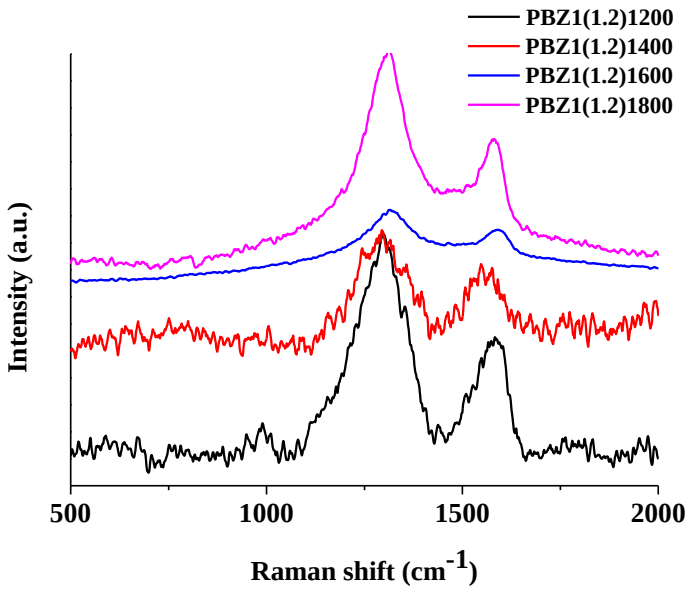

Figure V-42: Raman spectra of **SiBCN** powders obtained from sample **PBZ1** annealed under N_2 at 1200, 1400, 1600 and 1800°C.

All spectra show the typical characteristics of disordered graphite-like carbon, namely the *D*-peak located at 1350 cm^{-1} and the *G*-peak centered between 1550 and 1600 cm^{-1}. This obviously indicates carbon segregation to form disordered or nanocrystalline graphitic clusters. SiC and Si_3N_4 are not identified. The HTTGA study of the sample **PBZ1(1.2)1000** during annealing to 1600°C confirm the excellent stability of the SiBCN amorphous network since no weight losses are identified in this temperature range.

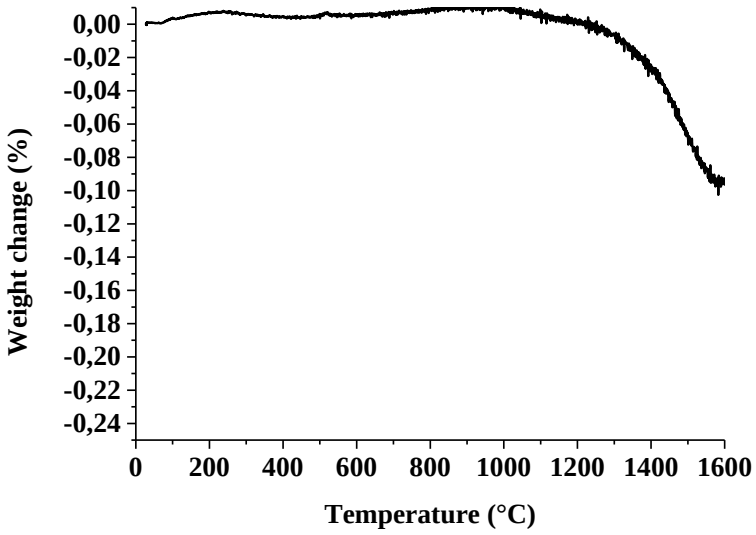

Figure V-43: HTTGA curve of **PBZ1 (1.2)1000** during annealing to 1600°C under N_2 (heating rate 5°C.min^{-1}).

5. CONCLUSION

A series of polyalumino(carbo)silazanes was synthesized by reaction of dimethylethylamine alane complex with the poly(carbo)silazanes. Two types were distinguished:

1- Starting from the dichloro(carbo)silane, and by means of ammonolysis we obtained the poly(carbo)silazane. The latter reacted with the alane complex and led to solid polyalumino(carbo)silazane that we described by "home-made" since we monitored all the steps (from the choice of the molecular precursor to the polymerization and the functionalization with Al);
2- Starting from a commercially available polycarbosilazane and modifying the latter with aluminum.

We synthesized also polyborocarbosilazanes following the second procedure to compare the effect of Al and B to polycarbosilazanes to follow the effect on the chemistry of polymers as well as on the properties of the final materials. In all cases, we investigated the polymer structure by means of FTIR and solid state NMR, the transition from the polymer organic state to the ceramic inorganic state by XRD, thermal gravimetric analyses, Raman spectroscopy… In general, the ceramic materials remain amorphous even at very high temperature, typically at ~1600°C. Further heat-treatment under N_2 at elevated temperatures tends to crystallize these materials into phases thermodynamically stable at a given chemical composition, such as SiC, Si_3N_4, free C, BN or AlN. We observed that the amorphous-to-crystalline transition is closely related to the composition and structure of the preceramic polymer.

After having discussed the synthesis and characterization of the "home-made" poly(carbo)aluminosilazanes, we demonstrated their capability, in particular the poly(allyl)aluminosilazane (PAAZ), since it exhibits the highest ceramic yield, to produce microcellular polymer-derived SiAlCN foams. In this way, we could obtain a porous microcellular material displaying the properties of the SiAlCN phase. For the preparation of SiAlCN foams from preceramic polymers, we followed the PDCs route and we used a sacrificial filler PMMA (with 25 μm as pore diameter) to be mixed with our polymer, then we applied the warm pressing of the mixture as shaping process. The as-obtained green body was pyrolyzed in order to burn out the sacrificial filler while converting the preceramic polymer into the desired ceramics. Warm pressing has a double role in our process. The first is to melt the preceramic polymer to form a viscous liquid at a reasonable temperature, which is forced by the pressure through the fillers microbeads in order to obtain a homogeneous biphasic structure. The second role is to increase the cross-linking degree

of the polymer giving a grade of rigidity to the polymer network, avoiding thus the depolymerization during the last step of the process *i.e.*, pyrolysis. To obtain the SiAlCN foams, we tested different ratio of PAAZ:PMMA, and we investigated the effect of the temperature and the pressure during the warm pressing. With a 30:70 weight ratio of PAAZ:PMMA, a temperature of 80°C and a pressure of 74 MPa, we succeeded in generating relatively high porous microcellular foams (75% of porosity with an average pore diameter of almost 22 μm).

GENERAL CONCLUSION AND OUTLOOK

This PhD work is a part of the FUNEA project (2011-2015) within the Marie Curie ITN 7th Framework program. In terms of technological applications, the project focuses on the energy applications of functional nitride-based materials with this addressing the main needs of the 21st century. To help meet this vision, this work consisted in elaborating potential **porous (carbo)nitrides** for **the hydrogen production** and **storage**.

The general objective of the present PhD work consisted in an investigation of the **synthesis, characterization** and **processing** of aluminum nitride (**AlN**) and boron nitride (**BN**) ceramics as well as the derived aluminum- and boron-modified siliconcarbonitride ceramics (**SiAlCN** and **SiBCN**, respectively) obtained by the Polymer-Derived-Ceramics (**PDCs**) route. As main application targets, we investigated their potentialities as **host porous materials** for the **nanoconfinement** of hydrogen carriers, namely **sodium alanate** and **ammonia borane**, and as **catalytic ordered mesoporous supports** for the **hydrogen generation**. This route involves typically three steps:

i) **Polymer synthesis** from mono- or oligomer precursors
ii) **Shaping** of the product (pressing, casting, injection molding…)
iii) **Pyrolysis** in inert or reactive atmosphere for the organic-inorganic transition

This PDCs route offers new opportunities for manufacturing **shaped advanced ceramics with tailor-made porosity**.

The **first chapter** is dedicated to the **state-of-the-art** related to the **applications** considered here as well as to the different **materials** we have prepared and characterized. In particular, we start the survey highlighting the "**hydrogen economy**" issue and the hurdles associated to **the production** and **storage**. We underline how the use of **porous materials** and in particular **porous inorganic materials** can be a solution for the drawbacks encountered. We focused our attention on the ceramic materials (**AlN, BN, SiAlCN, SiBCN**) as well as the hydrides (**$NaAlH_4$** and **NH_3BH_3**) we used. Therefore, we divided the present manuscript by type of material and reported a deep study, for each system, from the synthesis to the final application.

In the **second chapter,** we report the synthesis and the complete characterization of the **AlN** precursor, *i.e.*, the polyethyliminoalane (**PEIA**). The polymer structure as well as the polymer-to-ceramic conversion was investigated. In addition, the annealing behavior of AlN ceramics at different temperatures in nitrogen atmosphere was studied. Through the use of several complementary techniques of analysis such as FTIR spectroscopy, solid-state NMR X-ray diffraction and Raman spectroscopy, we have proposed a complete picture of the chemistry and structure evolution of AlN from the polymer. Based on this study, we have reported the production of **porous**

AlN i) by replication the structure of **ordered mesoporous carbon (CMK-3)** followed by a single step pyrolysis under ammonia at 1000°C, and ii) by catalyst-assisted hydroalumination and supercritical CO_2 drying followed by a two-step pyrolysis procedure under nitrogen and ammonia at 1000°C.

In the first type of porous AlN, meso-/macroporous powders with a BET SSA of 217 $m^2.g^{-1}$ and a pore volume of 0.71 $cm^3.g^{-1}$ are generated. Ordered mesoporosity was observed locally by HRTEM. In the second type of porous AlN, **AlN aerogels** as monoliths have been prepared. They could display high BET data (BET SSA of 511 $cm^3.g^{-1}$ and pore volume of 0.88 $m^2.g^{-1}$) which are closely related to the parameters of the process. Such materials are capable of serving as porous hosts for the nanoconfinement of **$NaAlH_4$** to study the effect of nanoconfinement on the dehydrogenation of $NaAlH_4$. We have presented preliminary results on the dehydrogenation process of **$NaAlH_4$** by thermolysis up to 200°C. First results show that the decomposition of the hydride starts at low temperature with a total weight loss of almost 7% measured at 200°C which is a superior value in comparison to the use of CMK-3 as host material. This study is under investigation to understand the effect of AlN on the dehydrogenation process of $NaAlH_4$.

In **chapter III**, we succeeded in preparing novel **porous BN** combining the PDCs route with the same processes described in Chapter II. However, instead of CMK-3 as template for AlN, we used **monolithic activated carbon** as template for BN. **Polyborazylene** (**PB**) obtained from borazine was used as **BN precursor**. The replicated BN represent **mesoporous BN monoliths** and exhibit a BET SSA ranging from 584 to 728 $m^2.g^{-1}$ and a total pore volume from 0.75 to 0.93 $cm^3.g^{-1}$ depending on the final annealing temperature. . A narrow pore size distribution centered at 5.8 nm has been calculated for the samples. As for the AlN aerogels, we succeeded in obtaining monolith-like porous aerogels. Here, we were able to propose several types of porosity going from microporosity to macroporosity. Maximum BET SSA of 358 $m^2.g^{-1}$ has been obtained while porous volume of 0.36 $cm^3.g^{-1}$ was calculated. These porous BN were used as host material to confine **NH_3BH_3** (AB). We focused on the thermolysis of AB, which is known to exhibit a relatively high temperature of dehydrogenation (110°C) along with the presence of undesired by-products such as borazine, diborane, ammonia. One of the solutions to reduce the temperature of dehydrogenation while evolution of undesired by-products is reduced or stopped is to confine AB into the porous BN (as we mentioned in Chapter II for $NaAlH_4$ in porous AlN). The composites **AB@porous BN** were able to liberate pure H_2 at low temperatures. Materials derived from mesoporous BN monoliths were found to be the best candidates with a release of almost 2 equiv. of H_2 at 200°C. This improvement is exclusively due to the effect of nanoconfinement, unlike the case of **porous carbons** where the

surface acidity contributed to the dehydrogenation of AB through acid-base reactions between $H^{\delta+}$ of COO-H and $H^{\delta-}$ of BH_3 [34].

In **chapters IV and V**, we underline how the needs of applications at high temperature and oxidative atmosphere (whether in catalysis, gas separation, water treatment, pollutant degradation…) have pushed the research work toward more stable systems. We describe in these chapters the **Si/Al/C/N** and **Si/B/C/N** systems and how the incorporation of Al and/or B to Si/C/N improved the thermal stability of the latter. We described two important approaches to produce Si(E)CN ceramics (E=Al, B): the **"building block approach"** and the **"single source approach".**

In **Chapter IV** we used the "**building block approach**" to synthesize **ordered mesoporous SiAlCN** powders. It consists in the mixing of two precursors, each one being a precursor of a phase contained in the targeted material. Here, we mixed the precursors of the Al(C)N and Si_3N_4 phases with various and controlled Al:Si ratios. The blended polymers have been used to infiltrate ordered mesoporous CMK-3. The solution infiltration-ceramic conversion-template removal cycle performed under nitrogen at 1000°C (2 h, ceramic conversion) then in NH_3 atmosphere at 1000°C (5 h, template removal) resulted in the formation of periodic mesoporous **SiAlCN** frameworks with surface areas of 182 to 326 $m^2.g^{-1}$, a pore size distribution of 4.1-5.9 nm and pore volumes varying from 0.51 to 0.65 $cm^3.g^{-1}$. By characterization using electron microscopy, X-ray diffraction, N_2 sorption, chemical analyses, and high temperature thermogravimetric analysis, we demonstrated that the amorphous powders display excellent mesopores uniformity and periodicity depending on the ceramic yield and therefore on the Al:Si ratio fixed during the polymer preparation. The materials show almost no mass change up to 1400 - 1470°C in flowing N_2 and the behavior in air up to 1000°C is closely dependent on the Al:Si ratio. Our objective was to grow **platinum nanoparticle**s of SiAlCN supports to form **nanocatalysts** for the **catalytic hydrolysis of $NaBH_4$**. However, there is usually a lack of direct comparison on the catalytic performance among mesoporous supports. As a consequence, we synthesized highly **ordered mesoporous silicon nitride (Si_3N_4)** in the form of nanoblocks. They displayed a surface area as high as 772.4 $m^2.g^{-1}$, a pore size distribution of 4.85 nm and a pore volume of 1.19 $cm^3.g^{-1}$. The as-obtained ordered mesoporous SiAlCN and Si_3N_4 materials were used as supports to synthesize and disperse Pt (nano)particles. The Pt (nano)particles were thus supported by powder impregnation and successfully assessed in our probe reaction, *i.e.*, hydrolysis of alkaline aqueous solution of sodium borohydride at 80°C. High hydrogen rates have been measured for these materials (with a maximum of 13.54 $L.min^{-1}.g^{-}1$ in the case of Pt/*omp*Si_3N_4) which are closely related to the textural properties of the support. We also demonstrated the interest of these PDCs-based nanocatalysts in comparison to platinum-supported CMK-3 nanocatalyts.

Chapter V was linked to Chapter IV. It was conducted around two potential ceramic systems: the first being **Si/Al/C/N** and the second **Si/B/C/N**, both produced by the **"single source precursor" approach** which consisted in the reaction of polycarbosilazanes with alane and borane. In a first part, we attempted to synthesize a series of **polyaluminosilazanes** starting from different types of dichlorosilanes, to compare their composition, structure, thermal behavior and microstructure evolution with high annealing temperatures. Because of the complex structure and composition of polymers determining the structure and performances of ceramics, detailed investigations of their molecular chemistry have been done. In addition, the control of the polymer-to-ceramic conversion through the design of the intermediate steps (to convert the polymer system into an inorganic intermediate) and the use of annealing treatments (to change the inorganic intermediate into the desired final nanostructure) has been investigated with full understanding to generate materials capable of performing in demanding conditions. As a proof of concept, we coupled the PDCs route to a sacrificial processing route in order to fabricate disk-shaped microcellular SiAlCN materials from a mixture of a selected polyaluminosilazane and PMMA beads with a pore diameter of 25 μm as sacrificial fillers. After warm pressing of the mixture followed by the pyrolysis of the composites which induced the conversion of polyaluminosilazanes into the SiAlCN composition while PMMA decomposed leaving voids, foams displaying an interconnected porosity of 75% with an homogeneously distribution of pores have been generated. We have in mind, in a close future, to assess the potentialities of these foams as catalyst support for the hydrogen generation from the degradation of methanol for example. Because we observed in this part that alanes exhibited a different selectivity with polycarbosilazanes in comparison of borane based on former studies, we have conducted a comparative study, in terms of chemistry, structure and thermal behavior between **SiAlCN and SiBCN ceramics**. They have been obtained by performing the reaction of alane and borane complexes with commercially available polycarbosilazanes. Clearly, dehydrocoupling is a preferred mechanism during the reaction between alanes and polycarbosilazanes whereas hydroboration proceeded as a major mechanism during the reaction between boranes and polycarbosilazanes. This as an effect not only on the pyrolytic conversion of resulting polymers, *i.e.*, boron-modified polycarbosilazanes exhibited a very high ceramic yield (84%), but also on the structural and textural properties of the derived ceramics. This approach shows that the new boron-modified polycarbosilazanes prepared in this chapter display potentialities to form microcellular foams.

Through this work, we were able to demonstrate the feasibility of tailoring porosity among different complex PDCs systems and to apply these materials for H_2 production and storage using

hydrides. A major challenge in the preparation of such materials is that the synthesis of the precursors and the derived ceramics must be performed and controlled with the greatest precision to maintain a high level of performance.

There are a lot of perspectives to imagine based on this work for energy and environment sciences. Because AlN is a piezoelectric material, we can imagine applying AlN aerogels for micro-/nanoscale sensors and actuators. They can also be very interesting for CO_2 capture because their surface chemistry can be beneficial for the CO_2 capture by chemisorption (collaboration with Prof. Yuji Iwamoto from NiTech, Nagoya (Japan) and Prof. Gian Domenico Soraru from Trento University (Italy).

Recently, interest has arisen in both the synthesis of BN as nanostructured and architectured compounds and its new applications such as selective gas sorbent, H_2 storage medium or for water treatment [248, 345, 346]. The development of "ceramic through chemistry" concepts where materials science, processing and chemistry of materials are combined rationally is one of the solutions to tailor the nanostructure and architecture of ceramics as we performed in this thesis. One of the ideas behind these concepts is to generate enhanced physical and chemical properties as well as unusual properties through the processes we proposed here. When it comes to the hydrogen storage and in particular the nanoconfinement of AB in the mesoporous BN, we will envisage the dispersion of metal nanoparticles (Pt, Ru or Co) in BN to create doped BN:hydrides, doping being intended to extend the dehydrogenation and further optimize the GHSCs. We will also study the regeneration of AB in order to investigate a solution for a continuous production of hydrogen inside the porosity of BN. As a first attempt, we had in mind to combine the effect of the nanoconfinement to the effect of the homogeneous catalysis, *i.e.*, dispersing nickel nanoparticles inside the porosity of mesoporous BN monoliths. The dehydrogenation of AB occurred at 30°C with a release of pure hydrogen. In the near future, we have in mind to optimize the protocol in order to further improve the AB dehydrogenation. Figure 1 summarizes the essential points covered in the part of this chapter from the elaboration of mesoporous BN monoliths to the application in AB nanoconfinement.

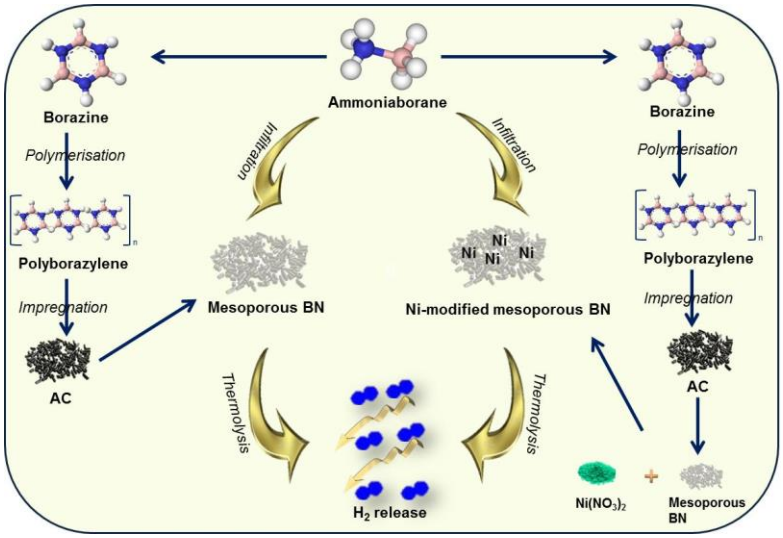

Figure 1: Porous BN: from elaboration to application.

BN also has enhanced physisorption properties due to the dipolar fields near its surface. We think that the structure similarity between BN and carbon graphite and its properties make porous BN a promising candidate like carbon as chromatographic supports for solid phase extraction and separation. This assumption is not only attributed to the properties of BN but also to the intrinsic nature of the B-N bond which introduces local polar character lacking in the carbon structure. This inherently allows sorption improvement especially when BN displays a controlled porosity. A breakthrough would be to prepare and use BN with a tailor-made porosity as powders and monoliths while being adapted for SPE and HPLC applications (collaboration with Rania Bakry, Institute of Analytical Chemistry and Radiochemistry, Innsbruck University).

Until now, we have covered the issues of the hydrogen production and storage. Motivated by the increasing demand in technical membranes for the hydrogen perm-selectivity and the treatment of fluids, we are interested in using the materials proposed in Chapter V: the (Si-(B/Al)-C-N) systems for such purposes due to their high thermal and chemical stability which is of crucial importance for the long-term stability of the membranes under real high-temperature operation conditions. Preliminary tests have been done concerning the deposition of preceramic polymers on porous alumina supports through the dip-coating process followed by a subsequent pyrolysis under N_2 to yield microporous ceramic membranes in respect to the phase transitions, microstructural characteristics, and pore size distributions, chemical and thermal stability. Major difficulties were encountered when we tried to deposit our boron- and aluminum- modified polysilazanes on the porous membranes: difficult solubility, high cross-linking degree, infiltration… Therefore, the tests

we first realize were a dip-coating of HTT1800 (before modification) in solution as shown in Figure 2. We managed to limit the infiltration of the polymer inside the macroporous support, by fixing a ratio of 20:80 (polymer:THF), a rate of 7.7 cm.min^{-1} and a residence time of 30 sec. Extensive study need to be done in order to optimize this process and to extrapolate the study to produce SiB(Al)CN microporous membranes.

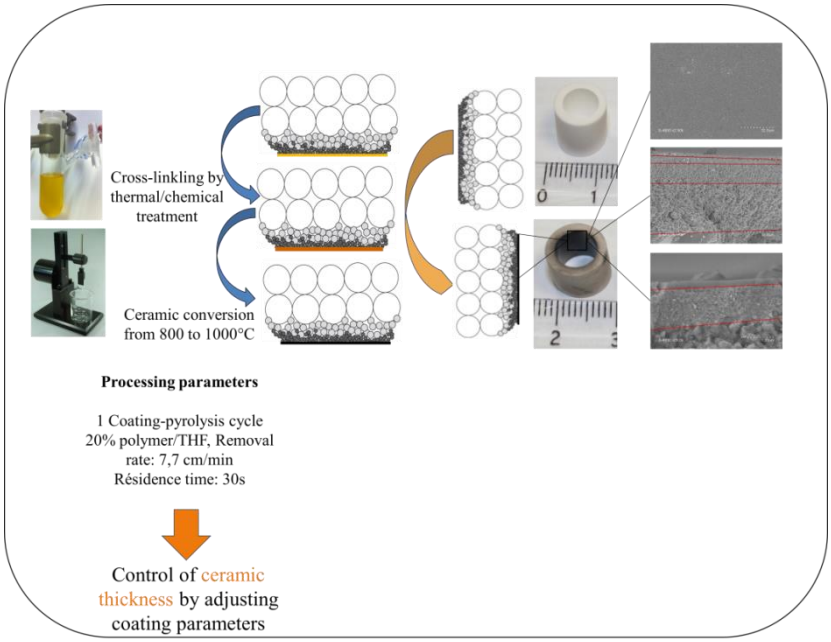

Figure 2: Experimental protocol for PDMCs elaboration.

REFERENCES

[1] Armaroli, N.; Balzani, V., ChemSusChem 2011, 4 (1), 21-36.
[2] Demirci, U. B.; Miele, P., Boron hydrides, high potential hydrogen storage materials. Nova Science Publishers: 2009.
[3] Züttel, A.; Borgschulte, A.; Schlapbach, L., Hydrogen as a future energy carrier. John Wiley & Sons: 2011.
[4] Steele, B. C.; Heinzel, A., Nature 2001, 414 (6861), 345-352.
[5] Hirose, K.; Hirscher, M., Handbook of hydrogen storage: new materials for future energy storage. John Wiley & Sons: 2010.
[6] Marder, T. B., Angewandte Chemie International Edition 2007, 46 (43), 8116-8118.
[7] Wurster, R.; Zittel, W. In Hydrogen energy, 1994.
[8] Riis, T.; Hagen, E. F.; Vie, P. J.; Ulleberg, Ø., IEA Hydrogen Implementing Agreement (IEA, Paris, 2005) 2005.
[9] Dufour, J.; Serrano, D.; Galvez, J.; Moreno, J.; Garcia, C., International journal of hydrogen energy 2009, 34 (3), 1370-1376.
[10] Crabtree, R. H., Energy & Environmental Science 2008, 1 (1), 134-138.
[11] Junge, H.; Boddien, A.; Capitta, F.; Loges, B.; Noyes, J. R.; Gladiali, S.; Beller, M., Tetrahedron Letters 2009, 50 (14), 1603-1606.
[12] Fukuzumi, S.; Kobayashi, T.; Suenobu, T., ChemSusChem 2008, 1 (10), 827-834.
[13] Hannauer, J.; Demirci, U. B.; Geantet, C.; Herrmann, J.-M.; Miele, P., International Journal of Hydrogen Energy 2012, 37 (14), 10758-10767.
[14] Karahan, S.; Zahmakıran, M.; Özkar, S., Dalton Transactions 2012, 41 (16), 4912-4918.
[15] Hügle, T.; Kühnel, M. F.; Lentz, D., Journal of the American Chemical Society 2009, 131 (21), 7444-7446.
[16] Demirci, U. B.; Akdim, O.; Andrieux, J.; Hannauer, J.; Chamoun, R.; Miele, P., Fuel Cells 2010, 10 (3), 335-350.
[17] Amendola, S. C.; Sharp-Goldman, S. L.; Janjua, M. S.; Spencer, N. C.; Kelly, M. T.; Petillo, P. J.; Binder, M., International Journal of Hydrogen Energy 2000, 25 (10), 969-975.
[18] Suda, S.; Sun, Y.-M.; Liu, B.-H.; Zhou, Y.; Morimitsu, S.; Arai, K.; Tsukamoto, N.; Uchida, M.; Candra, Y.; Li, Z.-P., Applied Physics A 2001, 72 (2), 209-212.
[19] Bai, Y.; Wu, C.; Wu, F.; Yi, B., Materials Letters 2006, 60 (17), 2236-2239.
[20] Krishnan, P.; Yang, T.-H.; Lee, W.-Y.; Kim, C.-S., Journal of Power Sources 2005, 143 (1), 17-23.
[21] Patel, N.; Patton, B.; Zanchetta, C.; Fernandes, R.; Guella, G.; Kale, A.; Miotello, A., International Journal of Hydrogen Energy 2008, 33 (1), 287-292.
[22] Demirci, U. B.; Miele, P., Physical Chemistry Chemical Physics 2014, 16 (15), 6872-6885.
[23] Schlapbach, L.; Züttel, A., Nature 2001, 414 (6861), 353-358.
[24] Tollefson; Jeff, Nature News 2010, 464 (7293), 1262-1264.
[25] Jones, A. D. K.; Bekkedahl, T.; Kiang, C., Nature 1997, 386, 377.
[26] Yang, J.; Sudik, A.; Wolverton, C.; Siegel, D. J., Chemical Society Reviews 2010, 39 (2), 656-675.
[27] Broom, D. P., Potential Storage Materials. In Hydrogen Storage Materials, Springer: 2011; pp 19-59.
[28] Rowsell, J. L.; Yaghi, O. M., Angewandte Chemie International Edition 2005, 44 (30), 4670-4679.
[29] Klontzas, E.; Tylianakis, E.; Froudakis, G. E., Nano letters 2010, 10 (2), 452-454.
[30] McKeown, N. B., International Scholarly Research Notices 2012, 2012.
[31] Züttel, A., Materials today 2003, 6 (9), 24-33.
[32] Bogdanović, B.; Schwickardi, M., Journal of Alloys and Compounds 1997, 253, 1-9.
[33] Züttel, A.; Wenger, P.; Rentsch, S.; Sudan, P.; Mauron, P.; Emmenegger, C., Journal of Power Sources 2003, 118 (1), 1-7.

[34] Gutowska, A.; Li, L.; Shin, Y.; Wang, C. M.; Li, X. S.; Linehan, J. C.; Smith, R. S.; Kay, B. D.; Schmid, B.; Shaw, W., Angewandte Chemie International Edition 2005, 44 (23), 3578-3582.
[35] Xiong, Z.; Yong, C. K.; Wu, G.; Chen, P.; Shaw, W.; Karkamkar, A.; Autrey, T.; Jones, M. O.; Johnson, S. R.; Edwards, P. P., Nature materials 2008, 7 (2), 138-141.
[36] Stephens, F. H.; Pons, V.; Baker, R. T., Dalton Transactions 2007, (25), 2613-2626.
[37] Sutton, A. D.; Burrell, A. K.; Dixon, D. A.; Garner, E. B.; Gordon, J. C.; Nakagawa, T.; Ott, K. C.; Robinson, J. P.; Vasiliu, M., Science 2011, 331 (6023), 1426-1429.
[38] Klooster, W. T.; Koetzle, T. F.; Siegbahn, P. E.; Richardson, T. B.; Crabtree, R. H., Journal of the American Chemical Society 1999, 121 (27), 6337-6343.
[39] Weaver, J.; Shore, S.; Parry, R., The Journal of Chemical Physics 1958, 29 (1), 1-2.
[40] Kodama, G.; Weaver, J.; LaRochelle, J.; Parry, R., Inorganic Chemistry 1966, 5 (5), 710-713.
[41] Thorne, L.; Suenram, R.; Lovas, F., The Journal of Chemical Physics 1983, 78 (1), 167-171.
[42] Parry, R.; Shore, S., Journal of the American Chemical Society 1958, 80 (1), 15-20.
[43] Weaver, J.; Shore, S.; Parry, R., The Journal of Chemical Physics 2004, 29 (1), 1-2.
[44] Lingam, H. K.; Chen, X.; Zhao, J. C.; Shore, S. G., Chemistry-A European Journal 2012, 18 (12), 3490-3492.
[45] Taylor, R.; Schultz, D.; Emery, A., Journal of the American Chemical Society 1958, 80 (1), 27-30.
[46] Hu, M.; Van Paasschen, J.; Geanangel, R., Journal of Inorganic and Nuclear Chemistry 1977, 39 (12), 2147-2150.
[47] Ramachandran, P. V.; Gagare, P. D., Inorganic Chemistry 2007, 46 (19), 7810-7817.
[48] Mayer, E., Inorganic Chemistry 1973, 12 (8), 1954-1955.
[49] Shore, S.; Parry, R., Journal of the American Chemical Society 1958, 80 (1), 12-15.
[50] Adams, R. M.; Beres, J.; Dodds, A.; Morabito, A. J., Inorganic Chemistry 1971, 10 (9), 2072-2074.
[51] Shore, S. G.; Parry, R. W., Journal of the American Chemical Society 1955, 77 (22), 6084-6085.
[52] Xu, Q.; Chandra, M., Journal of Power Sources 2006, 163 (1), 364-370.
[53] Sit, V.; Geanangel, R.; Wendlandt, W., Thermochimica acta 1987, 113, 379-382.
[54] Diwan, M.; Hwang, H. T.; Al-Kukhun, A.; Varma, A., AIChE journal 2011, 57 (1), 259-264.
[55] Moussa, G.; Moury, R.; Demirci, U. B.; Şener, T.; Miele, P., International Journal of Energy Research 2013, 37 (8), 825-842.
[56] Davis, R. E.; Gottbrath, J. A., Journal of the American Chemical Society 1962, 84 (6), 895-898.
[57] Demirci, U. B.; Miele, P., Journal of Power Sources 2010, 195 (13), 4030-4035.
[58] Sun, D.; Mazumder, V.; Metin, O. n.; Sun, S., ACS Catalysis 2012, 2 (6), 1290-1295.
[59] Heldebrant, D. J.; Karkamkar, A.; Hess, N. J.; Bowden, M.; Rassat, S.; Zheng, F.; Rappe, K.; Autrey, T., Chemistry of Materials 2008, 20 (16), 5332-5336.
[60] Stowe, A. C.; Shaw, W. J.; Linehan, J. C.; Schmid, B.; Autrey, T., Physical Chemistry Chemical Physics 2007, 9 (15), 1831-1836.
[61] Baumann, J.; Baitalow, F.; Wolf, G., Thermochimica acta 2005, 430 (1), 9-14.
[62] Orimo, S.-i.; Nakamori, Y.; Eliseo, J. R.; Züttel, A.; Jensen, C. M., Chemical reviews 2007, 107 (10), 4111-4132.
[63] Eberle, U.; Felderhoff, M.; Schueth, F., Angewandte Chemie International Edition 2009, 48 (36), 6608-6630.
[64] Bonatto Minella, C.; Lindemann, I.; Nolis, P.; Kießling, A.; Baró, M. D.; Klose, M.; Giebeler, L.; Rellinghaus, B.; Eckert, J.; Schultz, L., International Journal of Hydrogen Energy 2013, 38 (21), 8829-8837.
[65] Bogdanović, B.; Brand, R. A.; Marjanović, A.; Schwickardi, M.; Tölle, J., Journal of Alloys and Compounds 2000, 302 (1), 36-58.
[66] Sandrock, G.; Gross, K.; Thomas, G., Journal of Alloys and Compounds 2002, 339 (1), 299-308.

[67] Jensen, C. M.; Zidan, R.; Mariels, N.; Hee, A.; Hagen, C., International Journal of Hydrogen Energy 1999, 24 (5), 461-465.
[68] Kim, J. W.; Shim, J.-H.; Kim, S. C.; Remhof, A.; Borgschulte, A.; Friedrichs, O.; Gremaud, R.; Pendolino, F.; Züttel, A.; Cho, Y. W., Journal of Power Sources 2009, 192 (2), 582-587.
[69] Li, L.; Wang, Y.; Qiu, F.; Wang, Y.; Xu, Y.; An, C.; Jiao, L.; Yuan, H., Journal of Alloys and Compounds 2013, 566, 137-141.
[70] Wang, P.; Jensen, C. M., The Journal of Physical Chemistry B 2004, 108 (40), 15827-15829.
[71] Zidan, R. A.; Takara, S.; Hee, A. G.; Jensen, C. M., Journal of Alloys and Compounds 1999, 285 (1), 119-122.
[72] Bogdanović, B.; Felderhoff, M.; Pommerin, A.; Schueth, F.; Spielkamp, N., Advanced Materials 2006, 18 (9), 1198-1201.
[73] Fan, X.; Xiao, X.; Chen, L.; Han, L.; Li, S.; Ge, H.; Wang, Q., International Journal of Hydrogen Energy 2011, 36 (17), 10861-10869.
[74] Pukazhselvan, D.; Hudson, M.; Sinha, A.; Srivastava, O., Energy 2010, 35 (12), 5037-5042.
[75] Clark, T. J.; Russell, C. A.; Manners, I., Journal of the American Chemical Society 2006, 128 (30), 9582-9583.
[76] Cheng, F.; Ma, H.; Li, Y.; Chen, J., Inorganic Chemistry 2007, 46 (3), 788-794.
[77] Jaska, C. A.; Temple, K.; Lough, A. J.; Manners, I., Chemical Communications 2001, (11), 962-963.
[78] de Jongh, P. E.; Adelhelm, P., ChemSusChem 2010, 3 (12), 1332-1348.
[79] Park, J.-H.; Kim, S.-K.; Kim, H. S.; Cho, Y. J.; Park, J.; Lee, K. E.; Yoon, C. W.; Nam, S. W.; Kang, S. O., Chemical Communications 2013, 49 (92), 10832-10834.
[80] Li, Z.; Zhu, G.; Lu, G.; Qiu, S.; Yao, X., Journal of the American Chemical Society 2010, 132 (5), 1490-1491.
[81] Li, Y.; Song, P.; Zheng, J.; Li, X., Chemistry-A European Journal 2010, 16 (35), 10887-10892.
[82] Srinivas, G.; Travis, W.; Ford, J.; Wu, H.; Guo, Z.-X.; Yildirim, T., Journal of Materials Chemistry A 2013, 1 (13), 4167-4172.
[83] Nielsen, T. K.; Javadian, P.; Polanski, M.; Besenbacher, F.; Bystrzycki, J.; Jensen, T. R., The Journal of Physical Chemistry C 2012, 116 (39), 21046-21051.
[84] Gao, J.; Adelhelm, P.; Verkuijlen, M. H.; Rongeat, C.; Herrich, M.; van Bentum, P. J. M.; Gutfleisch, O.; Kentgens, A. P.; de Jong, K. P.; de Jongh, P. E., The Journal of Physical Chemistry C 2010, 114 (10), 4675-4682.
[85] Fan, X.; Xiao, X.; Shao, J.; Zhang, L.; Li, S.; Ge, H.; Wang, Q.; Chen, L., Nano Energy 2013, 2 (5), 995-1003.
[86] Zheng, S.; Fang, F.; Zhou, G.; Chen, G.; Ouyang, L.; Zhu, M.; Sun, D., Chemistry of Materials 2008, 20 (12), 3954-3958.
[87] Stavila, V.; Bhakta, R. K.; Alam, T. M.; Majzoub, E. H.; Allendorf, M. D., ACS nano 2012, 6 (11), 9807-9817.
[88] Baldé, C. P.; Hereijgers, B. P.; Bitter, J. H.; Jong, K. P. d., Journal of the American Chemical Society 2008, 130 (21), 6761-6765.
[89] Mera, G.; Tamayo, A.; Nguyen, H.; Sen, S.; Riedel, R., Journal of the American Ceramic Society 2010, 93 (4), 1169-1175.
[90] Pierson, H. O., Handbook of chemical vapor deposition: principles, technology and applications. William Andrew: 1999.
[91] Hench, L. L.; West, J. K., Chemical reviews 1990, 90 (1), 33-72.
[92] Colombo, P.; Mera, G.; Riedel, R.; Soraru, G. D., Journal of the American Ceramic Society 2010, 93 (7), 1805-1837.
[93] Riedel, R., Naturwissenschaften 1995, 82 (1), 12-20.
[94] Paine, R. T.; Narula, C. K., Chemical reviews 1990, 90 (1), 73-91.

[95] Kaya, K.; Takahashi, H.; Shibata, Y.; Kanno, Y.; Hirai, T., Japanese journal of applied physics 1997, 36 (part 1), 2837-2842.
[96] Dobrzański, L.; Staszuk, M., Journal of Achievements in Materials and Manufacturing Engineering 2010, 43 (2), 552-576.
[97] Xie, E.; Ma, Z.; Lin, H.; Zhang, Z.; He, D., Optical Materials 2003, 23 (1), 151-156.
[98] Stöckel, S.; Marx, G.; Goedel, W. A., Chemical Vapor Deposition 2007, 13 (10), 553-560.
[99] Brinker, C. J.; Scherer, G. W., Sol-gel science: the physics and chemistry of sol-gel processing. Gulf Professional Publishing: 1990.
[100] Hampden-Smith, M. J.; Klemperer, W. G.; Brinker, C. J. In Better ceramics through chemistry V, MRS Symposium Proceedings, 1992.
[101] Gabriel, A. O.; Riedel, R., Angewandte Chemie International Edition in English 1997, 36 (4), 384-386.
[102] Löffelholz, J.; Engering, J.; Jansen, M., Zeitschrift für anorganische und allgemeine Chemie 2000, 626 (4), 963-968.
[103] Colombo, P.; Mera, G.; Riedel, R.; Sorarù, G. D., Journal of the American Ceramic Society 2010, 93 (7), 1805-1837.
[104] Yajima, S.; Hayashi, J.; Omori, M.; Okamura, K., Nature 1976.
[105] Greil, P., Advanced Engineering Materials 2000, 2 (6), 339-348.
[106] Iwamoto, Y., Journal of the ceramic Society of Japan 2007, 115 (1348), 947-954.
[107] Majoulet, O.; Sandra, F.; Bechelany, M.; Bonnefont, G.; Fantozzi, G.; Joly-Pottuz, L.; Malchere, A.; Bernard, S.; Miele, P., J. Mater. Chem. A 2013, 1 (36), 10991-11000.
[108] Majoulet, O.; Salameh, C.; Schuster, M. E.; Demirci, U. B.; Sugahara, Y.; Bernard, S.; Miele, P., Chemistry of Materials 2013, 25 (20), 3957-3970.
[109] Gottardo, L.; Bernard, S.; Gervais, C.; Inzenhofer, K.; Motz, G.; Weinmann, M.; Balan, C.; Miele, P., Journal of materials chemistry 2012, 22 (16), 7739-7750.
[110] Bill, J.; Aldinger, F., Advanced Materials 1995, 7 (9), 775-787.
[111] Termoss, H.; Toury, B.; Pavan, S.; Brioude, A.; Bernard, S.; Cornu, D.; Valette, S.; Benayoun, S.; Miele, P., Journal of materials chemistry 2009, 19 (18), 2671-2674.
[112] Chew, K. W.; Sellinger, A.; Laine, R. M., Journal of the American Ceramic Society 1999, 82 (4), 857-866.
[113] Wynne, K. J.; Rice, R. W., Annual Review of Materials Science 1984, 14 (1), 297-334.
[114] Riedel, R.; Petzow, G.; Klingebiel, U., Journal of materials science letters 1990, 9 (2), 222-224.
[115] Masson, I.; Feiereisen, J.; Michel, J.; George, A.; Mocellin, A.; Blumenfeld, P., Journal of the European Ceramic Society 1994, 13 (4), 355-363.
[116] McCauley, J. W. Structure and Properties of Aluminum Nitride and AlON Ceramics; DTIC Document: 2002.
[117] Hussain, S. S.; Pigeat, P.; Rinnert, P. H.; UHP, N. Elaboration, caractérisation structurale et luminescence de dépots AIN dopés Er obenus par PVD magnétron RF. Nancy 1, 2010.
[118] Shiosaki, T.; Kawabata, A., Ferroelectrics 1982, 42 (1), 219-232.
[119] Merchant, P. P.; Ruby, R. C., Method of making tunable thin film acoustic resonators. Google Patents: 1999.
[120] Galvez, M.; Frei, A.; Meier, F.; Steinfeld, A., Industrial & Engineering Chemistry Research 2008, 48 (1), 528-533.
[121] Kuramoto, N.; Taniguchi, H., Journal of materials science letters 1984, 3 (6), 471-474.
[122] Interrante, L. V.; Lee, W.; McConnell, M.; Lewis, N.; Hall, E., Journal of The Electrochemical Society 1989, 136 (2), 472-478.
[123] Baixia, L.; Yinkui, L.; Yi, L., J. Mater. Chem. 1993, 3 (2), 117-127.
[124] Saito, Y.; Sugahara, Y.; Kuroda, K., Journal of the American Ceramic Society 2000, 83 (10), 2436-2440.

[125] Koyama, S.; Takeda, H.; Saito, Y.; Sugahara, Y.; Kuroda, K., Journal of materials chemistry 1996, 6 (6), 1055-1058.
[126] Janik, J. F.; Paine, R. T., Journal of organometallic chemistry 1993, 449 (1), 39-44.
[127] Ruff, J. K.; Hawthorne, M. F., Journal of the American Chemical Society 1961, 83 (3), 535-538.
[128] Sauls, F. C.; Interrante, L. V., Coordination chemistry reviews 1993, 128 (1), 193-207.
[129] Wiberg, E.; Hertwig, K.; Goubeau, J., Inorganic Chemistry 1948, 24, 155.
[130] Schleich, D. M., Method for production of high purity aluminum nitrides. US Patent 4 767 607: 1988.
[131] Tebbe, F. N.; Bolt, J. D.; Young, R. J., Adv. Ceram., 26 pp. 1989, 63.
[132] Bolt, J. D.; Tebbe, F. N., Adv. Ceram., 26 pp. 1989, 69.
[133] Jiang, Z.; Interrante, L. V.; Kwon, D.; Tham, F. S.; Kullnig, R., Inorganic Chemistry 1992, 31 (23), 4815-4822.
[134] Termoss, H.; Bechelany, M.; Toury, B.; Brioude, A.; Bernard, S.; Cornu, D.; Miele, P., Journal of the European Ceramic Society 2009, 29 (5), 857-861.
[135] R T Baker, J. D. B., G S Reddy, D C Roe, R H Staley, F N Tebbe and A J Vega, Muter Res Soc Symp Proc 1988, 121, 471.
[136] J D Bolt and F N Tebbe, Muter Res Soc Symp Proc 1988, 108, 337.
[137] Maya, L., Adv Ceram Muter 1986, 1, 150.
[138] A Ochi, H. K. B. a. W. E. R., Muter Res Soc Symp Proc 1988, 121, 663.
[139] Roesky, W. R. a. H. W., Adv Muter 1993, 5, 443.
[140] C B Ross, T. W. a. R. M. C., Chem Muter 1991, 3, 768.
[141] T Wade, J. P., E G Garza, C B Ross, D M Smith and R M Crooks, J Am Chem Soc 1992, 114, 9457.
[142] T Wade, J. P., G Garza, C B Ross, D M Smith and R M Crooks, Muter Res Soc Symp Proc 1992, 271, 857.
[143] Z Jiang, L. V. I., D Kwon, F S Tham and R Kullnig,, Inorg Chem 1991, 30, 995.
[144] Interrante, Z. J. a. L. V., Chem Muter 1990, 2, 439.
[145] Russel, M. M. S. a. C., J Am Ceram Soc 1989, 72, 1503.
[146] Russe, M. S. a. C., Muter Res SOC Symp Proc 1988, 121, 477.
[147] Russel, I. T. a. C., J Muter Sci 1990, 25, 3531.
[148] Russel, P. D. a. C., 1992 1992, 27, 133.
[149] Jensen, J. A., Muter Res SOC Symp Proc 1992, 271, 845.
[150] P R Coffman, W. T. P. a. S. K. D., Muter Res SOC Symp Proc 1990, 180, 709.
[151] L V Interrante, L. E. C., C Whitmarsh, W Lee, M Garbauskas and G A Slack,, Muter Res Soc Symp Proc 1986, 73, 359.
[152] Y Sugahara, T. O., 0 Tanegashima, K Kuroda and C Kato, J Ceram Soc Jpn 1992, 100, 101.
[153] 森勇介; 菅原義之, Journal of the Ceramic Society of Japan (日本セラミックス協会学術論文誌) 2006, 114 (1330), 461-472.
[154] Cesari, M.; Cucinella, S., The Chemistry of Inorganic Homo- and Heterocycles, Ed. by Sowerby, D. B. and Haiduc, I., Academic Presss, London, UK 1987, 167-190.
[155] Widany, J. Density-Functional Tight-Binding Calculations on the Structure of Complex Boron Nitride Systems. 1997.
[156] Wentorf Jr, R., Journal of Chemical Physics 1957, 26, 956.
[157] Bundy, F. P.; Wentorf, R. H., The Journal of Chemical Physics 1963, 38 (5), 1144-1149.
[158] Wills, R., International Journal of High Technology Ceramics 1985, 1 (2), 139-153.
[159] Pease, R. S., Acta Crystallographica 1952, 5 (3), 356-361.
[160] Lipp, A.; Schwetz, K. A.; Hunold, K., Journal of the European Ceramic Society 1989, 5 (1), 3-9.
[161] Stock, A.; Pohland, E., Ber. Dtsch. Chem. Ges 1926, 59, 2210-2215.

[162] Wideman, T.; Sneddon, L. G., Inorganic Chemistry 1995, 34 (4), 1002-1003.
[163] VOLKOV, V.; MYAKISHEV, K.; ILINCHIK, E.
[164] Lourie, O. R.; Jones, C. R.; Bartlett, B. M.; Gibbons, P. C.; Ruoff, R. S.; Buhro, W. E., Chemistry of Materials 2000, 12 (7), 1808-1810.
[165] Salles, V.; Bernard, S.; Li, J.; Brioude, A.; Chehaidi, S.; Foucaud, S.; Miele, P., Chemistry of Materials 2009, 21 (13), 2920-2929.
[166] Bechelany, M.; Bernard, S.; Brioude, A.; Cornu, D.; Stadelmann, P.; Charcosset, C.; Fiaty, K.; Miele, P., The Journal of Physical Chemistry C 2007, 111 (36), 13378-13384.
[167] Li, J.; Bernard, S.; Salles, V.; Gervais, C.; Miele, P., Chemistry of Materials 2010, 22 (6), 2010-2019.
[168] Thomas, J.; Weston, N.; O'connor, T., Journal of the American Chemical Society 1962, 84 (24), 4619-4622.
[169] Fazen, P. J.; Beck, J. S.; Lynch, A. T.; Remsen, E. E.; Sneddon, L. G., Chemistry of Materials 1990, 2 (2), 96-97.
[170] Sneddon, L. G.; Mirabelli, M. G.; Lynch, A. T.; Fazen, P. J.; Su, K.; Beck, J. S., Pure and Applied Chemistry 1991, 63 (3), 407-410.
[171] Gervais, C.; Maquet, J.; Babonneau, F.; Duriez, C.; Framery, E.; Vaultier, M.; Florian, P.; Massiot, D., Chemistry of Materials 2001, 13 (5), 1700-1707.
[172] Kim, D.; Economy, J., Chemistry of Materials 1994, 6 (4), 395-400.
[173] Kim, D. P.; Economy, J., Chemistry of Materials 1993, 5 (9), 1216-1220.
[174] Fazen, P. J.; Remsen, E. E.; Beck, J. S.; Carroll, P. J.; McGhie, A. R.; Sneddon, L. G., Chemistry of Materials 1995, 7 (10), 1942-1956.
[175] Mamantov, G.; Margrave, J., Journal of Inorganic and Nuclear Chemistry 1961, 20 (3), 348-351.
[176] Alauzun, J. G.; Ungureanu, S.; Brun, N.; Bernard, S.; Miele, P.; Backov, R.; Sanchez, C., Journal of materials chemistry 2011, 21 (36), 14025-14030.
[177] Charcosset, C.; Bernard, S.; Fiaty, K.; Bechelany, M.; Cornu, D., Dyn. Biochem., Process Biotechnol. Mol. Biol 2007, 1, 15-23.
[178] Zhong, W. Préparation de matériaux à base de nitrure de bore pour des applications' énergie'. Montpellier 2, 2012.
[179] Mazdiyasni, K.; Ruh, R., Journal of the American Ceramic Society 1981, 64 (7), 415-419.
[180] Sinclair, W.; Simmons, H., Journal of materials science letters 1987, 6 (6), 627-629.
[181] Funahashi, T. I., K.; Harita, A.; Uchimura, R. Mechanical properties and microstructure of Si3N4-BN composite ceramics. In Ceramic materials and components for engines. Tennery, V. J. (Ed.), Westerville (OH), Am. Ceram. Soc 1989, 968-976.
[182] Ruh, R.; Bentsen, L. D.; Hasselman, D., Journal of the American Ceramic Society 1984, 67 (5), c83-c84.
[183] Kusunose, T.; Sekino, T.; Choa, Y. H.; Niihara, K., Journal of the American Ceramic Society 2002, 85 (11), 2689-2695.
[184] Morris, J. R. T., R. A. Aluminum Nitride-Boron Nitride composite article and method of making same. 1987.
[185] Shimoda, H. Sintered hard alloys for cutting tools. Japanese patent 61,179,847,. 1986.
[186] Shakeri, M. S., International Journal of Minerals, Metallurgy, and Materials 2013, 20 (5), 450-455.
[187] Ionescu, E.; Kleebe, H.-J.; Riedel, R., Chemical Society Reviews 2012, 41 (15), 5032-5052.
[188] Bechelany, M. C.; Proust, V.; Gervais, C.; Ghisleni, R.; Bernard, S.; Miele, P., Advanced Materials 2014, 26 (38), 6548-6553.
[189] Interrante, L. V.; Moraes, K.; Liu, Q.; Lu, N.; Puerta, A.; Sneddon, L., Pure and Applied Chemistry 2002, 74 (11), 2111-2117.

[190] Moraes, K.; Vosburg, J.; Wark, D.; Interrante, L. V.; Puerta, A. R.; Sneddon, L. G.; Narisawa, M., Chemistry of Materials 2004, 16 (1), 125-132.
[191] Lewis, M.; Barnard, P., Journal of materials science 1980, 15 (2), 443-448.
[192] An, L.; Wang, Y.; Bharadwaj, L.; Zhang, L.; Fan, Y.; Jiang, D.; Sohn, Y.-h.; Desai, V. H.; Kapat, J.; Chow, L. C., Advanced Engineering Materials 2004, 6 (5), 337-340.
[193] Paciorek, K.; Nakahara, J.; Hoferkamp, L.; George, C.; Flippen-Anderson, J.; Gilardi, R.; Schmidt, W. R., Chemistry of Materials 1991, 3 (1), 82-87.
[194] Czekaj, C. L.; Hackney, M. L.; Hurley, W. J.; Interrante, L. V.; Sigel, G. A.; Schields, P. J.; Slack, G. A., Journal of the American Ceramic Society 1990, 73 (2), 352-357.
[195] Boury, B.; Seyferth, D., Applied organometallic chemistry 1999, 13 (6), 431-440.
[196] Dhamne, A.; Xu, W.; Fookes, B. G.; Fan, Y.; Zhang, L.; Burton, S.; Hu, J.; Ford, J.; An, L., Journal of the American Ceramic Society 2005, 88 (9), 2415-2419.
[197] Berger, F.; Weinmann, M.; Aldinger, F.; Müller, K., Chemistry of Materials 2004, 16 (5), 919-929.
[198] Mera, G.; Navrotsky, A.; Sen, S.; Kleebe, H.-J.; Riedel, R., Journal of Materials Chemistry A 2013, 1 (12), 3826-3836.
[199] Riedel, R.; Passing, G.; Schönfelder, H.; Brook, R., Nature 1992, 355 (6362), 714-717.
[200] Janakiraman, N.; Weinmann, M.; Schuhmacher, J.; Müller, K.; Bill, J.; Aldinger, F.; Singh, P., Journal of the American Ceramic Society 2002, 85 (7), 1807-1814.
[201] Su, K.; Remsen, E. E.; Zank, G. A.; Sneddon, L. G., Chemistry of Materials 1993, 5 (4), 547-556.
[202] Wideman, T.; Su, K.; Remsen, E. E.; Zank, G. A.; Sneddon, L. G., Chemistry of Materials 1995, 7 (11), 2203-2212.
[203] Nghiem, Q. D.; Jeon, J.-K.; Hong, L.-Y.; Kim, D.-P., Journal of organometallic chemistry 2003, 688 (1), 27-35.
[204] Srivastava, D.; Duesler, E. N.; Paine, R. T., European journal of inorganic chemistry 1998, 1998 (6), 855-859.
[205] Haberecht, J.; Krumeich, F.; Grützmacher, H.; Nesper, R., Chemistry of Materials 2004, 16 (3), 418-423.
[206] Haberecht, J.; Nesper, R.; Grützmacher, H., Chemistry of Materials 2005, 17 (9), 2340-2347.
[207] Baldus, P.; Jansen, M.; Sporn, D., Science 1999, 285 (5428), 699-703.
[208] Riedel, R.; Kienzle, A.; Dressler, W.; Ruwisch, L.; Bill, J.; Aldinger, F., Nature 1996, 382 (6594), 796-798.
[209] Bernard, S.; Weinmann, M.; Cornu, D.; Miele, P.; Aldinger, F., Journal of the European Ceramic Society 2005, 25 (2), 251-256.
[210] Bernard, S.; Weinmann, M.; Gerstel, P.; Miele, P.; Aldinger, F., Journal of materials chemistry 2005, 15 (2), 289-299.
[211] Gottardo, L.; Bernard, S.; Gervais, C.; Weinmann, M.; Miele, P., Journal of materials chemistry 2012, 22 (34), 17923-17933.
[212] Weinmann, M.; Schuhmacher, J.; Kummer, H.; Prinz, S.; Peng, J.; Seifert, H. J.; Christ, M.; Müller, K.; Bill, J.; Aldinger, F., Chemistry of Materials 2000, 12 (3), 623-632.
[213] Seyferth, D.; Plenio, H., Journal of the American Ceramic Society 1990, 73 (7), 2131-2133.
[214] Sing, K.; Everett, D.; Haul, R.; Moscou, L.; Pierotti, R.; Rouquerol, J.; Siemieniewska, T., Pure and Applied Chemistry 1985, 57 (4), 603-619.
[215] Hirschfeld, D.; Li, T.; Liu, D., Key Engineering Materials 1995, 115, 65-80.
[216] Volf, M. B.; Myhre, S. E.; Fink, K.; Čaślavský, C., Technical glasses. Pitman London: 1961.
[217] Sepulveda, P.; Binner, J., Journal of the European Ceramic Society 1999, 19 (12), 2059-2066.
[218] Colombo, P.; Griffoni, M.; Modesti, M., Journal of sol-gel science and technology 1998, 13 (1-3), 195-199.

[219] Shibuya, M.; Takahashi, T.; Koyama, K., Composites science and technology 2007, 67 (1), 119-124.
[220] Biasetto, L.; Francis, A.; Palade, P.; Principi, G.; Colombo, P., Journal of materials science 2008, 43 (12), 4119-4126.
[221] Hagiwara, H.; Green, D. J., Journal of the American Ceramic Society 1987, 70 (11), 811-815.
[222] GUSAKOVA, K.; GRIGORYEVA, O.; STAROSTENKO, O.; FAINLEIB, A.; GRANDE, D., Advances in progressive thermoplastic and thermosetting polymers, perspectives and applications, 219.
[223] Shi, Y.; Wan, Y.; Zhao, D., Chemical Society Reviews 2011, 40 (7), 3854-3878.
[224] G de Moraes, E.; Colombo, P., Materials Letters 2014, 128, 128-131.
[225] Borchardt, L.; Hoffmann, C.; Oschatz, M.; Mammitzsch, L.; Petasch, U.; Herrmann, M.; Kaskel, S., Chemical Society Reviews 2012, 41 (15), 5053-5067.
[226] Lu, A. H.; Schüth, F., Advanced Materials 2006, 18 (14), 1793-1805.
[227] Terrones, M.; Charlier, J.-C.; Gloter, A.; Cruz-Silva, E.; Terres, E.; Li, Y.; Vinu, A.; Zanolli, Z.; Dominguez, J.; Terrones, H., Nano letters 2008, 8 (4), 1026-1032.
[228] Ying, J. Y.; Mehnert, C. P.; Wong, M. S., Angewandte Chemie International Edition 1999, 38 (1-2), 56-77.
[229] Shi, Y.; Meng, Y.; Chen, D.; Cheng, S.; Chen, P.; Yang, H.; Wan, Y.; Zhao, D., Advanced Functional Materials 2006, 16 (4), 561-567.
[230] Rossinyol, E.; Prim, A.; Pellicer, E.; Arbiol, J.; Hernández-Ramírez, F.; Peiro, F.; Cornet, A.; Morante, J. R.; Solovyov, L. A.; Tian, B., Advanced Functional Materials 2007, 17 (11), 1801-1806.
[231] Brun, N.; Prabaharan, S. R.; Morcrette, M.; Sanchez, C.; Pécastaings, G.; Derré, A.; Soum, A.; Deleuze, H.; Birot, M.; Backov, R., Advanced Functional Materials 2009, 19 (19), 3136-3145.
[232] Lee, J.; Kim, J.; Hyeon, T., Advanced Materials 2006, 18 (16), 2073-2094.
[233] Vakifahmetoglu, C.; Menapace, I.; Hirsch, A.; Biasetto, L.; Hauser, R.; Riedel, R.; Colombo, P., Ceramics International 2009, 35 (8), 3281-3290.
[234] Colombo, P., Journal of the European Ceramic Society 2008, 28 (7), 1389-1395.
[235] Aegerter, M. A.; Leventis, N.; Koebel, M. M., Aerogels handbook. Springer: 2011.
[236] RamaswamyáAravind, P., Journal of materials chemistry 2012, 22 (16), 7676-7680.
[237] Borek, T. T.; Ackerman, W.; Hua, D.; Paine, R. T.; Smith, D. M., Langmuir 1991, 7 (11), 2844-2846.
[238] Borovinskaya, I. P.; Bunin, V. A.; Merzhanov, A. G., Mendeleev communications 1997, 7 (2), 47-48.
[239] Dibandjo, P.; Bois, L.; Chassagneux, F.; Cornu, D.; Letoffe, J. M.; Toury, B.; Babonneau, F.; Miele, P., Advanced Materials 2005, 17 (5), 571-574.
[240] Schlienger, S.; Alauzun, J.; Michaux, F.; Vidal, L.; Parmentier, J.; Gervais, C.; Babonneau, F.; Bernard, S.; Miele, P.; Parra, J., Chemistry of Materials 2011, 24 (1), 88-96.
[241] Perdigon-Melon, J. A.; Auroux, A.; Guimon, C.; Bonnetot, B., Journal of Solid State Chemistry 2004, 177 (2), 609-615.
[242] Lin, C.-A.; Wu, J.; Pan, J.-W.; Yeh, C.-T., Journal of Catalysis 2002, 210 (1), 39-45.
[243] Wu, J. C.; Fan, Y.-C.; Lin, C.-A., Industrial & Engineering Chemistry Research 2003, 42 (14), 3225-3229.
[244] Postole, G.; Caldararu, M.; Ionescu, N.; Bonnetot, B.; Auroux, A.; Guimon, C., Thermochimica acta 2005, 434 (1), 150-157.
[245] Taylor, S. H.; Pollard, A. J., Catalysis today 2003, 81 (2), 179-188.
[246] Ma, R.; Bando, Y.; Zhu, H.; Sato, T.; Xu, C.; Wu, D., Journal of the American Chemical Society 2002, 124 (26), 7672-7673.
[247] Neiner, D.; Karkamkar, A.; Linehan, J. C.; Arey, B.; Autrey, T.; Kauzlarich, S. M., The Journal of Physical Chemistry C 2008, 113 (3), 1098-1103.
[248] Weng, Q.; Wang, X.; Zhi, C.; Bando, Y.; Golberg, D., ACS nano 2013, 7 (2), 1558-1565.

[249] Li, J.; Lin, J.; Xu, X.; Zhang, X.; Xue, Y.; Mi, J.; Mo, Z.; Fan, Y.; Hu, L.; Yang, X., Nanotechnology 2013, 24 (15), 155603.
[250] Moussa, G.; Salameh, C.; Bruma, A.; Malo, S.; Demirci, U. B.; Bernard, S.; Miele, P., Inorganics 2014, 2 (3), 396-409.
[251] Yan, X.-B.; Gottardo, L.; Bernard, S.; Dibandjo, P.; Brioude, A.; Moutaabbid, H.; Miele, P., Chemistry of Materials 2008, 20 (20), 6325-6334.
[252] Majoulet, O.; Alauzun, J. G.; Gottardo, L.; Gervais, C.; Schuster, M. E.; Bernard, S.; Miele, P., Microporous and mesoporous materials 2011, 140 (1), 40-50.
[253] Wolf, E. A.; Fagan, R. J., High porosity aluminum nitride separator. Google Patents: 1993.
[254] Duperrier, S.; Gervais, C.; Bernard, S.; Cornu, D.; Babonneau, F.; Miele, P., Journal of materials chemistry 2006, 16 (30), 3126-3138.
[255] Toyoda, R.; Kitaoka, S.; Sugahara, Y., Journal of the European Ceramic Society 2008, 28 (1), 271-277.
[256] Schulz, S.; Bauer, T.; Hoffbauer, W.; Schmedt auf der Günne, J.; Doerr, M.; Marian, C. M.; Assenmacher, W., Journal of Solid State Chemistry 2008, 181 (3), 530-538.
[257] Trassl, S.; Motz, G.; Rössler, E.; Ziegler, G., Journal of the American Ceramic Society 2002, 85 (1), 239-244.
[258] Gregori, G.; Kleebe, H.-J.; Brequel, H.; Enzo, S.; Ziegler, G., Journal of non-crystalline solids 2005, 351 (16), 1393-1402.
[259] Jagannadham, K.; Sharma, A.; Wei, Q.; Kalyanraman, R.; Narayan, J., Journal of Vacuum Science & Technology A 1998, 16 (5), 2804-2815.
[260] Jones, B. H.; Lodge, T. P., Polym J 2012, 44 (2), 131-146.
[261] Washburn, E. W., Physical review 1921, 17 (3), 273.
[262] Sing, K. S., Pure and Applied Chemistry 1985, 57 (4), 603-619.
[263]http://www1.eere.energy.gov/hydrogenandfuelcells/storage/pdfs/targets_onboard_hydro_storage_explanation.pdf.
[264] Ahluwalia, R.; Hua, T.; Peng, J., International Journal of Hydrogen Energy 2012, 37 (3), 2891-2910.
[265] Brun, N.; Janot, R.; Sanchez, C.; Deleuze, H.; Gervais, C.; Morcrette, M.; Backov, R., Energy & Environmental Science 2010, 3 (6), 824-830.
[266] Fichtner, M., Physical Chemistry Chemical Physics 2011, 13 (48), 21186-21195.
[267] Nielsen, T. K.; Polanski, M.; Zasada, D.; Javadian, P.; Besenbacher, F.; Bystrzycki, J.; Skibsted, J.; Jensen, T. R., ACS nano 2011, 5 (5), 4056-4064.
[268] Stephens, R. D.; Gross, A. F.; Van Atta, S. L.; Vajo, J. J.; Pinkerton, F. E., Nanotechnology 2009, 20 (20), 204018.
[269] Schlienger, S.; Alauzun, J.; Michaux, F.; Vidal, L.; Parmentier, J.; Gervais, C.; Babonneau, F.; Bernard, S.; Miele, P.; Parra, J. B., Chemistry of Materials 2011, 24 (1), 88-96.
[270] Moussa, G.; Demirci, U. B.; Malo, S.; Bernard, S.; Miele, P., Journal of Materials Chemistry A 2014, 2 (21), 7717-7722.
[271] Rouquerol, J.; Avnir, D.; Fairbridge, C.; Everett, D.; Haynes, J.; Pernicone, N.; Ramsay, J.; Sing, K.; Unger, K., Pure and Applied Chemistry 1994, 66 (8), 1739-1758.
[272] Ertuğ, B., 2013.
[273] Sorarù, G. D.; Dalcanale, F.; Campostrini, R.; Gaston, A.; Blum, Y.; Carturan, S.; Aravind, P. R., Journal of materials chemistry 2012, 22 (16), 7676-7680.
[274] Moussa, G.; Bernard, S.; Demirci, U. B.; Chiriac, R.; Miele, P., International Journal of Hydrogen Energy 2012, 37 (18), 13437-13445.
[275] Li, L.; Yao, X.; Sun, C.; Du, A.; Cheng, L.; Zhu, Z.; Yu, C.; Zou, J.; Smith, S. C.; Wang, P., Advanced Functional Materials 2009, 19 (2), 265-271.
[276] Ross, D., Vacuum 2006, 80 (10), 1084-1089.
[277] Debe, M. K., Nature 2012, 486 (7401), 43-51.

[278] www.fueleconomy.gov/feg/fcv_PEM.shtml.
[279] Yadav, M.; Xu, Q., Energy & Environmental Science 2012, 5 (12), 9698-9725.
[280] Dalebrook, A. F.; Gan, W.; Grasemann, M.; Moret, S.; Laurenczy, G., Chem. Commun. 2013, 49 (78), 8735-8751.
[281] Cento, C.; Gislon, P.; Prosini, P., International Journal of Hydrogen Energy 2009, 34 (10), 4551-4554.
[282] Kojima, Y.; Kawai, Y.; Nakanishi, H.; Matsumoto, S., Journal of Power Sources 2004, 135 (1), 36-41.
[283] Zahmakiran, M.; Ozkar, S., Langmuir 2009, 25 (5), 2667-2678.
[284] Kouamé, N. A.; Robert, D.; Keller, V.; Keller, N.; Pham, C.; Nguyen, P., Environmental Science and Pollution Research 2012, 19 (9), 3727-3734.
[285] Blokhina, A.; Kurzina, I.; Sobolev, V.; Koltunov, K. Y.; Mamontov, G.; Vodyankina, O., Kinetics and Catalysis 2012, 53 (4), 477-481.
[286] Bernard, S.; Majoulet, O.; Sandra, F.; Malchere, A.; Miele, P., Advanced Engineering Materials 2013, 15 (3), 134-140.
[287] Passing, G.; Sporn, D.; Thierauf, A., Ceram. Trans. 1995, 58, 75-84.
[288] Hagen, E.; Grande, T.; Einarsrud, M. A., Journal of the American Ceramic Society 2004, 87 (7), 1200-1204.
[289] Bentsen, L. D.; Haselman, D.; Ruh, R., Journal of the American Ceramic Society 1983, 66 (3), C-40-C-41.
[290] Cheng, F.; Kelly, S. M.; Young, N. A.; Hope, C. N.; Beverley, K.; Francesconi, M. G.; Clark, S.; Bradley, J. S.; Lefebvre, F., Chemistry of Materials 2006, 18 (25), 5996-6005.
[291] Glatz, G.; Schmalz, T.; Kraus, T.; Haarmann, F.; Motz, G.; Kempe, R., Chemistry-A European Journal 2010, 16 (14), 4231-4238.
[292] Zaheer, M.; Keenan, C. D.; Hermannsdörfer, J.; Roessler, E.; Motz, G. n.; Senker, J. r.; Kempe, R., Chemistry of Materials 2012, 24 (20), 3952-3963.
[293] Mori, Y.; Ueda, T.; Kitaoka, S.; Sugahara, Y., Nippon seramikkusu kyokai gakujutsu ronbunshi 2006, 114 (6), 497-501.
[294] Zhao, D.; Feng, J.; Huo, Q.; Melosh, N.; Fredrickson, G. H.; Chmelka, B. F.; Stucky, G. D., Science 1998, 279 (5350), 548-552.
[295] Ryoo, R.; Joo, S. H.; Kruk, M.; Jaroniec, M., Advanced Materials 2001, 13 (9), 677-681.
[296] Bernard, S.; Miele, P., 2013.
[297] Fooken, U.; Khan, M. A.; Wehmschulte, R. J., Inorganic Chemistry 2001, 40 (6), 1316-1322.
[298] Löffelholz, J.; Jansen, M., Advanced Materials 1995, 7 (3), 289-292.
[299] Kim, H. E.; J Moorhead, A., Journal of the American Ceramic Society 1994, 77 (4), 1037-1041.
[300] Lavrenko, V.; Alexeev, A., Ceramics International 1983, 9 (3), 80-82.
[301] Bowen, P.; Highfield, J. G.; Mocellin, A.; Ring, T. A., Journal of the American Ceramic Society 1990, 73 (3), 724-728.
[302] Mera, G.; Navrotsky, A.; Sen, S.; Kleebe, H.-J.; Riedel, R., Journal of Materials Chemistry A 2013, 1 (12), 3826-3836.
[303] Hirayama, H.; Kawakubo, T.; Goto, A.; Kaneko, T., Journal of the American Ceramic Society 1989, 72 (11), 2049-2053.
[304] Jacobson, N. S.; Gogotsi, Y. G.; Yoshimura, M., J. Mater. Chem. 1995, 5 (4), 595-601.
[305] de Sola, E. R.; Torres, F. J.; Alarcón, J., Journal of the European Ceramic Society 2006, 26 (12), 2279-2284.
[306] Akdim, O.; Chamoun, R.; Demirci, U. B.; Zaatar, Y.; Khoury, A.; Miele, P., International Journal of Hydrogen Energy 2011, 36 (22), 14527-14533.
[307] Shi, Y.; Wan, Y.; Tu, B.; Zhao, D., The Journal of Physical Chemistry C 2008, 112 (1), 112-116.

[308] Murarka, S.; Chang, C.; Adams, A., Journal of The Electrochemical Society 1979, 126 (6), 996-1003.
[309] Cullis, A.; Canham, L. T.; Calcott, P., Journal of Applied Physics 1997, 82 (3), 909-965.
[310] Qi, G.-J.; Zhang, C.-R.; Hu, H.-F., Journal of nanoscience and nanotechnology 2006, 6 (5), 1486-1488.
[311] Pitchumani, R.; Li, W.; Coppens, M.-O., Catalysis today 2005, 105 (3), 618-622.
[312] Mason, G., Journal of Colloid and Interface Science 1982, 88 (1), 36-46.
[313] Funayama, O.; Tashiro, Y.; Kamo, A.; Okumura, M.; Isoda, T., Journal of materials science 1994, 29 (18), 4883-4888.
[314] Asoro, M.; Kovar, D.; Shao-Horn, Y.; Allard, L.; Ferreira, P., Nanotechnology 2010, 21 (2), 025701.
[315] Simagina, V.; Storozhenko, P.; Netskina, O.; Komova, O.; Odegova, G.; Samoilenko, T. Y.; Gentsler, A., Kinetics and Catalysis 2007, 48 (1), 168-175.
[316] Zhou, L.; Zhang, T.; Tao, Z.; Chen, J., Nano Research 2014, 7 (5), 774-781.
[317] Metin, Ö.; Özkar, S.; Sun, S., Nano Research 2010, 3 (9), 676-684.
[318] Mori, Y.; Sugahara, Y., Applied organometallic chemistry 2006, 20 (8), 527-534.
[319] Schuhmacher, J.; Berger, F.; Weinmann, M.; Bill, J.; Aldinger, F.; Müller, K., Applied organometallic chemistry 2001, 15 (10), 809-819.
[320] Jancke, H.; Engelhardt, G.; Mägi, M.; Lippmaa, E., Zeitschrift für Chemie 1973, 13 (11), 435-436.
[321] Li, Y. L.; Kroke, E.; Riedel, R.; Fasel, C.; Gervais, C.; Babonneau, F., Applied organometallic chemistry 2001, 15 (10), 820-832.
[322] Berger, F.; Mueller, A.; Aldinger, F.; Mueller, K., Zeitschrift für anorganische und allgemeine Chemie 2005, 631 (2-3), 355-363.
[323] Akitt, J., Progress in nuclear magnetic resonance spectroscopy 1989, 21 (1), 1-149.
[324] Choong Kwet Yive, N.; Corriu, R.; Leclercq, D.; Mutin, P.; Vioux, A., Chemistry of Materials 1992, 4 (6), 1263-1271.
[325] Hasegawa, Y. I., M.; Yajima, S. Ibid. 1980, 15, 720.
[326] Burns, G. T. A., T. P.; Hanneman, L. F.; Chandra, G.; Moore, J. A. J. Mater. Sci. 1987, 22, 2609.
[327] Müller, A.; Zern, A.; Gerstel, P.; Bill, J.; Aldinger, F., Journal of the European Ceramic Society 2002, 22 (9), 1631-1643.
[328] Gervais, C.; Babonneau, F.; Ruwisch, L.; Hauser, R.; Riedel, R., Canadian journal of chemistry 2003, 81 (11), 1359-1369.
[329] Riedel, R.; Mera, G.; Hauser, R.; Klonczynski, A., Journal of the Ceramic Society of Japan (日本セラミックス協会学術論文誌) 2006, 114 (1330), 425-444.
[330] Pinkas, J.; Wang, T.; Jacobson, R. A.; Verkade, J. G., Inorganic Chemistry 1994, 33 (19), 4202-4210.
[331] Verdecia, G.; O'Brien, K.; Schmidt, W.; Apple, T., Chemistry of Materials 1998, 10 (4), 1003-1009.
[332] Weinmann, M.; Haug, R.; Bill, J.; de Guire, M.; Aldinger, F., 1998.
[333] Monthioux, M.; Delverdier, O., Journal of the European Ceramic Society 1996, 16 (7), 721-737.
[334] Iwamoto, Y.; Völger, W.; Kroke, E.; Riedel, R.; Saitou, T.; Matsunaga, K., Journal of the American Ceramic Society 2001, 84 (10), 2170-2178.
[335] Cutler, I.; Miller, P.; Rafaniello, W.; Park, H.; Thompson, D.; Jack, K., 1978.
[336] Ruh, R.; Zangvil, A.; Barlowe, J., American Ceramic Society Bulletin 1985, 64 (10), 1368-1373.
[337] Zangvil, A.; Ruh, R., Journal of the American Ceramic Society 1988, 71 (10), 884-890.
[338] Aldinger, F.; Jansen, M., High Performance Non-oxide Ceramics. Springer: 2002.

[339] Ferrari, A.; Robertson, J., Physical review B 2000, 61 (20), 14095.
[340] Ferrari, A. C., Solid State Communications 2007, 143 (1), 47-57.
[341] Wang, H.; Zheng, S.-y.; Li, X.-d.; Kim, D.-p., Microporous and mesoporous materials 2005, 80 (1), 357-362.
[342] Fabien, S. Elaboration de matériaux céramiques poreux à base de SiC pour la filtration et la dépollution. Université Montpellier 2, Montpellier, 2014.
[343] Lacassagne, V.; Florian, P.; Montouillout, V.; Gervais, C.; Babonneau, F.; Massiot, D., Magnetic resonance in chemistry 1998, 36 (12), 956-959.
[344] Fyfe, C. A., Solid state NMR for chemists. Guelph, Ont.: CFC Press: 1983.
[345] Lei, W.; Portehault, D.; Liu, D.; Qin, S.; Chen, Y., Nature communications 2013, 4, 1777.
[346] Xiang, H.; Yang, J.; Hou, J.; Zhu, Q., The Journal of Chemical Physics 2007, 126 (24), 244707.

ANNEX A

A1- Solid-state NMR

When solids are placed in a magnetic field (B0), all nuclei of spin I□,0 undergo interactions of variable intensity:

. Zeeman • fs interaction (HZ)

. Chemical shift interaction (HCS)

. Dipolar interaction (HD)

. Scalar coupling interaction (HJ)

. Quadrupolar interaction (HQ)

The Hamiltonian of the spin is therefore writer as it follows:

H=HZ + HCS + HD + HJ + HQ (A1)

In solutions these interactions are averaged by the very fast molecular movements and in the absence of preferential orientation of the molecules, a single isotropic value is measured. In contrast, in the case of solids (polycrystalline powders) these interactions are not averaged as a result of the orientation of some crystallites along the magnetic field B0. Spectra are therefore constituted of broad bands resulting of the superposition of the contribution linked to each of the sample preferred orientations.

Magic Angle Spinning (MAS)

In order to improve the resolution of solid state NMR spectra, the magic angle spinning technique is commonly used. This consists on the rotation of the sample rotor at an angle of 54°44’ with respect to the spectrometer magnetic field. Indeed, interactions undergone by the sample can be written as a function of the inclination angle β of the rotor with respect to the magnetic field B0, according to the following relation:

ω=ω0 + ω2P2(cosβ) + ω4P4(cosβ) (A2) where P*i* are Legendre polynoms of degree i, and ω*i* are coefficients depending on the interaction and the orientation with respect to the rotor. Legendre polynoms P2 and P4 are defined as:

P2 = (3cos2β - 1)/2 (A3)

$P4 = (35\cos 4\beta - 30\cos 2\beta + 3)/8$ (A4)

According to equation A3, P2 equals zero when $\beta=54°44'$.

In the case of first order interactions P2 do not appear in Eq. (A2): the magic angle spinning allows therefore averaging all the interactions to their isotropic value and considerable improvement of the resolution of spectra. In the case of second order interactions (such as quadrupolar interaction of second order), Eq. (A2) has term P4, which does not equal zero at magic angle. Solid-state NMR spectra of quadrupolar nuclei exhibit therefore distortions and particular band shapes.

Cross Polarization (CP)

The cross polarization technique allows considerable improvement of the sensivity of rare spin nuclei and reduction of the acquisition time if compared to the simple-impulsion sequence. This technique is based on the transfer of a part of the magnetization on the abundant spin I (often 1H) toward rare spins S (in the present case 13C or 29Si) through the dipolar interaction, I-S. At the end of the experiment, the magnetization of abundant spins remains nearly unchanged, while that of rare spins is multiplied by 5 for 13C. In addition, the process of magnetization return to equilibrium is governed by the relaxation time of spins I (tI) and as often is very smaller than tS, the length of the acquisition is considerably diminished if compared to a simple-impulsion experiments performed on the nucleus of spin S. While it allows a great improvement of the solid state NMR-spectra resolution, the MAS technique does not allow the differentiation of protonated sites from non-protonated one. In order to solve this problem, the IRCP method was developed.

Inversion Recovery Cross Polarization (IRCP)

IRCP, or inversion recovery cross polarization, is a sequence similar to MAS but allowing

better differentiation of chemical sites according to the number of protons they are linked to (much like the DEPT and INEPT sequence in liquid-state NMR). It consists in the following action sequence:

– Rare spins polarization during a contact time Tc in order to reach the maximal magnetization Mmax, close to the equilibrium magnetization M0.

– 180° phase inversion during the time Ti (magnetization decreases, equals zero, and changes to reach values –M0 as Ti raises). The protonation degree of a nucleus is then reduced of its magnetization- transfer dynamics: the faster the transfer, the more protonated the nucleus is. In practice, magnetization-transfer dynamics is calculated from the time required to reach inversion of a NMR signal (from a positive to a negative value) on the spectrum.

ANNEX B

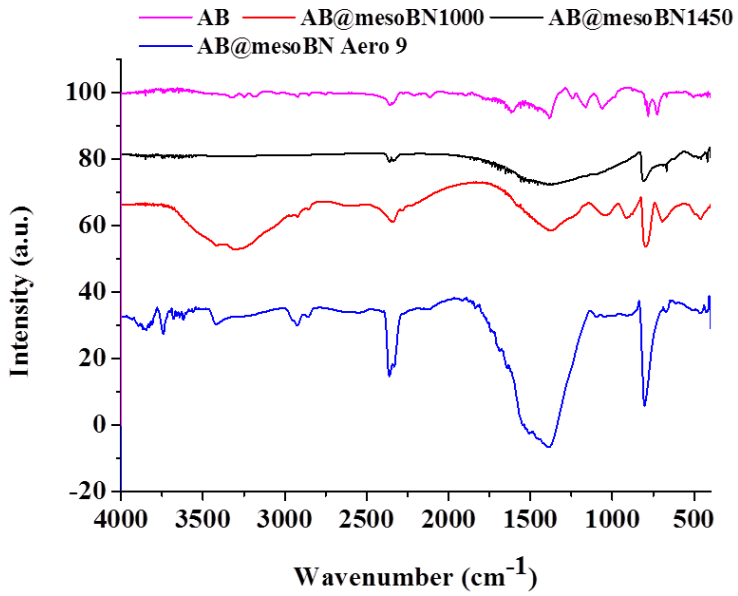

Figure ANNEX B-1: FTIR spectra of AB, AB@mesoBN1000, AB@mesoBN1450 and AB@meso BN Aero 9.

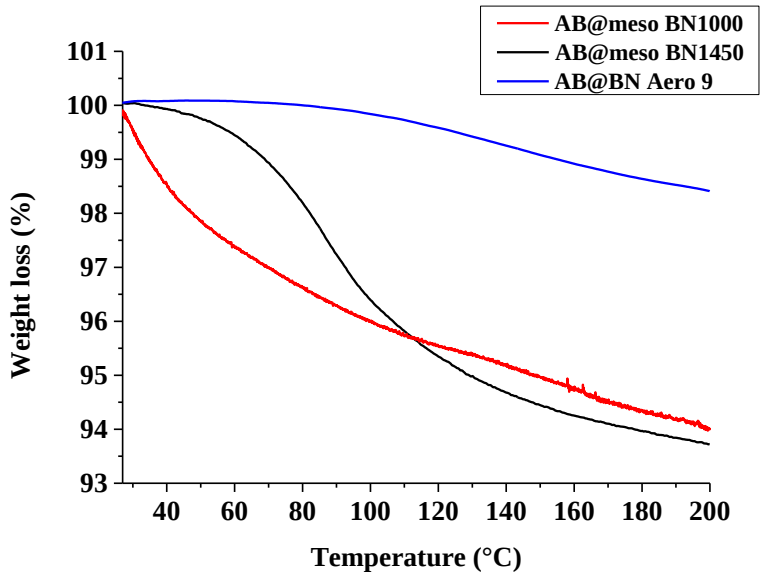

Figure ANNEX B-2: TGA curves of AB@mesoBN1000, AB@mesoBN1450 and AB@BN Aero 9 under N_2 up to 200°C with a heating rate of 5°C.min^{-1}.

Résumé de la thèse en français:

Dans un monde où la révolution industrielle a conduit à l'apparition de conflits graves impactant l'avenir de la planète et de l'humanité à cause du réchauffement climatique et de l'épuisement des ressources fossiles, la recherche s'est rapidement dirigée vers des énergies alternatives qui peuvent palier à ces problèmes. Une des solutions s'avère être le dihydrogène. Le dihydrogène, en raison de sa légèreté, son excellente densité énergétique et son abondance, s'est présenté comme le vecteur d'énergie du futur. Cependant, comme pour toute nouvelle technologie, le développement de l'hydrogène en tant que vecteur d'énergie, et donc le développement d'une économie basée sur l'hydrogène, se heurte à de nombreux problèmes scientifiques et techniques, qui sont liés à la production, le stockage, la distribution et l'utilisation.

Le dihydrogène n'est pas directement disponible dans la nature. Il a cependant l'avantage de pouvoir être produit à partir des trois grandes sources que sont les énergies fossiles, nucléaire et renouvelables. Pour être économiquement et écologiquement viable, la production de dihydrogène doit répondre à trois critères :

1. la compétitivité: les coûts de production ne doivent pas être trop élevés
2. le rendement énergétique: la production ne doit pas nécessiter trop d'énergie
3. la propreté: le processus de fabrication doit être non polluant.

Plusieurs méthodes de production sont aujourd'hui parfaitement opérationnelles (vaporeformage du méthane, électrolyse de l'eau…) mais aucune ne répond simultanément à ces trois critères. De nouvelles voies prometteuses (à partie de la biomasse) sont en cours d'élaboration.

D'autre part le stockage de l'hydrogène est un verrou technologique important et le développement de la pile à combustible en est tributaire. Les technologies de stockage de l'hydrogène sont plus ou moins matures, mais pas encore viables pour une large gamme d'applications, des technologies stationnaires aux applications automobiles, *via* les appareils électriques mobiles et portables.

Il est donc attendu des systèmes de stockage qu'ils soient : sûrs et efficaces, qu'ils permettent un stockage réversible ou à défaut que le cycle de l'hydrogène soit fermé par régénération, qu'ils présentent une température de déshydrogénation relativement faible (85°C pour les applications automobiles), une capacité de stockage en hydrogène de 5.5 % en masse (noté %m) et 40 $g.L^{-1}$

(critères pour 2015) et, qu'ils aient un coût de stockage compétitif. Dans ce contexte, le stockage chimique à l'état solide a montré des spécificités notables, et s'est particulièrement distingué au travers de matériaux capables de stocker jusqu'à 20%m d'hydrogène. Les matériaux à base d'aluminium et de bore, qui ont fait l'objet d'une recherche intensive cette dernière décennie, en sont des exemples typiques. En particulier, les matériaux comme l'alanate de sodium et l'ammoniaborane ont suscité un grand intérêt.

Dans l'idéal, pour ce type de matériaux, on cherche à i) obtenir une température de déshydrogénation basse, ii) minimiser la présence de coproduits gazeux lors de la génération de H_2 qui sont nuisibles pour la pile à combustible, iii) ce que le stockage soit thermodynamiquement réversible. Au mieux, ces matériaux, par exemple l'ammoniaborane (AB), ne peuvent être régénérés qu'à partir du recyclage des sous-produits (résidu solide) de thermolyse.

En essayant d'affiner les solutions pour la production et le stockage de l'hydrogène, la motivation de la recherche dans notre groupe, entre autres disciplines, était de concevoir, étudier et appliquer de nouveaux matériaux inorganiques, en particulier, des matériaux (carbo)nitrures fonctionnels pour les applications de l'énergie. Cette thèse fait partie du projet FUNEA "nitrures fonctionnels pour applications de l'énergie» au sein du 7e programme ITN-Marie Curie dans lequel l'Institut européen des membranes (IEM) est impliqué. L'objectif de ce projet est d'assurer les principaux besoins du 21eme siècle en mettant l'accent sur les applications énergétiques des nitrures. Pour atteindre cet objectif, huit groupes de recherche académiques européens ayant une expertise complémentaire dans la synthèse, le traitement et la caractérisation des matériaux, et cinq partenaires industriels, ont proposé une collaboration pour la recherche et la formation de chercheurs ESR et ER, ainsi que l'émergence d'une nouvelle génération de matériaux avec des fonctionnalités avancées (Figure 1).

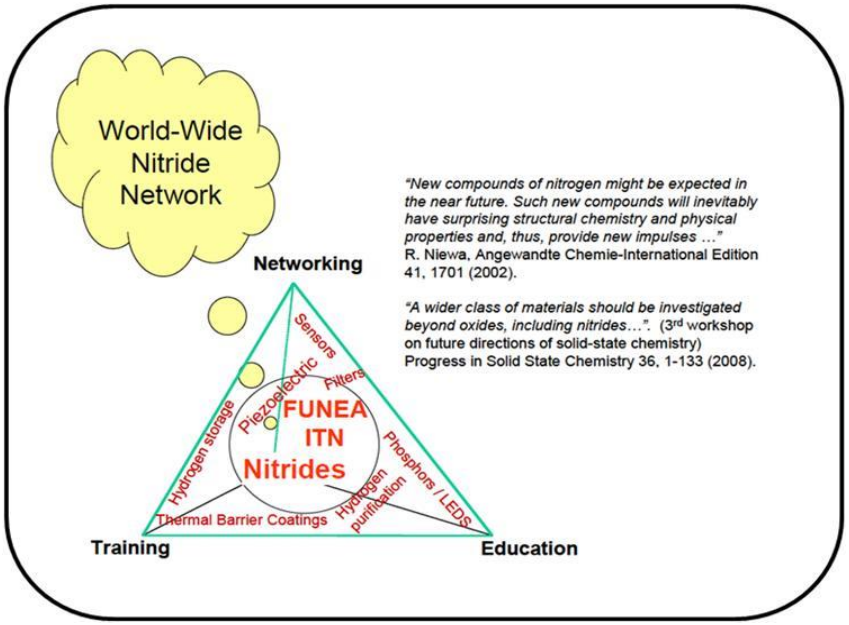

Figure 1: Vue schématique de l'environnement interdisciplinaire et intersectorielle du projet FUNEA.

La recherche présentée dans cette thèse se concentre sur la synthèse et la caractérisation des différents types de matériaux (carbo)nitrure dérivés de polymères précéramiques à porosité contrôlée, impliquant des systèmes binaires (nitrure d'aluminium AIN, nitrure de bore BN) et quaternaire (carbonitrure de silicium modifiés par l'aluminium et le bore) , respectivement, les systèmes SiAlCN et SiBCN). Ces compositions ont été préparés sous forme de matériaux poreux présentant un grand intérêt en tant que:

•support catalytique pour la production de l'hydrogène à partir de l'hydrolyse de $NaBH_4$

• matériau hôte pour le stockage solide de l'hydrogène par nanoconfinement des alanes et boranes.

Le Chapitre I présente les deux principaux points que nous avons mentionnés précédemment: i) la production, et ii) le stockage de l'hydrogène. Nous allons décrire pour chaque point, les matériaux que nous avons étudiés dans la présente thèse. Ensuite, nous allons donner un aperçu non seulement sur les (carbo)nitrure, mais aussi sur les matériaux poreux en particulier ceux dérivés de polymères précéramiques. L'objectif de cette partie portera sur l'intérêt de la voie polymère précéramique (PDC) pour préparer des céramiques poreuses et en particulier. Il était possible de classer les chapitres soit par type de matériaux ou par type d'application (génération d'hydrogène /stockage). Enfin, nous avons décidé de classer les chapitres suivants par type de matériau allant des systèmes binaires qui sont des matériaux conventionnels (AlN et BN) aux systèmes quaternaires

(SiAlCN et SiBCN) qui sont des matériaux plus sophistiqués. Les chapitres II, III et IV sont liées à l'élaboration, mise en forme et applications des matériaux alors que le dernier chapitre (chapitre V) est plus axé sur la chimie des matériaux. Tous ces chapitres impliquent la stratégie PDC pour préparer les matériaux concernés.

Le chapitre II décrit la synthèse et la caractérisation de AlN méso / macroporeux ainsi que des aérogels pour l'évaluation de la déshydrogénation de l'alanate de sodium qui combine une teneur gravimétrique en hydrogène relativement élevée avec des caractéristiques d'absorption/désorption intéressantes et de réversibilité en vue des applications pratiques.

Le chapitre III est consacré à la synthèse et la caractérisation des monolithes mésoporeux de type BN ainsi que les aérogels de nitrure de bore, qui serviront de matériaux hôtes pour confiner l'ammoniaborane, un complexe de stockage d'hydrogène chimique qui a été élu par le département d'énergie (DOE).

Le Chapitre IV rapporte la préparation de nitrures de silicium à porosité ordonnée comme supports catalytiques pour la production d'hydrogène à partir de borohydrure de sodium. En particulier, nous nous sommes concentrés sur la préparation de carbonitrure de silicium modifié par l'aluminium (SiAlCN) et nitrure de silicium (Si_3N_4) comme support pour les nanoparticules de platine (Pt).

L'addition d'AlN (chapitre II) ainsi que BN (Chapitre III), à la céramique à base de Si est connue par optimiser certaines des propriétés des matériaux résultants. Dans ce contexte, le chapitre V est consacré à la synthèse de polycarbosilazanes modifiés par l'aluminium et le bore à travers une approche de précurseurs à source unique. Une étude détaillée de la synthèse de polymères et de la conversion de polymère en céramique est prévue. Comme une preuve de concept de l'intérêt de cette approche, des mousses microcellulaires ont été préparées. Le manuscrit se termine par une conclusion qui résume les résultats et discussions proposées dans chaque chapitre et souligne quelques perspectives.

Le procédé de réplication d'un carbone mésoporeux (CMK-3) et la technologie d'aérogel (en collaboration avec Prof. Soraru, departement of engineering Trento-Italy) ont été appliqués avec succès pour préparer des matériaux AlN méso/macroporeux. L'objectif principal de ce chapitre était de préparer et de caractériser AIN obtenu à partir de la voie PDC. Par conséquent, nous avons étudié (i) la synthèse et la caractérisation d'un précurseur AIN appelé Poly(EthylIminoAlane) (PEIA) (ii) la conversion du PEIA en AIN, (iii) la caractérisation des matériaux finaux avec une attention particulière sur l'effet de la température d'élaboration sur l'évolution de la structure de PEIA en AlN. Puis, nous nous sommes concentrés sur la préparation de deux types d'AlN poreux: le premier type a été obtenu par imprégnation du CMK-3 avec le PEIA suivie d'une pyrolyse en une seule étape sous

ammoniac à 1000°C. Des matériaux méso/macroporeux avec une surface spécifique de 217 $m^2.g^{-1}$ et un volume poreux de 0,71 $cm^3.g^{-1}$ ont été généré. Le deuxième type d'AlN poreux a été obtenu par séchage supercritique du CO_2 suivie d'un processus de pyrolyse en deux étapes, sous azote, puis ammoniac jusqu'à 1000°C. Des aérogels de type AlN sous forme de monolithes ont été obtenus avec une surface spécifique pouvant atteindre 511 $cm^3.g^{-1}$ et un volume poreux de 0,88 m2.g-1). Cela n'a jamais été rapporté et ouvre donc la voie au développement d'AlN comme support catalytique (en raison de sa conductivité thermique élevée) (comme les matériaux piézoélectriques utilisés pour les capteurs). Dans cette thèse, nous avons étudié l'utilisation d'AlN poreux pour le stockage de l'hydrogène. Sur la base des résultats obtenus, il apparait que la déshydrogénation de $NaAlH_4$ est renforcée par le nanoconfinement dans des hôtes poreux et en particulier dans les aérogels de AlN. Les premiers résultats montrent que la décomposition de l'hydrure commence à basse température avec une perte de masse totale environ de 7% à 200°C. La vraie raison de cette différence marquée dans les capacités de stockage de l'hydrogène, en particulier par rapport à CMK-3, est pour l'instant inconnue, mais de façon non équivoque, nous avons proposé une discussion générale dans le présent chapitre.

Dans le Chapitre III, nous avons présenté deux méthodes pour obtenir des matériaux poreux BN. Dans une première méthode, nous avons procédé à la réplication d'un charbon actif sous forme de monolithe. Le procédé consiste à infiltrer ce matériau poreux par le polyborazylène (PB), à pyrolyser le composite obtenu et à éliminer ensuite par traitement thermique sous flux d'ammoniac le carbone. Les monolithes présentent une surface spécifique allant de 728 à 584 $m^2.g^{-1}$ et un volume poreux total de 0.93 à 0.75 $cm^3.g^{-1}$, en fonction de la température de recuit finale avec une distribution de taille de pores étroite centrée sur 5.8 nm. Ces monolithes ont été utilisés comme hôtes pour confiner l'AB avec l'objectif d'améliorer ses propriétés de déshydrogénation. Le composite AB@mesoBN1450 est capable de générer de l'hydrogène pur à de basses températures (40-50°C) par thermolyse.

Ces résultats très intéressants nous permettent d'imaginer l'élaboration d'autres matériaux à base de BN avec une surface spécifique plus grande, ou même de se servir du BN mésoporeux comme support de catalyseur en vue d'optimiser la déshydrogénation de l'ammoniaborane (Figure 2).

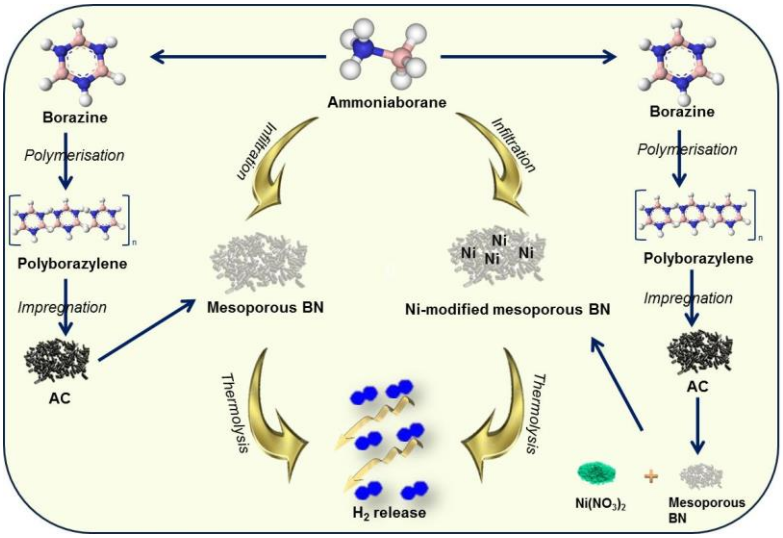

Figure 2: Préparation et application de BN mésoporeux.

Dans un second procédé, nous avons utilisé le même protocole appliqué dans le chapitre II pour l'élaboration des aérogels BN. Le mélange de la polyborazylène (PB) comme précurseur BN avec le DVB comme agent de réticulation dans des solutions très diluées, en présence de platine a conduit à la formation des aérogels monolithiques ayant des SSA aussi élevées que 358 $m^2.g^{-1}$ et un volume poreux de 0.36 $cm^3.g^{-1}$ après pyrolyse à 1000°C sous atmosphère d'azote. La température, la présence de catalyseur et le milieu fortement dilué, sont les paramètres essentiels à l'obtention de l'aérogel BN plus poreux. Ce dernier n'a pas montré des propriétés exceptionnelles d'adsorption de l'hydrogène après le nanoconfinement de AB. Cependant, d'autres caractérisations sont en cours afin d'optimiser le processus et de générer des matériaux plus poreux.

Des céramiques SiAlCN à porosité ordonnée ont été préparées et caractérisées pour être utilisées comme support catalytique de (nano)particules métalliques. Des poudres présentant une structure *P6mm* à symétrie hexagonale ont été synthétisées par nanocasting ou réplication en utilisant du carbone mésoporeux (CMK-3) comme matrice dure et des polymères précéramiques avec différents rapports Al:Si préparés en mélangeant le poly(perhydropolysilazane) ou PHPS (précurseur de Si_3N_4) et le poly(ethyliminoalane) ou PEIA (précurseur de AlCN). Le cycle infiltration-céramisation sous N_2 (2 h à 1000°C, la conversion en céramique), puis sous ammoniac 1000°C (5 h à 1000°C, l'élimination du CMK-3) a donné lieu à la formation de matériaux Si/Al/C/N mésoporeux ordonnés ayant une surface spécifique variant entre 182 à 326 m².g-1, une distribution de taille de pore de 4.1 à 5.9 nm et le volume poreux variant de 0.51 à 0.65 $cm^3.g^{-1}$. Par microscopie électronique, diffraction de rayons X, N_2 sorption, les analyses chimiques, et l'analyse thermogravimétrique à haute température, il a été démontré que les poudres amorphes présentent d'excellentes mésopores uniformes et périodiques en fonction du rendement céramique et donc du

rapport Al:Si fixé lors de la synthèse du polymère. Les matériaux ne aucune perte de masse jusqu'à 1400-1470°C sous flux d'azote et le comportement sous air jusqu'à 1000°C est étroitement dépendant du rapport Al:Si. En outre, en utilisant le même protocole, nous avons synthétisé des nanoblocs mésoporeux de Si_3N_4 hautement ordonnés. Ils sont caractérisés par une surface spécifique très élevée (772.4 $m^2.g$-1), une distribution de taille de pore de 4.85 nm et un volume de pores de 1.19 $cm^3.g^{-1}$. Les poudres céramiques *omp*SiAlCN *omp*Si_3N_4 obtenues ont été ensuite considérées comme supports potentiels pour synthétiser et disperser des (nano)particules de Pt. Ces matériaux mésoporeux hautement stables ont ainsi été évalués avec succès dans la réaction d'hydrolyse d'une solution aqueuse alcaline de borohydrure de sodium à 80°C. Des taux élevés d'hydrogène ont été mesurés pour ces matériaux. La performance est encore significativement supérieure à celle obtenue avec CMK-3 supporté par Pt qui est, en outre, difficile de récupérer après la réaction. En se basant uniquement sur l'évolution de H_2, l'échantillon *omp*Si_3N_4 est clairement le meilleur candidat pour l'hydrolyse catalytique de $NaBH_4$ comme le montre les courbes sur la figure 3.

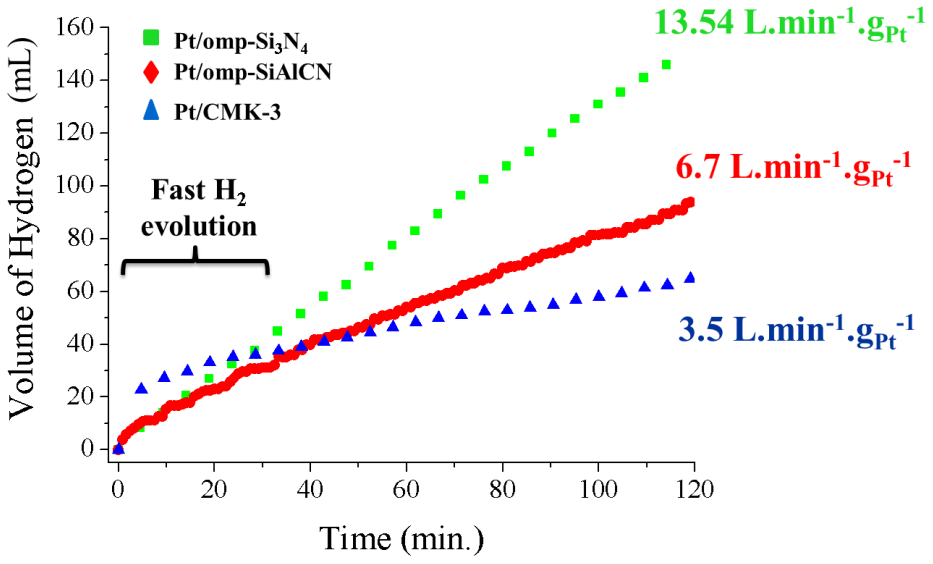

Figure 3: Evolution de H_2 en fonction du temps.

Cependant, plusieurs points doivent être soulignés: i) l'évolution des propriétés texturales du support après production de H_2, ii) Le comportement des nanoparticules de platine, de leur aptitude au frittage et la croissance, iii) la production de H_2 après des cycles successifs.

Une série de polyaluminocarbosilazanes a été synthétisée par réaction du complexe diméthyléthylamine alane avec les polycarbosilazanes. Deux types ont été distingués: 1- A partir du dichlorocarbosilane, et par le biais d'une ammonolyse on obtient le polycarbosilazane.

Ce dernier réagit avec le complexe alane et conduit au polyaluminocarbosilazane, 2- A partir d'un polycarbosilazane commercial et la modification de celui-ci avec de l'aluminium. Nous avons synthétisé également des polyborocarbosilazanes suivant la seconde procédure pour comparer l'effet de substitution de l'Al par du B sur la chimie des polymères, ainsi que sur les propriétés finales des matériaux. Dans tous les cas, nous avons étudié la structure du polymère par FTIR et RMN du solide, la transition de l'état organique polymère à l'état inorganique céramique par DRX, analyses thermogravimétriques, spectroscopie Raman ... En général, les matériaux céramiques restent amorphe même à de très hautes températures, généralement à ~1600°C. De plus le traitement thermique sous N_2 à température élevée a tendance à cristalliser ces matériaux en phases thermodynamiquement stables tels que SiC, Si_3N_4, C, BN ou AlN. Nous avons observé que la transition amorphe-cristallin est étroitement liée à la composition et la structure du polymère précéramique. Après avoir discuté de la synthèse et la caractérisation des polycarboaluminosilazanes, nous avons démontré leur capacité, en particulier le poly(allyl)aluminosilazane (PAAZ) présentant le rendement céramique le plus élevé, à produire des mousses microcellulaires SiAlCN. Pour la préparation de mousses SiAlCN à partir de polymères précéramiques, nous avons utilisé la voie PDC et nous avons mélangé des charges sacrificielles de Polymethylmethacrylate PMMA (avec 25 µm comme diamètre des pores) avec le polymère, puis nous avons appliqué le pressage à chaud du mélange en tant que processus de mise en forme. Après mise en forme, les pièces sont pyrolysées à 1000°C pour transformer le polymère en céramique tout en décomposant les sphères de PMMA (Figure 4).

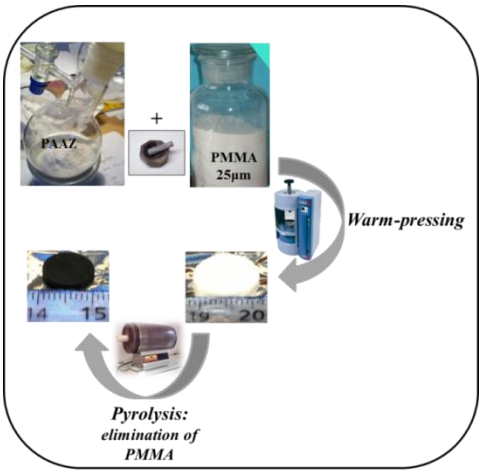

Figure 4: Protocole expérimental du pressage à chaud.

Les rampes de chauffe et de refroidissement doivent être faibles afin de ne pas engendrer de défauts au sein de la pièce voire un effondrement de celle-ci, notamment lorsque les gaz de

décomposition du PMMA s'évacuent. La pyrolyse permet de transformer le polymère en céramique par perte des groupements organiques entourant le squelette de base du polymère, tout en provoquant la décomposition des sphères PMMA entre 220°C et 420°C. Dans ce domaine de température, le polymère doit être suffisamment réticulé pour éviter l'effondrement de la structure poreuse du matériau après élimination du PMMA. Les pièces conservent leur forme originale après une pyrolyse à 1000°C. Cependant la perte de masse du PAAZ combinée à l'augmentation de la densité du matériau (polymère → céramique) provoque un retrait volumique de 40% dans le 3 dimensions. Différents échantillons ont été préparés selon cette stratégie. Ces échantillons ont alors été caractérisés à l'aide de différentes techniques pour fixer les paramètres du procédé qui permettent d'obtenir des mousses satisfaisant notre cahier de charges : mousse à porosité interconnectée et monomodale avec une répartition de pores relativement homogènes. Les paramètres optimaux pour obtenir des mousses microcellulaires ont été fixés comme suit : rapport massique PAAZ:PMMA = 30:70, température de compactage de 80°C et une pression de 74 MPa. Ces mousses présentent une porosité élevée de 75% avec un diamètre de pores moyen de 22 μm). Les perspectives pour ces matériaux sont nombreuses tant au niveau élaboration qu'en terme de caractérisation et d'application comme par exemple l'utilisation de ces mousses en tant que support de catalyseurs (métaux précieux, céramiques oxydes, oxynitrures et nitrures) ainsi que support d'adsorbants.

Pour conclure, ce travail a consisté à élaborer des matériaux poreux (carbo)nitrures potentiels pour la production de l'hydrogène et son stockage. L'objectif général de la thèse réside dans la synthèse, la caractérisation et la mise en forme du nitrure d'aluminium (AIN) et du nitrure de bore (BN) ainsi que silicocarbonitrures modifiés par Al et B (SiAlCN et SiBCN, respectivement) obtenus par la voie polymère précéramique PDC. Comme principaux objectifs de l'application, nous avons étudié leur potentiel en tant que matériaux hôtes pour le nanoconfinement de l'alanate de sodium et de l'ammoniaborane, et en tant que supports de catalyseur mésoporeux ordonnés pour la production d'hydrogène. Cette voie implique généralement trois étapes: i) la synthèse à partir de précurseurs de polymères ou oligomères, ii) la mise en forme du produit (pressage, réplication, imprégnation…), iii) la pyrolyse en atmosphère inerte ou réactive pour la conversion polymère-céramique. Cette voie offre de nouvelles possibilités pour la fabrication de céramiques avancées en contrôlant la porosité souhaitée. Grâce à ce travail, nous avons pu démontrer la faisabilité d'adapter la porosité entre les différents systèmes PDCs complexes et d'appliquer ces matériaux pour la production et le stockage de l'hydrogène. Un défi majeur dans la préparation de ces matériaux est que la synthèse des précurseurs et les dérivés de la céramique doit être effectuée et contrôlée avec une grande précision afin de maintenir un niveau élevé de performances. Il y a beaucoup de perspectives à imaginer sur la

base de ce travail pour l'énergie et la science de l'environnement. Vu le caractère piézo-électrique de AlN, on peut considérer l'application des aérogels AIN pour des capteurs micro/nanométriques. Ils peuvent aussi être très intéressants pour la capture de CO_2 parce que leur chimie de surface peut être bénéfique pour la capture du CO_2 par chimisorption (collaboration avec le professeur Yuji Iwamoto de NiTech, Nagoya (Japon) et le professeur Gian Domenico Soraru de l'Université de Trento (Italie). Nous avons mis en œuvre la méthode de réplication de charbon actif monolithique en la couplant à la voie PDCs (*Polymer-Derived Ceramics*) pour élaborer des monolithes BN mésoporeuses. Ces matériaux présentent une grande surface spécifique et ont été utilisés comme matériau hôte pour infiltrer AB en vue d'améliorer ses propriétés de déshydrogénation. Le nanocomposite formé libère de l'hydrogène pur à partir de 40°C. Ces résultats très intéressants nous permettent d'envisager plusieurs actions à la fois sur le nitrure de bore et sur le nanoconfinement. Nous nous sommes intéressés à combiner l'effet de la nanoconfinement à l'effet de la catalyse homogène Les propriétés chimiques des matériaux mettent en jeu principalement la réactivité de surface et les échanges aux interfaces. Les réactions chimiques sont donc d'autant plus importantes que les matériaux sont plus finement structurés. En catalyse on cherche donc à offrir dans un volume donné la plus grande aire d'interface possible avec le milieu extérieur. On cherche donc à obtenir des catalyseurs à grande porosité, qui doivent aussi permettre des chemins de circulation pour les réactifs et les produits de la réaction.

Jusqu'à présent, nous avons couvert les questions de la production d'hydrogène et stockage. Motivés par la demande croissante dans les membranes techniques pour la perm-sélectivité de l'hydrogène et le traitement des fluides, nous sommes intéressés par l'utilisation des matériaux proposés dans le chapitre V: les systèmes (Si- (B/Al) -CN) à ces fins en raison de leur stabilité thermique et chimique qui est d'une importance cruciale pour la stabilité à long terme des membranes dans des conditions de fonctionnement à haute température. Des essais préliminaires ont été effectués en ce qui concerne le dépôt de polymères précéramiques sur des tubes alumine poreux par le processus de revêtement par immersion suivi d'une pyrolyse ultérieure sous N_2 pour obtenir des membranes céramiques microporeuses. Les principales difficultés rencontrées sont : solubilité difficile, haut degré de réticulation, infiltration... On a réussi à limiter l'infiltration du polymère (HTT1800) dans le support macroporeux, en fixant un rapport de 20/80 (polymère: THF), un taux de 7.7 $cm.min^{-1}$ et un temps de séjour de 30 secondes. Plusieurs études sont nécessaires pour optimiser ce processus et pour extrapoler l'étude et produire des membranes microporeuses SiB(Al)NC.

Résumé en français: Les matériaux céramiques poreux présentent des propriétés de grand intérêt grâce à leur potentiel dans les applications de l'énergie. L'objectif général de cette thèse concerne le développement de matériaux (carbo)nitrures pour la production et le stockage de l'hydrogène (synthèse, caractérisation, propriétés et applications). La voie polymère précéramique, offrant un grand nombre de possibilités dans la chimie et la science des céramiques, est utilisée pour élaborer ces matériaux. Tout d'abord, nous avons préparé les systèmes binaires poreux tels que AlN et BN en répliquant la structure du CMK-3 et du charbon actif. Après pyrolyse, nous avons démontré la faisabilité de produire des nitrures avec une porosité adaptée. Par ailleurs, en couplant la voie polymère précéramique avec la technologie des aérogels, nous avons réussi à préparer des aérogels AlN et BN avec une porosité relativement élevée. Nous avons évalué le potentiel de ces matériaux poreux pour le nanoconfinement de deux hydrures chimiques, l'alanate de sodium et l'ammoniaborane, respectivement. Dans les deux cas, la nanoconfinement a déstabilisé le réseau de l'hydrure et a permis la libération de H_2 à de basses températures ; en outre, dans le cas de l'ammoniaborane confiné, aucun sous-produit gazeux indésirable n'a été détecté, ce qui confirme la pureté du H_2 dégagé. Deuxièmement, nous avons préparé des systèmes quaternaires poreux par association de AlN/BN avec des céramiques à base de silicium. En particulier, nous avons élaboré des céramiques SiAlCN en utilisant deux approches: la voie à « 2 sources » et la voie à « source unique ». En ce qui concerne la première, nous avons préparé des matériaux mésoporeux ordonnés qui ont été utilisés comme supports catalytiques pour l'hydrolyse d'une solution alcaline de borohydrure de sodium. Nous avons réussi à générer du H_2 avec des cinétiques élevées. En ce qui concerne la seconde approche, le travail a porté sur l'étude de la chimie de matériaux SiAlCN et SiBCN. Des mousses cellulaires SiAlCN ont été préparées par l'utilisation de charges sacrificielles.

Résumé en anglais: Porous inorganic materials are of great interest owing to their potential in energy applications. The general objective of the present thesis concerns the development of functional (carbo)nitrides for hydrogen generation and storage (material design, elaboration, properties and applications). The PDCs route, which offers a large number of opportunities in chemistry and ceramic sciences, has been applied to produce functional (carbo)nitrides materials. Firstly, we prepared porous binary systems such as AlN and BN by replicating the structure of CMK-3 and that of activated carbon. After pyrolysis and removal of the template, we demonstrated the feasibility of producing nitrides with tailored porosity. Moreover, by coupling the PDCs route with the aerogel technology, we succeeded in preparing polymer-derived AlN and BN aerogels. We assessed the potential of these porous AlN and BN materials in nanoconfinement of two chemical hydrides, namely sodium alanate and ammoniaborane, respectively. In both cases, the nanoconfinement destabilized the network of the hydride and favored the release of H_2 at low temperature. Besides, in the case of nanoconfined ammoniaborane, no evolution of undesired gaseous by-products was observed, which means that pure hydrogen was produced in our conditions. Secondly, we prepared porous quaternary systems through the association of AlN/BN with Si-based ceramics. In particular, we investigated the preparation of SiAlCN with tailored porosity by using two approaches: the "molecular building block" and "single-source precursor" approaches. Concerning the former, we investigated the preparation of ordered mesoporous materials to be used as catalytic supports for hydrolysis of alkaline solution of sodium borohydride. We succeeded in generating high amounts of H_2 with attractive kinetics. Concerning the latter approach, the work was focused on the investigation of the chemistry of SiAlCN and SiBCN materials with a particular focus on the elaboration of SiAlCN microcellular foams by a sacrificial processing route.

Discipline: Chimie et physico-chimie des matériaux

Laboratoire de recherche: Institut Européen des Membranes (IEM)-UMR-CNRS 5635. Université Montpellier 2- 300 Av. du Professeur Emile Jeanbrau.